Beyond the Bond

Optimizing the Material and Geometric Performance of Additively Manufactured Polymer Interlocking Interlayers to Enable Reversible, Structural Cast-Glass Assemblies

Master Thesis

Pieter van der Werf

TU Delft

Beyond the Bond

Optimizing the Material and Geometric Performance of Additively Manufactured Polymer Interlocking Interlayers to Enable Reversible, Structural Cast-Glass Assemblies

by

Pieter van der Werf
5526353

First supervisor	Dr. ir. Faidra Oikonomopoulou
Second supervisor	Dr. ing. Marcel Bilow
External delegate	Ir. Agnes van der Meij
Project Duration:	Nov, 2025 - Jun, 2026
Faculty:	Architecture and the Built Environment, Delft

TU Delft

Preface

This master's thesis marks the completion of my master's degree in Building Technology at TU Delft.

My passion for technology and engineering started at a very young age, as I was always building things together with my father. By the time I was in high school, I already knew that I wanted to study Architecture at TU Delft, and so in September 2021, I started my bachelor's degree with great excitement. As I progressed, I noticed that my interests gradually shifted from the design aspects of architecture towards its more technical and structural side. I wanted to learn more about structural logic and how it can be integrated into architectural design.

Near the end of my second year, I enrolled for the minor *Bend and Break* at the Faculty of Civil Engineering. During my favourite course there, my team and I had to design a reinforced concrete girder and push it to its limits to determine its load-bearing capacity. We ended up with the best performing design and that experience again sparked my interest in structural engineering. The Building Technology track perfectly combined my interests in both engineering and design, making it an easy choice for my master's. And while this thesis marks the end of that chapter, my academic time in Delft is not over yet. Driven by my eagerness to learn, I will continue with a pre-master at the Faculty of Civil Engineering next academic year.

Over the past few years, and particularly during this past year's graduation project, I have worked with great dedication and enthusiasm. This project specifically allowed me to combine my pragmatic mindset with my recently developed interest in 3D printing. Although this was an individual project, I would like to thank everyone who supported me along the way.

First of all, I would like to thank my mentors for their guidance, commitment, and support. A special thank you to **Dr. ir. Faidra Oikonomopoulou** for your incredible dedication and expertise. Your enthusiastic feedback was a constant source of motivation. Also a special thank you to **Dr. ing. Marcel Bilow**. Your sharp and practical feedback was of great value in developing my initial ideas into well-considered and feasible design solutions.

Next, thank you **Paul de Ruiter**, **Henry Kiksen**, and **Veronika Laszlo** for allowing me to use all the equipment in the LAMA Lab. Your interest in my work made the lab a great place to work. Also a big thank you to **Hans van Ginhoven** for waterjet cutting all test samples I needed on short notice.

Thank you to **Dr. ing. Navid Vafa** for your patience while finalising the shear testing setup, your amazing guidance during the experiments, and your help with the post-processing of all the data. It was a pleasure working with you, and I look forward to possible next steps to come. I would also like to thank **Ake Blom** for helping me assemble the shear setup within the short timeframe of the project.

I would like to thank my family for giving me the opportunity to pursue my ambitions and for supporting me every step of the way. I would also like to thank my fellow students, with whom I had the pleasure of collaborating on several memorable projects over the past few years. To my friends and roommates, thank you for your support and for all the fantastic moments we shared when I was not studying. In particular, to Guus, Joris, and Ruben, thank you for making my student life an unforgettable time.

Lastly, a very special thank you to Yasmine. I am incredibly grateful to have met you. Thank you for your love, support, and for being the person with whom I can share both my time and my ideas. I cherish everything we have done together so far and look forward to everything still to come.

Have fun reading!

Pieter van der Werf
Delft, June 2026

Abstract

Segmented cast-glass assemblies show high potential for transparent, compression-dominated architectural structures, but their reliance on permanent bonding methods currently limits disassembly, reuse, and closed-loop recycling. Directly 3D-printing polymer interlayers onto glass components offers a promising route toward mechanically interlocked, adhesive-free connections. However, the resulting glass–polymer adhesion, thermal stability, interlocking geometry, structural performance, and end-of-life removability require further investigation. This research therefore aims to optimise the material behaviour and geometric interlocking design of an additively manufactured polymer interlayer to achieve reversible and structurally reliable dry-fit connections between planar cast-glass units.

The study followed an iterative research-through-design methodology combining literature review, material screening, geometric development, vault-scale design application, mechanical validation, and demountability testing. Six FDM polymers were directly printed onto glass to evaluate adhesion reliability, thermal behaviour, and substrate recovery. Simultaneously, interlocking typologies were evaluated to define a printable hybrid geometry. For mechanical validation, the three most promising materials were combined with four variants of the developed hybrid interlocking typology, resulting in twelve glass–interlayer–glass specimens tested under combined normal and shear loading.

The material experiments identified reinforced PET-based polymers as the most viable direction, with PETG-CF providing the most favourable balance between adhesion, dimensional stability, print quality, and damage limitation. The final geometry combined distributed surface-based engagement with a removable-key locking mechanism, transferring shear forces through mechanical interlocking rather than permanent bonding. The demountable vault case study established a design shear demand of 1.10 kN per full interlayer. PETG-CF specimens significantly exceeded this demand; the two final geometries both showed utilisation factors below 0.19, with one providing the highest mechanical performance and the other offering the best balance between shear capacity, non-destructive removal, and material recovery.

This research demonstrates that a directly printed, mechanically interlocking polymer interlayer can provide a structurally effective and reversible connection strategy for planar cast-glass components. Thereby, it advances cast-glass construction beyond permanent bonding towards a validated proof-of-concept for adaptable, demountable, and circular structural glass assemblies.

Contents

1

Introduction

1.1. Background

Glass is a unique material with exceptional transparency and high architectural value. These properties, combined with its long-term durability, contribute to its widespread use in buildings. However, the architectural freedom it offers is highly limited by the inherent two-dimensional nature of mass-produced float glass, restricting its application primarily to windows, façades, and partitions (Oikonomopoulou et al., 2025; Van Kessel, 2025). Cast glass components overcome this limitation by enabling volumetric, free-form geometries through the casting process, allowing the design of self-supporting, compressive-only structures that leverage the exceptionally high compressive strength of glass (Oikonomopoulou, 2019). To realize such free-form structures at architectural scale, the glass must be segmented into brick-scale units to reduce annealing time and improve handling (Oikonomopoulou, Bristogianni, Barou, Veer, & Nijsse, 2018).

Segmentation introduces the need to join individual cast-glass units into larger structural assemblies. Currently, such segmented solutions—including the facade of *Crystal Houses* in Amsterdam, the *Crown Fountain* in Chicago, *Atocha Station Memorial* in Madrid, and the *Qaamat Pavilion* in Greenland—typically rely on permanent adhesive bonding techniques. While adhesives provide high structural performance, they create irreversible connections that contaminate the glass surface and prevent clean separation at the end of the service life (Oikonomopoulou & Bristogianni, 2022). As a result, despite glass being theoretically 100% recyclable, reuse and closed-loop recycling of architectural glass remain extremely rare, with most material being downcycled or landfilled (Oikonomopoulou et al., 2023).

Toward a reversible, adhesive-free solution, research by Oikonomopoulou, Bristogianni, Barou, and Veer (2018) at TU Delft explored dry-assembled interlocking cast-glass structures. This research demonstrated that structural stability and load transfer can be achieved through geometric interlocking rather than permanent bonding. Interlocking geometries were developed to provide kinematic constraint, self-alignment, and shear transfer, while a dry interlayer was introduced to mediate the glass–glass interface by preventing direct contact, redistributing stresses, and accommodating manufacturing tolerances. However, embedding interlocking directly in the glass geometry introduces high fabrication complexity, limited tolerance accommodation, and constrains scalability and design adaptability.

Building on this dry-assembly principle, a promising emerging solution developed by Oikonomopoulou et al. (2025) and Van Kessel (2025) is the use of a 3D-printed polymer mechanically interlocking interlayer. By shifting the interlocking function from the glass geometry to a removable, additively manufactured (AM) interlayer, precise geometric control and full customisation become possible without altering the glass components themselves. Such an approach enables dry-fit assembly, reuse, and clean end-of-life separation. However, the concept still requires optimisation and systematic investigation with respect to print parameters, material behaviour, joint geometry, and structural performance to enable a reversible and structurally reliable system for circular cast-glass construction.

1.2. Problem statement

Main problem statement

Free-form cast glass bricks show high but underexploited potential for circular structural assemblies, as current permanent bonding methods restrict reuse and recyclability. A promising emerging solution is the use of a 3D-printed polymer interlayer that enables mechanically interlocked, adhesive-free assemblies. However, polymer–glass adhesion challenges, thermal warping behaviour, and the limited development of interlocking geometries highlight the need for further optimisation to unlock the full potential of reversible cast-glass assemblies.

Sub-problems

1. Although current research identifies PLA and PETG as the most suitable polymers for 3D-printed interlayers in cast-glass assemblies, they still exhibit thermal warping, shrinkage, and inconsistent polymer–glass adhesion, thereby reducing interlayer reliability.
2. The design space of interlocking typologies for polymer interlayers remains largely unexplored, and the most effective geometries for achieving reliable, reversible connections in free-form cast-glass assemblies are still unknown.
3. There is limited research into the structural behaviour and failure mechanisms of polymer interlayers in cast-glass assemblies, leaving their shear resistance, stiffness, and load-transfer mechanisms unvalidated.
4. There is no established strategy for controlled end-of-life separation of the interlayer from the glass surface without causing damage to either material.

1.3. Objectives

General objective

This research aims to advance reversible assembly techniques for free-form cast-glass units by developing and optimising a 3D-printed polymer interlayer for structurally reliable, adhesive-free connections. The objective is to improve the interlayer's material behaviour, geometric interlocking performance, and end-of-life demountability, resulting in a validated proof-of-concept system that demonstrates safe load transfer and non-destructive reversibility.

Sub-objectives

1. Evaluate and optimise the material behaviour of AM polymers for dimensional stability, polymer–glass adhesion, and reliable printing performance.
2. Explore, parametrically model, and optimise interlocking geometries that ensure stable load-transfer while enabling reversible disassembly.
3. Improve the interlayer–glass interface by analysing contact behaviour, frictional performance, and end-of-life demountability to prevent damage to the glass.
4. Experimentally test and validate the mechanical performance of the optimised interlayer under shear loading, and assess its assembly/disassembly behaviour, reuse potential, and recyclability.

1.4. Research deliverables

The primary deliverable of this research is a validated and functional 3D-printed polymer interlayer prototype for the reversible, adhesive-free assembly of planar cast-glass units. Supporting outputs include material-specific print parameters, a novel interlocking geometry, the production and assembly strategy for a demountable glass vault, mechanical validation results, and an evaluation of demountability and reuse potential. Together, these products form a proof-of-concept framework for developing circular and reversible cast-glass assemblies.

1.5. Scope and boundary conditions

This research focuses on the interlayer connection between individual cast-glass units at component and assembly scale. The study is limited to compression-only assemblies composed of planar cast-glass bricks, allowing interlocking and load transfer to be achieved through the polymer interlayer rather than through complex glass geometry. Global building-scale performance and façade-system detailing are outside the scope.

Material

- Current research identifies PLA and PETG as most promising baseline candidates for 3D-printed interlayers in cast-glass assemblies.

Manufacturing

- Only Additive Manufacturing (FDM/FFF) is considered; no injection moulding or advanced industrial processes. The technique must be feasible using widely available equipment.

Performance

- The interlayer must maintain adequate mechanical and environmental performance over time. Long-term effects (creep, ageing, stiffness/strength degradation, weathering, humidity, UV exposure, thermal cycles) are assessed through short-term experiments and literature, not multi-year testing.
- The assembly must provide sufficient structural strength and stability for architectural applications under quasi-static mechanical loading.

Assembly

- The interlayer must be fully demountable from the glass at end-of-life without damaging or contaminating the glass.
- Adhesives, primers and permanent treatments at the interface are initially avoided to ensure clean demountability and recyclability, and are only considered if strictly required to meet minimum performance criteria.
- The design must allow custom geometries and modular flexibility within free-form cast-glass assemblies.

1.6. Research questions

Main research question

How can the material behaviour and geometric interlocking design of an additively manufactured polymer interlayer be optimised to achieve reversible and structurally reliable dry-fit connections between planar cast-glass units?

Sub-questions

1. Which polymer provides the most suitable adhesion behaviour and dimensional stability on planar cast glass, and how can its printing parameters be optimised to minimise defects and maximise performance?
2. What printing tolerances and process limitations arise when depositing an interlocking polymer interlayer directly onto planar cast glass, and how do these constraints restrict the feasible geometric design space?
3. How do different interlayer geometric typologies influence the mechanical engagement mechanisms and resulting load-transfer capacity of the dry-fit connection?
4. How do the optimised material and geometric parameters influence the shear, pull-off, and detachment performance of the glass–interlayer–glass assembly?
5. How can the interlayer be engineered to ensure controlled, non-destructive demountability of the glass units to support reuse and closed-loop recycling?

2

Approach and Methodology

2.1. Methodological framework

The research presented in this report builds on earlier work within the Building Technology track by Van Kessel (2025) on AM polymer interlayers for reversible cast-glass assemblies. It is structured as a literature-driven, experimentally validated research-through-design process, combining material testing, geometric development, mechanical validation, and design application. The sequencing and parallelisation of the research phases are presented in Appendix A.

The research begins with a literature study reviewing structural cast-glass assemblies, joinery techniques, dry and bonded interlayers, and mechanical interlocking typologies. A reference case study is used to position the research within an architectural assembly context. Additive manufacturing constraints, are analysed to understand tolerances, dimensional accuracy, thermal behaviour, and material-process limitations. These findings are synthesised into material requirements and design criteria for AM interlocking interlayers, establishing the initial material and geometric design space.

Based on these requirements, a material pre-selection is conducted. PLA and PETG are taken as baseline materials following Van Kessel (2025), while additional polymers, including fibre-reinforced variants, are considered. Materials are assessed qualitatively against printability, mechanical performance, thermal compatibility, interface behaviour, and circularity criteria, resulting in a reduced set of candidates for experimental testing. In parallel, interlocking typologies are evaluated for compatibility with planar glass interfaces, AM constraints, load transfer, and reversible assembly, leading to the selection of promising geometric design directions.

Experimental work on material-glass compatibility is conducted by 3D-printing directly onto float-glass samples. A custom multi-geometry test coupon is used to assess adhesion, warping, wetting, extrusion quality, and substrate recovery, while key parameters are varied using a one-factor-at-a-time approach. This phase establishes material-specific print settings and identifies the most promising polymers for further geometric development.

The interlocking geometry is developed iteratively through a research-through-design process using Rhino and Grasshopper. Demountability, placement-based assembly, shear transfer, tolerance accommodation, and FDM manufacturability are embedded as primary design drivers. The resulting geometry variants are then combined with the selected materials in a second experimental phase, in which print quality, warping, delamination, and material-geometry compatibility are evaluated at larger interface scale. This step narrows the material-geometry combinations for mechanical validation.

In parallel, a demountable glass vault is developed as a design application case. The vault translates the interlayer concept into an architectural assembly by defining the parametric geometry, production process, assembly sequence, tolerance strategy, and structural demand. Wind-load calculations and a Karamba3D model are used to determine the maximum shear demand that the interlayer must resist, providing a performance threshold for the subsequent shear tests.

Mechanical validation is conducted on selected glass-interlayer-glass specimens under combined normal and shear loading. Load-displacement behaviour, peak capacity, residual response, glass damage, and failure mechanisms are documented to evaluate the structural performance of each material-geometry combination. These results are compared with the shear demand derived from the vault model to assess whether the interlayer concept can resist the required lateral loads.

Demountability is evaluated through two end-of-life scenarios: direct component reuse and material-level recovery. The first scenario focuses on dismantling the vault, while the second evaluates controlled removal of the polymer interlayer from the glass substrate. Manual and tool-assisted removal tests are used to assess glass damage, polymer residue, removal effort, and reuse potential.

Following mechanical and demountability evaluation, a 1:1 scale three-brick assembly prototype is produced to translate the selected assembly principle into a tangible model. Due to available fabrication resources and required surface quality, the prototype uses separately printed interlayers bonded to the glass blocks. It is therefore not treated as additional validation of the final direct print-on-glass production method, but as a real-scale assembly demonstrator for evaluating physical fit, key insertion, spatial readability, and the overall assembly logic.

Together, these sequential and parallel methods form a coherent storyline from literature-informed definition, through material and geometric optimisation, to structural validation, demounting evaluation, architectural application, and real-scale prototyping. The result is a validated proof-of-concept framework for reversible polymer interlayers in circular cast-glass assemblies.

2.2. Research relevance

Socially, this research contributes to the transition towards circular construction by addressing one of the main limitations of current structural cast-glass assemblies: their reliance on permanent adhesive bonding. Adhesives can provide high structural performance, but they also prevent clean end-of-life separation and thereby complicate reuse, repair, and closed-loop recycling. By developing a reversible interlocking interlayer system, this research explores how cast-glass components can retain their material value beyond a single use cycle. The work therefore supports longer material lifespans and contributes to the broader shift from demolition-based construction towards recoverable and adaptable building systems.

Professionally, this research presents a design and fabrication method for reversible cast-glass assemblies using standardised planar glass components and AM polymer interlayers. By shifting geometric complexity from the glass unit to the interlayer, the system reduces the need for complex cast-glass geometries while maintaining design flexibility. The use of parametric modelling further enables the interlayer to be adapted to varying angles, assembly configurations, and structural requirements. This provides architects, engineers, and fabricators with a workflow in which material behaviour, digital design, fabrication constraints, and assembly logic are integrated from the start of the design process.

Scientifically, this study contributes experimental insight into the relationship between polymer material behaviour, FDM process parameters, interlocking geometry, and glass–polymer interface performance. It provides comparative data on adhesion, warping, delamination, print quality, substrate damage, shear response, failure mechanisms, and demountability for multiple polymer candidates. By combining material experiments, geometric design development, mechanical validation, and end-of-life removal tests, the research expands the knowledge base for reversible polymer interlayers in structural cast-glass assemblies. The findings also provide a methodological basis for future research into dry, mechanically interlocking interfaces for circular construction systems.

3

Literature review

3.1. Introduction

3.1.1. Cast glass components: the need for segmentation

Cast glass components offer high compressive strength and enable free-form volumetric geometries that are not achievable with planar float or laminated glass. Despite these advantages, cast glass fabrication is governed by a set of interrelated constraints that fundamentally limit feasible component size. Proper annealing is required to relieve residual internal stresses introduced during the fabrication process, with annealing time increasing exponentially with component volume. In addition, increasing component volume raises the likelihood of critical flaws, thereby lowering the probabilistic strength (Oikonomopoulou, 2019). Finally, the need for high-precision moulds, homogeneous mass distribution, and the weight of solid glass components increases cost and complicates handling and assembly. All together, these constraints make segmentation of cast glass structural applications unavoidable, resulting in assemblies composed of smaller, solid units, typically comparable in scale to masonry bricks (Oikonomopoulou, Bristogianni, Barou, Veer, & Nijsse, 2018).

3.1.2. Existing connection strategies for cast-glass assemblies

Segmented cast-glass structures inherently require a joinery system to connect individual units into a larger structural assembly. Because glass is brittle and highly sensitive to local stress concentration, these connections must accommodate fabrication tolerances, prevent direct glass-to-glass contact, and provide controlled load transfer between adjacent components (Oikonomopoulou, Bristogianni, Barou, & Veer, 2018). In compression-only cast-glass structures, the joint design therefore plays a critical role in both structural reliability and constructibility. Oikonomopoulou, Bristogianni, Barou, Veer, and Nijsse (2018) identify three main joinery strategies for segmented cast-glass assemblies: additional substructures, adhesive bonding, and dry mechanical interlocking (see Figure 3.1). Each approach differs significantly in their implications for structural behaviour, transparency, assembly complexity, and circularity.

Additional substructures

The first connection method relies on an additional load-bearing substructure, typically made of metal, to stabilise the glass assembly and carry tensile forces (see Figure 3.1a). The glass components mainly remain in compression, while the external structure provides global stability. While this approach enables structurally reliable systems, it increases material use and reduces transparency (Oikonomopoulou, Bristogianni, Barou, Jacobs, et al., 2018). When combined with adhesives or mechanical fixings, it also complicates disassembly and limits the reuse potential of the glass components.

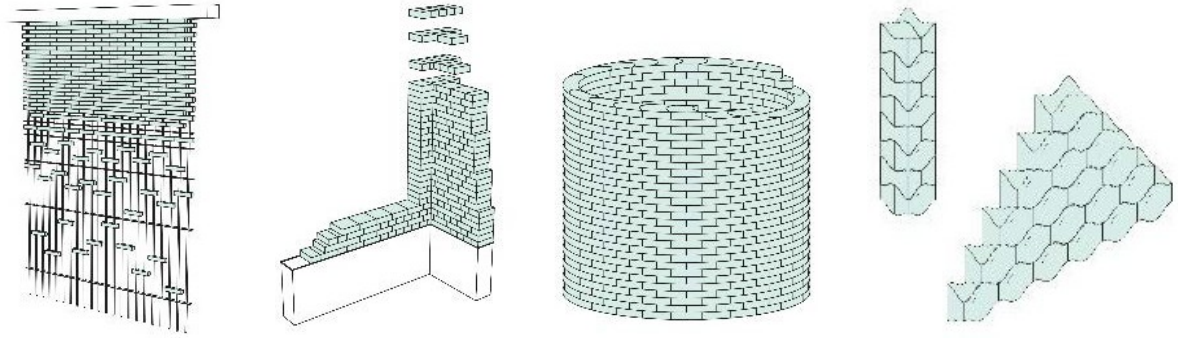

(a) Additional substructure **(b)** Adhesive bonding **(c)** Dry mechanical interlocking

Figure 3.1: Existing connection strategies for segmented cast-glass assemblies. Source: (Oikonomopoulou, Bristogianni, Barou, Veer, & Nijsse, 2018)

Adhesive bonding

A second widely used approach is the permanent bonding of glass components using stiff or flexible adhesives (see Figure 3.1b), such as silicones, polyurethanes, epoxies, or acrylates (Oikonomopoulou & Bristogianni, 2022). Adhesive bonding can create monolithic structural behaviour and achieve high load-bearing capacity while retaining transparency (Dimas et al., 2022). However, the irreversible nature of adhesive joints contaminates the glass surface, making clean disassembly, reuse, and closed-loop recycling difficult or impossible. In addition, adhesive bonding generally requires high fabrication precision and controlled assembly conditions, limiting adaptability and scalability (Oikonomopoulou & Bristogianni, 2022).

Dry mechanical interlocking

Dry mechanical interlocking relies on geometric constraints between components to achieve structural stability without permanent bonding (see Figure 3.1c). This strategy avoids adhesives and enables reversible assembly, making it highly relevant for circular cast-glass construction. It is well aligned with the compression-dominated behaviour of glass and can support self-aligning, demountable assemblies. However, a dry interlayer remains essential to prevent direct glass-to-glass contact, accommodate tolerances, and mediate load transfer between components. Compared with sub-structured and adhesively bonded systems, dry mechanical interlocking offers the most promising balance between structural performance, transparency, and circularity (Oikonomopoulou, Bristogianni, Barou, Jacobs, et al., 2018).

3.1.3. Existing dry interlayer systems

A dry interlayer is essential in segmented cast-glass assemblies because it prevents direct glass-to-glass contact, distributes stresses homogeneously, and compensates for surface asperities and fabrication tolerances. Without such an intermediate layer, local contact between brittle glass components can result in peak stresses and premature failure (Oikonomopoulou, Bristogianni, Barou, Jacobs, et al., 2018). Previous research therefore shows that the performance of dry-assembled glass structures depends on both the geometry of the glass units and material behaviour and detailing of the interlayer.

Monomaterial dry interlayers

Monomaterial interlayers consists of a single material and therefore offer a relatively simple fabrication route. Dimas et al. (2022) distinguish between polymers, elastomers, and metals. Polymers such as PU, PVC, PETG/Vivak, can provide good shear capacity and geometric adaptability, but are generally sensitive to long-term creep. Elastomers, such as neoprene, silicone, and PTFE, are effective in accommodating tolerances due to their flexibility, but there performance strongly depends on thickness, stiffness, and interface stability (Oikonomopoulou et al., 2019). Metals, such as aluminium or lead sheets, offer excellent creep resistance and stress distribution when applied in thin layers, but are prone to stiffness mismatch, direct glass contact, and limited compliance.

Hybrid dry interlayers

Hybrid interlayers combine multiple materials to balance stiffness, deformation capacity, and creep resistance. Examples include soft-core aluminium systems and laminated PU systems with embedded metal inserts. According to Dimas et al. (2022), these solutions can improve mechanical performance compared to monomaterial interlayers, but generally do so at the cost of increased fabrication complexity, reduced design flexibility, and more difficult scalability.

Overall, existing dry interlayers demonstrate the importance of the intermediate material in achieving safe load transfer and tolerance accommodation. However, they remain limited by trade-offs between stiffness, compliance, creep resistance, geometry, and fabrication complexity. This motivates the exploration of AM polymer interlayers, where material behaviour and geometric interlocking can be designed together within a single removable interface.

3.1.4. Emerging concept: 3D-printed interlocking polymer interlayer

While dry mechanical interlocking addresses many limitations of permanent bonding, its performance depends strongly on the design of the interface between adjacent glass components. Building on previous research by Van Kessel (2025), an emerging concept is the use of a 3D-printed polymer interlocking interlayer that shifts the interlocking function from the glass geometry to a removable interface layer (see Figure 3.2). This allows standardised planar glass components to be used, while geometric complexity, tolerance accommodation, and load-transfer mechanisms are integrated into the interlayer itself.

By directly depositing the polymer onto the glass surface, this method avoids permanent adhesives while still enabling the interlayer to remain fixed during assembly. Additive manufacturing further allows the interlocking geometry to be customised for different joint angles, component layouts, and structural requirements. In principle, this creates a dry-fit connection that combines controlled mechanical engagement with future demountability and reuse.

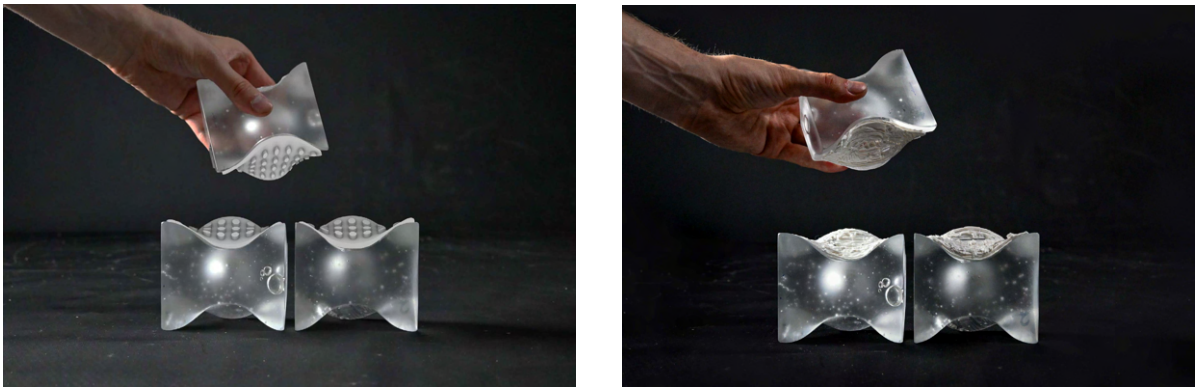

(a) Intended interlayer geometry **(b)** Fabricated interlayer geometry

Figure 3.2: 3D-printed interlocking polymer interlayer, showing the intended geometry and the fabricated result. Source: Van Kessel (2025)

However, the concept also introduces several unresolved challenges. Reliable polymer–glass adhesion must be achieved without primers or permanent bonding, while thermal shrinkage and warping during printing can compromise dimensional accuracy and interface stability. In addition, the structural behaviour, failure mechanisms, manufacturability, and demountability of 3D-printed interlocking polymer interlayers are still insufficiently established. This chapter therefore develops the theoretical foundation required to design, evaluate, and optimise such interlayers for reversible cast-glass assemblies.

3.2. Case study: The Glass Vault

The Glass Vault, also known as *LightVault*, is a 2 m high by 2.6 m wide double-curved glass brick vault (see Figure 3.3), built as a collaboration between *SOM*, *Princeton University's c.r.e.A.te lab* and *Form Finding Lab*, with assistance from the *TU Delft Glass Group*. The vault was assembled live during the *Anatomy of Structure 2020 exhibition* in London using 338 un-machined standard cast-glass bricks and served as a proof-of-concept for compressive-only glass masonry structures (Parascho et al., 2021).

For this research, *The Glass Vault* is used as a reference case because it demonstrates that complex cast-glass vaulting can be achieved using standard brick-shaped components, computational design, and a carefully controlled assembly sequence. At the same time, the project exposes a key limitation of current cast-glass construction: its reliance on permanent epoxy putty as an interlayer. While this interlayer enabled tolerance compensation and structural stability, it prevents clean disassembly and limits reuse or closed-loop recycling. This makes *The Glass Vault* a highly relevant precedent for developing a demountable alternative utilizing polymer interlayers.

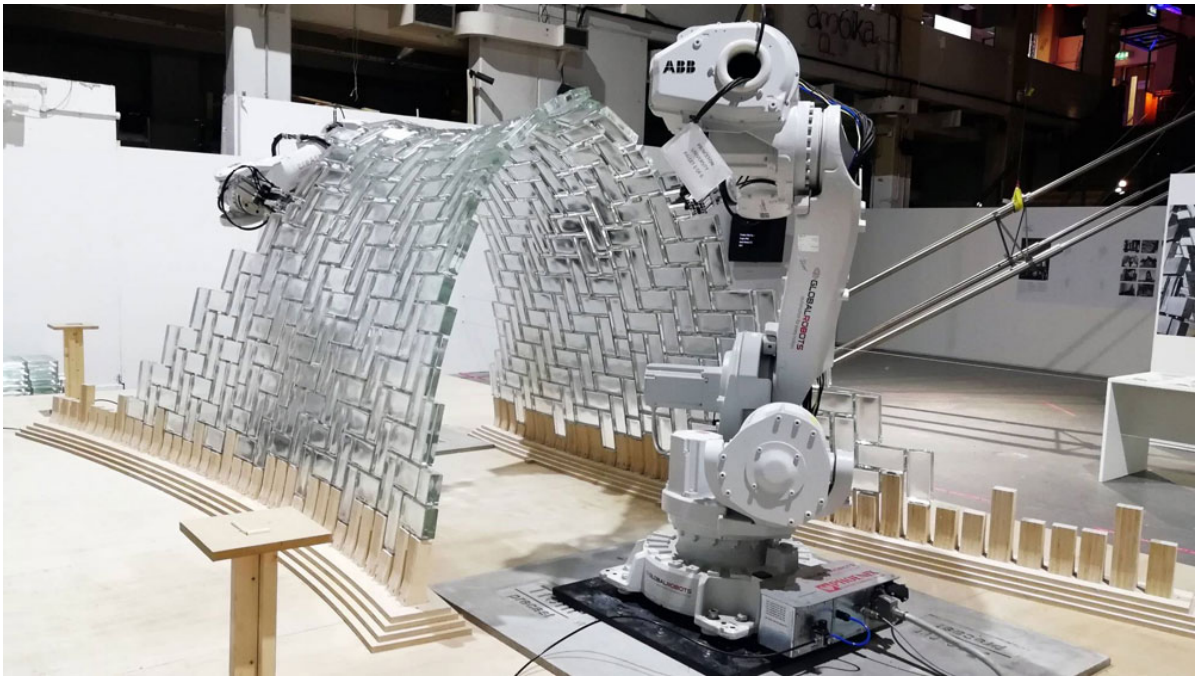

Figure 3.3: The *Glass Vault*, a robotically assembled cast-glass brick vault used as a reference case for this research. Image credit: Maciej Grzeskowiak

Design and construction overview

The Glass Vault used a herringbone tessellation pattern to create an interlocking brick layout that ensures stability during and after assembly (Parascho et al., 2021). Due to the project's limited budget, the bricks were not post-processed, resulting in size deviations of approximately $\pm$ 1 mm. To accommodate these deviations, the interlayer system consisted of opaque grey PIG™ Multi-Purpose Epoxy Putty, combined with standardised wooden wedges where needed. This allowed the varying gaps created by mapping flat bricks onto a double-curved geometry to be absorbed during construction (Oikonomopoulou & Bristogianni, 2022; Parascho et al., 2021).

Assembly process and sequence

The vault was assembled using two stationary, cooperating robotic arms (see Figure 3.3). Parascho et al. (2021) explain that to eliminate the need for temporary scaffolding, the robots alternated roles: one arm supported the partially completed structure while the other placed a new brick and held it in position until the fast-setting epoxy, with a handling time of approximately 3–5 minutes (Oikonomopoulou & Bristogianni, 2022), had hardened.

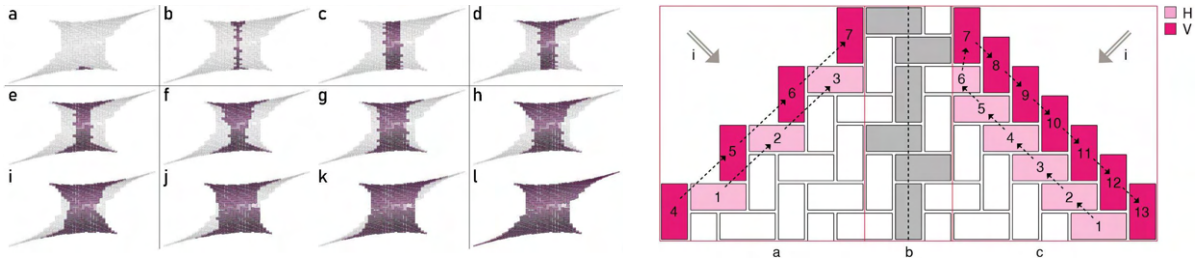

(a) Assembly sequence

(b) Diagonal stepping construction sequence

Figure 3.4: Overview of *The Glass Vault* assembly sequence, illustrating the construction logic and diagonal expansion strategy. Source: Parascho et al. (2021)

The construction sequence followed a specific geometric logic, starting with a central arch that established the initial load-bearing spine of the vault (see Figure 3.4a). From this central arch, the structure expanded diagonally outwards, ensuring proper weight transfer and stability (see Figure 3.4b). This diagonal stepping sequence distinguishes the two expansion patterns (a and c), the central arch (b), the brick insertion direction (i), and the alternating horizontally (H) and vertically (V) oriented bricks. Bricks were bonded only on the bottom and one side to simplify robotic path planning and avoid alternating between vertical and horizontal placement (Parascho et al., 2021; Parascho et al., 2020).

Tolerance management and structural behaviour

Because the cast-glass bricks were not post-processed, dimensional deviations and gap variations were unavoidable. The epoxy putty was selected for its high creep resistance, rigidity, and gap-filling capacity, allowing gaps up to 17.5 mm to be absorbed. Wooden wedges were additionally used for larger discrepancies (Oikonomopoulou & Bristogianni, 2022). Structurally, the vault exhibits membrane behaviour. During construction, the epoxy putty provided sufficient shear tensile strength of 6.2 MPa and compressive strength of 55 MPa to support the self-weight of up to five cantilevered glass bricks (Oikonomopoulou & Bristogianni, 2022; Parascho et al., 2020). Once the final keystone brick closed the central arch, the forces redistributed through the compression-only geometry, transferring the self-weight safely to the foundation (Xi Han et al., 2023).

Assembly challenges and solutions

The main design challenge of *The Glass Vault* was the mapping of standard flat bricks onto a double-curved surface, which generated large and irregular joint gaps. This was mitigated through computational optimisation of the tessellation pattern, ensuring that approximately 80% of the gaps remained below the 17.5 mm threshold that could be accommodated by the epoxy putty. In combination with adaptive robotic path planning, the thick and mouldable interlayer enabled the vault to be assembled despite the dimensional variation of the un-machined bricks (Parascho et al., 2021).

For this research, the most important lesson is that the interlayer is not a secondary detail, but a critical enabling component. In *The Glass Vault*, the epoxy putty simultaneously provided tolerance compensation, temporary stability during construction, and structural load transfer in the completed assembly. However, because it is permanent, the same interlayer also prevents the system from being circular. This creates the central design challenge addressed in this thesis: developing an interlayer that can provide comparable assembly and structural functions while remaining reversible.

Case study conclusions

The Glass Vault demonstrates that complex glass masonry can be realised using standard cast-glass bricks, a compression-only vault geometry, robotic assembly, and a high-fill interlayer capable of absorbing significant tolerance variation. However, the use of permanent epoxy putty prevents clean disassembly and limits material circularity. The demountable vault later developed in this research builds on these lessons by replacing the permanent interlayer with an AM, removable polymer interlayer. Rather than reproducing *The Glass Vault* directly, this research translates its compression-dominated vault principle into a modular and reusable system. The central-arch and diagonal-expansion sequence are used as assembly references, while the interlayer is redesigned to support reversible construction, controlled load transfer, and future component recovery.

3.3. Planar vs non-planar cast glass components

Dry-stacked cast-glass assemblies can be realised using either planar components with flat contact interfaces or non-planar components with curved or interlocking interfaces. In both cases, a compliant interlayer is required to prevent direct glass-to-glass contact, distribute stresses, accommodate surface asperities, and support reversible assembly (Oikonomopoulou et al., 2025). The key difference lies in where the interlocking function is introduced. For non-planar components, interlocking and angular variation are embedded directly in the glass component. In planar components, the glass remains standardised and the interlocking function is shifted to the interlayer.

Planar cast-glass components (see Figure 3.5a) are characterised by a flat and repeatable interface, making them compatible with conventional Cartesian additive manufacturing workflows (Van Kessel, 2025). This allows the interlayer geometry to control alignment, shear transfer, and angular variation while keeping the glass components simple and reusable. Non-planar cast-glass components (see Figure 3.5b), by contrast, are characterised by (double) curved interfaces, integrating geometric variation directly into the glass itself. While this can provide interlocking at the component level, it also increases casting complexity, demands higher fabrication precision, and often requires component-specific interlayers or multi-axis fabrication methods (Dimas et al., 2022; Oikonomopoulou, Bristogianni, Barou, Jacobs, et al., 2018; Van Kessel, 2025).

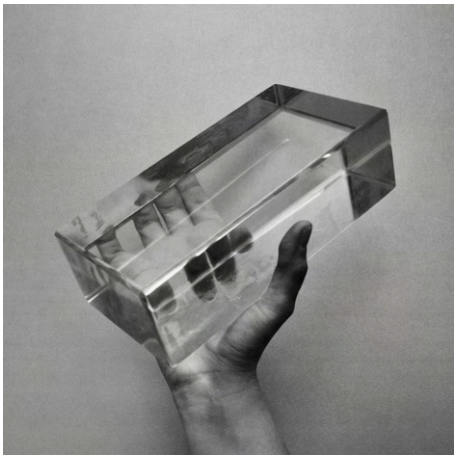

(a) Planar cast-glass component. Image credit: Faidra Oikonomopoulou

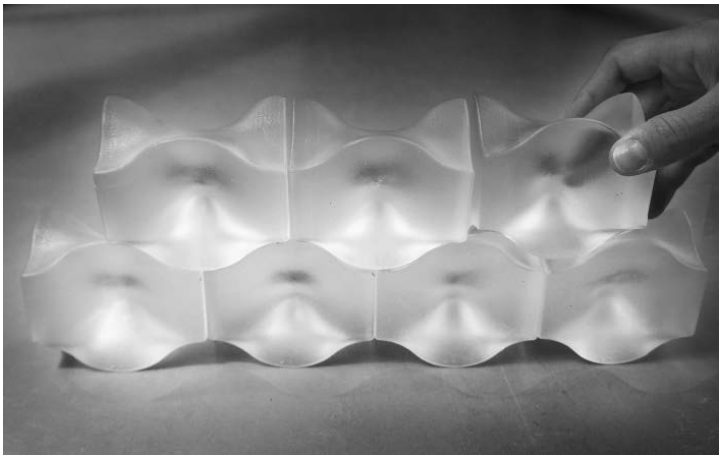

(b) Non-planar cast-glass component. Source: Oikonomopoulou, Bristogianni, Barou, and Veer (2018).

Figure 3.5: Comparison between planar and non-planar cast-glass component strategies

The main implications of both strategies, synthesised from Dimas et al. (2022), Oikonomopoulou, Bristogianni, Barou, Jacobs, et al. (2018), Oikonomopoulou et al. (2025), and Van Kessel (2025), are summarised in Table 3.1.

The comparison shows that both strategies can support dry-stacked glass assemblies, but they introduce complexity differently. Non-planar systems place complexity in the glass component itself, which can support geometric interlocking, but increases fabrication complexity and limits standardisation. By contrast, planar systems keep the glass components simple and shift the complexity to the functional interlayer. This makes the interlayer responsible not only for stress mediation and tolerance accommodation, but also for shear transfer, alignment, and geometric adaptability.

For this research, the planar strategy is therefore selected. When the interlayer already provides mechanical interlocking, load transfer, and angular variation, additional interlocking within the glass geometry becomes redundant. By using planar cast-glass components, the system can rely on standardised, reusable glass units while using the AM interlayer to facilitate application-specific geometry. This reduces fabrication risk, improves repeatability, and allows structural variation, such as curvature or arching, to be introduced through the removable interlayer rather than through bespoke glass components.

Table 3.1: Comparison of planar and non-planar cast-glass component strategies

Aspect	Planar components	Non-planar components	Implication for this research
Interface geometry	Flat	Curved or interlocking	Provides a controlled substrate for direct additive manufacturing.
Source of interlocking	Interlayer	Glass component	Eliminates the need for complex, high-risk cast-glass geometries.
Glass fabrication complexity	Medium	High	Minimizes casting risks, mould complexity, and post-processing efforts.
Interlayer fabrication	Cartesian AM	Multi-axis AM	Enables accessible, standard, and highly repeatable interlayer production.
Repeatability and robustness	High	Sensitive	Reduces accumulated fabrication risks across the assembly.
Design adaptability	High customisation	Fixed geometry	Allows glass component reuse by simply updating the interlayer design.
Scalability	Modular production	Bespoke components	Establishes a scalable foundation for circular cast-glass structures.

3.4. Interlayer requirements and design criteria

In segmented compressive glass assemblies, the interlayer plays a critical role in enabling structural safety, constructibility, and circularity. Because glass is brittle and highly sensitive to local stress concentrations, direct glass-to-glass contact must be avoided. The interlayer therefore acts as a stress-mediating layer between adjacent glass components, redistributing contact stresses and accommodating surface asperities and dimensional tolerances. For a reversible system, the interlayer must also support non-destructive disassembly, allowing the glass components to be recovered without permanent contamination at end-of-life (Oikonomopoulou, Bristogianni, Barou, Jacobs, et al., 2018; Oikonomopoulou et al., 2019).

This section defines the requirements and design criteria that will be used to guide the development of the interlocking interlayer. The material requirements describe what the interlayer material must be capable of, while the design criteria define how these capabilities must be translated into an AM interlocking geometry.

3.4.1. Material requirements for dry interlayers

For a dry interlayer to function reliably, the material must balance stress redistribution, tolerance accommodation, interface stability, mechanical durability, and reversibility (Oikonomopoulou, Bristogianni, Barou, Jacobs, et al., 2018). The key material requirements listed in Table 3.2 are derived from literature on dry interlayers in segmented glass assemblies, including Dimas et al. (2022), Oikonomopoulou, Bristogianni, Barou, Jacobs, et al. (2018), Oikonomopoulou et al. (2019, 2025), and Van Kessel (2025). These requirements are independent of the final interlocking geometry and provide a selection framework for evaluating candidate materials in Section 3.5.

The first requirement is reliable and adhesive-free adhesion to the glass substrate. For directly printed interlayers, this bond is achieved through thermoplastic wetting and mechanical interaction with the glass surface rather than through permanent adhesives or primers (Oikonomopoulou et al., 2025). Therefore, the glass-polymer interface is a critical point in the system: it must be strong enough to keep the interlayer in place during its lifespan, while still allowing controlled removal at end-of-life. Previous research identifies this interface as the structural weak link, particularly because brittle delamination can occur under shear loading (Oikonomopoulou et al., 2025; Van Kessel, 2025).

Table 3.2: Material requirements for dry interlayers in segmented cast-glass assemblies

Category & Key material criteria	Requirement
Primary - functional	
Direct adhesion to glass substrate	Reliable, without primers or adhesives
Stress redistribution and contact mediation	Satisfactory
Geometric adaptability and tolerance accommodation	Ability to be shaped in desired geometry
Thickness	Approximately 1-3 mm
Primary - material performance	
Stiffness / Young's modulus	$E < 50$ GPa
Shore hardness	60A – 80A; 10D – 40D
Compressive strength	$\geq$ 1 – 2 MPa
Creep resistance	Satisfactory under sustained compression
Tear strength	$\geq$ 34 N/mm, where applicable
Secondary	
Durability and environmental resistance	Water, fire, UV, and service-temperature resistance
Reversibility and circularity	Enables clean disassembly, reuse, or recycling
Optical compatibility	Preferably visually compatible with glass
Thermal expansion compatibility	As compatible as possible with the applied glass

The interlayer must also redistribute stresses and accommodate tolerances. Its role is to mediate contact between brittle glass components by compensating for surface micro-asperities and dimensional deviations (Oikonomopoulou, Bristogianni, Barou, Jacobs, et al., 2018). This requires a material that can be formed into the desired interlayer geometry with sufficient dimensional control (Dimas et al., 2022), while also providing enough compliance to prevent local peak stresses (Oikonomopoulou, Bristogianni, Barou, & Veer, 2018). Based on previous research by Dimas et al. (2022), an interlayer thickness of approximately 1–3 mm is generally considered suitable for balancing stress redistribution and dimensional control.

Mechanical stability is governed by a combination of stiffness, hardness, compressive strength, creep resistance, and tear resistance. According to Dimas et al. (2022), the material should be softer and more compliant than glass to prevent stress concentrations, but also not so soft that excessive deformation or creep compromises the stability of the assembly. Sufficient compressive strength is required to resist permanent loads from self-weight (Dimas et al., 2022), while creep resistance is essential for long-term performance under sustained compression (Oikonomopoulou, 2019). Tear resistance is particularly relevant for softer polymers and elastomers, where sharp glass edges could otherwise damage the interlayer and lead to direct glass contact (Dimas et al., 2022).

Secondary requirements include durability, optical compatibility, thermal expansion compatibility, and circularity. For outdoor or façade applications, resistance to moisture, UV radiation, fire, and temperature variation becomes important, although these criteria depend strongly on the intended application and regulations. Optical compatibility is desirable but not treated as a primary requirement in this research, because limiting the material selection to transparent polymers would unnecessarily restrict the experimental design space. Reversibility, however, remains essential: the interlayer must enable the glass components to be recovered intact and uncontaminated, either for direct reuse or recycling (Dimas et al., 2022).

3.4.2. Design criteria for additively manufactured interlocking interlayers

The material requirements define the interlayer material behaviour, but they do not determine how the interlocking function should be realised geometrically. Because this research shifts mechanical interlocking from the glass component to the polymer interlayer, additional design criteria are required. These criteria address the structural behaviour of the interlock, the limitations of FDM fabrication, and the need for reversibility and design adaptability.

The design criteria in Table 3.3 were established by synthesizing the work of Oikonomopoulou, Bristogianni, Barou, Jacobs, et al. (2018), Oikonomopoulou et al. (2025), and Van Kessel (2025). They are used to evaluate interlocking typologies in Section 3.7 and to guide the geometric design development in Chapter 5.

Table 3.3: Design criteria for additively manufactured interlocking interlayers

Category	Key design criteria
Mechanical interlock & geometric stability	Kinematic movement confinement
	Effective shear transfer
	Self-alignment & geometric damping
	Elastic averaging capacity
AM fabrication fidelity & printability	Geometric printability
	Continuous toolpath optimization
	Thermal stability (warping resistance)
	Feature resolution vs. nozzle Size
Versatility & circularity logic	Multidimensional adaptability (variable angles)
	Engineered reversibility trigger(s)
	Interfacial reliability (direct adhesion)

The first category of criteria concerns mechanical interlock and geometric stability. The interlayer geometry must restrict relative movement between adjacent glass units, transfer shear forces, and promote self-alignment for an efficient, and reliable assembly (Oikonomopoulou, Bristogianni, Barou, Jacobs, et al., 2018). Ideally, the interlayer should also utilise its material compliance to provide some degree of elastic averaging, allowing small fabrication deviations to be distributed across multiple features rather than concentrated in a single point (Oikonomopoulou et al., 2025; Van Kessel, 2025).

The second category concerns additive manufacturing fidelity and printability. Because the interlayer will be produced using Fused Deposition Modeling (FDM), the geometry must respect limitations such as nozzle diameter, overhang angles, anisotropy, toolpath continuity, and thermal shrinkage. Features must be large enough to print reliably, rounded enough to reduce stress concentrations, and arranged in a way that minimises warping and delamination during cooling (Oikonomopoulou et al., 2025).

The third category concerns versatility and circularity. The interlayer geometry must accommodate different assembly angles and configurations, especially for vaults or arches where adjacent glass components meet at varying orientations (Oikonomopoulou, Bristogianni, Barou, Jacobs, et al., 2018). At the same time, the system must include a clear demounting strategy, either through removable locking elements, mechanical release mechanisms, or controlled detachment from the glass substrate. Interfacial reliability is included here as well because the geometry and printing strategy directly influence the interlayer adhesion quality, failure mode, and end-of-life demountability (Oikonomopoulou et al., 2025).

3.4.3. From requirements to experimental evaluation

Together, the material requirements and design criteria establish the evaluation framework for the rest of the research. The material requirements are used in section Section 3.5 to initially screen and select candidate polymers before experimental testing. The design criteria are used in Section 3.7 to compare and evaluate interlocking typologies and in Chapter 5 to guide the development of the final interlayer geometry.

Not all formulated requirements can be optimised simultaneously. For example, high stiffness may improve transfer but reduce tolerance accommodation, and strong adhesion may improve assembly stability but complicate demountability at end-of-life. The following chapters therefore focus on identifying the most promising balance between material behaviour, geometric performance, manufacturability, and reversibility, rather than maximising each criterion independently.

3.5. Interlayer material selection

The interlayer material must balance printability, mechanical performance, dimensional stability, interface reliability, and reversibility. The material requirements defined in Section 3.4 provide the framework for selecting candidate polymers for experimental evaluation. No single polymer is expected to satisfy all requirements simultaneously; material selection inherently involves trade-offs between structural performance, glass compatibility, processability, durability, and end-of-life recovery. This section first reviews the baseline materials identified in previous research, then explores improved and alternative polymer candidates, and finally selects a set of materials for experimental testing.

3.5.1. Baseline materials from previous research

Previous research by Van Kessel (2025) evaluated several AM interlayer materials for cast-glass assemblies. As summarised in Table 3.4, PLA and PETG were identified as the most promising baseline polymers due to their combination of printability, adhesion to glass, and mechanical behaviour. Other candidates were excluded due to excessive creep, poor adhesion, limited printability, incompatible processing requirements, or unavailable filament formats.

Table 3.4: Baseline interlayer material candidates evaluated in previous research

Material	Status	Key suitability	Primary limitation
Neoprene	Excluded	Flexible; suitable for tolerance accommodation.	Excessive creep; incompatible with FDM.
Aluminium	Excluded	Excellent creep resistance and stress distribution.	Incompatible with available AM process; high stiffness mismatch.
Heat-cured silicone	Excluded	High adaptability and cushioning capacity.	Incompatible with available printing infrastructure.
Surlyn	Excluded	Potential for strong glass bonding.	Not available as suitable FDM filament.
TPU	Tested	Flexible; good tolerance accommodation.	Poor glass adhesion, insufficient stiffness, and poor printability.
Flex polyester	Tested	Moderate adhesion and flexible behaviour.	Inconsistent printability and corner lifting.
PC-ABS	Tested	High-strength potential.	Failed prints; requires an enclosed printer.
PETG	Selected	Strong adhesion, ductility, and chemical resistance.	High thermal shrinkage and warping risk.
PLA	Selected	High dimensional stability, easy printing, and clean reversibility.	Limited thermal and environmental durability.

Although PLA and PETG form a useful reference baseline, neither material fully satisfies the requirements for a durable, structurally reliable, and reversible interlayer. PLA is highly printable and dimensionally stable, but its low thermal resistance and limited environmental durability restrict long-term application. PETG offers better toughness and durability, but its higher thermal shrinkage introduces warping, residual stresses, and potential glass damage. These trade-offs are summarised in Table 3.5.

The comparison shows that standard PLA and PETG represent two opposing material tendencies. PLA is a biodegradable thermoplastic that provides process reliability and clean reversibility, while PETG is a copolyster that provides better mechanical and environmental performance at the cost of increased processing complexity and higher thermal stresses. For this reason, the following material selection focuses on improved PET-based candidates and fibre-reinforced variants, while retaining PLA-based materials as reference or backup options.

Table 3.5: Trade-offs between PLA and PETG as baseline interlayer materials

Property		PLA		PETG
Warping / shrinkage	+	Excellent dimensional stability; low shrinkage (Oikonomopoulou et al., 2025; Rimkus et al., 2024).	−	More prone to warping due to higher thermal shrinkage (Oikonomopoulou et al., 2025).
Glass adhesion	+	Reliable adhesion at moderate printing temperatures (Oikonomopoulou et al., 2025).	+	Strong adhesion, but requires higher printing temperatures (Oikonomopoulou et al., 2025).
Mechanical behaviour	−	Stiff and strong, but relatively brittle (Budziński & Federowicz, 2025; Rasal & Hirt, 2009).	+	Tougher and more ductile (Guessasma et al., 2019).
Thermal performance	−	Low glass transition temperature; heat sensitive (Van Kessel, 2025).	+	Higher service temperature and better thermal stability (Budziński & Federowicz, 2025).
Environmentel durability	−	Susceptible to UV, humidity, and ageing (Rimkus et al., 2024).	+	Better weathering and chemical resistance (Oikonomopoulou et al., 2025).
Reversibility / removal	+	Easier to remove by reheating (Van Kessel, 2025).	−	More difficult to remove due to stronger adhesion (Van Kessel, 2025).
Processing	+	Easy and stable to print (Van Kessel, 2025).	−	More sensitive to stringing, oozing, and thermal stress (Guessasma et al., 2019; Van Kessel, 2025).

3.5.2. Alternative polymer candidates

To address the limitations of standard PLA and PETG, additional polymer candidates were explored and the results are summarized in Table 3.6 The main strategy is the use of polymer matrix composites, specifically short fibre-reinforced polymers, which can improve stiffness, dimensional stability, and thermal behaviour while remaining compatible with standard FDM printing (Li et al., 2015; Zotti et al., 2025). Carbon fibre and glass fibre reinforcement are particularly relevant because they can reduce shrinkage and increase mechanical performance (Kováčová et al., 2020; Wang et al., 2017). However, reinforcement also introduces trade-offs, including reduced ductility, increased brittleness, altered melt flow, and possible interface reliability issues.

Continuous fibre-reinforced composites were not selected because they require specialised equipment and introduce additional fabrication complexity (Dickson et al., 2017). Instead, the material selection focuses on commercially available short fibre-reinforced filaments and modified PET-based polymers that can be processed with accessible FDM equipment.

The additional candidates can be grouped into three main categories. The PET-based materials are the most relevant because they build directly on the favourable durability and toughness of PETG while attempting to improve dimensional stability and print quality. PETG-HF tests whether improved flow behaviour can enhance wetting and deposition quality, while PETG-GF, PETG-CF, and PET-CF test the effect of fibre reinforcement on stiffness, shrinkage, and interface behaviour. PLA-CF is retained as a backup because it offers the print reliability of PLA with improved stiffness. The PA6-, ABS-, and ASA-based candidates are less suitable for this research due to processing complexity, moisture sensitivity, thermal mismatch, or uncertain adhesion to glass.

Table 3.6: Expected advantages and risks of alternative polymer candidates for directly printed interlayers

Material	Selection role	Key pros / suitability	Main risks / limitations
PETG-HF (Bambu Lab, n.d.-i)	High-flow PETG.	Higher melt flow, better extrusion consistency, and improved wetting.	Thermal shrinkage and residual stresses remain critical.
PETG-GF (Elegoo, n.d.)	Glass-fibre PETG.	Improved stiffness and dimensional stability; reduced warping risk.	Reduced ductility; possible brittle interface behaviour.
PETG-CF (Bambu Lab, n.d.-g)	Carbon-fibre PETG.	Improved stiffness, strength, and thermal stability.	Reduced ductility; potential glass–polymer interface sensitivity.
PET-CF (Bambu Lab, n.d.-e)	High-performance PET.	High dimensional stability, low thermal expansion, and high mechanical performance.	Increased stiffness and brittleness; demanding processing; higher cost.
PLA-CF (Bambu Lab, n.d.-l)	Reinforced PLA backup.	Excellent printability and dimensional stability; higher stiffness than PLA.	Brittle behaviour; limited environmental durability.
PA6-CF (Bambu Lab, n.d.-c)	High-strength PA.	High strength, stiffness, and thermal resistance.	Moisture sensitivity, demanding print conditions, and uncertain glass adhesion.
PA6-GF (Bambu Lab, n.d.-d)	Toughened PA alternative.	Improved toughness compared with PA6-CF; high thermal resistance.	Moisture sensitivity, demanding print conditions, and uncertain interface behaviour.
ABS-GF (Bambu Lab, n.d.-a)	Reinforced ABS benchmark.	Improved stiffness and technical performance.	High warping tendency, thermal mismatch, and poor glass adhesion.
ASA-CF (Bambu Lab, n.d.-b)	Weather-resistant benchmark.	UV/weather resistance and dimensional stability.	Thermal mismatch with glass and unfavourable interface behaviour.

3.5.3. Material selection for experimental testing

To compare the candidate polymers systematically, Table 3.7 evaluates their printability, expected adhesion, warping behaviour, durability, and overall application potential. The evaluation is based on literature, manufacturer data, and previous experimental findings. The table is intended as a qualitative screening tool rather than a definitive material ranking, since the final suitability of each polymer depends on its behaviour when printed directly onto glass.

The comparison shows that PET-based materials provide the most favourable balance between printability, interface behaviour, dimensional stability, and durability. PETG-GF and PET-CF show the highest initial potential, while PETG-HF and PETG-CF remain relevant for assessing the influence of processability and stiffness. PLA-CF is retained as a backup material, whereas PA6-, ABS-, and ASA-based candidates are excluded from experimental testing due to processing complexity or interface risk.

Table 3.7: Comparative evaluation of candidate polymers for directly printed interlayer applications

Material	Printability	Adhesion	Warping	Durability	Potential	Source
PLA	**5**	**Excellent**	**Low**	**Poor**	+	(Van Kessel, 2025)
PETG	**3.5**	**Excellent**	**Moderate / high**	**Good**	+	(Van Kessel, 2025)
PETG-HF	**4.5**	*Excellent*	*Moderate / high*	**Good**	+	(Bambu Lab, n.d.-i)
PETG-GF	**4**	*Good*	*Low*	**Good / excellent**	++	(Elegoo, n.d.)
PETG-CF	**4**	*Good*	*Low / moderate*	**Good**	+	(Bambu Lab, n.d.-g)
PET-CF	**3**	*Good / excellent*	*Very low*	**Excellent**	++	(Bambu Lab, n.d.-e)
PLA-CF	**4.5**	*Good / excellent*	*Very low*	**Poor / moderate**	±	(Bambu Lab, n.d.-l)
PA6-CF	**2.5**	*Low / moderate*	*Moderate*	**Moderate**	–	(Bambu Lab, n.d.-c)
PA6-GF	**2.5**	*Moderate*	*Low / moderate*	**Moderate**	–	(Bambu Lab, n.d.-d)
ABS-GF	**3.5**	*Low*	*Moderate / high*	**Moderate**	–	(Bambu Lab, n.d.-a)
ASA-CF	**3**	*Low*	*Low / moderate*	**Excellent**	–	(Bambu Lab, n.d.-b)

Note. Printability is rated from 1 = poor to 5 = excellent. Potential is rated as ++ = high, + = promising, ± = backup, and – = low suitability for this application. Bold values indicate characteristics supported by literature or previous experimental validation, whereas italic values indicate expected behaviour inferred from material properties.

Based on this evaluation, six materials are selected for experimental testing. Table 3.8 gives an overview of the relevant properties and main challenge per material. PLA is included as the baseline reference material from previous research. PLA-CF is included as a reinforced PLA backup. PETG-HF, PETG-GF, PETG-CF, and PET-CF are selected as the primary PET-based candidates, each representing a different strategy for improving printability, dimensional stability, or mechanical performance.

Table 3.8: Properties and expected challenges of polymers selected for experimental testing.

Property	Unit	PLA	PLA-CF	PETG-HF	PETG-GF	PETG-CF	PET-CF
Young's modulus	[GPa]	2.58	2.79	1.81	—	2.46	4.73
Bending modulus	[GPa]	2.75	3.95	2.05	3.35	2.91	5.32
Bending strength	[MPa]	76	89	64	83	70	131
Impact strength	$[\mathrm{kJ\,m^{-2}}]$	26.6	23.2	31.5	51.9	41.2	36.0
T_g	$[^\circ\mathrm{C}]$	60	63	66	—	68	75
HDT[a]	$[^\circ\mathrm{C}]$	57	55	69	74	74	205
CTE[b]	$[10^{-6}/\mathrm{K}]$	68–78	68–78	120–123	120–123	120–123	21–22
Main challenge		Durability; ageing	Durability; brittleness	Thermal shrinkage	Reduced ductility	Reduced ductility	Processing; brittleness

Note. Data from manufacturer Technical Data Sheets (Bambu Lab, n.d.-f, n.d.-h, n.d.-j, n.d.-k, n.d.-m; Elegoo, n.d.), unless specified.

[a] Measured at 0.45 MPa.

[b] Source: base material ranges from Granta EduPack. Applies as general-purpose range for PLA-based materials, unfilled range for PETG-based materials, and 30% carbon fibre reinforced range for PET-CF.

Overall, the selected material set enables a systematic evaluation of the main trade-offs relevant to directly printed interlocking interlayers. PLA and PLA-CF provide reference and backup behaviour, while the PET-based candidates test the influence of improved flow, glass-fibre reinforcement, carbon-fibre reinforcement, and higher-performance PET chemistry. These materials form the basis for the material experiments in Chapter 4, where their actual adhesion, warping behaviour, print quality, removability, and glass compatibility are evaluated experimentally.

3.6. FDM tolerances and process limitations

This section analyses the primary process, material, and interface limitations that govern FDM fabrication on glass substrates. Due to its discrete, layer-wise nature, FDM inherently introduces process-induced imperfections. These limitations arise from the interaction between material behaviour, thermal cycles, machine accuracy, and substrate conditions.

For directly printed interlocking interlayers, these limitations are not only fabrication concerns; they directly define the feasible geometric design space. Feature size, layer adhesion, thermal shrinkage, warping, and glass–polymer adhesion all influence whether an interlocking geometry can be printed reliably, remain attached to the glass, and transfer load without premature failure. The key relationships between influencing factors and their implications are summarised in Table 3.9.

Process and material limitations

Fused Deposition Modelling (FDM) is a layer-wise additive manufacturing process in which a thermoplastic filament is extruded in a semi-liquid state along predefined toolpaths in a Cartesian coordinate system. The final geometry is generated through the sequential deposition, cooling, and solidification of material, as defined by the CAD model sliced into G-code (Lalegani Dezaki et al., 2021).

As a result, FDM parts are inherently anisotropic: their strength and stiffness depend on build orientation, toolpath direction, and bonding quality between adjacent filaments and layers (Ngo et al., 2018). Incomplete fusion between deposited lines and layers can result in porosity, reduced interlayer strength, and local defects (Penumakala et al., 2020). The structural integrity of FDM parts therefore depends heavily on the quality of bonding between deposited filaments (Bellehumeur et al., 2004). These process-induced imperfections are especially relevant for interlocking geometries, where small features must transfer concentrated shear forces.

Thermal cycling during printing introduces residual stresses, which can result in material shrinkage and macroscopic distortion, commonly observed as warping (Penumakala et al., 2020). Warping can compromise base-layer adhesion and reduce dimensional accuracy (Baechle-Clayton et al., 2022). Mitigation strategies therefore focus on controlling heat distribution and reducing stress concentrations, for example by minimising large flat base areas, using fillets, and adding sacrificial brims (Lalegani Dezaki et al., 2021). A stable thermal environment remains critical, as fluctuations in process or ambient temperature can lead to non-uniform adhesion and density inconsistencies within the printed component (Baechle-Clayton et al., 2022).

Material behaviour further influences print quality. FDM materials must operate within a narrow rheological window, where melt viscosity is low enough for extrusion but high enough to retain geometric stability after deposition (Parulski et al., 2021). This balance is material-dependent, meaning different polymers show varying sensitivity to temperature and process conditions (Novák et al., 2018). Filament diameter variation directly affects extrusion flow and dosing accuracy, while inconsistent material feed can lead to under-extrusion, over-extrusion, or internal defects (Korte & Quodbach, 2018). Hygroscopic materials are particularly sensitive to storage and drying conditions, as moisture uptake can degrade extrusion behaviour and reduce mechanical performance (Lalegani Dezaki et al., 2021; Zotti et al., 2025).

Print-on-glass interface constraints

Printing directly onto glass introduces additional constraints compared with printing on a conventional build plate. According to Van Kessel (2025), thermal cycling induces residual stresses due to the mismatch in thermal expansion between the polymer and glass substrate. These stresses result in shrinkage and warping, particularly pronounced at edges and corners. When adhesion is strong, the resulting interface stresses can become high enough to cause local glass damage (referred to as *chipping*).

Adhesion between polymer and glass is governed mainly by wetting, mechanical interaction, and friction rather than molecular bonding, making it highly sensitive to process conditions and surface quality. Increasing substrate temperature or surface roughness can improve wetting and contact, but excessive temperatures may reduce bond stability (Baechle-Clayton et al., 2022). Reliable adhesion therefore requires a clean glass surface, as contaminants inhibit wetting; cleaning with isopropyl alcohol (IPA) is essential prior to deposition (Van Kessel, 2025).

Table 3.9: FDM process limitations, influencing factors, and implications for directly printed interlayers

Category & aspect	Primary influencing factors	Implications
Process physics		
Layer adhesion	Nozzle temperature, cooling rate, extrusion pressure, interlayer bonding quality	Anisotropic mechanical behaviour and reduced interlayer strength
Porosity formation	Filament spacing, extrusion consistency, print speed	Internal voids reducing stiffness and dimensional stability
Thermal behaviour		
Thermal shrinkage	Polymer CTE, cooling rate, ambient temperature	Global dimensional deviation from intended geometry
Residual stresses	Thermal gradients during cooling, build plate temperature	Internal stresses leading to geometric distortion
Warping	Material shrinkage, part geometry, thermal gradients	Corner lifting and reduced base-layer adhesion
Machine limitations		
Axis positioning	Stepper motor resolution, belt tension, skew calibration	Small positional deviations affecting dimensional accuracy
Extrusion consistency	Feed reliability, filament quality, diameter variation	Under- or over-extrusion causing local geometric inaccuracies
Geometric resolution limits		
Nozzle constraints	Nozzle size, extrusion width	Defines minimum printable feature size and limits detail resolution
Layer height selection	Slicer settings, nozzle diameter	Trade-off between vertical resolution and interlayer strength
Stair-stepping	Layer thickness, surface inclination angle	Surface roughness and geometric approximation errors on inclined or curved surfaces
STL discretisation	Mesh resolution of exported CAD model	Faceted approximation of curved geometries
Material behaviour		
Melt rheology	Polymer viscosity, extrusion temperature	Poor bonding or geometric instability outside the optimal temperature range
Filament tolerance	Manufacturing variability of filament	Inconsistent extrusion flow and dimensional deviations
Hygroscopicity	Ambient humidity, filament storage/conditioning	Degraded extrusion behaviour and reduced mechanical properties
Print-on-glass interface		
Polymer–glass adhesion	Surface cleanliness, bed temperature, surface roughness	First-layer stability and interface reliability
Expansion mismatch	Difference between polymer and glass CTE	Interface stresses, warping, or detachment
Elephant's foot	Residual nozzle pressure, bed temperature, first-layer height	Lateral spreading of the base layer, causing dimensional inaccuracies

At the same time, adhesion must remain reversible. The interface must be strong enough to keep the interlayer attached during printing, assembly, and loading, but not so strong that removal damages the glass substrate. This creates a critical design trade-off: increasing adhesion improves interface stability, but can also increase the risk of glass chipping or difficult end-of-life separation. Previous work also showed that PLA can be removed by reheating due to its relatively low glass transition temperature, although this strategy becomes less suitable for higher-performance polymers with stronger adhesion or higher thermal resistance (Van Kessel, 2025).

A final print-on-glass limitation is the reduced resilience for first-layer defects. Because glass is rigid and non-compliant, it does not compensate for extrusion irregularities. Effects such as elephant's foot, local over-extrusion, or poor nozzle-height calibration therefore directly influence dimensional accuracy at the interface (Grgić et al., 2023).

Dimensional accuracy and tolerance control

FDM dimensional accuracy is limited by machine calibration, nozzle diameter, layer height, slicer settings, and STL discretisation. Typical dimensional accuracy for FDM is approximately $100\ \mu$m (Turner & Gold, 2013), corresponding to ISO IT9–IT14 tolerance grades (Lieneke et al., 2016). However, FDM printers do not inherently interpret engineering tolerance specifications, meaning dimensional accuracy depends on CAD modelling, slicer interpretation, and software-based compensation rather than direct process control (Grgić et al., 2023).

Machine calibration further affects accuracy, particularly through axis alignment and motion precision (Grgić et al., 2023). Nozzle diameter introduces a fundamental trade-off: larger diameters improve print speed and strength but reduce geometric accuracy and limit feature resolution (Solomon et al., 2021). This constraint is especially critical for interlocking geometries, where small features may print inaccurately, round off due to extrusion width, or become mechanically weak.

Layer height introduces a similar trade-off. Smaller layer heights improve surface quality and vertical resolution, while larger layer heights can improve interlayer bonding and structural strength at the expense of geometric fidelity (Solomon et al., 2021). Inclined and curved surfaces are also affected by stair-stepping, where the layered nature of FDM approximates continuous slopes through discrete steps. This effect can be mitigated by decreasing layer height, either globally or through adaptive slicing (Solomon et al., 2021). Additional inaccuracies arise from STL discretisation, where curved CAD geometries are approximated by faceted mesh surfaces (Ngo et al., 2018).

Synthesis: FDM constraints as design drivers

The preceding analysis shows that successful direct-on-glass FDM printing is governed by the interaction between thermal behaviour, material response, machine accuracy, and interface control. Thermal expansion mismatch, porosity, anisotropy, and dimensional inaccuracies define the primary limitations on structural performance. Reliable interlayer behaviour therefore depends on both material selection and geometric design.

These limitations translate directly into design strategies for the interlocking interlayer, as summarised in Table 3.10. Features must be significantly larger than the nozzle diameter, sharp corners should be avoided, and toolpaths should be kept as continuous as possible to reduce defects and stress concentrations (Lalegani Dezaki et al., 2021; Solomon et al., 2021). Large uninterrupted bonded areas should be treated carefully, as they can increase shrinkage stresses and promote warping or delamination (Baechle-Clayton et al., 2022; Penumakala et al., 2020). Tolerance-absorbing geometries and elastic averaging are therefore essential to compensate for unavoidable inaccuracies in both the glass and the printed geometry (Van Kessel, 2025).

Rather than being fixed constraints, FDM limitations define the design space for interlocking geometries. Resolution limits, thermal stresses, and interface behaviour must be addressed simultaneously through geometry, material choice, and print strategy. In this context, the interlayer geometry becomes the main tool for compensating for process variability.

The most important design consequences are the need for robust feature dimensions, smooth transitions, controlled base-layer adhesion, and distributed load transfer. Elastic averaging is particularly relevant because it allows local deviations to be redistributed across multiple contact points rather than concentrated in a single feature. This supports self-alignment and improves tolerance accommodation at the assembly scale.

Finally, the structural reliability of the system remains strongly governed by the glass–polymer interface. If delamination occurs before the interlocking features properly engage, the mechanical potential of the geometry cannot be fully utilized. The following typology and geometry-development sections therefore treat FDM constraints not as secondary fabrication issues, but as primary design drivers for a reversible, mechanically interlocking polymer interlayer.

Table 3.10: Design implications and mitigation strategies for FDM-printed interlocking polymer interlayers

Limitation	Manifestation	Implication	Mitigation strategy
Limited nozzle resolution	Minimum feature size	Inconsistent features	Use features significantly larger than the nozzle diameter
Anisotropy	Weak interlayer bonding	Shear failure	Align load paths with favourable print directions; use high-density infill
Stair-stepping	Rough surfaces	Reduced fit accuracy	Prefer shallow slopes; adjust layer height or use adaptive slicing
Thermal shrinkage	Dimensional deviation	Tolerance mismatch	Introduce tolerance buffers and avoid over-constrained fits
Warping / stresses	Corner lifting	Reduced adhesion	Use fillets, brims, and avoid large uninterrupted flat areas
Elephant's foot	Lateral base spreading	Geometry inaccuracy	Calibrate first-layer height and compensate in the slicer
Extrusion inconsistency	Over- or under-extrusion	Irregular surface	Control filament condition, extrusion temperature, and flow calibration
Tolerance gaps	Cumulative deviations	Part misalignment	Employ elastic averaging and distributed contact points
Glass adhesion	Brittle delamination	Sudden interface failure	Clean with IPA; control bed temperature and first-layer wetting

3.7. Interlocking interlayer typologies

Building on the design criteria established in Section 3.4.2 and the decision to use planar cast-glass components in Section 3.3, this section evaluates interlocking strategies that can be integrated directly into the interlayer geometry. Because the glass components remain planar and standardised, the interlocking function must be provided by the interlayer itself. This shifts geometric complexity away from the brittle glass component and into a removable, AM interface (Oikonomopoulou, Bristogianni, Barou, Jacobs, et al., 2018).

The aim of this section is not to select one final geometry, but to identify which interlocking typologies are most suitable for further design development. The typologies are evaluated based on their load-transfer mechanism, compatibility with FDM fabrication, ability to accommodate tolerances, and potential for reversible assembly. Four main typologies are considered:

1. **Geometric mechanical interlocking**, where load transfer is governed primarily by rigid shape engagement.
2. **Discrete compliant interlocking**, where engagement relies on local elastic deformation of discrete features.
3. **Distributed surface-based interlocking**, where load transfer is spread across many repeated surface features.
4. **Multi-scale hybrid interlocking**, where macro-scale geometry and micro-scale surface interaction are combined.

Geometric mechanical interlocking

Geometric mechanical interlocking relies on shape-driven engagement between matching features. Load transfer is achieved through direct contact between rigid geometries, making this family highly effective for kinematic confinement and shear resistance. Typical examples include sliding dovetails, T-slots, and keyed stacking systems.

(a) Sliding dovetail interlock **(b)** Sliding T-slot interlock **(c)** Keyed stacking geometry

Figure 3.6: Geometric mechanical interlocking typologies

The sliding dovetail (Figure 3.6a) is a male–female interlocking system in which a trapezoidal tenon engages with a matching groove through linear sliding. It provides strong resistance against separation in multiple directions, except along the sliding direction. However, the geometry is tolerance-sensitive and difficult to fabricate cleanly with FDM due to overhangs, sharp corners, and potential stress concentrations at the base of the feature (Davaasambuu et al., 2025).

The sliding T-slot (Figure 3.6b) follows a similar engagement principle, but uses an L-shaped or T-shaped profile to provide mechanical confinement (Brown et al., 2023). It can perform well under shear loading, but sharp internal corners and unsupported overhangs make it difficult to print without support structures (Davaasambuu et al., 2025).

Keyed geometry stacking (Figure 3.6c) uses discrete protrusions or keys to align components and restrict lateral movement. This strategy is relevant because it separates placement from locking: components can first be positioned and then mechanically activated using a secondary locking element (Van Kessel, 2025). However, if the features are too rigid or tolerance-sensitive, local stress concentrations and assembly difficulties may occur.

Overall, geometric mechanical interlocking provides the clearest load-transfer mechanism, but requires careful adaptation to avoid sharp features, over-constrained fits, and sliding-only assembly logic.

Discrete compliant interlocking

Discrete compliant interlocking relies on local elastic deformation of individual features, typically through snap-fit or click-fit mechanisms. These systems are attractive for reversible assembly because they can engage and disengage without separate fasteners. Examples include arrowhead or cantilever snap-fits and pin-and-spring systems such as ShroomLock.

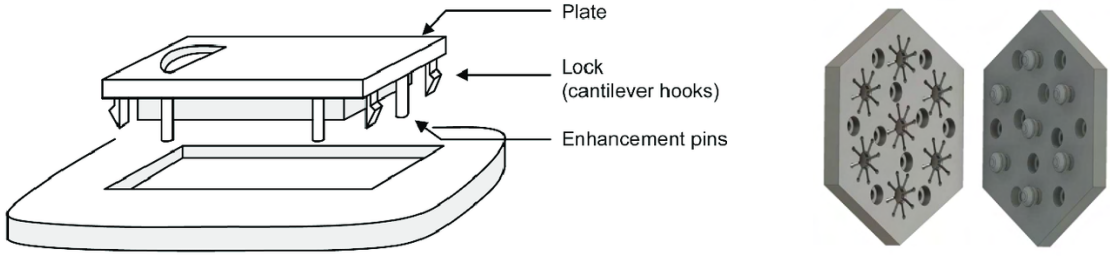

(a) Arrowhead and cantilever snap-fit interlocking **(b)** ShroomLock pin-and-spring system

Figure 3.7: Discrete compliant interlocking typologies. Source: Gloyer et al. (2023).

Arrowhead and cantilever snap-fits use flexible arms that deform during insertion and return to their original position after engagement (Figure 3.7a). This makes them effective for self-locking connections in polymer products (Bolmin et al., 2023). However, their application in thin interlayers is limited because they require either highly flexible materials or slender features. In standard FDM polymers, such features are prone to plastic deformation, fracture, or inconsistent performance due to print anisotropy (Gloyer et al., 2023; Wayken, 2023).

ShroomLock-type systems (Figure 3.7b) are more explicitly developed for FDM and demonstrate good repeatability when printed in suitable orientations. However, their performance depends strongly on print quality, surface roughness, and the orientation of both pin and spring elements. Since direct printing onto glass constrains the print orientation and limits support possibilities, these systems are difficult to translate directly into a flat interlayer (Gloyer et al., 2023).

Discrete compliant interlocking therefore offers strong reversibility potential, but is less suitable for this research due to interlayer thickness limits, material brittleness, and print-orientation constraints.

Distributed surface-based interlocking

Distributed surface-based interlocking relies on many repeated surface features rather than one dominant locking element. This category includes principles from Interlocking Metasurfaces, but only the aspects relevant to low-profile, FDM-printable polymer interlayers are considered here.

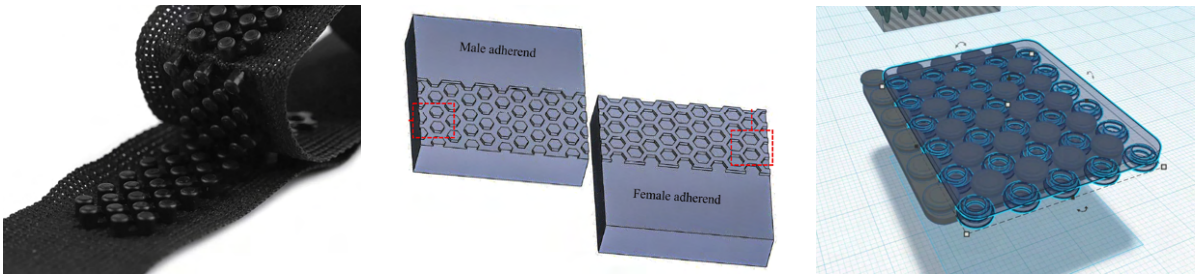

(a) Velcro-inspired stacking pins **(b)** Hexagonal shear-optimised pattern **(c)** Low-profile shear features

Figure 3.8: Distributed surface-based interlocking typologies

Velcro-inspired stacking pins (Figure 3.8a) use dense arrays of small protrusions to create distributed resistance through collective engagement. Load transfer is spread over many contact points, which reduces dependence on any single feature. This makes the strategy highly relevant for tolerance accommodation and elastic averaging. However, performance depends strongly on feature resolution, nozzle calibration, and repeatable printing of small details (Van Kessel, 2025).

Hexagonal shear-optimised patterns (Figure 3.8b) use repeating cell geometries to provide multidirectional in-plane shear resistance. Their main advantage is that they can distribute load relatively evenly across a surface. However, nozzle diameter limits the minimum wall thickness and tends to round small features, which can reduce the effectiveness of the intended interlock (Naat et al., 2025).

Low-profile knob-like features (Figure 3.8c) use short, wide protrusions to maximise contact area while reducing bending stresses at the base. This makes them more compatible with FDM than slender pin-like features. Although their vertical interlock is limited, they are promising for shear transfer, tolerance accommodation, and reversible engagement when combined with a separate locking mechanism (Brown et al., 2023).

Distributed surface-based interlocking is therefore highly relevant for this research because it supports elastic averaging, self-alignment, and tolerance distribution. Its main limitation is the need to keep features large and robust enough for reliable fabrication.

Multi-scale hybrid interlocking

Multi-scale hybrid interlocking combines macro-scale geometric constraint with micro-scale or distributed surface interaction. These systems aim to improve load transfer, robustness, and tolerance accommodation by using multiple engagement mechanisms at once.

Pile-based interlocks (Figure 3.9a) use slender pins to convert shear forces into normal and frictional interaction along the pin surfaces. This can distribute loads efficiently, but tall slender features are vulnerable to weak layer bonding and base failure (Peralta Marino et al., 2022). Their required feature height also conflicts with the limited thickness available for polymer interlayers in glass assemblies.

(a) Pile-based interlocks **(b)** Macro sliding geometry combined with interlocking metasurfaces

Figure 3.9: Multi-scale hybrid interlocking typologies. Source: Peralta Marino et al. (2022)

Macro sliding geometries combined with surface-based interlocking (Figure 3.9b) use larger sliding features to provide global kinematic confinement, while smaller surface textures improve local contact and stress distribution. This strategy is mechanically promising, but difficult to realise reliably with standard FDM because it requires accurate fabrication across multiple feature scales. Small deviations can accumulate and compromise fit or engagement (Peralta Marino et al., 2022).

Multi-scale hybrid interlocking is therefore conceptually relevant, but too fabrication-sensitive in its full form for the current direct print-on-glass workflow. However, the underlying principle remains useful: combining clear geometric confinement with distributed contact can improve robustness if the geometry is simplified.

Evaluation of interlocking typologies

To compare the typologies, Table 3.11 evaluates them against the design criteria established in Section 3.4.2. The evaluation focuses on mechanical stability, printability, tolerance accommodation, adaptability, and reversibility.

Table 3.11: Comparative evaluation of interlocking typologies for directly printed interlayers

Category / performance criterion	Geometric mechanical interlocking	Discrete compliant interlocking	Distributed surface-based interlocking	Multi-scale hybrid interlocking
Mechanical interlock and geometric stability				
Kinematic movement confinement	++	+	+	++
Effective shear transfer	++	+	+	++
Self-alignment and geometric damping	+	++	+	+
Elastic averaging capacity	±	+	++	±
AM fabrication fidelity and printability				
Geometric printability	++	±	+	−
Continuous toolpath optimisation	++	±	±	−
Thermal stability / warping resistance	±	−	+	−
Feature resolution relative to nozzle scale	++	+	±	−
Versatility and circularity logic				
Multidimensional adaptability / variable angles	+	−	++	−
Engineered reversibility triggers	±	++	+	±
Interfacial reliability / direct adhesion	+	±	±	±

Note. ++ = highly suitable, + = suitable, ± = conditionally suitable, and − = unsuitable for this application.

Geometric mechanical interlocking performs strongest in kinematic confinement and shear transfer. It offers a clear and predictable load path, but its performance depends heavily on dimensional accuracy. Without some form of compliance or tolerance buffer, rigid interlocking geometries can become difficult to assemble or vulnerable to local stress concentrations.

Discrete compliant interlocking performs well in self-alignment and reversibility, but its suitability is limited by material and fabrication constraints. Thin snap-fit features are difficult to print reliably using standard FDM and are vulnerable to fracture when printed in stiff or fibre-reinforced polymers. This makes the typology less suitable for direct print-on-glass interlayers.

Distributed surface-based interlocking performs best in elastic averaging and multidimensional adaptability. By distributing contact over many repeated features, it can accommodate local deviations and reduce dependence on a single precise engagement point. Its main limitation is feature resolution: the geometry must remain large enough to print reliably and resist rounding caused by nozzle diameter constraints.

Multi-scale hybrid interlocking offers high theoretical performance by combining multiple load-transfer mechanisms. However, this also increases fabrication complexity. Because printing on glass already introduces limitations related to resolution, warping, and interface reliability, highly complex multi-scale systems are considered too sensitive for the current research scope.

Synthesis: design directions for geometry development

Addressing research sub-question 3 at the typology level, the comparative evaluation shows that, geometric mechanical interlocking and distributed surface-based interlocking are the most promising typologies for further development. Geometric mechanical interlocking provides reliable shear transfer and kinematic confinement, while distributed surface-based interlocking provides tolerance accommodation, elastic averaging, and adaptability.

The following geometry development should therefore not adopt one typology directly. Instead, it should combine the strengths of both: the clear load-transfer logic of geometric mechanical interlocking with the distributed contact and tolerance-buffering behaviour of surface-based interlocking. This direction is especially relevant for directly printed polymer interlayers, where FDM limitations require robust feature dimensions, rounded transitions, and redundancy across the interface.

Discrete compliant systems and complex multi-scale hybrid systems remain valuable references, but they are not selected as primary design directions. Their dependence on thin flexible features, specific print orientations, or high-resolution multi-scale accuracy makes them less compatible with the limited interlayer thickness and direct print-on-glass workflow used in this research.

Two primary design directions therefore emerge:

- **Geometric mechanical interlocking combined with a relatively stiff polymer**
  → prioritising dimensional stability, precise kinematic confinement, and predictable shear transfer.
- **Distributed surface-based interlocking combined with a relatively ductile polymer**
  → leveraging elastic averaging, tolerance accommodation, and robust distributed engagement.

In the following design-development phase, these directions are treated as guiding strategies rather than final solutions. The final geometry should combine mechanical confinement, distributed contact, printable features, and removable locking elements into a simplified hybrid system suitable for reversible cast-glass assemblies.

3.8. Synthesis and research positioning

This literature study establishes the theoretical and design framework for developing a reversible, additively manufactured polymer interlayer for structural cast-glass assemblies. The chapter shows that the main challenge lies in joining segmented cast-glass systems so they can become structurally reliable, manufacturable, and circular. The interlayer must mediate contact between brittle glass components, accommodate tolerances, transfer shear forces, remain compatible with FDM fabrication, and allow non-destructive disassembly at end-of-life.

3.8.1. Literature synthesis

The reviewed literature confirms that segmentation is unavoidable for free-form structural cast-glass applications. Large monolithic cast-glass components are restricted by annealing time, casting complexity, sensitivity to flaws, cost, and handling limitations. As a result, architectural cast-glass structures require brick-scale components that must be joined into larger assemblies. Existing connection strategies, such as additional substructures and adhesive bonding, can provide structural reliability, but they compromise transparency and end-of-life recovery. Dry mechanical interlocking therefore offers the most promising solution towards circular cast-glass construction, provided that direct glass-to-glass contact is prevented by a suitable interlayer.

Previous research on dry interlayers shows that the interlayer must combine stress redistribution, tolerance accommodation, creep resistance, sufficient compressive strength, and reversibility. However, currently used interlayer materials often involve trade-offs between stiffness, compliance, long-term stability, fabrication complexity, and demountability. This motivates the use of an AM polymer interlayer, where material behaviour and interlocking geometry can be designed together within a removable interface.

The Glass Vault case study demonstrates that standard cast-glass bricks can create a complex compression-dominated assembly when the interlayer provides sufficient tolerance compensation, temporary construction stability, and load transfer. However, its use of permanent epoxy putty also illustrates the main circularity limitation of current cast-glass construction. For this research, the case study therefore functions as both a precedent and a design challenge: the new interlayer must provide comparable assembly and structural functions while remaining reversible.

A key conclusion of the literature study is that planar cast-glass components provide the most suitable characteristics for this research. When the interlocking function is shifted to the polymer interlayer, additional interlocking within the glass component itself becomes redundant. Planar glass units significantly reduce casting complexity, improve repeatability, and enable reuse across various assemblies. Geometric variation, angular adaptation, and mechanical interlocking can instead be introduced through the customisable interlayer.

The material review identifies PET-based fibre-reinforced polymers as the most promising direction for experimental testing. PETG-GF and PET-CF show high potential due to their balance between stiffness, dimensional stability, durability, and reduced shrinkage. PETG-HF and PETG-CF remain relevant for assessing the influence of processability, flow behaviour, and carbon-fibre reinforcement. PLA and PLA-CF are retained as backup materials because of their printability and dimensional stability, but their limited long-term durability restricts their suitability for final application.

The review of FDM tolerances and process limitations shows that additive manufacturing constraints directly define the feasible design space. Nozzle diameter, layer height, anisotropy, porosity, thermal shrinkage, warping, first-layer quality, and glass–polymer adhesion all influence whether an interlocking geometry can be printed reliably and perform structurally. These limitations will therefore be treated as primary design drivers.

Finally, the typology review identifies two promising geometric directions. Geometric mechanical interlocking provides clear kinematic confinement and predictable shear transfer, while distributed surface-based interlocking provides tolerance accommodation, elastic averaging, and redundancy across the interface. The final geometry development should therefore combine both typology principles into a simplified, 3D-printable hybrid solution with robust features and removable locking elements.

3.8.2. Research gaps

Despite the progress made in previous research, several gaps remain. First, reliable glass–polymer adhesion without primers or permanent adhesives is still not fully established. The interlayer must adhere strongly enough to remain stable during fabrication, assembly, and service life, but it must also remain removable without damaging or contaminating the glass substrate. This balance between adhesion and reversibility remains one of the central unresolved challenges.

Second, the polymer material behaviour for direct printing on glass substrates requires further experimental validation. Previous work identified PLA and PETG as promising baseline materials, but both have clear limitations. PLA is dimensionally stable and removable, but lacks long-term durability. PETG offers better toughness and environmental resistance, but is more prone to thermal shrinkage, warping, and interface stresses. The performance of fibre-reinforced and modified PET-based alternatives on glass also requires experimental validation.

Third, the geometric design space for AM interlocking interlayers remains underdeveloped. Current interlocking typologies provide useful principles, but many are too tolerance-sensitive, too dependent on thin flexible features, or too complex for direct fabrication on glass. A novel geometry is needed that can transfer shear effectively while remaining printable, tolerant to fabrication deviations, and reversible.

Fourth, the structural behaviour and failure mode of glass–interlayer–glass connections require validation. It is not yet clear whether failure will be governed by the glass–polymer interface, the printed interlocking geometry, the polymer material itself, or a combination of these. Understanding these failure mechanisms and their hierarchy is essential for designing a reliable structural system. Finally, end-of-life demountability remains insufficiently resolved. Heating the polymer to its glass transition temperature may enable removal for some materials, but this approach is not ideal for larger components or higher-performance polymers. Controlled mechanical removal strategies and demounting triggers must therefore be investigated to support component reuse and material recovery.

3.8.3. Research positioning and next steps

This research responds to these gaps by treating the interlayer as a coupled material, geometric, fabrication, and circularity problem. The objective is to develop an interlayer system in which material behaviour, FDM process constraints, glass-polymer adhesion, load transfer, and demountability work in perfect harmony.

Within this framework, the literature review defines the initial design space rather than the final solution. The selected polymer candidates provide the material starting point, while the typology review identifies the geometric principles most relevant for reversible interlocking. The subsequent research therefore focuses on testing how these material and geometric assumptions perform when translated into physical glass–interlayer specimens.

This positioning leads to an experimentally driven design process in which material selection, geometry development, interface behaviour, structural performance, and demountability are evaluated in relation to one another. The central objective is to determine whether a directly printed polymer interlayer can provide sufficient adhesion, controlled shear transfer, manufacturable geometry, and non-destructive reversibility for planar cast-glass assemblies.

The literature review therefore establishes the framework for the remainder of the thesis: a transition from theoretical material and typology selection towards experimental validation of a reversible, mechanically interlocking polymer interlayer system.

4

Material experiments

4.1. Experimental setup & methodology

4.1.1. Experimental overview

The material experiments were designed to systematically evaluate the compatibility of the pre-selected set of FDM polymers (Section 3.5.3) when deposited directly onto float glass substrates. The primary objective was to identify the most suitable polymer candidates and determine the optimal printing parameters required for reliable, direct interlayer deposition.

To ensure a consistent comparison across different materials, each filament was tested using a multi-geometry coupon. This specimen was custom designed to reveal specific printing phenomena within a single print, focussing on four key performance indicators:

- **Adhesion reliability:** The strength and stability of the polymer-glass bond during and after the printing process.
- **Thermal behaviour:** The extent of corner-induced warping and isotropic shrinkage during the cooling phase.
- **Extrusion & wetting:** The quality of the material flow and its ability to interface effectively with the glass surface.
- **Substrate recovery:** The ability to remove the polymer from the glass without leaving unwanted residue, damaging the substrate or requiring excessive force.

The experimental methodology integrated material evaluation with parameter optimization. For each filament, a baseline configuration (sample 0) was established, derived from manufacturer presets in Bambu Studio and previous research by Van Kessel (2025). Using a one-factor-at-a-time approach, parameters were then iteratively adjusted from this baseline. This allowed for the simultaneous optimization of printing settings and the assessment of material suitability, eventually narrowing the selection to the most promising candidates for the final application. Images of the fabricated specimens for each tested filament prior to evaluation are provided in Appendix B.

4.1.2. Materials

The following filaments were selected in Section 3.5.3 for experimental evaluation:

1. PLA
2. PLA-CF
3. PETG-HF
4. PETG-GF
5. PETG-CF
6. PET-CF

To ensure consistency, all materials were sourced from Bambu Lab, with the exception of PETG-GF, which was sourced from Elegoo due to availability constraints.

Strict moisture control was implemented to prevent hygroscopic degradation. All filaments were stored separately in airtight bags with desiccant and dried in a blast oven (see Figure 4.1a) according to manufacturer specifications prior to use. A minor deviation was necessary for PET-CF: while the manufacturer (Bambu Lab) recommends drying at 80°C for 8-12 hours, the oven's maximum capacity was 75°C. To compensate, the drying duration was maintained at 75°C for a full 12 hours. No visual indicators of residual moisture, such as bubbling or stringing, were observed during the subsequent printing process. Finally, during operation, filaments were housed in a closed, active filament dryer to minimize ambient moisture absorption (see Figure 4.1c, right).

4.1.3. Glass substrate

The printing substrate consisted of 150 x 150 mm samples of 8 mm thick clear Pilkington float glass (see Figure 4.1b). To ensure consistent adhesion conditions across all test cycles, a standardized surface preparation protocol was implemented.

First, any polymer residue from previous experiments was removed using a putty knife. Then, the glass was meticulously cleaned with 99,9% isopropyl alcohol (IPA) and high-quality paper towel to remove fingerprints, dust and other contaminants that could impede proper adhesion.

Due to the high adhesion strength of certain filaments, mechanical removal occasionally resulted in glass chipping. In instances of minor chipping, the substrate continued to be used. If major chipping occurred, the print location was slightly shifted to an undamaged area of the glass; if the extent of the damage made this impossible or risked affecting the results, the glass substrate was replaced entirely. This ensured that the surface topography remained consistent and did not provide artificial mechanical interlocking for subsequent samples.

(a) Blast furnace used for filament drying

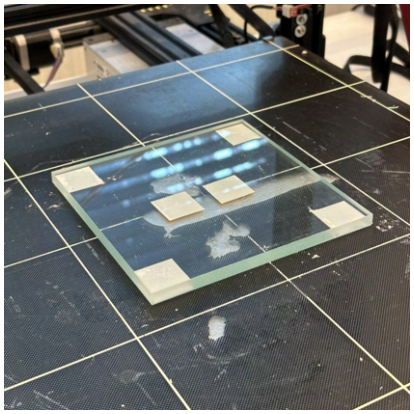

(b) Glass substrate secured to the print bed with small patches of double sided tape

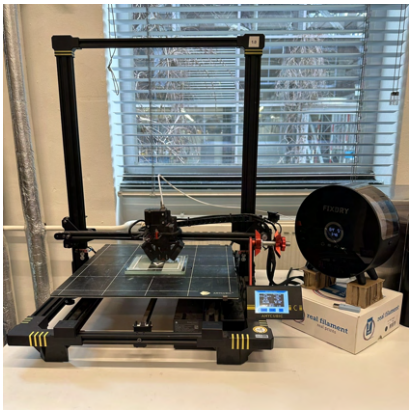

(c) Additive manufacturing setup with filament dryer

Figure 4.1: Experimental setup for direct polymer deposition on glass

4.1.4. Additive manufacturing setup

Experimental prints were executed on an Anycubic Chiron equipped with a 1.0 mm hardened steel nozzle (Figure 4.1c). Bambu Studio was used as the slicing software, utilizing a custom printer preset developed for the Chiron by the LAMA Lab at the Faculty of Architecture, TU Delft.

To ensure maximum part density and consistent thermal mass, all specimens were printed with 100% infill using a concentric pattern. The single top and bottom layers were also set to a concentric pattern to maintain geometric symmetry. The layer height was set to 0.2 mm for the initial layer to maximize surface wetting and adhesion, while subsequent layers were maintained at 0.3 mm. To prevent the accumulation of vertical defects, the seam position was randomized for every printed layer.

A significant adjustment was made to the print head travel settings: the Z-hop (nozzle retraction height during non-printing moves) was increased from the standard 0.4 mm to 2.0 mm. This served as a precautionary measure to prevent the nozzle from striking any deformed features or warped edges that might emerge during the experimental iterations. For environmental monitoring, the ambient temperature and humidity were recorded at the beginning of each test cycle.

4.1.5. Print bed preparation

The glass substrates were placed directly onto the heated print bed and secured using double-sided tape (Figure 4.1b). Initial tests used two full-length strips of tape; however, the resulting bond made substrate removal excessively difficult. Consequently, all subsequent samples were secured using small patches of tape at all corners and the centre, which provided sufficient lateral stability during printing while still allowing for (relatively) easy removal.

Because the glass and tape increased the build plate height by approximately 8.25 mm, a manual Z-offset was required. This was done by vertically repositioning the two Z-axis limit switches located on either side of the printer frame. Final precision adjustments were performed using the manual levelling screws located beneath the print bed. Once the height was established, a rigorous bed-levelling procedure was conducted. This was repeated whenever the filament or glass substrate changed.

1. **Thermal stabilization:** Heat the print bed to the target temperature (material dependent) and allow a minimum of 5 minutes for the glass substrate to reach thermal equilibrium.
2. **Nozzle preparation:** Ensure the nozzle tip is clean and free of residual polymer debris.
3. **Manual levelling:** Insert a standard sheet of printer paper between the nozzle and the glass. Adjust the bed height at each corner until a slight, consistent resistance if felt when moving the paper.
4. **Iterative adjustment:** Repeat the levelling across all corners in a diagonal cross-pattern. The process was typically repeated three times to ensure accuracy across the entire surface.
5. **Validation:** Print a thin, circular test specimen (two or three layers high) to verify extrusion consistency. Minor adjustments were made in real-time during this validation print if necessary.

4.1.6. Test coupon design

A custom test coupon was developed (Figure 4.2) to simultaneously isolate and evaluate various printing phenomena associated with direct-on-glass deposition. The geometry integrates several distinct features, each designed to monitor a specific material response.

Warping and stress concentrations:

- **Square frame:** Designed with sharp 90° corners to maximize stress concentrations and detect the onset of corner-induced warping or peeling.
- **Square frame - filleted:** Features filleted corners to decouple stress concentrations from global shrinkage. This serves as a comparative baseline to the outer frame, evaluating how reduced local stress affects overall dimensional stability.
- **Triangular pad:** Utilizes a sharp-tip, hollow geometry to specifically test the polymer's susceptibility to local lifting and delamination under high-shrinkage conditions.

Shrinkage behaviour:

- **Circular ring:** Utilized to detect pure isotropic shrinkage and evaluate uniform edge-lift, independent of corner-stress effects.

Adhesion consistency and extrusion quality:

- **Circular pad:** Provides a solid geometry with continuous surface area to evaluate baseline adhesion strength and the mechanical effort required for removal after cooling.
- **Micro-pad array:** Evaluates adhesion consistency and repeatability across the glass sample.
- **Flow and wetting lines:** Two single-track extrusions designed to assess extrusion stability, nozzle-to-glass wetting behaviour, and the consistency of the initial layer bond.

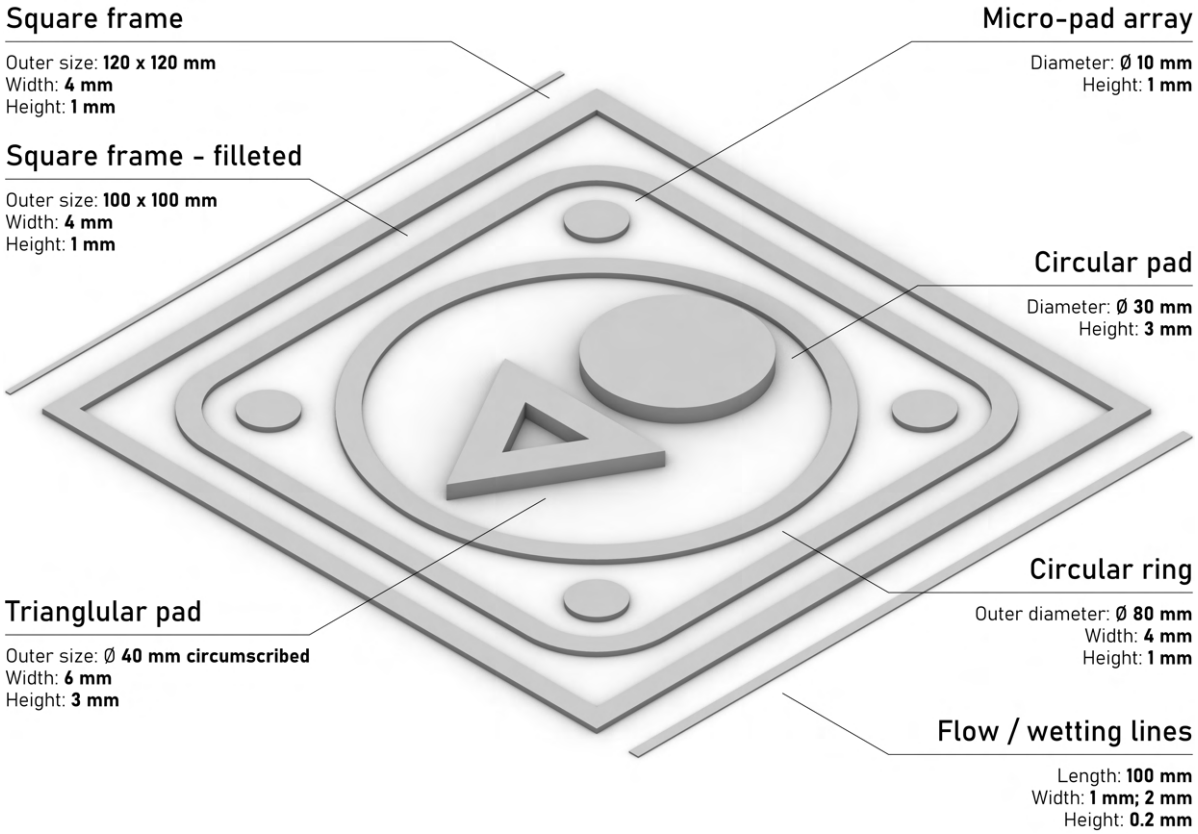

Figure 4.2: Custom multi-geometry test coupon for evaluating polymer deposition on glass

4.1.7. Parameter optimisation strategy

The initial printing parameters for each filament were derived from the manufacturer presets provided by the Bambu Lab slicing software. These presets served as a validated baseline reflecting the manufacturer's recommended processing conditions. This baseline was further refined using the findings from Van Kessel (2025) to create a custom initial profile for each material, defined as sample 0.

An iterative one-factor-at-a-time strategy was used in the optimisation process; for each successive sample, only a single parameter was modified while all the others remained constant. This allowed the isolated effect of individual parameters to be observed. The following parameters were systematically investigated:

- **Nozzle temperature** [°C]
- **Print bed temperature** [°C]
- **Print speed** (including specific first-layer speed) [mm/s]
- **Cooling fan speed** [%]

The order in which these parameters were optimised was determined by the specific material characteristics and foreseen printing challenges. Parameters were iteratively tuned to achieve an optimal balance between the following five performance criteria:

- **Minimal thermal warping:** Reducing corner-lift and internal stresses.
- **Stable polymer wetting:** Ensuring the material spreads effectively across the glass.
- **Consistent extrusion behaviour:** Maintaining a steady flow without defects.
- **Strong adhesion:** Ensuring the bond remains secure during and after the printing process.
- **Controlled removability:** Allowing for the detachment of the part after cooling without substrate damage.

4.1.8. Experimental procedure

A standardized procedure was followed for each experimental iteration to ensure consist evaluation across the different materials:

1. **Substrate preparation:** Clean the glass surface using the protocol defined in Section 4.1.3
2. **Thermal stabilization:** Heat the print bed and allow the glass substrate to reach thermal equilibrium (minimum 5 minutes).
3. **Environmental logging:** Record ambient temperature and humidity.
4. **Deposition:** Print the custom test coupon.
5. **Cooling phase:** Allow the print bed and substrate to cool to below 30°C.
6. **Assessment:** Evaluate warping, perform manual removal, and record qualitative observations.

To evaluate the results, two qualitative scales were established. Additional context, such as substrate damage, was also recorded.

Warping evaluation:

- **None:** No visible warping; geometry remains flat
- **Low:** Slight, barely noticeable deformation
- **Moderate:** Minor edge lift, geometry still usable
- **High:** Clear visible warping; geometry compromised
- **Severe:** Large corner lift / global distortion; print unusable

Adhesion evaluation:

- **Excellent:** Strong bonding, no visible lift, consistent over full area
- **Good:** Fully bonded during print; requires deliberate force to remove
- **Moderate:** Fully printed, but can be removed easily by hand; local weak zones
- **Poor:** Partial detachment, corners lifting, adhesion unreliable
- **Failed:** Detaches during the print or immediately after cooling

4.2. PLA (Bambu Lab)

PLA was selected as baseline reference material because of its ease of processing, dimensional stability, and reliable adhesion behaviour reported in previous research. Although PLA is not considered a primary candidate for final application due to its limited thermal and environmental durability, it provides a useful benchmark for evaluating the behaviour of the other selected materials. The optimisation process started from the parameters used by Van Kessel (2025) and was refined according to the experimental procedure described in Section 4.1. The resulting PLA print-parameter optimisation sequence and final selected settings are summarised in Table 4.1, providing the basis for the key findings discussed after the table.

Table 4.1: PLA print-parameter optimisation results on glass

Sample	Bed temp. [°C]	Nozzle temp. [°C]	Print speed [mm/s]	Fan cooling [%]	Adhesion	Warping
0	60	210	30, 60	0 » 0 » 30	Good	None
1	60	**220**	30, 60	0 » 0 » 30	Moderate	None
2	60	**200**	30, 60	0 » 0 » 30	Moderate	None
3	**55**	210	30, 60	0 » 0 » 30	Poor	None
4	**65**	210	30, 60	0 » 0 » 30	Moderate	None
5	60	210	30, 60	**0**	Moderate	None
6	60	210	30, 60	**0 » 0 » 60**	Poor	None
7	60	210	**20, 40**	0 » 0 » 30	Poor	None
8	60	210	**40, 80**	0 » 0 » 30	Moderate	None
Final	60	210	30, 60	0 » 0 » 30		

Note. Commas indicate layer-based changes; » indicates stage-based changes.

Key findings

All PLA samples demonstrated excellent thermal stability, with no warping or chipping observed. While the material's low CTE and high stiffness make it easy to process, its adhesion remains geometry-dependent. Elements with larger surface areas, such as the circular and triangular pads, consistently achieved better bond strength, whereas thinner elements like lines and frames remained easily removable by hand, indicating that PLA lacks the ability to achieve the required level of overall adhesion.

PLA demonstrated a high sensitivity to parameter adjustments during the optimization process. A nozzle temperature of 210°C and a bed temperature of 60°C proved optimal; lowering the nozzle temperature to 200°C (Sample 2) or the bed temperature to 55°C (Sample 3) resulted in noticeable reduced adhesion strength. Conversely, increasing the bed temperature to 65°C (Sample 4) led to first-layer flow issues, likely due to exceeding the glass transition temperature of 60°C (Bambu Lab, n.d.-k).

Cooling and print speed also significantly influenced bond strength. Excessive cooling negatively impacted adhesion; specifically, increasing the fan speed to 60% after ⅔ of the layers (Sample 6) resulted in elements being easily removed by hand. Print speed adjustments similarly affected performance. While reducing the speed to 40 mm/s (Sample 7) resulted in a high print quality, it compromised the adhesion. Increasing the first-layer speed to 40 mm/s (Sample 8) caused instability on the first layer, although this was eventually resolved during subsequent layers.

Conclusion

PLA demonstrates excellent processability and compatibility with glass, resulting in good adhesion for elements with larger surface areas. The optimal parameters were identified as a 210°C nozzle temperature, 60°C bed temperature, 60 mm/s print speed (with 50% speed on the first layer), and 30% fan speed (after ⅔ of the layers).

4.3. PLA-CF (Bambu Lab)

PLA-CF was selected as a reinforced PLA-based backup material because it combines the processability of PLA with improved stiffness and dimensional stability. The addition of carbon fibres is expected to improve mechanical performance, but also increases brittleness and may affect wetting behaviour on the glass substrate. Because the base polymer remains PLA, its long-term thermal and environmental durability remains limited compared with the PET-based candidates. The optimisation process followed the experimental procedure described in Section 4.1. The resulting PLA-CF print-parameter optimisation sequence and final selected settings are summarised in Table 4.2, providing the basis for the key findings discussed after the table.

Table 4.2: PLA-CF print-parameter optimisation results on glass

Sample	Bed temp. [°C]	Nozzle temp. [°C]	Print speed [mm/s]	Fan cooling [%]	Adhesion	Warping
0	60	230	20, 40	0, 0, 40	Good	None
1	60	**220**	20, 40	0, 0, 40	Moderate	None
2	60	**240**	20, 40	0, 0, 40	Good	None
3	60	240	**30, 60**	0, 0, 40	Moderate	None
4	60	240	**20, 60**	0, 0, 40	Moderate	None
5	**50**	240	20, 40	0, 0, 40	Poor	None
6	**70**	240	20, 40	0, 0, 40	Good	None
7	70	240	20, 40	**0**	Good	None
8	70	240	20, 40	**0, 0, 80**	Moderate	None
Final	70	240	20, 40	0		

Note. Commas indicate layer-based changes.

Key findings

PLA-CF demonstrated exceptional thermal stability, exhibiting no warping or chipping across all samples. While the printing process was smooth and consistent, the material's adhesion proved especially sensitive to thermal input variations. The initial test (Sample 0) yielded good results where some elements required deliberate force for removal. However, reducing the nozzle temperature to 220°C (Sample 1) resulted in a noticeably lower bond strength, making most elements easily removable by hand. Increasing the nozzle temperature to 240°C (Sample 2) significantly improved wetting, requiring the use of tools for removal of most of the elements.

Print speed and bed temperature also played a critical role in the interfacial bond. Increasing the first-layer print speed to 30 mm/s (Sample 3) impaired adhesion, and even with a first-layer speed of 20 mm/s and subsequent layers at 60 mm/s (Sample 4), the adhesion remained moderate. Bed temperature proved equally important: reducing it to 50°C (Sample 5) led to inconsistent, poor adhesion, while increasing it to 70°C (Sample 6) resulting in consistent and strong bonding, with all elements requiring deliberate force and tools for removal.

Maintaining the cooling fan at 0% (Sample 7) yielded the best, most consistent adhesion result. In contrast, increasing the fan speed to 80% (Sample 8) promoted faster solidification, which resulted in reduced bond strength and allowed all elements to be removed by hand.

Conclusion

PLA-CF demonstrated excellent layer consistency and, with optimized print parameters, provides a good level of adhesion that frequently requires mechanical tools to remove the test coupon. The optimal parameters were identified as a 240°C nozzle temperature, 70°C bed temperature, 40 mm/s print speed (with 50% speed on the first layer), and 0% fan speed. Deviations, particularly regarding reduced nozzle/bed temperatures or increased fan speeds, were found to consistently impair adhesion quality.

4.4. PETG-HF (Bambu Lab)

PETG-HF was selected as a high-flow PETG variant to evaluate whether improved melt flow and extrusion consistency could improve wetting, deposition quality, and first-layer adhesion on glass. Compared with standard PETG, it is expected to offer better processability, but the material remains sensitive to thermal shrinkage and residual stresses during cooling. It therefore provides a useful comparison between improved printability and the adhesion and warping challenges typically associated with PETG-based filaments. The PETG-HF print-parameter optimisation sequence and final selected settings are summarised in Table 4.3, providing the basis for the key findings discussed after the table.

Table 4.3: PETG-HF print-parameter optimisation results on glass

Sample	Bed temp. [°C]	Nozzle temp. [°C]	Print speed [mm/s]	Fan cooling [%]	Adhesion	Warping
0	90	240	30, 60	0, 0, 40	**Failed**	—
1	90	240	**5, 20**	0, 0, 40	**Moderate**	**None**
2	90	240	**10, 40**	0, 0, 40	**Moderate**	**None**
3	90	240	**10, 60**	0, 0, 40	**Poor**	**None**
4	90	**250**	10, 40	0, 0, 40	**Good**	**None**
5	90	**230**	10, 40	0, 0, 40	**Poor**	**None**
6	90	**255**	10, 40	0, 0, 40	**Good**	**None**
7	**80**	255	10, 40	0, 0, 40	**Moderate**	**None**
8	**100**	255	10, 40	0, 0, 40	**Good**	**None**
9	100	255	10, 40	**0**	**Good**	**None**
10	100	255	10, 40	**0, 0, 60**	**Good**	**None**
Final	100	255	10, 40	0		

Note. Commas indicate layer-based changes.

Key findings

PETG-HF exhibited stable printing performance, with no signs of chipping or warping. Initial attempts demonstrated that the material is highly sensitive to first-layer dynamics. The first print (Sample 0) failed immediately due to poor adhesion at 30 mm/s. Further refinement demonstrated that adhesion is heavily dependent on slower initial print speeds; a first-layer speed of 10 mm/s followed by 40 mm/s for subsequent layers (Sample 2) proved optimal. Increasing speeds beyond 40 mm/s (Sample 3) compromised both adhesion and layer consistency.

Thermal management was equally important. The material required high temperatures to achieve sufficient wetting on the glass substrate. A nozzle temperature of 230°C (Sample 5) proved insufficient, causing poor first-layer adhesion and minor printing errors. Conversely, 255°C was identified as the optimal nozzle temperature for proper wetting and adhesion. At this temperature, the bond strength shifted from easily removable by hand to requiring deliberate manual force for removal.

Bed temperature and active cooling significantly influenced the integrity of the interface as well. Lowering the bed temperature to 80°C (Sample 7) resulted in reduced adhesion, whereas increasing it to 100°C (Sample 8) further improved wetting to maximise the polymer-glass bond. At 100°C, all elements of the test coupon required deliberate force to be removed. Regarding cooling, maintaining the fan at 0% (Sample 9) yielded the highest adhesion and layer quality. While the low-viscosity nature of PETG-HF at 255°C can lead to stringing and oozing, the absence of active cooling successfully minimized these defects as well.

Conclusion

PETG-HF demonstrates high compatibility with glass, showing good adhesion and no warping, provided the parameters are carefully controlled. The ideal parameters were identified as a 255°C nozzle temperature, 100°C bed temperature, 10 mm/s initial layer speed (40 mm/s for subsequent layers), and 0% fan speed.

4.5. PETG-GF (Elegoo)

PETG-GF was selected as a glass-fibre reinforced PETG variant to evaluate whether fibre reinforcement could improve stiffness, dimensional stability, and resistance to warping while retaining the general processability of PETG. The material is expected to offer better dimensional control than unreinforced PETG, but the addition of glass fibres may also reduce ductility and increase the risk of brittle interface behaviour. The optimisation process followed the experimental procedure described in Section 4.1. The resulting PETG-GF print-parameter optimisation sequence and final selected settings are summarised in Table 4.4, providing the basis for the key findings discussed after the table.

Table 4.4: PETG-GF print-parameter optimisation results on glass

Sample	Bed temp. [°C]	Nozzle temp. [°C]	Print speed [mm/s]	Fan cooling [%]	Adhesion	Warping
0	90	240	5, 20	0, 0, 40	**Excellent**	**None**
1	90	240	**10, 40**	0, 0, 40	**Excellent**	**None**
2	90	240	**20, 60**	0, 0, 40	**Excellent**	**None**
3	90	**255**	20, 40	0, 0, 40	**Excellent**	**None**
4	90	**230**	20, 40	0, 0, 40	**Good**	**None**
5	**80**	255	20, 40	0, 0, 40	**Excellent**	**None**
6	**100**	255	20, 40	0, 0, 40	**Excellent**	**None**
7	100	255	20, 40	**0**	**Excellent**	**None**
8	100	255	20, 40	**0, 0, 60**	**Excellent**	**None**
Final	100	255	20, 40	0, 0, 60		

Note. Commas indicate layer-based changes.

Key findings

PETG-GF demonstrated stable printing performance with excellent adhesion and no signs of warping. However, chipping of the glass substrate was a recurring issue due to the high polymer-glass bond strength, particularly when removing the circular pads. After only four samples, the cumulative chipping damage necessitated a substrate replacement. Despite this, the first-layer adhesion was not negatively affected throughout the series.

Initial testing (Sample 0) utilized slow printing speeds (5 mm/s first layer, 20 mm/s subsequent layers), which resulted in slight edge burning. Increasing the speed to 40 mm/s (with a 20 mm/s first layer) in Sample 2 proved the best balance between speed and consistent adhesion quality. Adjustments to the nozzle temperature also proved critical: increasing this from 240°C to 255°C (Sample 3) significantly improved adhesion, however this also resulted in severe chipping when removing the print. Reducing the nozzle temperature to 230°C (Sample 4) provided good adhesion, but minor adhesion issues were observed on the first layer.

A strong correlation between bed temperature and bond strength was observed. At 80°C (Sample 5), adhesion was moderate; however, increasing the bed temperature to 100°C (Sample 6) resulted in a bond so strong that removal required mechanical tools and excessive force, causing severe substrate damage. Fan speed adjustments were crucial for balancing adhesion and ease of print removal. Maintaining the fan at 0% (Sample 7) resulted in the highest adhesion, necessitating bed reheating for removal. Increasing the fan speed to 60% after the second layer (Sample 8) provided an optimal balance, ensuring reliable adhesion without excessive removal force or substrate damage.

Conclusion

PETG-GF exhibits excellent adhesion and thermal stability, but its high bond strength requires precise parameter control to avoid glass damage. The optimal settings were identified as a 255°C nozzle temperature, 100°C bed temperature, 40 mm/s print speed (with 50% first-layer speed), and 60% fan speed after the second layer. These settings balance reliable adhesion with safer removal and consistent print quality.

4.6. PETG-CF (Bambu Lab)

PETG-CF was selected as a carbon-fibre reinforced PETG variant to evaluate whether fibre reinforcement could improve stiffness, dimensional stability, and resistance to warping while maintaining sufficient printability on glass. Compared with PETG-GF, the carbon-fibre reinforcement is expected to provide a tougher and less brittle material response, but it may still increase stiffness and affect removability from the glass substrate. The PETG-CF print-parameter optimisation sequence and final selected settings are summarised in Table 4.5, providing the basis for the key findings discussed after the table.

Table 4.5: PETG-CF print-parameter optimisation results on glass

Sample	Bed temp. [°C]	Nozzle temp. [°C]	Print speed [mm/s]	Fan cooling [%]	Adhesion	Warping
0	90	240	5, 20	0, 0, 40	**Excellent**	**None**
1	90	240	**10, 40**	0, 0, 40	**Excellent**	**None**
2	90	240	**20, 40**	0, 0, 40	**Good**	**None**
3	90	**255**	10, 40	0, 0, 40	**Excellent**	**None**
4	90	**230**	10, 40	0, 0, 40	**Good**	**None**
5	**80**	255	10, 40	0, 0, 40	**Excellent**	**None**
6	**100**	255	10, 40	0, 0, 40	**Excellent**	**None**
7	90	255	10, 40	**0**	**Excellent**	**None**
8	90	255	10, 40	**0, 0, 60**	**Excellent**	**None**
Final	90	255	10, 40	0		

Note. Commas indicate layer-based changes.

Key findings

PETG-CF demonstrated excellent thermal stability with no observed warping. A notable advantage of this material was its durability on the glass substrate, which lasted for six printing cycles before requiring replacement (50% improvement over PETG-GF). While the material remained prone to leaving minor residue upon removal, this was easily managed via mechanical scraping, using a putty knife. Unlike the glass-fiber variant, PETG-CF proved to be tougher and less brittle, facilitating easier handling during removal.

Initial adhesion (Sample 0) was exceptionally strong and consistent, requiring significant force and the use of tools for removal. While slow (5 mm/s first layer, 20 mm/s subsequent layers), this baseline provided high-quality layers with negligible stringing. Increasing the print speed to 40 mm/s with a 10 mm/s first layer speed (Sample 1) successfully reduced print time by nearly 50% without compromising adhesion. However, increasing the first-layer speed to 20 mm/s (Sample 2) degraded adhesion strength, confirming that a 10 mm/s first-layer speed is essential for optimal results.

Thermal parameters were critical in regulating the bond strength. Increasing the nozzle temperature to 255°C (Sample 3) resulted in strong, consistent adhesion, whereas 230°C (Sample 4) resulted in a weaker, though still acceptable, bond. Bed temperature adjustments revealed a distinct upper limit for reversibility: while 80°C and 90°C provided stable performance, 100°C (Sample 6) resulted in excessively high adhesion that induced glass chipping. Consequently, 90°C was identified as the threshold for maintaining stability without compromising the substrate. Finally, fan speed was optimized for optimal print removal; maintaining 0% fan speed (Sample 7) yielded the cleanest layers, while 60% fan speed (Sample 8) slightly reduced adhesion, facilitating easier removal without sacrificing quality.

Conclusion

PETG-CF provides high-strength adhesion and consistent layer quality. The optimal settings were identified as a 10 mm/s first-layer speed (40 mm/s for subsequent layers), 255°C nozzle temperature, 90°C bed temperature, and 0% fan speed. These parameters optimize the balance between adhesion strength and the ease of print removal, while the material's toughness significantly extends the service life of the glass substrate.

4.7. PET-CF (Bambu Lab)

PET-CF was selected as a carbon-fibre reinforced PET-based material to evaluate whether a higher-performance polymer could improve stiffness, dimensional stability, and thermal resistance compared with the PETG candidates. The material is expected to offer strong mechanical performance and reduced warping risk, but it is also more brittle and more demanding to process. PET-CF is ideally printed in an enclosed environment; however, this was not available in the LAMA Lab setup. The optimisation process followed the experimental procedure described in Section 4.1. The resulting PET-CF print-parameter optimisation sequence and final selected settings are summarised in Table 4.6, providing the basis for the key findings discussed after the table.

Table 4.6: PET-CF print-parameter optimisation results on glass

Sample	Bed temp. [°C]	Nozzle temp. [°C]	Print speed [mm/s]	Fan cooling [%]	Adhesion	Warping
0	90	255	5, 20	0	**Excellent**	**None**
1	90	255	**10, 40**	0	**Excellent**	**None**
2	90	255	**20, 40**	0	**Excellent**	**None**
3	90	**245**	20, 40	0	**Excellent**	**None**
4	**80**	245	20, 40	0	**Excellent**	**None**
5	**100**	245	20, 40	0	**Excellent**	**None**
6	90	245	20, 40	**0, 0, 30**	**Good**	**None**
7	90	245	20, 40	**0 » 0 » 60**	**Excellent**	**None**
Final	90	245	20, 40	0 » 0 » 60		

Note. Commas indicate layer-based changes; » indicates stage-based changes.

Key findings

PET-CF proved to be the most challenging material to process, characterized by significant brittleness and a high susceptibility to oozing. A nozzle temperature of 255°C served as the initial baseline, since hardware limitations prevented a higher manufacturer recommended temperature. Initial prints (Sample 0) exhibited excessively strong adhesion, resulting in severe substrate chipping and significant residue. Increasing the filament retraction distance gradually from 0.8 mm to 1.6 mm, successfully mitigated the oozing observed in initial trials.

Print speed was the primary parameter for improving reversibility. Increasing the first-layer speed to 10 mm/s and subsequent layers to 40 mm/s (Sample 1) reduced substrate residue and chipping. Further adjusting the first-layer speed to 20 mm/s (Sample 2) successfully balanced strong and consistent adhesion with manageable ease of removal. A critical refinement occurred with the nozzle temperature: reducing it to 245°C (Sample 3) yielded the cleanest printing results, maintaining high bond strength while virtually eliminating the residue and severe chipping encountered at higher temperatures.

The interaction between bed temperature and fan cooling provided final control over the interface. Bed temperature adjustments showed minimal impact, though 100°C (Sample 5) marginally reduced the bond strength compared to 90°C. Fan speed was essential for suppressing stringing; while 30% fan speed resulted in inconsistent adhesion, a 60% fan speed during the final third of the print (Sample 7) provided the optimal balance. This configuration secured strong, consistent bonding while minimizing the mechanical effort required for removal and preserving the integrity of the glass substrate.

Conclusion

PET-CF delivers exceptional print quality and mechanical performance, provided the parameters are strictly tuned to manage its inherent brittleness. The optimal settings were identified as a 245°C nozzle temperature, 90°C bed temperature, 40 mm/s print speed (with 50% for the first layer), and 60% fan speed (applied during the final third of the layers). These parameters successfully minimized glass substrate damage and residue, proving that PET-CF can be effectively utilized as a high-performance interlayer when thermal and cooling profiles are precisely controlled.

4.8. Material evaluation and selection

To answer research sub-question 1, the series of material experiments identifies fibre-reinforced filaments, specifically PETG-CF and PETG-GF, as the primary candidates for a reversible interlayer due to their favourable consistency and all-round performance. These materials offered the optimal balance between printability, adhesion strength, and dimensional stability when deposited directly onto a glass substrate. PET-CF also demonstrated high potential, with strong adhesion and consistent printing behaviour. However, its brittleness and sensitivity to thermal variations make it more demanding; nevertheless, when processed with optimized parameters, it shows potential to be a highly effective interlayer material. In contrast, PETG-HF is considered a secondary candidate, as its high-flow nature led to less consistent adhesion results compared to the fibre-reinforced filaments.

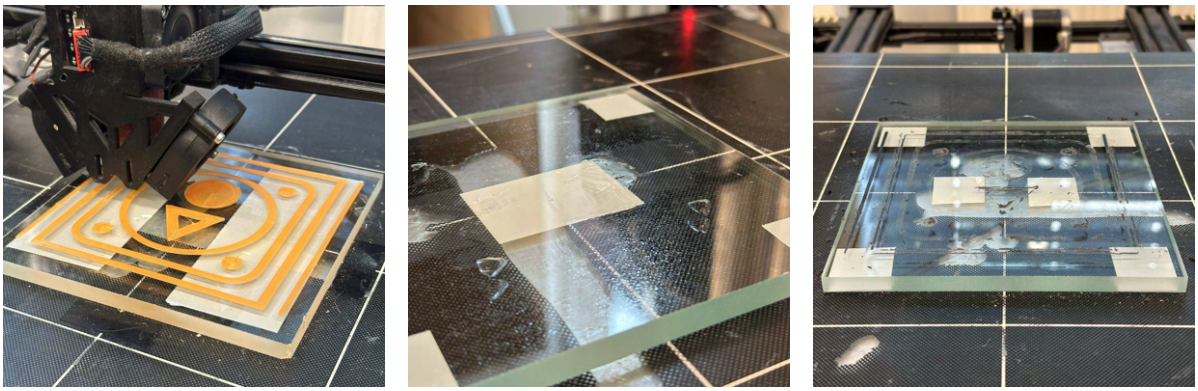

(a) Direct deposition of the custom test coupon onto a glass substrate

(b) Glass chipping caused by excessive polymer–glass adhesion during removal

(c) Polymer residue remaining on the glass surface after interlayer removal

Figure 4.3: Key representative observations from the material optimisation experiments

Representative examples of the key observations made during the material experiments are shown in Figure 4.3. These observations revealed the important trade-offs between printability, adhesion strength, and reversibility. A critical finding shown in Figure 4.3b, was the occurrence of glass chipping, which was exclusive to fibre-reinforced PET-based filaments. This resulted from the significant difference in CTE between the polymer and the glass. The high adhesion strength of these filaments allowed residual stresses to exceed the tensile strength of the glass, causing local chipping during removal. In some PETG-CF samples, removal also left minor polymer residue on the glass (see Figure 8.3), indicating strong adhesion can compromise clean substrate recovery even when the glass itself remains intact. In contrast, PLA-based filaments showed no chipping due to their lower CTE mismatch and lower overall bond strength.

Consequently, PLA-CF is taken forward as backup material. While its limited environmental durability makes it unsuitable for real-world outdoor applications, its superior mechanical performance compared to regular PLA makes it a more robust backup should the other candidates fail in a later stage of the research.

5

Geometric design evolution

5.1. Design framework and evaluation criteria

This chapter develops the geometry for the interlocking interlayer. By isolating the geometric design from material performance, this research-through-design process systematically evaluates how the geometry of the interlayer influences load transfer, assembly logic, tolerance accommodation, demountability, and fabrication complexity.

The development is guided by the design criteria established in the literature study: mechanical interlocking and geometric stability, additive manufacturing fidelity and printability, and versatility and circularity logic. The geometry must therefore provide reliable shear transfer through kinematic confinement, distribute load evenly across the interface, remain printable using FDM, avoid unnecessary thermal deformation, and allow placement-based assembly with reversible interlocking. These criteria form the framework for the iterative design evolution described in the following sections.

5.2. Evolution of the interlocking geometry

5.2.1. V1: Transition from sliding assembly to direct placement

Figure 5.1 shows how the design evolution began with a simple sliding dovetail geometry, which represent a clear example of geometric mechanical interlocking. This typology was selected because it provides a direct load path, strong kinematic confinement, and predictable shear transfer. However, in its base form, the sliding dovetail requires the upper component (shown in red) to be inserted through a full-length sliding movement. This makes the system impractical for larger cast-glass assemblies, where components preferably can be placed directly into position rather than slid through the full joint length.

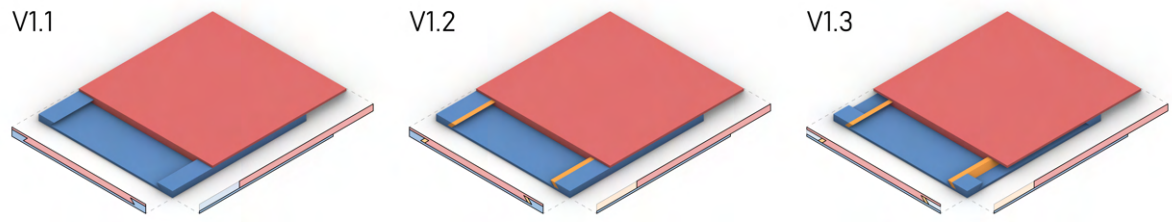

Figure 5.1: Evolution of the V1 interlocking geometry from continuous sliding assembly towards direct placement and post-placement locking. Each variant is shown in isometric view together with two cross-sectional views taken through the centre of the specimen.

In V1.1, the geometry therefore worked mechanically but remained too dependent on continuous sliding. In V1.2, a small amount of material was removed from the sides of the dovetail to create sufficient clearance for direct placement of the upper component. The removed material was then reintroduced as separate locking keys (shown in orange), allowing the interlocking function to be activated on command after placement. In V1.3, additional clearance was introduced in the perpendicular direction, enabling engagement from two orthogonal sides. This made the concept more suitable for corner conditions, and more complex assembly configurations.

The V1 series demonstrated that the sliding dovetail principle could be adapted towards placement-based assembly. However, the geometry remained relatively rigid and tolerance sensitive. Its sharp edges also introduced potential stress concentrations that could promote warping or delamination. Overall it was not ideal for FDM printing and so these limitations motivated the transition towards a more distributed interlocking strategy.

5.2.2. V2: Development of a distributed hybrid interlock

Figure 5.2 shows how the V2 series evolves the design from a single continuous interlocking feature to a distributed hybrid system. The aim was to improve redundancy, reduce tolerance sensitivity, and create a geometry that is better aligned with FDM fabrication constraints. Instead of relying on one precise dovetail connection, the V2 series distributes the interlocking function across multiple repeated features.

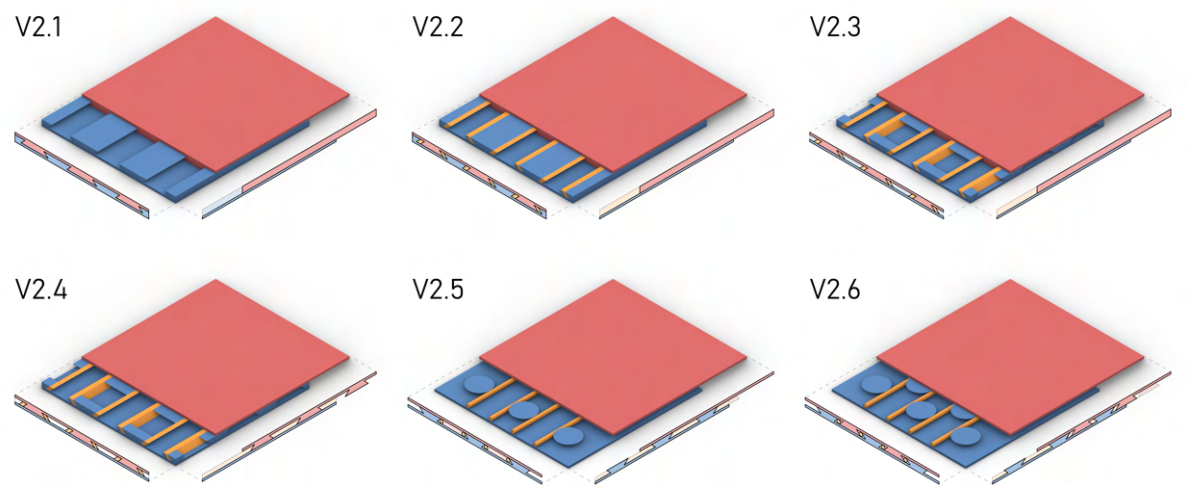

Figure 5.2: Evolution of the V2 geometry from a single dovetail interlock towards a distributed hybrid interlocking system. Each variant is shown in isometric view together with two cross-sectional views taken through the centre of the specimen.

V2.1 divides the single dovetail of the V1 series into a set of multiple smaller ones. This reduces dependence on one continuous feature and begins to distributed shear transfer across the interface. In V2.2 and V2.3, the removable keys are further integrated into the system, allowing the upper and lower interlayer halves to be placed first and locked afterwards. This retains the mechanical engagement of the dovetail principle while improving assembly flexibility. In V2.4, more material is removed from the linear ribs, transforming them into localised protruding features (referred to as *knobs* from now on). This creates a more surface-based interlock in which load transfer is distributed across repeated contact points rather than concentrated along continuous ridges.

The final design steps focus on improving printability and robustness. In V2.5, the square knobs are modified to make them round. This removes sharp corners, improves toolpath continuity, and reduces the risk of local stress concentrations during cooling. Additionally, the locking keys can also be simplified into cylindrical rods, which are easier to insert because they are not orientation-specific. V2.6 refines this knob-and-key system into the final geometry by increasing the density and regularity of the knobs. The result is a hybrid interlock that combines geometric confinement with distributed surface interaction.

Compared with the V1 series, the V2 geometry is less dependent on a single precise sliding feature and more redundant against of local deviations. It therefore better matches the design criteria established in the literature study: mechanical confinement is maintained, while the distributed layout improves robustness, tolerance accommodation, and manufacturability.

5.3. Functional analysis of the final geometry

Load transfer and kinematics

Under combined normal and shear loading, the final V2.6 geometry operates as a hybrid system. Shear resistance is provided by the geometric engagement between the rounded knobs and the cylindrical locking keys. Once the keys are inserted, they create a continuous load path across the interface and restrict relative sliding between the glass components.

Compression is distributed across the array of knobs and their surrounding instead of concentrating into one continuous ridge. This increases the effective load-transfer area and helps reduce local peak stresses. Additionally, the normal force acting on the distributed contact points generates frictional resistance, which complements the mechanical interlock and thereby enhances overall structural stability.

Assembly and reversibility

The final interlocking system prioritizes placement-based assembly. Components are easily positioned, and the keys are inserted to activate the interlocking function. This logic simplifies construction while still allowing for diagonal sliding as a secondary engagement mode when sequential placement is obstructed. Reversibility is achieved by removing the keys, allowing the glass components to be disassembled without damaging the interlayer or glass, thereby supporting circular economy principles.

Robustness and tolerance accommodation

The distributed knob layout enables a degree of elastic averaging. The connection is formed by collective engagement of multiple contact points, rather than relying on the precise fit of one continuous dovetail. Small deviations caused by FDM inaccuracies, glass surface irregularities, or minor assembly tolerances can therefore be distributed across the interface. This redundancy is important for direct printing on glass, where small dimensional deviations are difficult to avoid. The final geometry is therefore designed not only for ideal mechanical engagement, but also for realistic fabrication and assembly conditions.

Manufacturability for FDM

The transition from sharp dovetail features to rounded knobs directly responds to the limitations of FDM fabrication. Rounded features reduce stress concentrations, improve toolpath continuity, and lower the risk of warping or delamination during cooling. The knob dimensions are also kept significantly larger than the nozzle diameter, improving the reliability and repeatability of the printed features. In addition, the cylindrical keys simplify post-print assembly because they do not require a specific rotational orientation during insertion.

5.4. Parametric definition

The final geometry is defined through a Grasshopper script, allowing the main design parameters to be quickly adjusted and tuned. This parametric setup makes it possible to adapt the geometry to different material behaviours, interlayer thicknesses, key diameters, and assembly conditions. It also forms the basis for the geometry variants tested in the combined material and geometry experiments in Chapter 6. The geometry is controlled by four primary parameters:

1. **Knob diameter:** Controls the spatial density of knobs, their contact area, and bending stiffness.
2. **Overlap / offset:** Determines the clearance for the keys and resulting tightness of the lock.
3. **Knob Height:** Influences the key diameter and total interlayer thickness.
4. **Knob angle:** Influences the diameter of the knobs at their base and their resistance to bending or shear deformation.

Together, these parameters allow the final geometry to be adapted without changing the underlying assembly principle. This makes the system suitable for iterative optimisation and for future adjustment to different glass geometries or structural requirements.

5.5. Remaining challenges

Although V2.6 addresses the main design criteria, several aspects still require experimental validation:

- **Local stress concentrations:** Despite the use of rounded features, the transition between the knob and the base layer remains a critical location. Under high shear loads, failure may initiate at the knob base, especially if interlayer bonding between printed layers is insufficient.
- **Print accuracy limits:** The performance of the interlock depends on the fit between the knobs and the keys. Dimensional deviations inherent to FDM may result in excessive play, reducing stiffness, or mechanical interference, preventing proper assembly.
- **Interaction with material behaviour:** The geometry cannot be fully separated from the polymer material properties. Stiffer materials may improve load transfer but increase the risk of brittle feature failure, while more compliant materials may improve tolerance accommodation but allow excessive deformation before the interlock fully engages.

The final geometry should therefore be understood at a conceptual level and satisfies the geometric, assembly, and fabrication criteria. In doing so, the design development addresses research sub-question 2 by translating the identified FDM process limitations and printing tolerances into a feasible geometric design space for the interlocking interlayer. Its actual performance will depend on the interaction between material selection, print quality, interlayer adhesion, and mechanical loading, which are evaluated in the following experimental chapters.

6

Combined geometry and material experiments

6.1. Experimental overview

This chapter evaluates the coupled behaviour of the materials and geometry to develop an optimized, reversible interlayer system. While the material-specific experiments in Chapter 4 provided valuable insights into polymer performance, the aim of this phase is to test these materials within the context of the final interlayer geometry (V2.6) developed in Chapter 5. A deeper understanding of how specific materials interact with geometric variants is crucial for selecting the most promising combinations for subsequent mechanical validation.

The primary objective is to minimize and ultimately prevent warping and delamination, two significant challenges in 3D-printing directly on glass. The materials tested include PETG-HF, PETG-GF, PETG-CF, and PET-CF. PLA-CF was also included as back-up material. These materials were selected based on their performance in the material experiments (Chapter 4), but their behaviour required further assessment within the context and constraints of the final geometry to optimize printability and structural integrity.

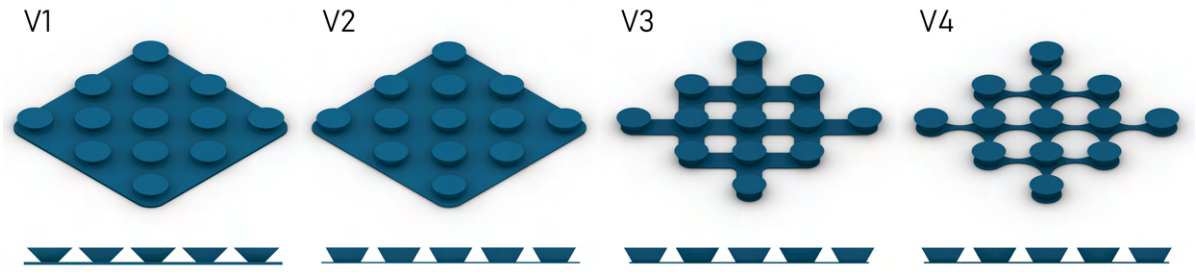

Figure 6.1: Geometry variants evaluated in the combined material and geometry experiments

Figure 6.1 shows the four variants of the final geometry that were evaluated:

- **V1:** 1.0 mm base layer, 45° knob angle, 5 mm knob height, offset tuned for ⌀ 5 mm keys.
- **V2:** 0.5 mm base layer, 60° knob angle, 5 mm knob height, offset tuned for ⌀ 5 mm keys.
- **V3 & V4:** Specifically designed for PETG-HF to resolve severe warping and delamination issues. These variants utilize cross-hatch patterns (rectilinear for V3 and organic for V4), thereby trying to reduce the contact area and internal stresses.

By the end of this chapter, the highest-potential material and geometry combinations are identified to proceed to the mechanical validation phase.

6.2. Results

The experiments were conducted on 100 x 100 x 8 mm float glass samples using the optimized printing parameters from the material experiments in Chapter 4. During these experiments, fan speed and filament retraction distances were further refined to improve the printability and final quality of the knobs. To resolve issues with the glass substrate rotating in place during the print, the top and bottom surface patterns were changed after a few samples from concentric to monotonic (line) patterns. Additionally, this adjustment reduced the amount of non-printing operations, resulting in less stringing and oozing for most of the samples. Table 6.1 provides an overview of the combined material and geometry results. The following sections discuses the results for each material in greater detail.

The transition from the V1 geometry to V2, shown in Figure 6.1, aimed to minimize the internal stresses responsible for warping and delamination by reducing the base layer thickness. Additionally, the steeper 60° knob angle in V2 reduced the overhang angle and thereby improved print quality of the knobs significantly compared to the 45° angle in V1.

Table 6.1: Results of the combined material and geometry experiments

Sample	Geometry	Surface	Infill	Fan cooling	Retraction distance	Warping	Delamination
PETG-HF	V1	Concentric	Concentric	0 » 60	0.8	Severe	High
PETG-HF	V2	Monotonic	Concentric	0 » 60	2.0	None	Full
PETG-HF	V3	Monotonic	Concentric	0 » 60	2.0	None	Full
PETG-HF	V4	Monotonic	Concentric	0 » 60	2.0	None	High
PETG-GF	V1	Concentric	Concentric	0 » 60	1.2	High	High
PETG-GF	V2	Monotonic	Concentric	0 » 60	2.0	None	None
PETG-CF	V1	Monotonic	Concentric	0 » 60	1.2	Low	Moderate
PETG-CF	V2	Monotonic	Concentric	0 » 60	2.0	None	Low
PET-CF	V1	Monotonic	Concentric	0 » 60	2.0	None	Low
PET-CF	V2	Monotonic	Concentric	0 » 60	2.0	None	None
PLA-CF	V1	Monotonic	Concentric	0 » 80	0.8	Low	None
PLA-CF	V2	Monotonic	Concentric	0 » 80	0.8	None	Moderate

6.2.1. PETG-HF

PETG-HF consistently struggled with delamination across all four geometries. In the V1 geometry, the sample exhibited severe, uneven delamination shortly after removing the glass substrate from the heated bed. This resulted in significant warping and glass chipping overnight. Print quality was also poor due to excessive stringing and oozing caused by the concentric surface pattern, which requires many non-printing movement operations.

The V2 variant improved print quality and eliminated warping through increased filament retraction distance and reduced base layer thickness, but full delamination still occurred. Variants V3 (rectilinear cross-hatch) and V4 (organic cross-hatch) successfully avoided warping. However, while V4 showed the best adhesion of the four variants with several points of contact remaining intact, delamination remained high.

This result is somewhat counter-intuitive, because breaking up the continuous base would initially be expected to reduce internal stresses and therefore improve adhesion. The most plausible explanation is that the cross-hatch geometry also introduces a much larger exposed edge length while also reducing the total bonded interface area. The increased edge length creates more locations where edge lifting and delamination can initiate. At the same time, the reduced bonded surface area means that, once delamination starts, the remaining attached area is relatively small. As a result, the same absolute amount of detachment represents a much larger relative portion of the total bonded interface. This explains why V3 and V4 still showed high delamination.

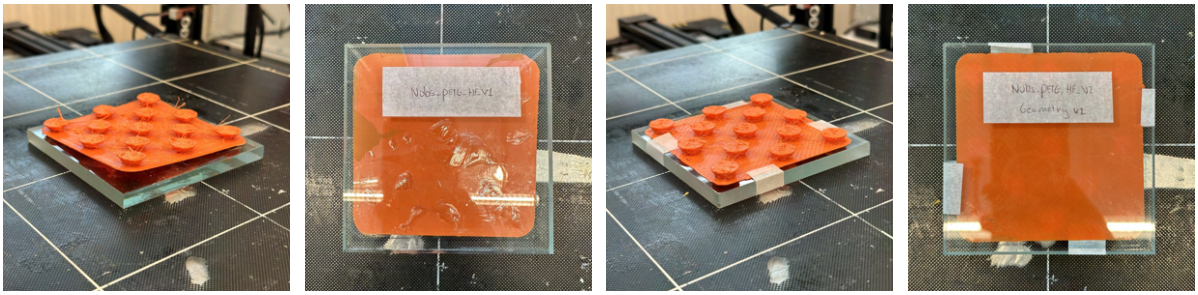

(a) V1, isometric view **(b)** V1, underside view **(c)** V2, isometric view **(d)** V2, underside view

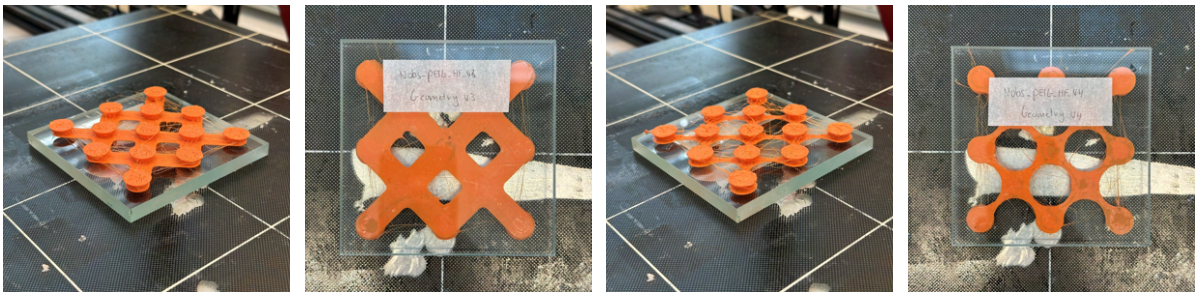

(e) V3, isometric view **(f)** V3, underside view **(g)** V4, isometric view **(h)** V4, underside view

Figure 6.2: PETG-HF samples printed with geometry variants V1–V4

6.2.2. PETG-GF

PETG-GF showed the most dramatic improvement between V1 and V2. The V1 sample initially appeared successful but warped severely overnight, leading to major chipping of the glass substrate and close to 80% delamination. Poor print quality, primarily due to oozing, was also observed as a result of the concentric movements of the nozzle.

The V2 geometry resolved these issues entirely. The reduced base layer thickness eliminated residual cooling stresses, thereby preventing warping and delamination. Transitioning to a monotonic (line) pattern and a 2.0 mm filament retracting distance significantly improved the overall print quality, though minor oozing persisted. The 60° angle of the knobs in V2 also significantly improved printability comparedt to V1.

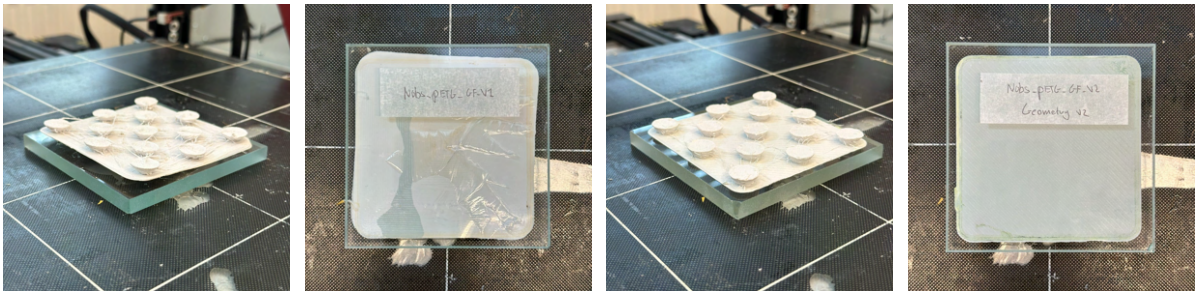

(a) V1, isometric view **(b)** V1, underside view **(c)** V2, isometric view **(d)** V2, underside view

Figure 6.3: PETG-GF samples printed with geometry variants V1 and V2

6.2.3. PETG-CF

PETG-CF demonstrated consistent behaviour from the beginning. The V1 sample showed edge delamination (5–10 mm wide) visible through the glass substrate but maintained clean layers. The V2 variant performed slightly better, with only negligible signs of delamination at the outer edges. The steeper knob angle in V2 resolved the minor imperfections seen at the base of the knobs in V1. Overall, PETG-CF with the V2 geometry provided a very clean, reliable print result.

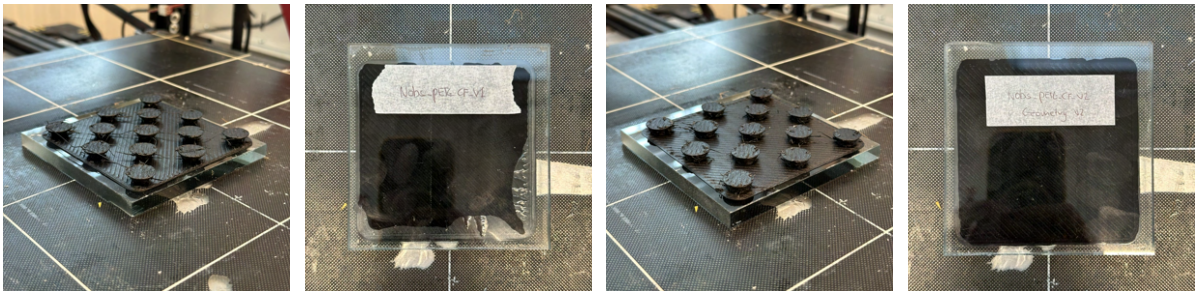

(a) V1, isometric view **(b)** V1, underside view **(c)** V2, isometric view **(d)** V2, underside view

Figure 6.4: PETG-CF samples printed with geometry variants V1 and V2

6.2.4. PET-CF

PET-CF exhibited excellent, consistent adhesion. While V1 showed minor edge delamination and slight glass chipping overnight, the V2 variant resolved these issues completely. The V2 geometry resulted in a robust, clean print with minimal stringing. The reduced base layer thickness provided the necessary flexibility to accommodate thermal contraction without pulling away from the glass substrate.

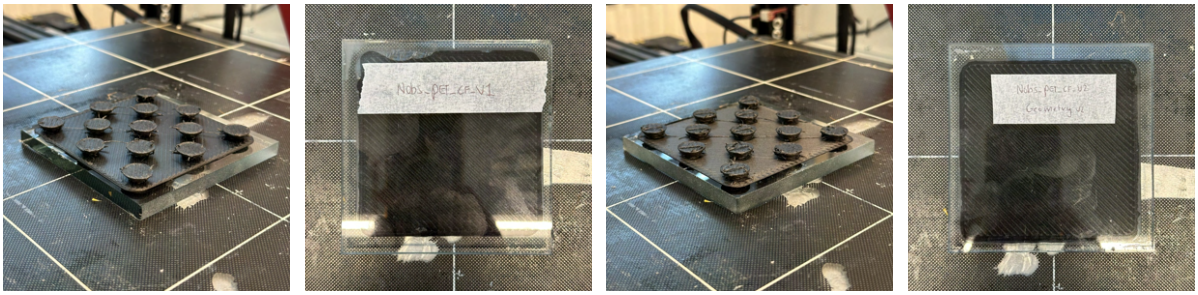

(a) V1, isometric view **(b)** V1, underside view **(c)** V2, isometric view **(d)** V2, underside view

Figure 6.5: PET-CF samples printed with geometry variants V1 and V2

6.2.5. PLA-CF

As backup material, PLA-CF was easy to print with virtually no stringing or oozing observed. In V1, there was slight delamination visible from the underside of the glass substrate, but no visible edge gaps. In V2, the print quality remained high, though delamination actually increased on two of the edges. However, no warping occurred in either sample, and the material remains a viable, albeit not preferred, option.

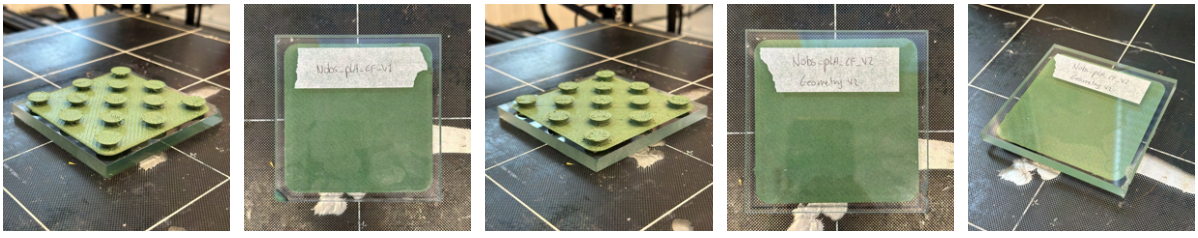

(a) V1, isometric view **(b)** V1, underside view **(c)** V2, isometric view **(d)** V2, underside view **(e)** V2, isometric underside

Figure 6.6: PLA-CF samples printed with geometry variants V1 and V2

6.3. Material–geometry selection

Based on these results, PETG-GF, PETG-CF, and PET-CF are selected for mechanical validation. These materials demonstrated the best balance of adhesion, print quality, and stress management when paired with the V2 geometry.

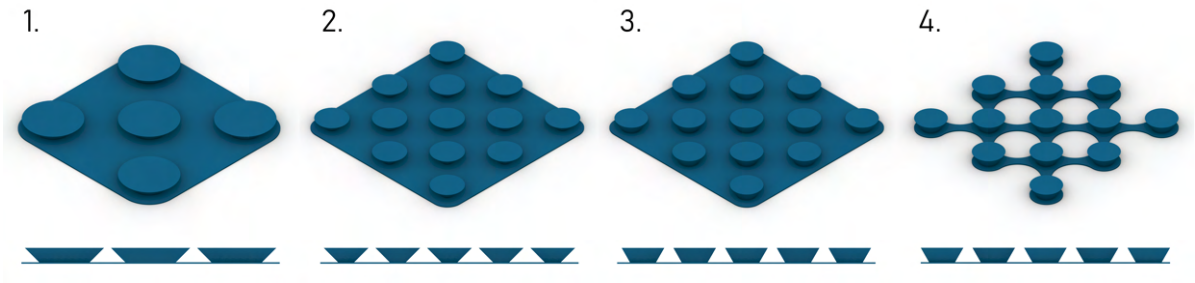

Figure 6.7: Geometry variants selected for mechanical validation

For the shear testing phase, these three materials will be tested across four configurations, all utilizing a 0.5 mm thick base layer (see Figure 6.7):

1. Large knobs + 45° angle + full base layer
2. Small knobs + 45° angle + full base layer
3. Small knobs + 60° angle + full base layer
4. Small knobs + 60° angle + organic cross-hatch pattern

These combinations will be evaluated for their shear load-bearing capacity, failure mechanism and ease of demountability at end-of-life to ensure they can be removed without damaging the glass substrates.

7

Demountable glass vault

7.1. Introduction

This chapter presents the design of a fully demountable glass vault as a practical application case for the interlocking interlayer system developed in Chapter 5. The design is inspired by the compression-only *Glass Vault* case study from Section 3.2. While that reference vault relied on permanent epoxy putty, this demountable design uses the AM interlayer in combination with removable stainless-steel keys to facilitate assembly and disassembly. The vault translates the interlayer geometry, production method, and assembly logic into a complete design application case.

The geometry is modelled parametrically in Rhino using Grasshopper to generate block positions and custom interlayer angles based on a 2D catenary input curve. This parametric design provides the basis for wind-load calculations and a Karamba3D finite element model to determine the maximum interlayer shear loads. These calculated loads are later evaluated against mechanical shear-test results to determine the optimal material-geometry combination selected in Chapter 6 for final application.

7.2. Parametric vault design

Figure 7.1 shows the full Grasshopper script used to parametrically define the demountable vault geometry. It starts by generating a 2D catenary curve based on a predefined width and height. This catenary curve is divided into segments corresponding to the height of the glass bricks. The structure uses standardized planar glass bricks measuring 200 × 100 × 50 mm. Additional joint spacing is included between the segments to reserve space for the interlayers, establishing the initial 2D section layout.

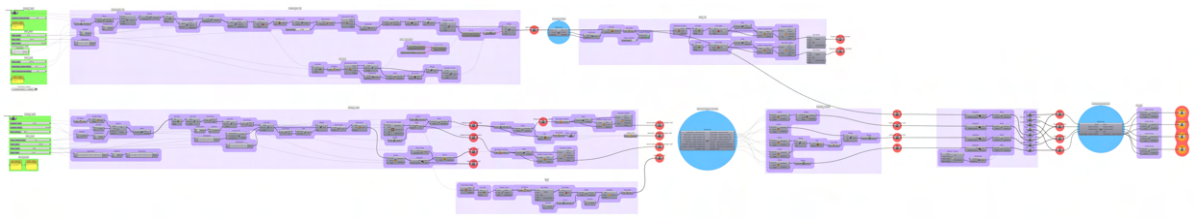

Figure 7.1: Grasshopper script for the parametric demountable glass vault design

The bricks are then extruded into 3D. The parametric interlayer model produced in Chapter 5 is imported, allowing the flat side of each interlayer to align directly with the underside of each glass brick. On the opposite side of each brick, the required angled interlayer profile is generated to enable the vault curvature. These profiles are generated by lofting between the required base curves to create the angular transition between adjacent blocks. A 50/50 overlap tessellation pattern is achieved by shifting alternating bricks by half a brick length. The bricks are then arrayed to the desired vault length and mirrored to generate the full vault geometry.

Using AM to handle the individual angular variations shifts geometric complexity from the cast-glass components to the interlayers, enabling the use of standardized planar bricks. The primary brick layout and interlayer generation are fully parametric. Secondary refinements, such as varying brick lengths to adjust local side curvatures, are completed manually in the current model but could be integrated into the parametric workflow in future versions.

7.3. Production process

The production process shown in Figure 7.2 represents a proposed conceptual workflow for fabricating the glass-interlayer components of the demountable glass vault. In theory, this process would enable both sides of each planar brick to be printed with the required interlayer geometries. However, the process should be interpreted as one feasible strategy, not as the optimal or only possible production method for translating the direct print-on-glass principle to vault-scale components. It is therefore presented as a conceptual production scenario that identifies the main fabrication steps, technical requirements, and potential challenges involved in producing the demountable vault components.

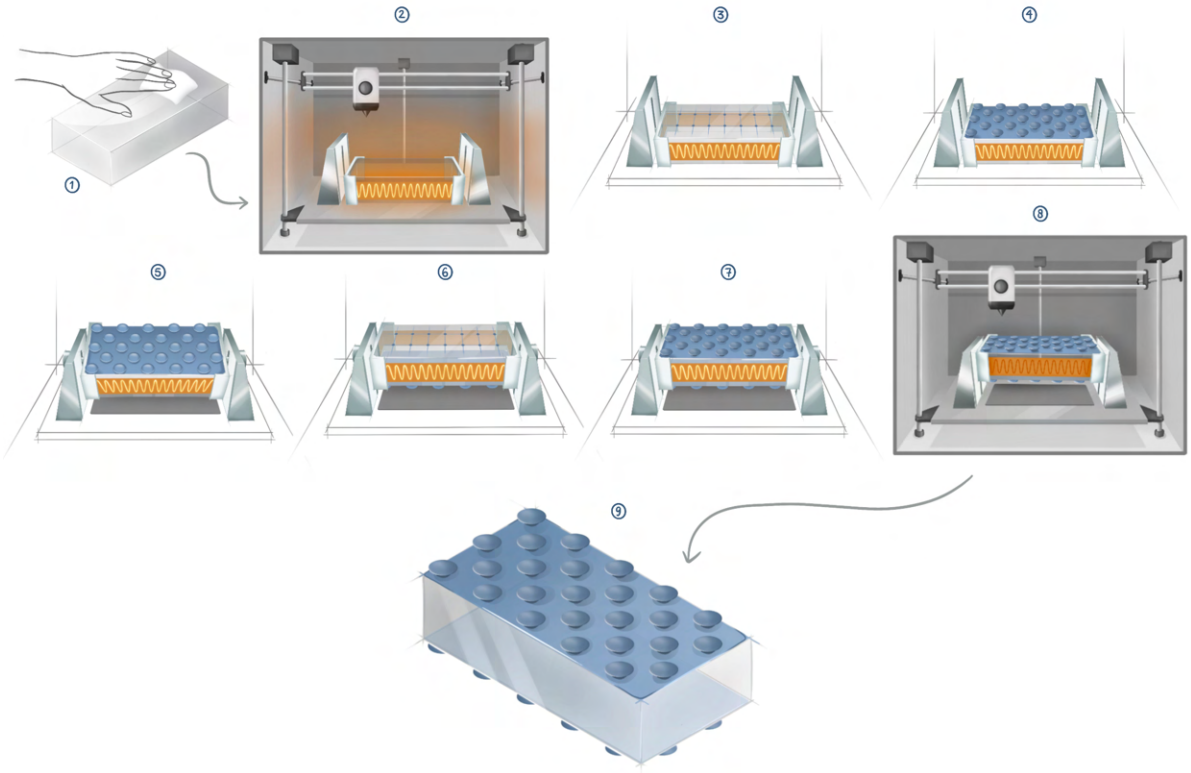

Figure 7.2: Proposed production process for the demountable glass vault components

1. **Cold-state preparation & manual loading:** The process begins with the glass brick at room temperature. Both 200 × 100 mm faces are thoroughly cleaned using 99.5% IPA and lint-free wipes to remove manufacturing oils, dust, and fingerprints, ensuring reliable polymer-glass adhesion. Electric heating pads are attached to the four side faces of the brick, which is then manually placed into a custom cradle inside an enclosed 3D printer. The cradle supports the brick by its edges to maintain its position while enabling automated rotation. Small exposed glass zones remain at the top and bottom due to the filleted interlayer edges, allowing the cradle to prevent the block from sliding vertically during printing.
2. **Thermal stabilization:** The heated print bed, side heating pads, and enclosed chamber bring the brick to its required target temperature. For the first printed side, the brick rests directly on the print bed with a conductive graphite thermal pad in between to maximize heat transfer. The side heating pads apply heat to the four edge faces, while the heated print bed warms the enclosed chamber to minimize convective heat loss from the glass during printing.

3. **Phase A — Thermal calibration:** Once the glass block reaches thermal equilibrium, the nozzle probes the top surface in a grid pattern. This calibration step allows the printer to dynamically compensate for vertical thermal expansion, levelness deviations, and minor inaccuracies in cradle positioning.
4. **Phase A — Primary side printing:** The more complex angled interlayer face is printed first due to its longer print duration. Printing this side first allows it to benefit directly from conductive heating via the print bed and graphite pad. A hardened steel 0.6 mm nozzle is used to increase print speed and strength, and to prevent clogging when printing fibre-reinforced polymers, without sacrificing dimensional accuracy. Active fan cooling is initially turned off to maintain the glass substrate at its target temperature. After the base layer is complete, limited fan cooling may be introduced to print the interlocking knobs consistently.
5. **Automated mid-print rotation:** After completing the first interlayer side, the cradle lifts the glass brick from the print bed and rotates it 180° to expose the unprinted face as the new top surface.
6. **Phase B — Post-flip calibration:** Following rotation, a second grid calibration identical to Step 3 is performed to ensure optimal first-layer adhesion on the secondary side.
7. **Phase B — Secondary side printing:** The simpler, faster flat interlayer profile is printed onto the secondary face. Direct contact with the print bed is lost, so the side heating pads become the primary heat source and operate at a higher capacity, while the print bed remains heated to maintain a warm chamber and reduce heat loss.
8. **Passive cooling:** Upon print completion, all heating elements are turned off. The finished component remains inside the enclosed printer chamber to cool gradually to room temperature, limiting residual stresses between the glass and polymer. The block can be safely removed after approximately 60–90 minutes.
9. **Manual removal and final inspection:** The fully cooled block is removed from the cradle for visual inspection. The block is evaluated for polymer-glass adhesion on both faces, visible delamination, edge lifting, knob print quality, dual-side print alignment, glass damage, and surface residue. Defective components are either rejected or designated for rework.

7.4. Assembly method

This section outlines the assembly mechanics and sequential construction workflow of the demountable glass vault design. It defines the global assembly logic, the detailed layout of the initial arch layers, the full vault expansion sequence, assembly tolerances, and the disassembly protocol.

7.4.1. Assembly logic

Each standard glass brick contains a flat interlayer on one face and an angled interlayer on the opposite face, with the angled face always oriented upward during assembly (see Figure 7.3a). To guide on-site workers, the top interlayer face features coloured assembly markings embedded via an Automatic Material System (AMS). Keystones are an exception; they feature flat interlayers on both sides and contain no visual markings, making them easily distinguishable (see Figure 7.3b).

The primary markers are red circular indicators with a thin white outer rim and number in the centre. Counting upward from the foundation (layer 0), this number indicates the target layer. Because bricks within the same layer are identical, the marker only needs to specify the layer index. Non-standard row terminations are built using two successive shorter bricks. These boundary bricks retain the same layer number but use a different marker colour to indicate their edge placement.

Additionally, the top interlayer face incorporates two simple red guide circles (see Figure 7.3a). These circles mark where the primary numbered markers of the next layer must align. This intuitive visual pairing allows installers to quickly centre the primary markers of an incoming brick over the guide circles of the underlying layer, accurately establishing the upward orientation, target layer, and 50/50 overlap tessellation pattern.

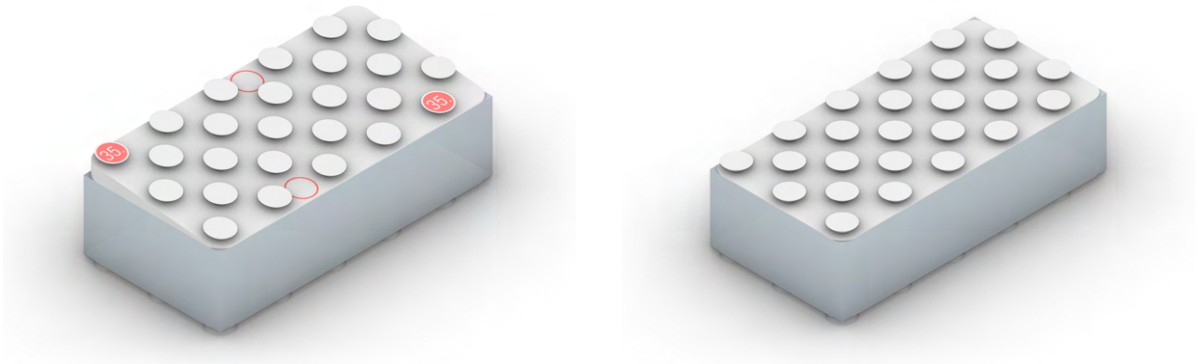

(a) Standard glass-interlayer component **(b)** Keystone component

Figure 7.3: Standard and keystone glass-interlayer components for the demountable vault

Placement-based assembly

The default installation method for a new component is direct downward placement onto the bricks below. The installer selects a block matching the current layer and aligns its numbered markers over the red guide circles of the preceding layer, as shown by step 1 in Figure 7.4a. Once full-surface contact is achieved, four stainless-steel keys are immediately inserted to lock the component into place, as shown by step 2 in Figure 7.4a. These keys act as the primary load-bearing structural elements, transferring shear forces through the interlocking knobs of the interlayer into subsequent blocks. Chamfers on both ends of the keys allow them to self-centre during entry, thereby simplifying installation.

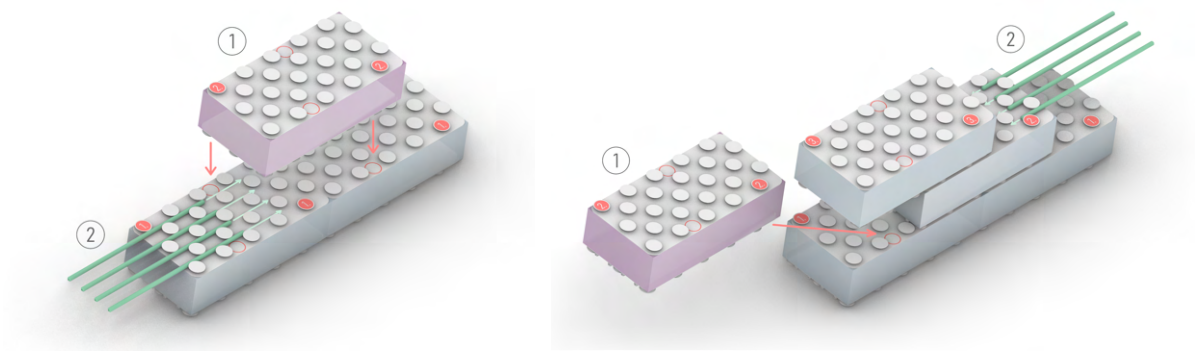

(a) Placement-based assembly **(b)** Diagonal sliding-based assembly

Figure 7.4: Assembly methods for locking demountable glass-interlayer components

Diagonal sliding-based assembly

A secondary installation method occurs naturally as a consequence of constructing a central arch with a 50/50 overlap tessellation pattern. In some exceptional cases, direct downward placement is physically obstructed by adjacent earlier placed bricks. In these locations, the new component must be inserted via a diagonal sliding motion, as shown by step 1 in Figure 7.4b. The worker aligns the numbered marker with the row of its corresponding guide circle and slides the brick diagonally into place, using the geometric clearance provided by the angled interlayer face. Because keys are omitted until a brick has made full contact with the two bricks below, unkeyed blocks directly above retain slight vertical play and can be deflected upward to ease insertion. Once full contact is established, the keys are inserted immediately to lock the assembly, as shown by step 2 in Figure 7.4b.

7.4.2. Assembly sequence: central arch

The step-by-step construction chronology of the initial layers of the central arch is illustrated in Figure 7.5. Newly added bricks and keys are highlighted in pink and green, respectively. Additionally, the bricks are indexed by their layer number first and their chronological placement sequence within that layer second. Note that this labelling is distinct from the physical layer numbers embedded in the interlayers and is used strictly for illustrative explanation in Figure 7.5.

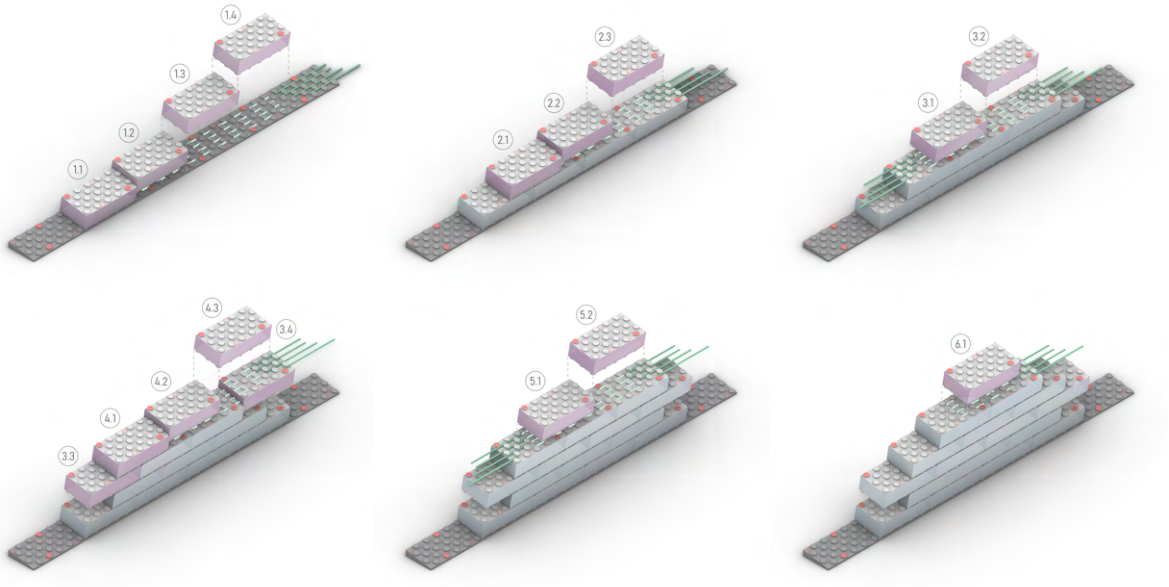

Figure 7.5: Assembly sequence for the first layers of the central arch

Construction begins from the foundation layer, with a central arch acting as the spine of the structure, similar to *The Glass Vault* case study. However, this demountable vault design constructs the central arch four blocks wide simultaneously to provide a broader starting base and improve global stability for subsequent diagonal expansion. Temporary scaffolding supports the central arch during construction and remains in place until the arch is completed.

Bricks are placed symmetrically from both sides of the foundation upward using the visible top-side markers. Once full contact is achieved, the four stainless-steel keys are inserted to activate the shear-transfer mechanism and lock the block into the assembly. Steps 1.1–3.2 establish the baseline pattern. Subsequently, Steps 3.2–6.1 are repeated up both halves of the central arch in parallel. This placement loop continues until both halves meet at the top, where the final unmarked flat-faced keystones are inserted to establish a continuous, load-bearing central arch across its full width. Once closed, this central arch provides a stable, self-supporting spine from which the diagonal expansion of the vault can progress.

7.4.3. Assembly sequence: full vault expansion

Automated, self-supporting robotic construction deployed for *The Glass Vault* was out of scope for this specific project, so the demountable glass vault deliberately uses temporary scaffolding to support the central arch during construction. However, the assembly sequence does in principle allow for full autonomous robotic construction. Once the central arch is fully completed and keyed, it develops inherent stability and allows the remainder of the vault to expand without ongoing scaffolding support. The full demountable vault construction sequence progresses as illustrated in Figure 7.6.

The main body of the vault uses standardized 200 mm long bricks arranged in a 50/50 staggered tessellation pattern. As shown in the elevation and top view of the vault in Appendix C, shorter brick lengths are introduced in a regular pattern to generate a much steeper curvature on two of the four opposing sides. This is facilitated by the 20 mm knob spacing of the interlayer geometry, which allows the brick lengths to vary in precise 20 mm intervals. Using this modularity, a specific repeating sequence of 180, 160, 140, and 120 mm bricks is integrated alongside the regular 200 mm bricks every five layers. In the appendix drawings, the darker blue the brick is, the shorter its length. To maintain a consistent assembly logic, these non-standard bricks are always placed as pairs at the end of a row, rather than as single isolated bricks.

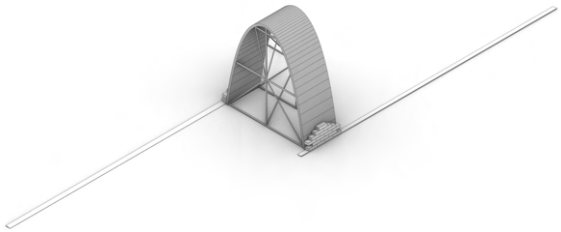

(a) Temporary scaffolding and start of central arch

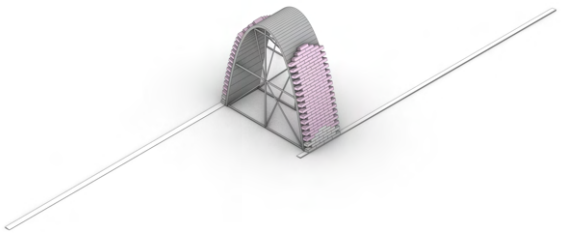

(b) Central arch continues upward

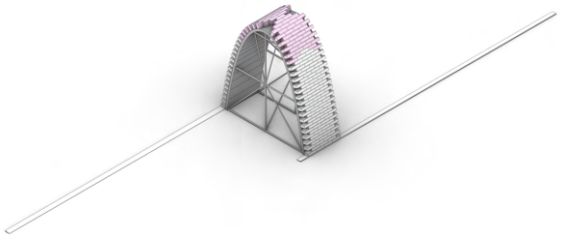

(c) Closing the central arch by inserting a keystone

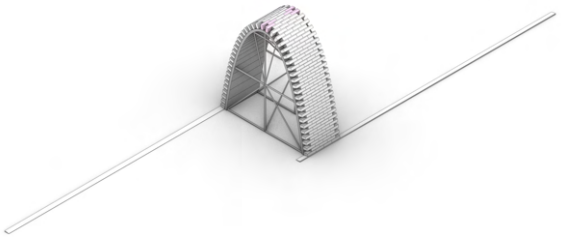

(d) Completing central arch and removing temporary scaffolding

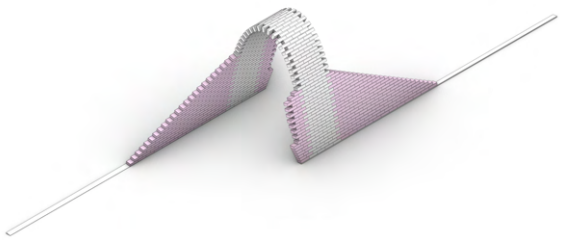

(e) First diagonal outward expansion

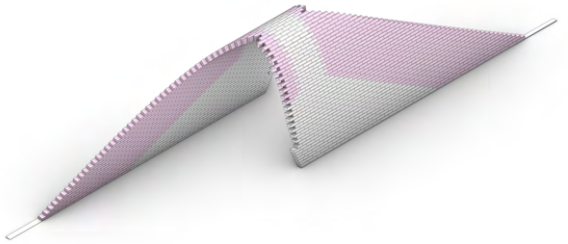

(f) Repetition up to the next keystone

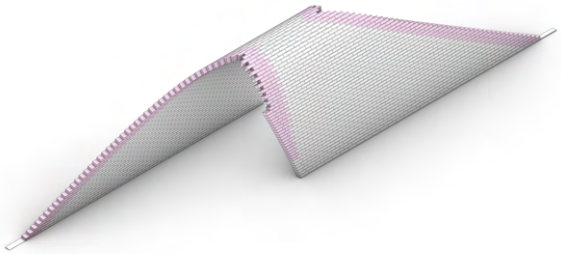

(g) Balanced construction from all sides

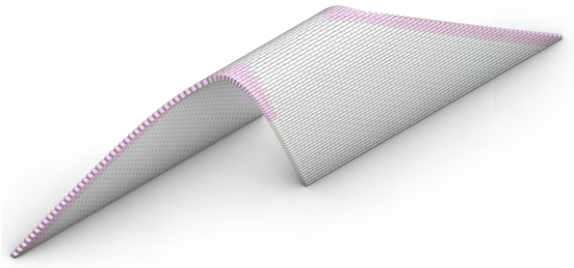

(h) Completed vault

Figure 7.6: Assembly sequence of the full vault

7.4.4. Assembly tolerance accommodation

Because the vault is dry-assembled from a large number of discrete masonry components, manufacturing deviations and geometric inaccuracies can quickly occur and accumulate. These variations originate from dimensional tolerances in the glass casting, geometric variations during interlayer printing, manual placement errors, and cumulative alignment deviations across multiple stacked layers. Consequently, the global assembly system must incorporate localized tolerance accommodation to absorb these errors and prevent them from obstructing subsequent block installation. This resilience is achieved through the following three primary mechanisms:

1. **In-plane adjustability via nob spacing:** The spacing and offset of the repeating knob pattern provides limited but sufficient side-to-side adjustability in the in-plane direction between neighbouring bricks to accommodate typical $\pm$ 1 mm deviations of the bricks. If necessary, installers can slightly shift previously positioned blocks laterally to fit a new component, even after the keys are inserted, making the global system significantly less sensitive to minor placement errors across long horizontal rows.
2. **Precision key clearance:** The spaces designed to house the stainless-steel keys are detailed with a nominal diameter of 5.2 mm, while the keys themselves are machined to a precise diameter of 5.0 mm. This deliberate 0.2 mm clearance ensures that the keys can be easily inserted by hand, while still enabling effective shear transfer. Small chamfers on both ends of the keys further assist entry by providing an automatic self-centring effect.
3. **Localized polymer compliance:** The 3D-printed polymer interlayer possesses a limited degree of local compliance that helps absorb small dimensional variations between adjacent block faces. This compliance is limited and material-dependent, so the system should still be considered a relatively precise assembly.

The synergy between the key clearance and controlled polymer compliance allows the unclosed central arch to deform to a certain extent during the early construction phase. This localized elasticity is especially valuable in foreseen situations where the arch needs to flex outward slightly to create enough temporary clearance to insert the keystones. This behaviour is analogous to the brick bending technique in complex *LEGO* construction, where minor fabrication tolerances between rigid individual bricks accumulate to allow larger-scale global curvature or controlled flexibility within the assembly.

Furthermore, while most bricks are added to the assembly via direct placement, the wedge profile created by the angled interlayer side inherently provides slightly greater clearance on the insertion face during diagonal sliding operations. As a result, it naturally guides and accommodates the required sliding kinematics without necessitating additional complex assembly systems.

Crucially, these integrated tolerance mechanisms are designed to absorb minor inaccuracies rather than systemic production failures. If an interlayer suffers from severe thermal warping, major print defects, or out-of-spec dimensions, the component will fail to fit correctly, highlighting the importance of the critical final production quality-control inspection detailed in Figure 7.2.

7.5. Prototype as assembly demonstrator

To demonstrate the assembly logic of the demountable glass vault, a physical prototype of a small vault fragment was fabricated. The main purpose of this prototype was to make the assembly principle, including its tolerances and limitations, understandable at real scale. It supports the explanation of glass block positioning, interlayer engagement, key insertion, and overall constructability.

Before producing the final prototype, angled interlayer print trials were performed directly on glass. These small experiments validated that the interlayer geometry could also be printed on glass at the angles required for the vault. PETG-GF (see Figure 7.7) and PETG-CF (see Figure 7.8) were tested, in configurations with and without a continuous base layer, in order to assess the influence of the base layer on the print behaviour and adhesion of larger, stiffer geometries. The trials confirmed that angled interlayer geometries could be printed with sufficient geometric definition. They also highlighted that print strategy and edge detailing strongly influenced print quality and initial delamination behaviour. In particular, the use of a brim helped reduce edge lifting during and after printing.

These angled print tests were conducted because, within the available timeframe and fabrication facilities, producing a setup similar to the one described in Figure 7.2, was not feasible. The trials therefore demonstrate that the principle of directly printing angled interlayers on glass is possible, but they do not represent the fabrication method used for the final prototype.

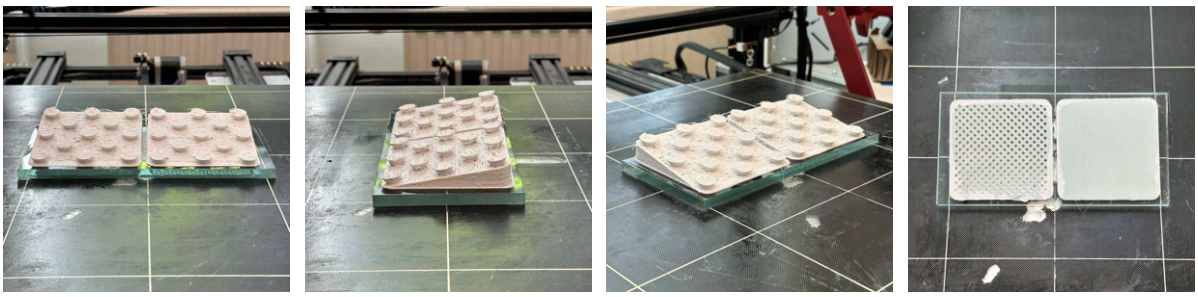

(a) Front view **(b)** Side view **(c)** Isometric view **(d)** Bottom view

Figure 7.7: Direct print-on-glass trial of an angled PETG-GF interlayer, used to assess the printability of vault-specific joint geometries

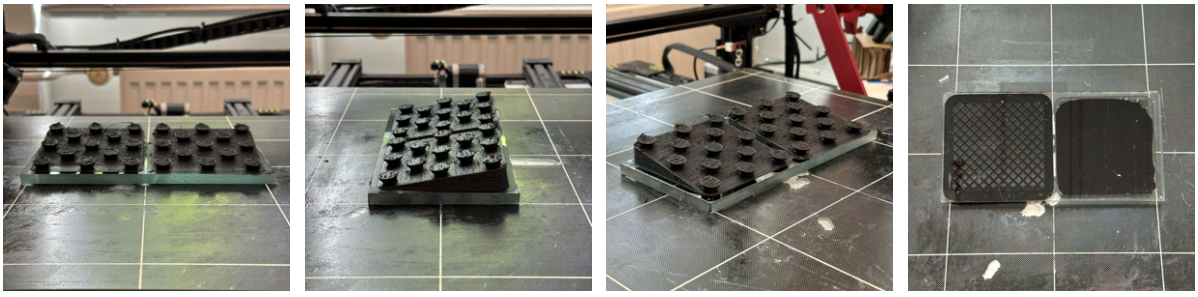

(a) Front view **(b)** Side view **(c)** Isometric view **(d)** Bottom view

Figure 7.8: Direct print-on-glass trial of an angled PETG-CF interlayer, used to assess the printability of vault-specific joint geometries

For the demonstrator shown in Figure 7.9, the interlayers were printed separately on a more accurate 3D printer and were later connected to the glass blocks. This approach was chosen to achieve a cleaner visual result, more accurate positioning, and a reliable demonstration of the assembly principle. The bottom two glass bricks have a grey, regular interlayer on the bottom and a white, angled one on the top, representing the typical components in the vault. The third, top glass block have grey, regular interlayers on both the top and bottom, representing a keystone component.

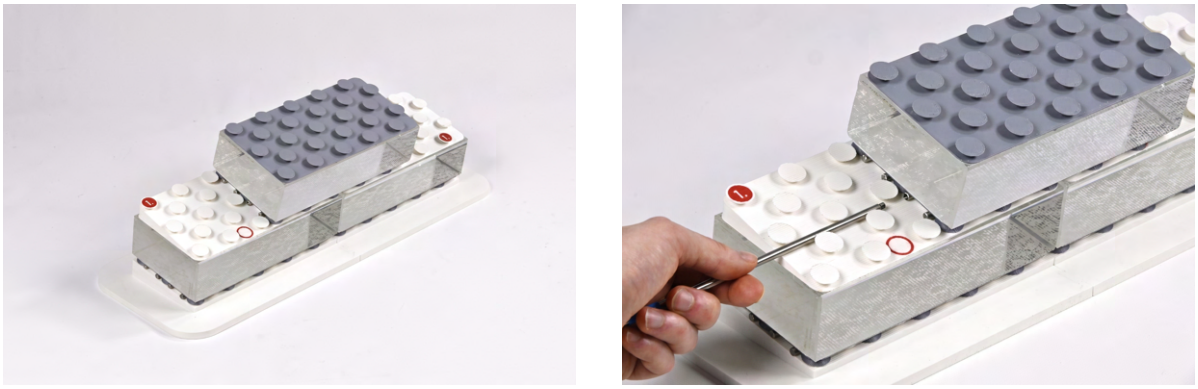

(a) Full three-block demonstrator assembly **(b)** Tool-assisted removal of the keys

Figure 7.9: Physical demonstrator of the interlayer system for the demountable glass vault assembly

The prototype should therefore not be interpreted as structural validation or as proof that the complete system can already be directly printed onto full cast-glass blocks. It also does not replace the direct print-on-glass experiments or the mechanical shear tests. Instead, its value lies in demonstrating fit, assembly sequence, spatial readability, interlocking engagement, and the final locking action of the stainless-steel keys.

7.6. Final design overview

Figure 7.10 shows a render of the final demountable vault design. It provides an overall impression of the vault geometry and should be read as a visual synthesis of the parametric vault design, production logic, and assembly method described in the previous sections. The complete set of drawings, documenting the vault through a plan, elevation, sections, and connection details, is included in Appendix C. Together, the render and drawings provide the geometric and technical overview of the final design before its structural demand is evaluated in the following section.

Figure 7.10: Render impression of the demountable glass vault, illustrating the overall geometry and transparency of the structure

7.7. Structural demand: wind load and Karamba model

To validate subsequent experimental shear testing results, the demountable glass vault was evaluated under lateral wind loading. The comprehensive wind load calculations and analysis are detailed in Appendix D. First, the peak wind velocity pressure was calculated according to EurocodeApplied.com (n.d.), resulting in a peak pressure (q_p) of $0.682\,\text{kN/m}^2$. Second, a global Finite Element Analysis (FEA) was implemented on a shell model of the demountable glass vault using Karamba3D in Grasshopper to analyse load distribution under the critical Ultimate Limit State (ULS) combination of gravity and wind loading.

The structural analysis yields two key results for the global vault behaviour. First, the simulation confirms pure compression-only behaviour under the design loads, with a maximum vertical compressive support reaction of $2.58\,\text{kN}$ and no vertical tensile uplift. Second, the isolated lateral reactions reveal a peak horizontal shear force of $1.10\,\text{kN}$ acting outward along the foundation boundary. This peak horizontal force represents the maximum shear load that must be resisted by the combined mechanical interlock and friction of a single interlayer, establishing the precise performance threshold used to validate the experimental shear testing results in Chapter 9.

8

Demounting strategy

8.1. Introduction

Demountability of the connection system is essential for circularity, as it directly influences both reuse potential and clean material recovery. Two end-of-life scenarios are considered for the demountable glass vault from Chapter 7. Although the vault is used as the main case study, the strategies are applicable to the broader interlocking interlayer concept.

1. **Assembly-level reuse:** the vault is dismantled and rebuilt elsewhere using the same components.
2. **Material-level recovery:** the vault is dismantled and the interlayers are removed from the glass, allowing the glass components to be reused with a new interlayer or recycled without contamination.

Both scenarios require a quick, controlled, and non-destructive process, preferably using simple tools. The main performance requirements are limited glass damage, minimal residue, low removal effort, and no need for specialised industrial equipment.

8.2. Disassembly for direct component reuse

The first scenario is the preferred end-of-life route, because it preserves the highest material value: the complete components can be reused directly. Disassembly of the vault follows the reverse assembly sequence of Section 7.4.3), starting at the exposed boundary blocks where the keys are accessible. Once the keys are extracted, the end bricks can be removed, immediately exposing the keys of the next consecutive block within that row. The central arch must remain intact until all surrounding diagonal extensions have been systematically cleared. Before disassembling the central arch, the temporary scaffolding must be reinstalled to support the unclosed arch halves while the remaining keys are removed.

Once the demountable glass vault is fully assembled, most keys are entirely concealed and physically inaccessible due to the overlapping geometry of adjacent bricks. Physical access is restricted to the exposed keys underneath the bricks at the end of a row. This internal nesting prevents accidental or unauthorised removal of internal keys. However, even the exposed edge keys are difficult to remove by hand or with standard hand tools, such as pliers.

To facilitate rapid, non-destructive disassembly, each stainless-steel key is detailed with an internal M3 female threaded bore on both ends. A custom extraction tool with a matching M3 male threaded tip can be screwed directly into the exposed key, allowing the operator to pull the key out a illustrated in Figure 8.1. The extraction tool can be operated manually or connected to a standard cordless drill. The barrel of the tool matches the 5 mm diameter of the keys, ensuring automatic self-alignment during insertion. Future iterations of this tooling system could be developed to engage and extract all four keys of a brick simultaneously, further reducing disassembly time.

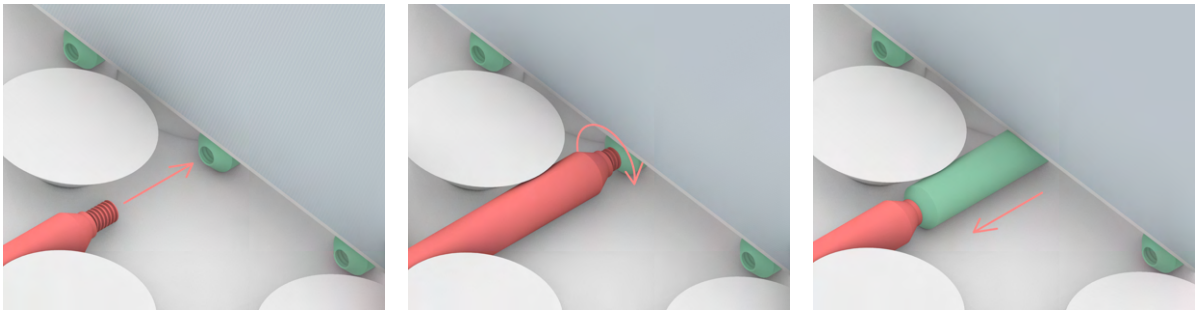

(a) Inserting the extraction tool **(b)** Engaging the threaded key **(c)** Extracting the key

Figure 8.1: Key extraction sequence for disassembling the demountable glass-interlayer connection

The removable keys therefore establish a reversible structural connection. During use, the concealed internal joints keep the system secure against accidental removal or tampering. At end-of-life, the same system allows controlled disassembly, enabling the glass-interlayer components to be recovered intact, transported, and reassembled elsewhere.

8.3. Interlayer removal for material recovery

Although direct component reuse is the preferred end-of-life route, material-level recovery becomes relevant when a different interlayer geometry is required, when the existing interlayer is damaged, or when the glass component itself must be recycled without polymer contamination. In this scenario, the key requirement is that removal of the interlayer should limit damage to the glass substrate and leave minimal polymer residue.

Earlier work by Van Kessel (2025) showed that a PLA interlayer can be removed from glass by heating it to its glass transition temperature of approximately 60 °C. However, this approach is less suitable for large-scale use, as it requires heating the complete glass component to the respective glass transition temperature of the polymer. This becomes even less practical for the high-performance fibre-reinforced polymers used in this research, which generally have higher glass transition temperatures. Therefore, this research explored dry, low-energy mechanical removal strategies.

8.4. Interlayer removal experiment

Method

For the selected materials from Chapter 6 — PETG-GF, PETG-CF, and PET-CF — the four removal geometries shown in Figure 8.2 were experimentally tested.

(a) Full base layer **(b)** Cross hatch pattern **(c)** Organic cross hatch pattern **(d)** Central air inlet

Figure 8.2: Interlayer removal test geometries for material demounting experiments

The samples were printed on 100 × 200 × 8 mm float-glass substrates using the optimised print parameters from the preceding material and geometry experiments. After printing, all samples were left to stabilise for at least 24 hours before testing. Removal was first attempted manually without tools. When required, a simple putty knife was used to initiate or continue delamination. In addition, compressed air was tested as a possible delamination trigger for Geometry 4. However, this method did not work reliably in the tested configuration.

Evaluation criteria

The test results were assessed qualitatively, similar to the results in Chapters 4 and 6, using the five criteria summarised in Table 8.1.

Table 8.1: Evaluation criteria for interlayer removal experiments

Criterion	Main relevance
Initial delamination	Indicates bond condition before removal
Ease of removal	Indicates practicality and required effort
Tools used	Indicates process complexity
Glass damage (chipping)	Determines reuse potential
Residue	Determines cleaning and recycling quality

Results

Table 8.2 gives an overview of the results of the demounting experiments. PETG-GF showed moderate initial delamination and was generally easy to remove. Minor glass chipping occurred in some samples, but no polymer residue was observed. PETG-CF showed stronger adhesion and was the most difficult material to remove, especially in geometries with a larger bonded contact area. This corresponded with increased glass chipping and minor residue (see Figure 8.3), although the residue could be removed by light scraping with a putty knife.

Table 8.2: Interlayer removal results for PETG-GF, PETG-CF, and PET-CF

Sample	Geometry	Initial delamination	Demounting	Tools used	Glass chipping	Residue left
PETG-GF	V1	Low	Easy	Putty knife	None	None
PETG-GF	V2	Moderate	Easy	Putty knife	Low	None
PETG-GF	V3	Moderate	Very easy	Putty knife	Low	None
PETG-GF	V4	Moderate	-	-	-	-
PETG-CF	V1	Low	Very hard	Putty knife	Moderate	Low
PETG-CF	V2	Low	Hard	Putty knife	Low	Moderate
PETG-CF	V3	Moderate	Moderate	Putty knife	None	Moderate
PETG-CF	V4	None	-	-	-	-
PET-CF	V1	Low	Very easy	-	None	None
PET-CF	V2	Moderate	Very easy	-	None	None
PET-CF	V3	High	Very easy	-	None	None
PET-CF	V4	None	-	-	-	-

Note. Initial delamination, glass chipping, and residue are assessed from none to severe. Demounting effort is assessed from very easy to very hard.

(a) PETG-CF V1 **(b)** PETG-CF V2 **(c)** PETG-CF V3

Figure 8.3: Polymer residue left on the glass substrate after removal of the PETG-CF interlayers

PET-CF showed the easiest and cleanest removal behaviour, with no observed glass chipping or residue. However, this was accompanied by higher initial delamination. The cross-hatch variants, geometries 2 and 3, generally improved removability by reducing the bonded base area. Delamination using compressed air was not successful in the tested configuration.

Discussion

The results indicate that manual dry removal is feasible for interlayers with a thin, flexible base layer. Reducing the bonded base area further improves removability, but may also increase initial delamination due to the higher edge-to-surface-area ratio. PET-CF was the easiest material to remove, but this should be interpreted carefully, as the high initial delamination suggests a weaker interface bond. PETG-CF showed the strongest interface adhesion, making clean end-of-life separation more difficult. PETG-GF appears to offer the most balanced compromise between interface stability and removability.

Compressed air remains a potential strategy for future development, but the tested geometry did not provide a reliable air path. First, achieving an airtight seal between the air gun and the interlayer was difficult due to limited print accuracy and lack of a proper connection method. As a result, more manual pressure had to be applied to the interlayer, leaving insufficient space for air to enter beneath the interlayer. A second iteration with internal air vents was also unsuccessful, because the 0.5 mm thick base layer consisted of only two printed layers, causing the vents to close during printing.

The other removal tests suggest that compressed air is not necessary for the thin regular interlayer sides, which can already be removed mechanically with limited effort. However, compressed air may be more relevant for the angled interlayer sides, where the larger material volume increases stiffness. Future work should therefore investigate whether this infill can be redesigned to form controlled air paths for delamination.

8.5. Final demounting strategy

The primary demounting strategy is direct component reuse: the keys are removed, the vault is dismantled in reverse assembly sequence, and the intact components are transported and rebuilt elsewhere. If direct reuse is not possible, the secondary strategy is dry mechanical removal of the interlayer. For the thinner regular interlayer sides, removal with a simple tool and moderate effort is feasible. For the angled interlayer sides, future research should design the interlayer with integrated removal features, such as open internal channels, exposed infill, or dedicated air paths for compressed-air delamination. Heating remains a possible fallback strategy, but is not preferred due to its high time and energy demand and limited scalability. Addressing research sub-question 5, the developed demounting strategy demonstrates that controlled, non-destructive separation of both the glass units and the interlayer is achievable, thereby supporting direct reuse, material recovery, and closed-loop recycling.

9

Mechanical validation

9.1. Introduction

This chapter validates the mechanical performance of the interlocking interlayer system under shear loading. It evaluates whether the material–geometry combinations selected in Chapter 6 can transfer shear forces in a controlled and structurally meaningful way. The main mechanical loads considered are lateral forces caused by wind and accidental live loads, such as people leaning or falling against the vault assembly. The test therefore focuses on the local glass–interlayer–glass connection rather than on the complete vault structure.

All specimens are tested under a constant normal load of approximately 0.6 kN, representing the compressive self-weight acting on the most loaded interlayer in the reversible vault design from Chapter 7. The shear load is then applied until failure to determine the maximum capacity, load–displacement behaviour, and governing failure mode.

Section 9.2 provides a high-level discussion of the results, focusing on the overall response, material-related trends, geometry-related trends, failure modes, and resulting design implications. The normal load calculation, specimen preparation, experimental setup, loading procedure, and individual specimen results are provided in Appendix E. The key results are summarised in Table 9.1.

9.2. Mechanical test results and interpretation

All specimens initially showed an approximately linear loading phase. However, the slope differed significantly across the samples, showing that both material and geometry influenced the stiffness of the interlayer. Various failure behaviours were observed, ranging from sudden drops in capacity to progressive loss of load-bearing capacity, including specimens that showed several smaller intermediate drops before final failure. After peak failure, the curves all showed a residual plateau, which can be attributed to friction between the glass and the interlayer after the mechanical interlock had partially or fully failed.

Peak load alone is therefore not sufficient for selecting the best material–geometry combination. Failure mode, glass substrate damage, stiffness, residual friction, and end-of-life demountability must also be considered. Additionally, initial delamination strongly influenced the results, meaning that not all observed differences can be attributed solely to material or geometry. Since PETG-CF was tested at a lower loading speed than PET-CF and PETG-GF, the results should be interpreted as comparative design trends rather than absolute material rankings.

The dissipation energy results support the same trend. PETG-CF specimens generally absorbed more energy before complete loss of capacity, indicating a more stable post-peak response than the PET-CF and PETG-GF series. This confirms that controlled deformation and residual resistance are relevant performance indicators in addition to peak load.

Table 9.1: Summary of mechanical validation results for all tested specimens

ID & Geometry		Peak load [N]	Displacement [a] [mm]	Stiffness [b] [N/mm]	Shear stress Base [MPa]	Shear stress Knobs [MPa]	Failure mode(s)
PETG-CF							
S1	1	2689.6	4.17	645.1	0.29	1.35	B
S2	2	3158.2	2.61	1209.4	0.34	3.72	B
S3	3	5137.1	3.82	1345.4	0.57	3.59	B, SR
S4	4	3656.7	2.93	1249.4	0.80	2.56	SR, B
PET-CF							
S5	1	773.7	2.08	372.2	0.08	0.39	D
S6	2	2116.4	2.42	873.1	0.23	2.50	SR, B, PS
S7	3	3049.6	4.67	652.4	0.33	2.13	SR, B, PS
S8	4	853.6	0.99	864.0	0.19	0.60	D, TR
PETG-GF							
S9	1	1184.7	1.81	655.0	0.13	0.59	D
S10	2	2613.6	2.74	954.9	0.28	3.07	D
S11	3	1773.7	2.05	866.7	0.19	1.24	D
S12	4	617.7	1.69	365.0	0.13	0.43	D

Note. Failure modes: B = Bearing; SR = Shear rupture; D = Delamination; PS = Pure shear; TR = Tensile rupture.

[a] At peak load.

[b] 0–peak range.

Material-related trends

PETG-CF was the best-performing material. It showed the highest and most consistent shear performance, resisted initial delamination most effectively, and generally failed through bearing failure, occasionally combined with shear rupture of the printed geometry, rather than sudden interface delamination. This means the intended mechanical interlocking was properly activated. Additionally, PETG-CF outperformed both other materials in 0–peak stiffness for most geometries and showed the highest residual friction plateau after peak failure, while causing little to no damage to the glass substrate.

PET-CF showed high initial stiffness, but its response was less stable. Geometry 1 and 4 were strongly affected by initial delamination, while geometry 2 and 3 performed much better and failed through more favourable mechanisms. This indicates that PET-CF can work, but only when the geometry provides sufficient bonded surface area and distributes the load consistently. Of the three tested materials, PET-CF was also the most difficult to process consistently.

PETG-GF is mechanically promising, but highly limited by its interface behaviour. It often showed high initial stiffness values, but all four specimens ultimately failed through unfavourable sudden full delamination. Therefore, the measured stiffness could not be fully utilised. Together with the moderate glass damage observed across the samples, PETG-GF is the least suitable material for a reversible interlayer in its current form.

Geometry-related trends

Geometry 2 and 3 proved to be the strongest designs. Both showed relatively low initial delamination, better load distribution, and higher peak performance than geometry 1 and 4. Moreover, they produced the most favourable failure modes, especially when combined with PETG-CF or PET-CF.

Geometry 2 demonstrated the highest knob-area shear stress capacity, especially when combined with PETG-CF. Geometry 3 combined with PETG-CF produced the highest peak load and base-area shear stress capacity. From a design perspective, geometry 3 is slightly more attractive because the steeper 60° knob angle increases the connection area to the base while reducing the overhang. This significantly improves printability and consistency.

Geometry 1 proved to be too coarse. The large elements caused more initial delamination and glass chipping, while also concentrating the load on individual elements. The larger knobs also meant that only two keys could be used instead of four, making the force distribution even less favourable.

Geometry 4 demonstrated a clear trade-off between demountability and mechanical reliability. The reduced base area of the organic cross-hatch pattern improves removal potential, as discussed in Chapter 8, but it also increases the total edge length relative to the bonded surface area. This made the interlayer much more susceptible to initial delamination before testing.

Failure mode analysis

The observed failure modes can broadly be divided into interface-controlled failure and geometry-controlled failure. Sudden full delamination of the interlayer from the glass was the most unfavourable failure mode, since it was brittle, difficult to predict, and resulted in an immediate loss of mechanical engagement. This was especially problematic for PETG-GF and for geometries with either large concentrated features or reduced bonded surface area.

More favourable failure modes occurred when the load was successfully transferred from the stainless-steel keys into the printed knobs. Bearing failure at the knob base was the most common and informative: it confirms that the interlocking mechanism was activated and that failure no longer occurred primarily at the glass–polymer interface. Shear rupture is also more favourable than delamination, since it indicates local failure within the printed geometry rather than global interface failure. However, both bearing failure and shear rupture point towards local stress concentrations around the knob base or key-contact region. Pure shear failure, resulting in fracture of a knob, was observed only rarely, suggesting that the knob body itself was generally less critical than the transition between the knob and the base layer.

Glass chipping was an unfavourable secondary damage mechanism because it directly conflicts with the circular objective of non-destructive reuse. Even when a specimen achieved high shear resistance, visible damage to the glass substrate may limit its suitability for reversible applications. Finally, no failure of the stainless-steel keys was observed, indicating that the keys were not the limiting component in the tested configurations.

Mechanical validation sub-conclusion

The shear test series shows that the interlocking principle is mechanically effective when delamination does not govern the response. In those cases, failure shifted from the glass–polymer interface to bearing failure or shear rupture of the knobs, confirming that the keys successfully transferred load into the interlayer. Among the tested combinations, PETG-CF with geometry 3 performed best mechanically, because it showed a high peak load, high shear stress capacity, and good printability. PETG-CF with geometry 4 showed slightly lower mechanical capacity, but remains relevant because of its more favourable end-of-life removal behaviour, as established in Chapter 8. For this reason, both PETG-CF-S3 and PETG-CF-S4 are taken forward in the wind-load validation. However, the repeated occurrence of bearing failure and shear rupture near the knob base identifies this transition as the critical detail. Future refinement iterations should therefore introduce a fillet or smoother transition at the knob base to reduce stress concentrations.

9.3. Wind load validation

Having identified PETG-CF-S3 as the mechanically strongest combination and PETG-CF-S4 as the most balanced alternative, the shear test results are used to validate whether both specimens can resist the shear demand calculated for the demountable glass vault. The wind load calculation and Karamba analysis in Appendix D provide the relevant lateral shear force of 1.10 kN that a single full interlayer must transfer. However, this shear demand cannot be compared directly with the peak force of the tested specimens, since the vault interlayer and the test specimens have different base and knob areas. Therefore, the comparison is made using the shear stress in both the base and the knobs.

First, PETG-CF-S3 is compared with the calculated vault demand in Table 9.2. This specimen represents the mechanically strongest tested combination and is therefore used to assess the maximum structural reserve capacity of the interlocking interlayer system.

Table 9.2: Comparison between vault shear demand and tested shear capacity of specimen PETG-CF-S3

	Force	Base area	Knob area	Base shear stress	Knobs shear stress	Utilisation base	Utilisation knobs
	[kN]	[mm^2]	[mm^2]	[MPa]	[MPa]	[-]	[-]
Vault demand	1.10	17939	2180	0.061	0.50	0.11	0.14
Tested capacity	5.14	9211	1432	0.57	3.59	–	–

The calculated wind-induced shear stresses remain substantially below the experimentally obtained capacity of PETG-CF-S3. The base reaches a utilisation of 0.11, while the knobs reach a utilisation of 0.14. This confirms that PETG-CF-S3 can resist the peak wind-induced shear forces in the vault with considerable reserve capacity. The slightly higher utilisation in the knobs indicates that the knob region governs the response, which is consistent with the observed failure behaviour during shear testing. The remaining reserve capacity also provides tolerance for local imperfections, partial delamination, or minor variations in print quality.

PETG-CF-S4 is also compared with the calculated vault demand in Table 9.3. This specimen is mechanically less strong than PETG-CF-S3, but is highly relevant because the demounting tests discussed in Chapter 8 show that geometry 4 provides more favourable end-of-life removability.

Table 9.3: Comparison between vault shear demand and tested shear capacity of specimen PETG-CF-S4

	Force	Base area	Knob area	Base shear stress	Knobs shear stress	Utilisation base	Utilisation knobs
	[kN]	[mm^2]	[mm^2]	[MPa]	[MPa]	[-]	[-]
Vault demand	1.10	7649	2228	0.14	0.49	0.18	0.19
Tested capacity	3.66	4589	1428	0.80	2.56	–	–

The calculated wind-induced shear stresses also remain below the experimentally obtained capacity of PETG-CF-S4. The base reaches a utilisation of 0.18, while the knobs reach a utilisation of 0.19. Although these utilisation values are higher than those of PETG-CF-S3, they remain well below full capacity. This confirms that PETG-CF-S4 can also resist the calculated wind-induced shear demand of the vault, while offering the advantage of easier end-of-life removal from the glass.

9.4. Conclusion

The conducted shear tests demonstrate that the interlocking interlayer concept is capable of transferring sufficient shear force. In several specimens, failure occurred within the interlayer geometry rather than directly at the glass–polymer interface, confirming that the bond was sufficient to activate the intended mechanical interlocking mechanism under shear loading. The final geometry selection depends on the design priority. Among the tested combinations, PETG-CF combined with geometry 3 showed the most favourable mechanical behaviour, providing the highest and most consistent shear performance while limiting premature delamination. The wind load validation further confirmed that this combination can resist the calculated shear demand in the demountable glass vault.

When end-of-life demountability is also considered, PETG-CF combined with geometry 4 provides a relevant alternative. Although its mechanical capacity is lower than that of geometry 3, it showed more favourable removal behaviour, with limited residue and no observed glass chipping. geometry 3 is therefore preferred where maximum mechanical performance and structural reserve are required, while geometry 4 is more suitable where reversibility and repeated removal from the glass substrate are prioritised.

The results also show that failure behaviour is as important as peak load capacity. Progressive bearing failure of the knobs is preferred over sudden full delamination, since it is more controlled and predictable. The knob–base transition was identified as the governing region, indicating that future optimisation should focus primarily on reducing stress concentrations and improving load distribution in this area.

In answering research sub-question 4, the shear experiments confirm that the interlocking principle is structurally feasible, but successful application requires balancing shear capacity, interface stability, controlled failure behaviour, and non-destructive reversibility. Further repeated testing under cyclic, long-term, and environmental loading conditions remains necessary before the system can be considered fully validated for safe structural application.

10

Discussion

10.1. System-level interpretation of the findings

This research demonstrates that a directly 3D-printed polymer interlayer can function as more than a passive contact-mediating layer between cast-glass components. Literature review on segmented cast-glass assemblies identifies the interlayer as a necessary interface that prevents direct glass-to-glass contact, redistributes stresses, and accommodates dimensional tolerances. This thesis extends that role by showing that the interlayer can also become the primary source of interlocking, shear transfer, assembly control, reversibility, and component reuse.

This shift is significant because previous dry interlocking cast-glass systems generally incorporated the interlocking geometry directly into the glass components. Although structurally effective, this increases casting complexity and limits standardisation. By moving the interlocking function into a replaceable 3D-printed polymer interface, the glass components themselves can remain planar, simple, and reusable across different applications. The geometric complexity is instead transferred to the interlayer, where it can be more easily customised, replaced, and iterated.

The main contribution of this research is therefore not a single optimised material or definitive interlocking geometry, but a design logic for reversible cast-glass assembly. The research demonstrates that the interlocking interlayer must be treated as a coupled material-geometric design problem. Material behaviour, print parameters, interlocking geometry, demountability, and circularity cannot be judged independently. For instance, a polymer that adheres very strongly may perform exceptionally well under shear loading, but become less attractive when clean interlayer removal is required at end-of-life. Because of these inherent trade-offs, the system should not be assessed using a single criterion such as maximum peak load, highest stiffness, or easiest removal. Instead, the most suitable material-geometry combination depends entirely on the intended application. A permanent structure in a remote or demanding environment, such as the Qaammat Pavilion, might prioritize strong adhesion and maximum shear capacity. Conversely, more temporary assemblies, such as the Qwalala sculpture, would dictate a design that prioritizes clean demountability for uncontaminated glass component reuse.

At the same time, these results should be interpreted as proof-of-concept validation rather than a complete, building-ready solution. By testing a representative connection of the designed demountable vault, the research successfully validates the dry-interlocking principle at a local mechanical, material, and geometric level. However, this local validation does not yet establish complete structural design values, long-term environmental durability, or large-scale production reliability. Nevertheless, it proves that an adhesive-free, interlocking polymer interlayer can enable structurally meaningful and reversible cast-glass assembly, while clearly identifying the manufacturing and material barriers that must be solved before broader architectural implementation.

10.2. Interface behaviour and material trade-offs

The material experiments confirm that direct FDM printing onto glass is feasible for the selected polymer candidates, but they also show that the glass-polymer interface remains the most sensitive part of the system. This supports the literature-based assumption that material selection for dry interlayers cannot be based only on mechanical properties. Processability, dimensional stability, interfacial reliability, and reversibility are equally important.

The interface should therefore not be treated as a problem of maximising adhesion alone. To contextualise this, it is useful to compare the system to the permanent epoxy putty used in *The Glass Vault* case study. While an epoxy putty guarantees excellent monolithic load transfer and accommodates tolerances perfectly, it creates an irreversible chemical bond that makes end-of-life separation impossible without damaging the glass. The 3D-printed interface proposed in this research deliberately seeks a more balanced compromise. Adhesion must be strong enough to prevent warping during printing, keep the interlayer attached during handling, and allow the interlocking geometry to engage properly before premature delamination occurs. However, excessive adhesion increases removal effort, residue, and the risk of localised glass damage. The aim is therefore controlled interfacial reliability: the interlayer must remain stable during production, assembly, and loading, while still allowing an appropriate end-of-life scenario.

Compared with earlier PLA-based interlayers by Van Kessel (2025), the fibre-reinforced PET-based materials tested in this research shift the system towards higher stiffness, improved dimensional stability, better environmental durability, and stronger resistance to delamination. PETG-CF emerged as the most convincing material from a structural reliability perspective. It resisted initial delamination most consistently and generally showed a more controlled mechanical behaviour. The stable glass-polymer interface that makes PETG-CF attractive mechanically also makes it less straightforward from a material recovery perspective. However, this is not necessarily a contradiction if direct component reuse is treated as the primary circular strategy. If the glass and interlayer remain attached and are reused together over multiple use cycles, stronger adhesion becomes an advantage instead of a limitation.

PETG-GF is an important comparative case. Based on the literature review and initial material experiments, it appeared to be a highly promising candidate because of its printability, dimensional stability, and removability. However, the shear tests showed that it is less suitable for structural use in its current form, because it consistently failed by sudden full-interface delamination. This behaviour was strongly influenced by the initial delamination caused by printing the larger interlayer geometries close to the glass edge. This does not make PETG-GF irrelevant, but it demonstrates that good material-screening performance does not automatically translate into reliable structural behaviour once all elements and external effects are combined.

PET-CF should also be interpreted carefully. It was not printed under ideal enclosed-printer conditions, meaning its full potential may not have been reached. Its high stiffness and thermal stability remain promising, but its brittleness, processing sensitivity, and cost make it less attractive than PETG-CF for the current system. The material comparison therefore refines the selection framework: the most suitable material provides sufficient adhesion without brittle, unpredictable, or damaging failure, rather than being simply the strongest or easiest to remove polymer.

These findings explain why the initial material test coupon should be interpreted as a broad comparative screening tool rather than a fully representative adhesion test. The coupon did not include a sufficiently large or structurally representative bonded area, and the materials were assessed soon after cooling to room temperature, which underestimated delayed stabilisation effects. In the later combined material-geometry specimens, initial delamination became much more pronounced across the tested materials, proving that interface behaviour is heavily dependent on the geometry that is printed onto it.

10.3. Geometry, mechanical behaviour, and structural reliability

The final interlocking geometry can be considered successful because it translates the dry-interlocking principle into a form that remains compatible with standard FDM printing. It avoids overhangs that need support structures, sharp corners, tolerance-sensitive sliding mechanisms, and highly complex mechanical interlocks. At the same time, it introduces a distributed knob-based contact surface that spreads engagement across many repeated features. This makes the system far less dependent on

a single, precise interlocking element and more capable of accommodating small deviations through collective behaviour.

One of the strongest design decisions is the introduction of removable keys. The keys separate placement and locking into two distinct actions: the glass component can first be positioned, after which the connection is mechanically activated by inserting the cylindrical keys. This improves constructability and directly supports reversibility, because the connection can be deactivated by removing the keys without damaging the glass or the interlayer. Compared with purely compliant snap-fit systems, this novel typology with removable keys is more suitable for stiff fibre-reinforced polymers. This ultimately yields a structurally safer assembly, as mechanical locking ensures monolithic behaviour between components rather than relying on elastic deformation and friction to keep them together.

The geometry combines several mechanisms: geometric engagement between knobs and keys, distributed surface contact, frictional resistance under normal load, tolerance accommodation through repeated features, and redundancy through multiple load paths. The shear tests confirm that this concept can transfer sufficient forces under combined normal and shear loading. However, the validation remains connection-level validation. The tests assessed a modified local glass-interlayer-glass specimen, not the complete vault as a global structural system.

The wind analysis of the demountable vault design established a horizontal shear demand of approximately 1.10 kN per interlayer. The PETG-CF shear specimens, despite representing only half the area of a full interlayer, reached peak loads between 2.69 kN and 5.14 kN. The calculated utilisation factors for two of the four most promising geometries were below 0.19 for both the knobs and base. While such a low utilisation factor might seem over-engineered in standard structural contexts, in structural glass applications, this level of redundancy and high safety margin is strictly necessary to account for the brittle nature of the material, dynamic environmental loading, and potential long-term fatigue. These results demonstrate that the interlocking concept safely exceeds the shear demand for this specific demountable vault design.

The comparison between the specific geometry variations used during shear testing is particularly important, as it illustrates how geometry governs the distribution of residual stresses, edge effects, and adhesion demand across the interface. Geometry 1 demonstrated that large knobs together with strong adhesion from PET-based polymers can result in residual stresses high enough to damage the glass substrate prior to testing. This is a critical finding because it proves that larger features are not automatically beneficial for achieving higher capacity in a brittle glass system if they shift the failure mechanism directly into the glass substrate.

(a) Initial engagement of the interlocking keys during shear loading, showing limited wedging and deformation prior to peak load

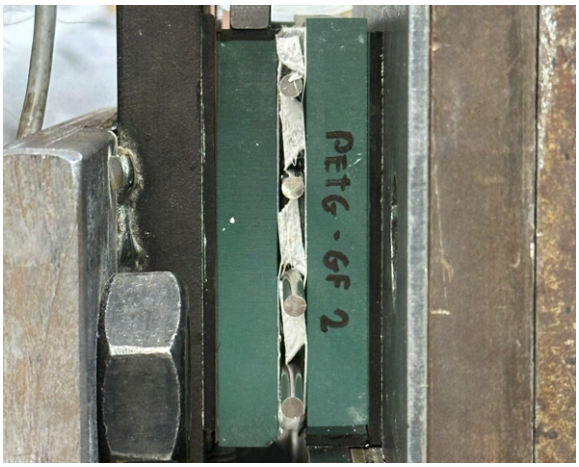

(b) Advanced wedging behaviour near peak load, showing increased key engagement and local deformation

Figure 10.1: Representative images illustrating the wedging behaviour observed during shear testing in several material-geometry combinations

Geometries 2 and 3 provided superior balance. Their distributed knobs allowed the keys to engage properly, while their base contact area was sufficient to reduce premature delamination. The observed increase in normal force during some tests was mainly associated with these geometries and can be attributed to the interaction between the angled knobs and cylindrical keys. Figure 10.1 shows how under shear load, local rotation and wedging can develop, thereby increasing the normal force.

Geometry 4 illustrates the opposite problem to geometry 1. Its reduced surface area resulted in too much exposed edge length, which made the specimen highly sensitive to initial delamination; it often failed before the wedging mechanism could even develop. This confirms that geometries 2 and 3 represent the most promising middle ground: they use neither large, overly stiff knob elements that risk glass substrate damage, nor a highly reduced base layer pattern that undermines interface reliability.

The PETG-CF test results are highly valuable because sufficient interface adhesion allowed the weak point to shift from the glass-polymer interface towards the printed geometry itself. This is positive in one sense, because it means that the interface no longer always fails first, as observed in previous research. However, it also reveals the next governing design problem. Stress concentrates locally at the base of the knobs. If the load is not evenly distributed due to print deviations or tolerances, a limited number of knobs may engage first and have to carry the full load. This shows that once the interface is reliable enough, the knob-base transition becomes a critical structural detail. Future geometry development should therefore focus on this transition point through local reinforcement, fillets around the knob base, smoother load paths, and altered knob angles.

10.4. Demountability, circularity, and translation to vault scale

The highest-value circular strategy for the proposed system is direct reuse of the complete glass-interlayer component. In this scenario, the keys are removed, the structure is disassembled in reverse order, and the glass components are reused with the interlayers still attached. This avoids repeated interlayer removal, cleaning, reprinting, and potential glass damage. It also reframes the PETG-CF trade-off: if the interlayer remains durable and well attached over multiple use cycles, strong adhesion becomes desirable rather than problematic.

This distinction clarifies two different levels of reversibility. Assembly-level reversibility means that the structure can be taken apart by removing the keys and recovering the glass-interlayer components. Material-level reversibility means that the polymer interlayer can be removed from the glass so both materials can be recovered or recycled separately. For this system, assembly-level reversibility should be considered the primary route, while material-level separation should be treated as a secondary recovery strategy for cases where the interlayer is damaged, the glass is damaged, or the component geometry is no longer useful.

Compared with existing adhesively bonded cast-glass assemblies, the proposed system does not yet offer the same maturity, durability, or construction readiness. However, it directly addresses their main circularity limitation: irreversible bonding. The keys enable non-destructive disassembly of the system. This is the most important circular contribution of the research, even though full material separation remains partly unresolved.

The demountability experiments indicate that mechanical removal of the regular interlayer side with a thin base layer is feasible, but the thicker angled interlayer sides remain more difficult. These require further investigation of integrated removal features rather than relying on simple manual separation. Delamination by using compressed air as a trigger remains promising for these thicker interlayers, but this requires further investigation of reliable air paths that can be maintained during printing. Heating the components to the polymer's glass transition temperature remains technically possible, but should be considered as a fallback strategy because it requires significant time and energy, making it difficult to scale to larger glass components. Local heating for example, by using a heat gun or heated wire, may provide a more realistic intermediate solution, but this still requires further validation.

The demountable vault demonstrates architectural potential and assembly logic, but should not be overclaimed as structural validation. The material coupons and shear specimens validate local interface and connection behaviour, while the vault introduces questions about global load paths, tolerance accumulation, construction sequencing, long-term compression, repeated key insertion, and full-scale handling. The prototype should be seen as an assembly demonstrator rather than proof of final structural performance, because its fabrication route differs from the intended direct print-on-glass workflow.

The main translation challenge remains production scale. Printing on small flat glass coupons is fundamentally different from printing on full cast-glass bricks. Full-scale components introduce greater thermal mass, dimensional deviations, edge irregularities, two-sided printing requirements, and positioning challenges. A custom printing setup is necessary, particularly to integrate local heating and precise positioning into one workflow.

While FDM is inherently a relatively slow layer-by-layer process, it should not be dismissed as a bottleneck for architectural scale. Although production may require longer before construction begins, it significantly accelerates the subsequent on-site assembly process. Automated printers can theoretically operate 24/7, which human workers cannot until the technology allows for full autonomous on-site construction. Furthermore because the resulting components utilize dry connections, assembly requires no specialized equipment on site. Together with the rapid emergence of large-scale print farms, continuously increasing printing speeds, and advanced robotic FDM setups, mass-customised direct printing is becoming increasingly viable.

The demountable vault design also raises a standardisation question regarding the angled interlayers. Fully custom interlayer angles are possible through parametric design, but discrete standard angles may be more realistic if the system is developed into a reusable building kit. A theoretical alternative to printing thick custom volumes could be to directly print flat, standard base interlayers onto the glass, and use separate mass-produced angled elements (e.g., via injection moulding) to create the curvature. This strategy would further improve reuse flexibility and reduce the application specific nature of the components. Additionally, it would enable a wider range of materials with potentially more suitable mechanical or optical properties.

10.5. Limitations and future research recommendations

Several limitations of this research must be acknowledged. First, all experimental results are based on small coupons and local shear specimens. The findings therefore support connection-level validation and comparative design trends, but they do not yet yield statistically robust structural design values. Furthermore, the mechanical validation focused exclusively on short-term, quasi-static shear loading. Long-term and environmental effects such as creep, fatigue, ageing, UV exposure, humidity, thermal cycling, impact, seismic behaviour, and repeated assembly/disassembly cycles remain outside the experimental scope. Consequently, the core research question moving forward is no longer simply whether a printed interlocking interlayer is possible, but whether its long-term polymer behaviour, structural reliability, and repeated reuse performance can be made predictable enough for architectural implementation. This requires future work to shift from proof-of-concept experimentation towards systematic, large-scale validation across several key domains.

Interface behaviour and material refinement

Future material testing must begin with improved coupon design. While the current test coupon was useful as a broad screening tool, future iterations should include larger structurally representative bonded areas, edge-sensitive geometries, and both immediate and delayed post-print inspections to better capture stabilisation effects. The potential of PET-CF should be re-evaluated using an enclosed, actively heated printer before its structural viability is definitively judged. Additionally, future interface research should systematically fine-tune ideal edge distances, brims, and base layer patterns to control how the printed geometry guides residual stresses and delamination paths. Finally, while optical compatibility was deliberately treated as a secondary requirement in this study, future material development should explore transparent or translucent polymers to respect the visual continuity that makes cast glass architecturally desirable.

Geometry optimisation and end-of-life demountability

At the local geometric level, future development should prioritise the structural transition between the base layer and the interlocking knobs. To reduce the stress concentrations observed during testing, future geometries should incorporate filleted bases, smoother load paths, local reinforcement, and optimised knob angles. To validate these refinements, mechanical testing should be expanded to include larger sample sets, varied shear directions, isolated knob tests, and unloading-reloading cycles. In parallel, future demountability research must develop integrated removal features for the thicker angled interlayers. Concepts such as open infill, integrated air channels, reduced bond areas, or integrated pull-tabs have high potential, but they must be co-designed alongside mechanical optimisation, as these removal strategies directly affect the bonded-area distribution.

Translation to architectural scale and production

The final, and perhaps most critical, area for future research is the transition from local joints to global structural systems. Future assembly research should test larger cast-glass components, focusing on tolerance accumulation across multiple joints, two-sided printing, and positioning accuracy. Designing and physically testing a larger arch or vault segment would be an essential next step to connect the local shear behaviour validated in this thesis to assembly-scale construction logic. This scale-up will inevitably require the development of a custom, FDM setup with integrating local heating to directly print onto two sides of the glass bricks. Finally, future architectural detailing must address the realities of outdoor implementation by developing non-adhesive weatherproofing details, such as integrated TPU-based edge sealing strategies.

11

Conclusion

The central question this research aimed to answer was:

How can the material behaviour and geometric interlocking design of an additively manufactured polymer interlayer be optimised to achieve reversible and structurally reliable dry-fit connections between planar cast-glass units?

By systematically exploring the interdependent aspects of this question, this thesis demonstrates that an AM polymer interlayer can enable reversible, structural connections between planar cast-glass components. This is achievable when material behaviour, interlocking geometry, and assembly logic are developed as one integrated system. The interlocking function was successfully shifted from the glass component into the polymer interlayer, allowing simple, planar brick-shaped glass units to be used without requiring complex component-level geometry. The primary contribution of this work is a coupled system in which material adhesion, printed interlocking geometry, removable keys, and assembly sequencing work together to realise reversible, circular construction.

The final outcome is a validated proof-of-concept with significant structural potential, providing a solid foundation for future implementation. The conducted shear tests provide strong empirical evidence for the structural performance of the connection, while the physical prototype confirms the feasibility of the assembly logic and process. Although the demountable vault served as a demanding design case to evaluate the complexity of variable inter-component angles, the developed system is more widely applicable and extends beyond this specific architectural case. Ultimately, this research marks an important transition from permanently bonded cast-glass assemblies towards reversible, structural AM interlayer systems.

11.1. Material behaviour and printability

Fibre-reinforced PET-based polymers proved to be the most viable material direction for directly printed interlayers on glass substrates. Within the tested material set, PETG-CF was selected as the primary material for this research, although this does not exclude potentially better alternatives in future studies. Initial material and geometry experiments identified PETG-CF, PETG-GF, and PET-CF as promising candidates in terms of printability, adhesion, dimensional stability, and compatibility with the developed interlocking typology. Following the subsequent demountability and shear testing stages, PETG-CF emerged as the most suitable candidate, showing the most reliable interface performance and overall structural capacity.

While PETG-GF performed well across most evaluation criteria, its sudden full-delamination failure mode made it unsuitable for structural applications where predictable, ductile failure is essential for safety. PET-CF remains a technically viable material with high performance potential, but proved less practical for this specific study due to its demanding printing conditions and higher material cost. PLA-CF served as a valuable backup material up to and including the combined material-geometry experiments. However, its limited environmental durability restricts its viability for real-world outdoor appli-

cations. While warping behaviour could largely be controlled through optimised print parameters and geometry, initial interface delamination remained a critical challenge throughout the experiments. In addition, glass chipping represents a notable material-interface risk, caused by the combination of strong interface adhesion and residual stresses resulting from thermal expansion mismatch. Ultimately, material selection requires a careful balance between printability, adhesion, dimensional stability, interface safety, and end-of-life demountability.

11.2. Geometric interlocking and assembly logic

This work successfully shifted the interlocking function from the glass component to the AM polymer interlayer, enabling simple planar glass bricks to function within a structurally connected, reversible system. The final V2.6 geometry introduces a hybrid typology that combines the mechanical performance of geometric interlocking with the distributed load transfer of surface-based interlocking. The primary geometric achievement lies in the clear separation between component placement and subsequent locking. Components can first be positioned, after which the keys are inserted to activate the mechanical interlock. The cylindrical keys physically connect the top and bottom sections of the interlayer, thereby establishing a clear shear-transfer path between adjacent glass components. Once the keys are inserted, relative movement between the components is mechanically confined, meaning that movement under load can only occur through interlayer deformation or interface delamination. Conversely, removing the keys initiates the primary circular strategy, which prioritises assembly-level disassembly and the reuse of intact glass-interlayer components over multiple use cycles.

The matrix of rounded knobs provides distributed contact areas that help reduce stress concentrations by spreading normal and shear forces across the full interface. Rounding these knobs significantly improved FDM compatibility by eliminating sharp corners and maintaining toolpath continuity. The feasible design space was strongly governed by FDM constraints, including nozzle resolution, thermal shrinkage, first-layer adhesion, toolpath continuity, and the need to avoid sharp corners or slender features. As a result, the final geometry favours robust, rounded, and distributed features rather than highly detailed or compliant mechanisms. Rounding the knobs also allowed the keys to become cylindrical, making them easy to insert without requiring a specific orientation. Additionally, the distributed layout enhances tolerance accommodation, as minor deviations caused by printing, glass surface irregularities, or assembly alignment can be absorbed across multiple contact points. In a broader context, this geometric typology is widely applicable to planar cast-glass assemblies where structural integrity, controlled assembly sequencing, reliable shear transfer, and systemic reversibility are required.

11.3. Translation to vault scale and structural validation

The demountable vault functioned as a demanding design case to evaluate the translation of the local connection design into a comprehensive architectural assembly logic. This case study was especially insightful because it required variable angles between planar cast-glass components, introducing a significantly higher degree of complexity than a standard straight wall. The production strategy was conceptually resolved by defining a plausible fabrication method for directly printing an interlayer on both sides of each glass brick. The integration of assembly markings represents another important outcome, as these indicators visually clarify the construction logic and reduce the need for highly specialised workers. While the AM process shifts fabrication time to the off-site prefabrication phase, the resulting dry-fit system significantly accelerates and simplifies on-site construction compared to traditional adhesive-bonded methods by eliminating the need for specialised equipment or curing times on site. The assembly sequence, which starts with the construction of a central arch and expands systematically outwards, is well suited to temporary scaffolding and offers clear potential for future automated robotic construction workflows. The constructed prototype serves as an assembly demonstrator to validate physical fit, key insertion, and construction sequencing, rather than as a direct structural evaluation of direct print-on-glass adhesion.

The demountable vault design provided the structural demand for mechanical validation, resulting in a calculated shear force of 1.10 kN per full interlayer. Even though the tested specimens represented only about half of the full interlayer contact area, all tested PETG-CF configurations significantly exceeded this demand under quasi-static shear loading, confirming the structural capacity of the connection. PETG-CF combined with geometry 3 reached a peak load of 5.14 kN, corresponding to individual utilisation ratios of 0.11 for the base and 0.14 for the knobs. PETG-CF combined with geometry 4 reached a peak load of 3.66 kN, resulting in utilisation ratios of 0.18 for the base and 0.19 for the knobs. Beyond peak load capacity, the mechanical shear tests validated favourable, ductile failure modes. Specifically, the observation of bearing and shear rupture within the interlayer, rather than sudden interface delamination, confirmed that the mechanical interlock activated successfully under load.

11.4. Demountability and final system balance

Demountability provides the primary circular value of this system, allowing durable and recyclable planar cast-glass components to move beyond single-use, permanently bonded assemblies. The preferred end-of-life scenario is assembly-level reuse, where the keys are removed, the assembly is dismantled, and the full glass-interlayer components are reused without separating the polymer from the glass. Material-level recovery serves as a secondary route when component reuse is unfeasible, for example when the interlayer or glass is damaged, or when a different interface angle is required for a new configuration. Mechanical interlayer removal tests demonstrated that material-level recovery is possible, but the detachment process requires further research and fine-tuning to improve efficiency and reliability.

The final system selection balances peak load capacity with failure mode, residual friction, energy dissipation, stiffness, glass damage, and end-of-life demountability. Progressive bearing failure represents the most desirable failure mode, whereas sudden delamination is the least desirable because it indicates an unpredictable and abrupt loss of interface adhesion. Geometry 3, which features a continuous base layer and medium-sized knobs with 60-degree angles, offers the highest structural capacity and interface reliability. It is therefore suitable for high-load, long-term applications where components remain assembled and interlayer removal is rare. Geometry 4 has a similar knob configuration but uses an organic cross-hatch base layer pattern, creating a better balance between structural performance and ease of removal. It is therefore better suited to scenarios where repeated demounting, adaptation, or interlayer replacement are foreseen. Both geometries possess distinct characteristics suited to different reuse scenarios and performance priorities, offering design flexibility for individual project requirements. Overall, systemic reversibility is technically viable, but it requires precise fine-tuning of the material-interface behaviour, removal methodology, and geometric configuration based on the intended application.

11.5. Concluding synthesis

This research demonstrates a structurally effective and mechanically validated proof-of-concept connection for planar cast-glass components. This was achieved through the integrated development of suitable material behaviour, a mechanical interlocking typology, and assembly and disassembly logic. The proposed system allows standard planar glass bricks to become integrated structural elements without relying on permanent adhesives or complex geometric shaping of the glass itself. The resulting output forms a unified connection system, design framework, and proof-of-concept construction strategy.

Current validation remains limited to short-term laboratory experiments, localised shear testing, demounting trials, and an architectural assembly prototype. Further research and development are necessary to evaluate long-term durability, material creep under sustained load, environmental weathering, repeated reuse cycles, larger-scale structural testing, and the scaling of direct print-on-glass production methods. Despite these remaining future steps, this system contributes to circular cast-glass construction by combining reversibility, structural connection, and the reuse of standard components. Consequently, this thesis advances cast-glass construction beyond permanent bonding towards adaptable, recoverable, and mechanically interlocking structural assemblies.

12

Impact

12.1. Impact on circular structural assemblies

Circularity in structural assemblies is often not limited by the material itself, but rather by the way components are connected. Permanent adhesive-based joining methods may provide reliable, continuous structural connections, but they also make future separation, repair, and reuse difficult or impossible. This research uses cast glass as challenging cast study, because it is brittle, valuable, and highly sensitive to damage. However, the broader impact lies in demonstrating an alternative connection logic: structural load transfer can be achieved through a reversible intermediate interface rather than through permanent bonding.

By shifting the complexity of the connection into a separate interlayer, the main structural component can remain simple, durable, and reusable. The interlayer is the contact mediator that accommodates tolerances, provides alignment, transfers (shear) forces, and enables disassembly. This thesis develops the principle through an AM polymer interlayer for cast glass, but the core concept is not limited to one material, geometry, or production method. It forms the foundation towards a wider design principle for circular construction where structural assemblies should be detailed so load transfer and future disassembly are both considered from the start.

12.2. Sustainability: reuse, reversibility and recycling

Once glass components are removed from an assembly, they can be reused intact in different configurations to create new structures elsewhere. The use of standardized, planar bricks significantly increases this reuse potential, as the components are not bound to one specific global geometry. Variation can instead be achieved through the interlayer design, without bespoke glass units for every configuration. Especially glass components featuring a flat interface on both sides, such as the keystones in the reversible glass vault design, allow for great architectural freedom.

Reversibility is achieved by replacing adhesive bonding with mechanical interlocking activated by removable keys. The main sustainability advantages of this system is the controlled separation of materials at end-of-life. The polymer interlayer functions as a replaceable interface between the far more durable glass components, allowing the glass to remain available for future reuse. By avoiding permanent adhesives, the connection remains dry and reversible, making maintenance, replacement, and future adaptation far more feasible.

Clean separation between the polymer and glass is also important for recycling. Although some polymer residue may remain after removal, this can be mechanically removed, avoiding the permanent contamination typically associated with adhesive bonding. This improves the potential for closed-loop recycling of the glass and separate recovery of the polymer interlayer. On a macro level, this supports circular economy principles in which building components are not treated as traceable and recoverable material assets instead of fixed, single-use elements. Thereby, the system directly contributes to the broader shift towards buildings as temporary material banks.

12.3. Impact on design and fabrication practice

The developed interlayer strategy shows how joints can become adaptable design components rather than fixed products. Parametric modelling enables the interlayer geometry to be tuned to different brick orientations, angles, contact conditions, and assembly configurations. This creates a workflow in which material behaviour, interlocking geometry, fabrication constraints, and structural performance are evaluated together. Therefore, the impact extents beyond the specific geometry developed in this thesis and demonstrates a broader design method for reversible structural interfaces

In this research, FDM was used because it enables rapid, low-volume, and project-specific production without custom moulds or specialized industrial tooling. For larger production volumes, other methods such as injection moulding or CNC milling could be explored. However, the chosen fabrication method directly influences tolerances, precision, scalability, cost, and geometric freedom. This means that the fabrication method, interlayer geometry, and reversibility should be treated as interdependent design decisions from the start.

12.4. Potential applications beyond the vault

In its current state, the presented system is most directly applicable to small-scale vault, arches, and vertical assemblies where components primarily need to be positioned, locked, and later recovered. Less structurally demanding applications, such as interior glass partitions or walls, provide a logical first implementation step. Temporary pavilions, exhibitions, and art installations are also highly relevant, since reversibility, transportability, and component reuse are especially valuable in these contexts.

A clear reference example is *Qwalala*, a cast-glass sculpture by Pae White (see Figure 12.1). The artwork was originally exhibited in Venice and was later permanently relocated to Claremont McKenna College in California. This relocation required a renewed structural assessment because the loading conditions changed due to the increased seismic risk at the new location. The sculpture consists of more than 1500 cast-glass bricks bonded with structural silicone (Aloui & Bao, 2024). A reversible interlocking interface could significantly simplify such relocation scenarios, since the glass components could be dismantled, transported, and reassembled without relying on repeated adhesive bonding or destructive separation.

Figure 12.1: *Qwalala* sculpture by Pae White. Image credit: Enrico Fiorese.

Figure 12.2: Qaammat Pavilion, Greenland. Image credit: Julien Lanoo.

The system may also be valuable in remote or difficult construction locations. Adhesive bonding generally requires controlled conditions, skilled execution, and careful curing, which are not always easy to guarantee on site. The *Qaammat Pavilion* in Greenland (see Figure 12.2) illustrates this challenge: it was built in a remote Arctic location under limited-budget conditions and needed a simple construction process suitable for local assembly (Oikonomopoulou et al., 2022). A reversible interlayer system shifts much of the precision and quality control to the production phase, allowing the actual on-site assembly to become faster, easier, and less dependent on environmental conditions. Larger outdoor applications, such as façades, bridges, or permanent public structures, also remain possible but would require further validation regarding long-term durability, fire resistance, UV exposure, creep, and weathering.

13

Reflection

13.1. Positioning of the graduation topic within the studio

The graduation topic of this research is positioned within the Building Technology studio as a combination of material research, structural design, digital fabrication, reversible assembly, and circular construction. The project responds to the current limitations of permanent adhesive bonding in structural cast-glass assemblies by exploring a reversible alternative through 3D-printed polymer interlocking interlayers. The topic fits well within the Building Technology studio because it connects architectural design with technical experimentation, fabrication constraints, structural validation, and sustainability. While the project is novel and niche in its specific application to cast-glass assemblies, the underlying principles of reversibility, material optimisation, and demountable construction have much broader relevance. The technical depth of the project was expected and ultimately became one of its strengths, as the graduation process allowed the concept to be physically tested rather than remaining just a theoretical design proposal.

13.2. Reflection of the research approach

The research approach worked well because it followed a systematic route, starting with the literature study and proceeding through material experiments, geometric development, combined material-geometry testing, vault design, mechanical validation, demounting evaluation, and prototyping. The literature study provided the starting point for selecting alternative promising material candidates and an interlocking typology, while the experiments tested whether these assumptions worked in practice, particularly in the context of directly printing on glass.

The strongest aspect of the method was the systematic workflow, in which material behaviour, interlocking geometry, printability, assembly logic, and structural performance were developed in relation to one another. FDM printing proved to be a very valuable research tool because it enabled rapid iteration, extensive physical testing, and direct adjustments when uncertainties appeared.

The demountable vault design had to be developed before the final validation phase because it provided the structural shear demand needed to evaluate the mechanical test results. This made the vault more than just a final design application; it also functioned as a tool for giving architectural and structural meaning to the experimental findings.

13.3. Reflection on the results and methodology

The method led to the intended result: a validated proof-of-concept for a reversible interlocking polymer interlayer system for planar cast-glass units, supported by a complete storyline from material and geometry selection to mechanical testing and architectural translation. The developed interlocking geometry enabled coherent assembly logic, reliable mechanical engagement, and assembly-level reversibility. The mechanical shear tests strongly support the concept at connection level, particularly because the tested specimens could be compared with the shear demand derived from the demountable vault.

One important and unexpected insight was the influence of overnight cooling and base-layer thickness on warping behaviour. The first combined material-geometry specimens used a 1 mm base layer, which initially appeared to perform well. However, after cooling overnight, significant warping and detachment issues emerged, particularly in the PET-based material. Because FDM enabled rapid iteration, reducing the base-layer thickness to 0.5 mm significantly improved the behaviour of the fibre-reinforced PET-based materials, which subsequently showed little to no signs of warping or delamination. This clearly demonstrated that system performance was influenced not only by material selection but also by relatively small geometric and fabrication-related decisions.

The main weakness of the method was its broad experimental scope, as each experiment required its own setup, procedure, assessment, and interpretation. As a result, less time remained towards the end of the project to focus on the secondary demounting strategy for removing the printed interlayer from the glass substrate. The project therefore focussed primarily on the more favourable primary reversibility scenario, in which the glass components can be separated and reused as complete units. This prioritisation was logical, as optimising interlayer removal would only become meaningful after identifying materials and geometries with sufficient mechanical performance.

The one-factor-at-a-time material optimisation approach worked well as an initial systematic exploration but also had some limitations, since much of the assessment remained qualitative and certain behaviours only became apparent after longer cooling periods. Future research could improve upon this method by refining the test coupon, using more quantitative assessment methods, and allowing longer observation time after printing.

The main opportunity of the method is its applicability to future testing of alternative materials, improved geometries, and new interlayer configurations. The main threats or uncertainties relate to direct printing on both sides of full glass bricks, long-term material behaviour, repeated reuse, environmental durability, and scaling the concept towards architectural applications.

13.4. Relationship between studio method, research and design

The chosen method aligns well with the studio's research-through-design approach. The project combined technical literature research, physical experimentation, digital and parametric design, fabrication testing, mechanical validation, and architectural translation. The graduation process therefore reflects the broader methodological framework of the Building Technology studio, in which design questions are investigated through technical research and research findings are translated back into design decisions.

Throughout the project, research and design were highly interdependent. Research informed the design by defining material requirements, geometric criteria, printability constraints, and structural demands. At the same time, design generated new research questions, especially when the vault design and interlocking geometry revealed practical challenges related to assembly, tolerances, and validation. The vault design was therefore an analytical tool that helped establish the required structural performance targets. The graduation process can thus be characterised as a research-through-design approach, in which design decisions continuously informed further technical investigation.

13.5. Ethical and moral reflection

No major ethical dilemmas were encountered during the project, primarily because the research did not involve human participants. The main professional responsibility was to avoid overstating the maturity of the proposed system, as the project remains a proof-of-concept rather than a construction-ready solution. Sustainability must also be framed carefully. While the system improves reversibility and reuse potential, it still relies on polymer materials and requires further environmental and long-term performance assessment. The project should therefore be positioned as a technically promising step towards circular cast-glass construction while clearly acknowledging the need for further validation.

13.6. Personal process and learning

A key personal learning point, particularly as a perfectionist, was the need to make design decisions under uncertainty when not all experimental results were available. The process demonstrated the value of rapid prototyping and small-scale experiments as effective ways to reduce uncertainty and support informed decision-making. It also highlighted the importance of setting priorities within a limited timeframe and choosing the develop a coherent full-system proof-of-concept rather than fully optimising specific individual aspect.

Beyond the technical outcomes, I found it highly rewarding to work on this project. The combination of material research, experimentation, design development, and fabrication made the process both engaging and challenging. I am very pleased with the final outcome and how the project developed throughout the graduation process. Despite the inevitable challenges and uncertainties, the research resulted in a coherent final concept that successfully addressed the original research ambitions and provide a strong foundation for future development.

References

Aloui, O., & Bao, M. (2024). Structural design optimization of cast glass artwork via a digital design solution. *Glass Structures and Engineering*, *9*(3), 383–396. https://doi.org/10.1007/s40940-024-00278-9

Baechle-Clayton, M., Loos, E., Taheri, M., & Taheri, H. (2022). Failures and Flaws in Fused Deposition Modeling (FDM) Additively Manufactured Polymers and Composites. *Journal of Composites Science 2022, Vol. 6, Page 202*, *6*(7), 202. https://doi.org/10.3390/JCS6070202

Bambu Lab. (n.d.-a). ABS-GF. https://eu.store.bambulab.com/nl/products/abs-gf

Bambu Lab. (n.d.-b). ASA-CF. https://eu.store.bambulab.com/nl/products/asa-cf

Bambu Lab. (n.d.-c). PA6-CF. https://eu.store.bambulab.com/nl/products/pa6-cf

Bambu Lab. (n.d.-d). PA6-GF. https://eu.store.bambulab.com/nl/products/pa6-gf

Bambu Lab. (n.d.-e). PET-CF. https://eu.store.bambulab.com/nl/products/pet-cf

Bambu Lab. (n.d.-f). PET-CF technical data sheet, version 3 [PDF]. https://store.bblcdn.eu/s8/default/df83cdd0401b4c169d7883a3e7bd2c8a/Bambu_PET-CF_Technical_Data_Sheet.pdf

Bambu Lab. (n.d.-g). PETG-CF. https://eu.store.bambulab.com/nl/products/petg-cf

Bambu Lab. (n.d.-h). PETG-CF technical data sheet, version 3 [PDF]. https://store.bblcdn.com/626e4f424bf345ae965ad0ddfcaf2459.pdf

Bambu Lab. (n.d.-i). PETG-HF. https://eu.store.bambulab.com/nl/products/petg-hf

Bambu Lab. (n.d.-j). PETG-HF technical data sheet, version 1 [PDF]. https://store.bblcdn.com/ce12d65176a94f1086e6aefa238e62e2.pdf

Bambu Lab. (n.d.-k). PLA Basic technical data sheet, version 3 [PDF]. https://store.bblcdn.eu/s8/default/073e722a4aa44f7cbfdc419d597475cc/Bambu_PLA_Basic_Technical_Data_Sheet.pdf

Bambu Lab. (n.d.-l). PLA-CF. https://eu.store.bambulab.com/nl/products/pla-cf

Bambu Lab. (n.d.-m). PLA-CF technical data sheet, version 2 [PDF]. https://store.bblcdn.eu/s8/default/aefa8303ad8d40248b0d86dfdad46518/Bambu_PLA-CF_Technical_Data_Sheet_V3.pdf

Bellehumeur, C., Li, L., Sun, Q., & Gu, P. (2004). Modeling of bond formation between polymer filaments in the fused deposition modeling process. *Journal of Manufacturing Processes*, *6*(2), 170–178. https://doi.org/10.1016/S1526-6125(04)70071-7

Bolmin, O., Young, B., Leathe, N., Noell, P. J., & Boyce, B. L. (2023). Interlocking metasurfaces. *Journal of Materials Science*, *58*(1), 411–419. https://doi.org/10.1007/s10853-022-08015-9

Brown, N. K., Young, B., Clark, B., Bolmin, O., Boyce, B. L., & Noell, P. J. (2023). Optimized design of interlocking metasurfaces. *Materials and Design*, *233*. https://doi.org/10.1016/j.matdes.2023.112272

Budziński, B., & Federowicz, K. (2025). Evaluation of PLA and PETG as 3D-Printed Reference Materials for Compressive Strength Testing. *Materials*, *18*(16). https://doi.org/10.3390/ma18163794

Davaasambuu, K., Dong, Y., Pramanik, A., & Basak, A. K. (2025, July). Mechanisms and Performance of Composite Joints Through Adhesive and Interlocking Means—A Review. https://doi.org/10.3390/jcs9070359

Dickson, A. N., Barry, J. N., McDonnell, K. A., & Dowling, D. P. (2017). Fabrication of continuous carbon, glass and Kevlar fibre reinforced polymer composites using additive manufacturing. *Additive Manufacturing*, *16*, 146–152. https://doi.org/10.1016/j.addma.2017.06.004

Dimas, M., Oikonomopoulou, F., & Bilow, M. (2022). IN BETWEEN: An Interlayer Material Study Towards Circular, Dry-Assembly, Interlocking Cast Glass Block Structures. *Challenging Glass Conference 8: Conference on Architectural and Structural Applications of Glass, CGC 2022*. https://doi.org/10.47982/cgc.8.416

Elegoo. (n.d.). PETG-GF. https://eu.elegoo.com/products/petg-gf-filament-1-75mm-colored-1kg

EurocodeApplied.com. (n.d.). Calculation of wind peak velocity pressure - Eurocode 1. https://eurocodeapplied.com/design/en1991/wind-peak-velocity-pressure

Gloyer, P., Schek, L. N., Flöttmann, H. L., Wüst, P., & Völlmecke, C. (2023). Extrusion-Based Additive Manufacturing-Driven Design and Testing of the Snapping Interlocking Metasurface Mechanism ShroomLock. *Inventions 2023, Vol. 8, Page 137*, *8*(6), 137. https://doi.org/10.3390/INVENTIONS8060137

Grgić, I., Karakašić, M., Glavaš, H., & Konjatić, P. (2023). Accuracy of FDM PLA Polymer 3D Printing Technology Based on Tolerance Fields. *Processes*, *11*(10). https://doi.org/10.3390/pr11102810

Guessasma, S., Belhabib, S., & Nouri, H. (2019). Printability and Tensile Performance of 3D Printed Polyethylene Terephthalate Glycol Using Fused Deposition Modelling. *Polymers 2019, Vol. 11, Page 1220*, *11*(7), 1220. https://doi.org/10.3390/POLYM11071220

Korte, C., & Quodbach, J. (2018). Formulation development and process analysis of drug-loaded filaments manufactured via hot-melt extrusion for 3D-printing of medicines. *Pharmaceutical Development and Technology*, *23*(10), 1117–1127. https://doi.org/10.1080/10837450.2018.1433208

Kováčová, M., Kozakovičová, J., Procházka, M., Janigová, I., Vysopal, M., Černičková, I., Krajčovič, J., & Špitalský, Z. (2020). Novel hybrid PETG composites for 3D printing. *Applied Sciences (Switzerland)*, *10*(9). https://doi.org/10.3390/app10093062

Lalegani Dezaki, M., Mohd Ariffin, M. K. A., & Hatami, S. (2021). An overview of fused deposition modelling (FDM): research, development and process optimisation. *Rapid Prototyping Journal*, *27*(3), 562–582. https://doi.org/10.1108/RPJ-08-2019-0230

Li, F., Liu, Y., Qu, C. B., Xiao, H. M., Hua, Y., Sui, G. X., & Fu, S. Y. (2015). Enhanced mechanical properties of short carbon fiber reinforced polyethersulfone composites by graphene oxide coating. *Polymer*, *59*, 155–165. https://doi.org/10.1016/j.polymer.2014.12.067

Lieneke, T., Denzer, V., Adam, G. A., & Zimmer, D. (2016). Dimensional Tolerances for Additive Manufacturing: Experimental Investigation for Fused Deposition Modeling. *Procedia CIRP*, *43*, 286–291. https://doi.org/10.1016/j.procir.2016.02.361

Naat, N., Hajlaoui, K., Mezlini, S., & da Silva, L. F. (2025). Enhanced mechanical interlocking in adhesive joints through precision-engineered surface patterns on 3D-printed PLA adherends. *International Journal of Adhesion and Adhesives*, *142*. https://doi.org/10.1016/j.ijadhadh.2025.104132

Ngo, T. D., Kashani, A., Imbalzano, G., Nguyen, K. T., & Hui, D. (2018). Additive manufacturing (3D printing): A review of materials, methods, applications and challenges. *Composites Part B: Engineering*, *143*, 172–196. https://doi.org/10.1016/J.COMPOSITESB.2018.02.012

Novák, M., Boleslavská, T., Grof, Z., Waněk, A., Zadražil, A., Beránek, J., Kovačík, P., & Štěpánek, F. (2018). Virtual Prototyping and Parametric Design of 3D-Printed Tablets Based on the Solution of Inverse Problem. *AAPS PharmSciTech 2018 19:8*, *19*(8), 3414–3424. https://doi.org/10.1208/S12249-018-1176-Z

Oikonomopoulou, F., Bristogianni, T., Barou, L., Veer, F. A., & Nijsse, R. (2018). The potential of cast glass in structural applications. Lessons learned from large-scale castings and state-of-the art load-bearing cast glass in architecture. *Journal of Building Engineering*, *20*, 213–234. https://doi.org/10.1016/j.jobe.2018.07.014

Oikonomopoulou, F., Bristogianni, T., van der Velden, M., & Ikonomidis, K. (2022). The adhesively-bonded glass brick system of the Qaammat Pavilion in Greenland: From research to realization. *Architecture, Structures and Construction*, *2*(1), 39–62. https://doi.org/10.1007/s44150-022-00031-2

Oikonomopoulou, F. (2019). *Unveiling the third dimension of glass Solid cast glass components and assemblies for structural applications* (tech. rep.).

Oikonomopoulou, F., & Bristogianni, T. (2022). Adhesive solutions for cast glass assemblies: ground rules emerging from built case studies on adhesive selection and experimental validation. *Challenging Glass 8: Conference on Architectural and Structural Applications of Glass, CGC 2022*, 293–317. https://doi.org/10.1007/s40940-022-00178-w

Oikonomopoulou, F., Bristogianni, T., Barou, L., Jacobs, E., Frigo, G., Veer, F. A., & Nijsse, R. (2018). A novel, demountable structural glass system out of dry-assembly, interlocking cast glass components. *Challenging Glass 6: Conference on Architectural and Structural Applications of Glass, CGC 2018 - Proceedings*, 11–26. https://doi.org/10.7480/cgc.6.2118

Oikonomopoulou, F., Bristogianni, T., Barou, L., & Veer, F. (2019). Dry interlayers out of cast polyurethane rubber for interlocking cast glass structures: Experimental exploration and validation. *Advances in Engineering Materials, Structures and Systems: Innovations, Mechanics and Applications - Proceedings of the 7th International Conference on Structural Engineering, Mechanics and Computation, 2019*, 1709–1714. https://doi.org/10.1201/9780429426506-295

Oikonomopoulou, F., Bristogianni, T., Barou, L., & Veer, F. (2018). Interlocking cast glass components, Exploring a demountable dry-assembly structural glass system. *Heron*, *63*(1/2). https://www.researchgate.net/publication/329917259

Oikonomopoulou, F., DeBrincat, G., & Fuhrmann, S. (2023). Glass and circularity. *Glass Structures and Engineering*, *8*(2), 165–166. https://doi.org/10.1007/s40940-023-00230-3

Oikonomopoulou, F., Massimino, D., Guha, S., Bigler, T., Van Kessel, E., Bristogianni, T., & Becker, K. (2025). Reversible joinery methods for full glass vaults made of cast or 3D printed glass components. *Proceedings of the IASS Annual Symposium 2025: The living past as a source of innovation*.

Parascho, S., Han, I. X., Beghini, A., Miki, M., Walker, S., Bruun, E. P. G., Adriaenssens, S., Parascho, S., Han, I. X., Beghini, A., Miki, M., Walker, S.-T., Bruun, E. P. G., & Adriaenssens, S. (2021). LightVault: A Design and Robotic Fabrication Method for Complex Masonry Structures. *Advances in Architectural Geometry*, *25*.

Parascho, S., Han, I. X., Walker, S., Beghini, A., Bruun, E. P. G., & Adriaenssens, S. (2020). Robotic vault: a cooperative robotic assembly method for brick vault construction. *Construction Robotics*, *4*(3-4), 117–126. https://doi.org/10.1007/s41693-020-00041-w

Parulski, C., Jennotte, O., Lechanteur, A., & Evrard, B. (2021). Challenges of fused deposition modeling 3D printing in pharmaceutical applications: Where are we now? *Advanced Drug Delivery Reviews*, *175*, 113810. https://doi.org/10.1016/J.ADDR.2021.05.020

Penumakala, P. K., Santo, J., & Thomas, A. (2020). A critical review on the fused deposition modeling of thermoplastic polymer composites. *Composites Part B: Engineering*, *201*, 108336. https://doi.org/10.1016/J.COMPOSITESB.2020.108336

Peralta Marino, G., De la Pierre, S., Salvo, M., Díaz Lantada, A., & Ferraris, M. (2022). Modelling, additive layer manufacturing and testing of interlocking structures for joined components. *Scientific Reports*, *12*(1). https://doi.org/10.1038/s41598-022-06521-z

Rasal, R. M., & Hirt, D. E. (2009). Toughness decrease of PLA-PHBHHx blend films upon surface-confined photopolymerization. *Journal of Biomedical Materials Research - Part A*, *88*(4), 1079–1086. https://doi.org/10.1002/jbm.a.32009

Rimkus, A., Šalna, R., & Gribniak, V. (2024). Evaluating the PLA aging effects on the mechanical performance of 3D-printed components. *Proceedings of International Structural Engineering and Construction*, *11*(2). https://doi.org/10.14455/ISEC.2024.11(2).SUS-01

Solomon, I. J., Sevvel, P., & Gunasekaran, J. (2021). A review on the various processing parameters in FDM. *Materials Today: Proceedings*, *37*(Part 2), 509–514. https://doi.org/10.1016/J.MATPR.2020.05.484

Turner, B. N., & Gold, S. A. (2013). A review of melt extrusion additive manufacturing processes: II. Materials, dimensional accuracy, and surface roughness. https://doi.org/10.1108/RPJ-02-2013-0017

Van Kessel, E. C. (2025). *Glass Unlocked: Designing an Additively Manufactured Reversible Interlayer Connection for Structural Use of Free-Form Glass Units* [Doctoral dissertation, TU Delft].

Wang, X., Jiang, M., Zhou, Z., Gou, J., & Hui, D. (2017, February). 3D printing of polymer matrix composites: A review and prospective. https://doi.org/10.1016/j.compositesb.2016.11.034

Wayken. (2023, March). Snap Fit Joints: Types, Benefits, and Best Practices. https://waykenrm.com/blogs/snap-fit-joints/

Xi Han, I., P.G. Bruun, E., Marsh, S., Tavano, M., Adriaessens, S., & Parascho, S. (2023). From Concept to Construction. *Proceedings of the 40th Annual Conference of the Association of Computer Aided Design in Architecture (ACADIA)*, *1*, 614–623. https://doi.org/10.52842/conf.acadia.2020.1.614

Zotti, A., Paduano, T., Napolitano, F., Zuppolini, S., Zarrelli, M., & Borriello, A. (2025). Fused Deposition Modeling of Polymer Composites: Development, Properties and Applications. *Polymers*, *17*(8), 1054. https://doi.org/10.3390/POLYM17081054

A

Planning

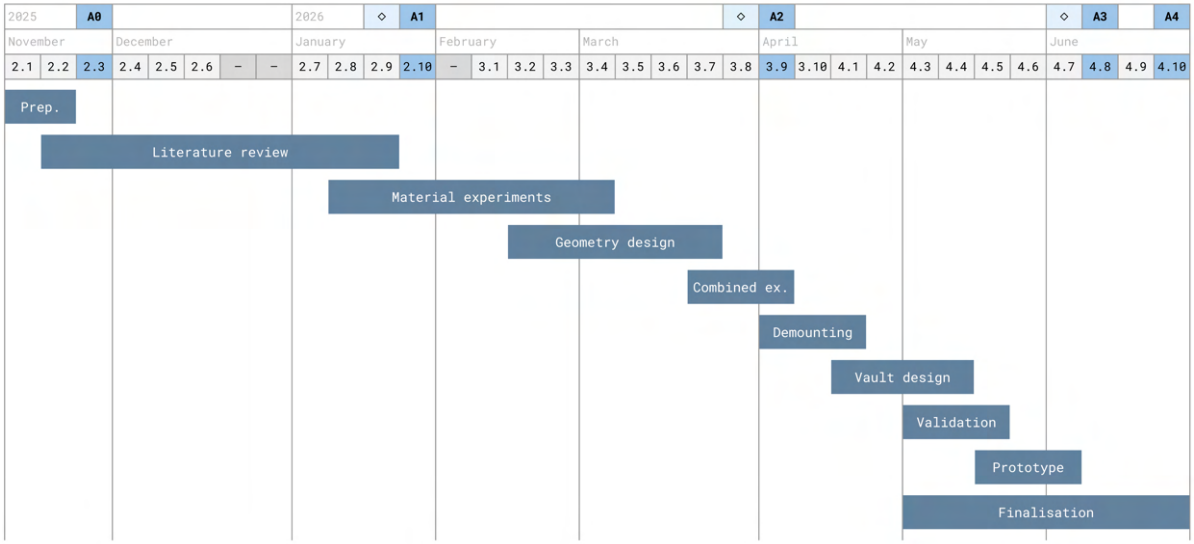
2025
A0
2026
A1
A2
A3
A4
November
December
January
February
March
April
May
June
2.1 2.2 2.3 2.4 2.5 2.6 – – 2.7 2.8 2.9 2.10 – 3.1 3.2 3.3 3.4 3.5 3.6 3.7 3.8 3.9 3.10 4.1 4.2 4.3 4.4 4.5 4.6 4.7 4.8 4.9 4.10
Prep.
Literature review
Material experiments
Geometry design
Combined ex.
Demounting
Vault design
Validation
Prototype
Finalisation

B

Material experiment specimens

Note: Not all fabricated specimens were photographed prior to evaluation. The image presented in this appendix therefore only document the ones available from the material optimisation experiments.

B.1. PLA

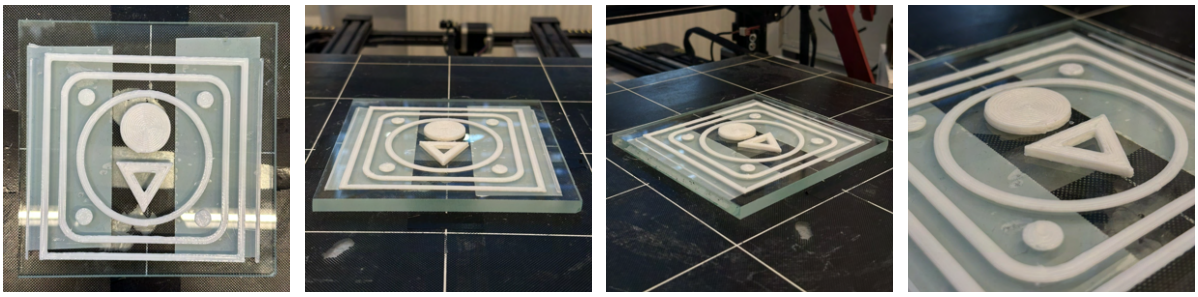

Figure B.1: PLA - Sample 0

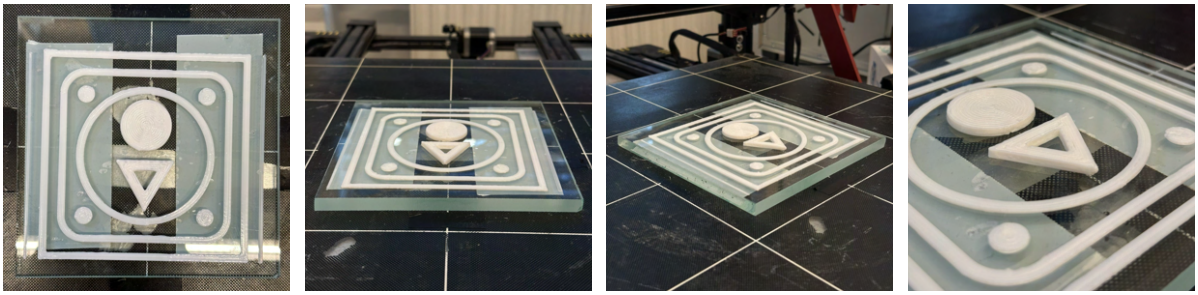

Figure B.2: PLA - Sample 1

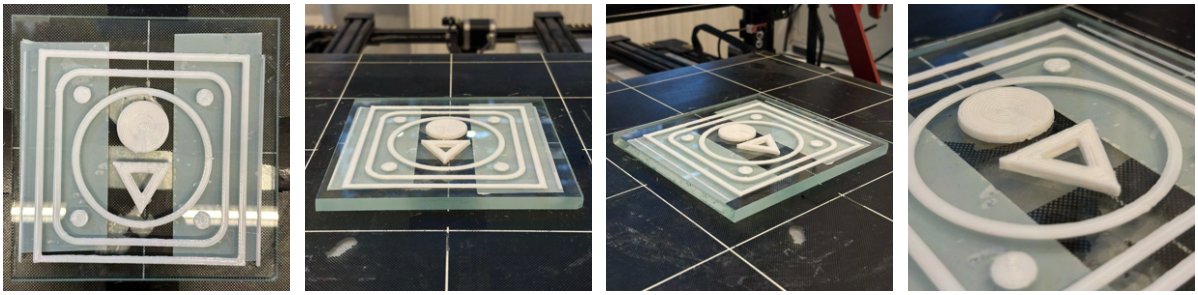

Figure B.3: PLA - Sample 2

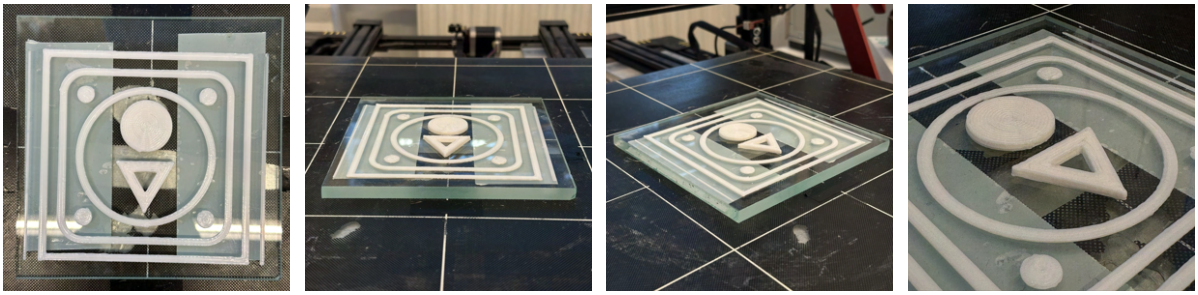

Figure B.4: PLA - Sample 3

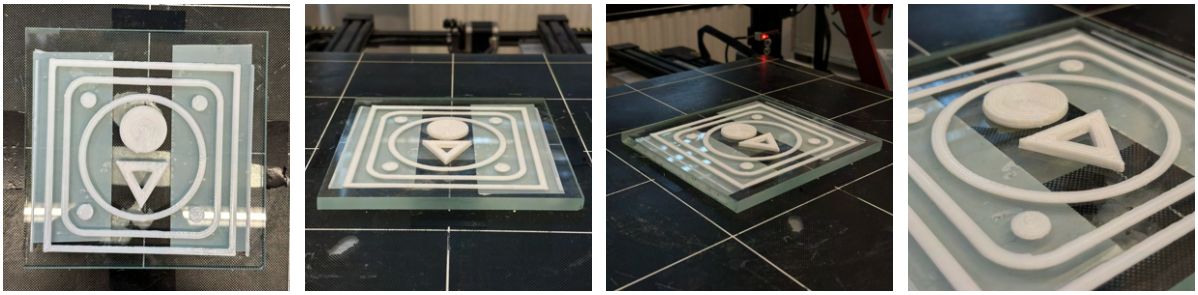

Figure B.5: PLA - Sample 6

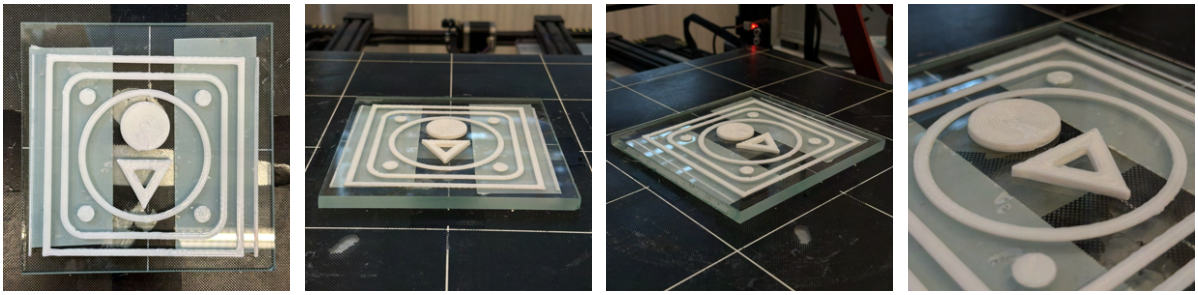

Figure B.6: PLA - Sample 8

B.2. PLA-CF

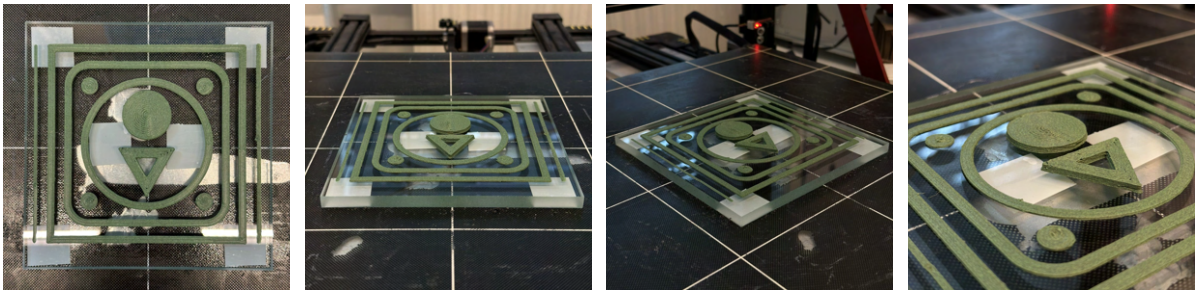

Figure B.7: PLA-CF - Sample 0

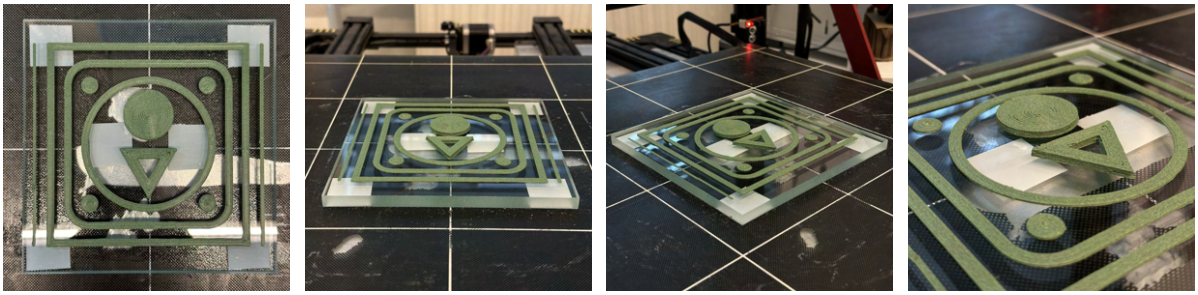

Figure B.8: PLA-CF - Sample 1

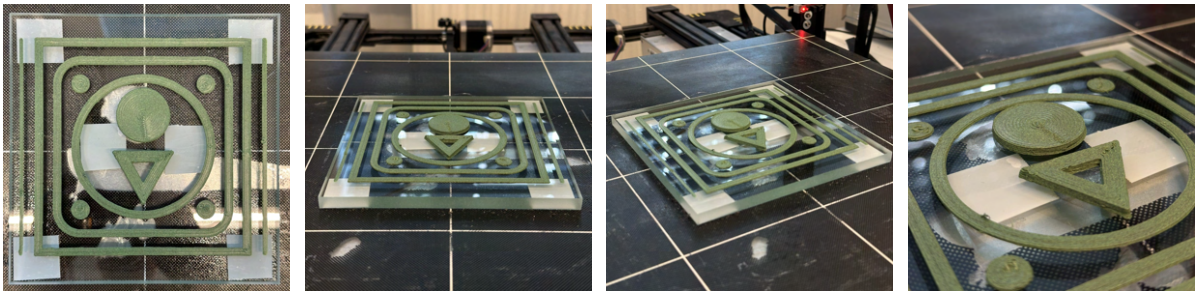

Figure B.9: PLA-CF - Sample 2

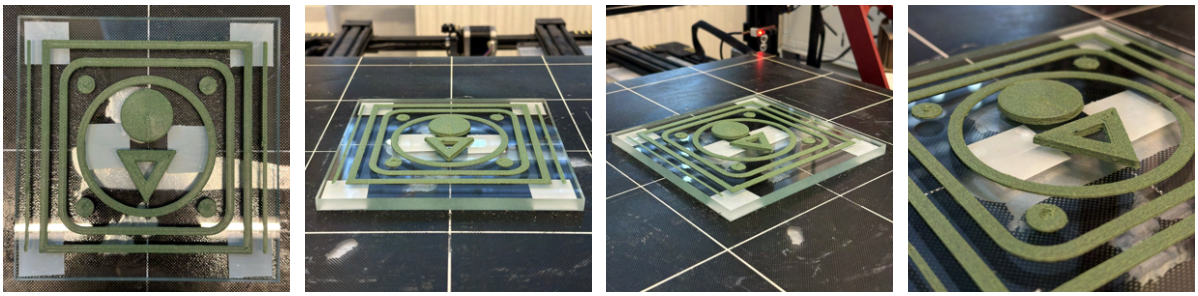

Figure B.10: PLA-CF - Sample 3

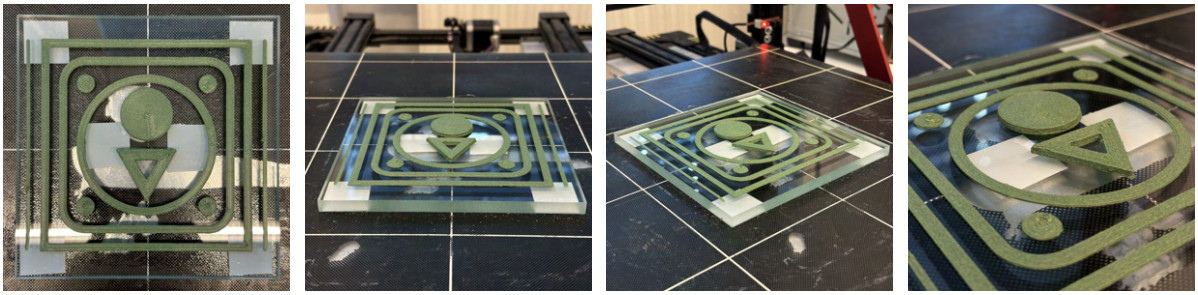

Figure B.11: PLA-CF - Sample 4

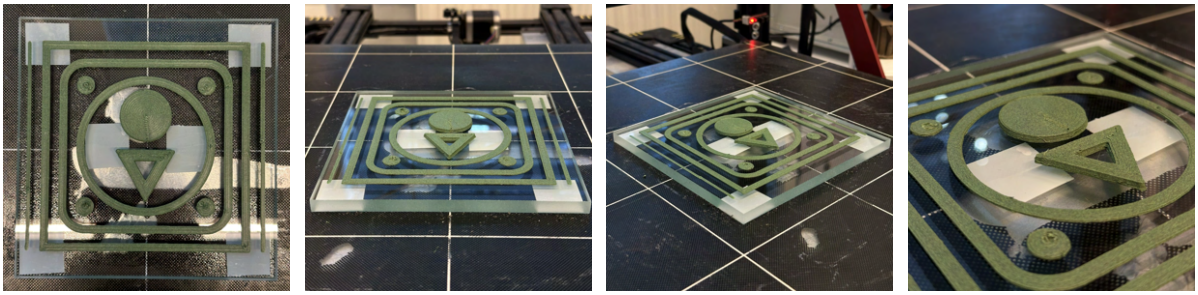

Figure B.12: PLA-CF - Sample 5

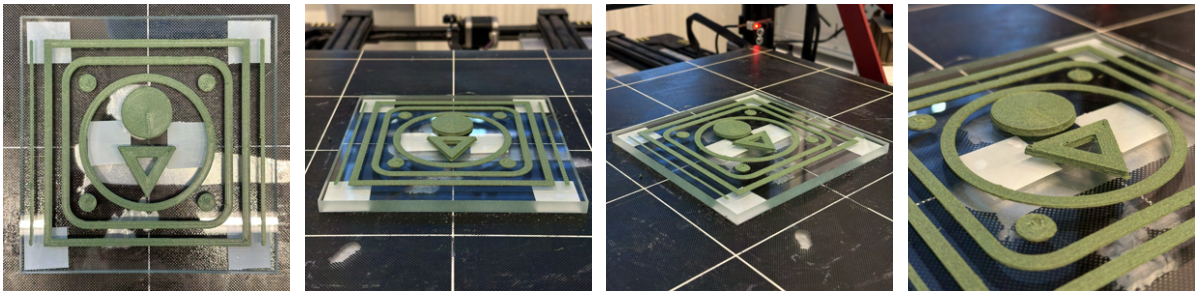

Figure B.13: PLA-CF - Sample 6

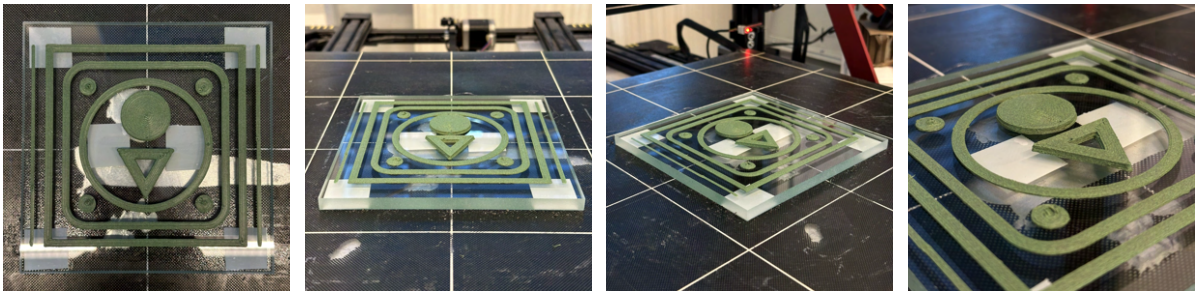

Figure B.14: PLA-CF - Sample 7

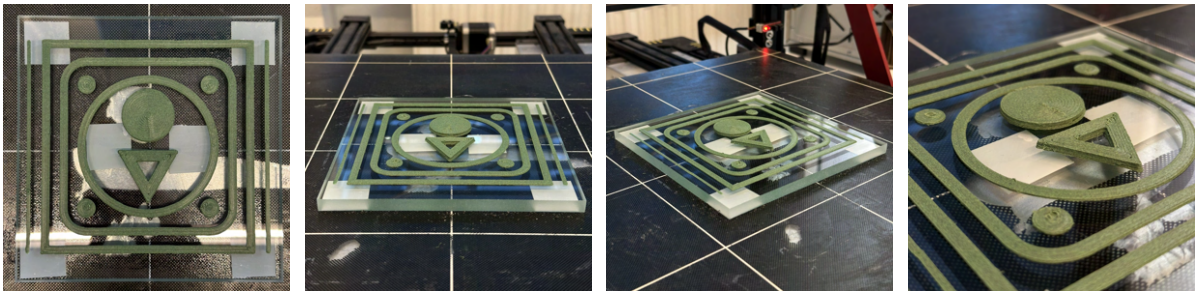

Figure B.15: PLA-CF - Sample 8

B.3. PETG-HF

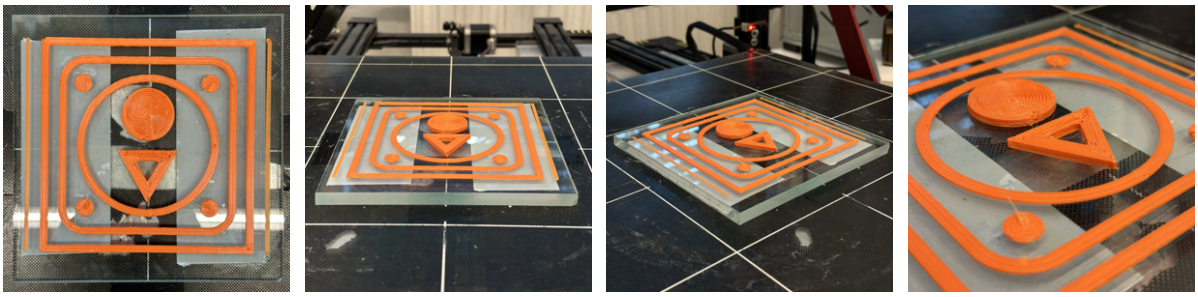

Figure B.16: PETG-HF - Sample 2

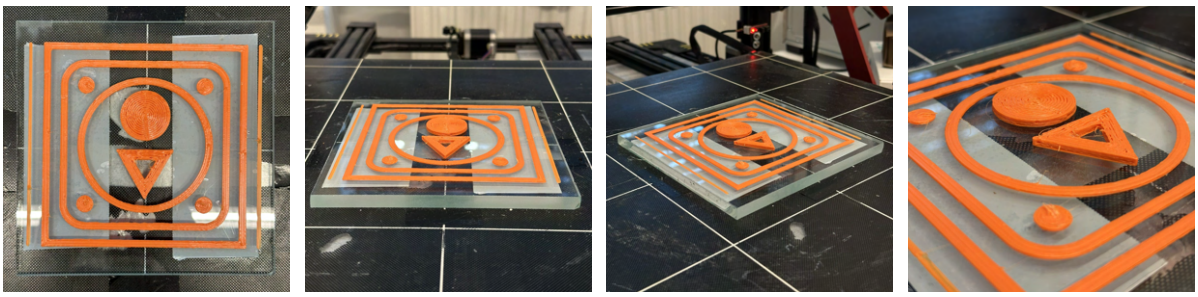

Figure B.17: PETG-HF - Sample 3

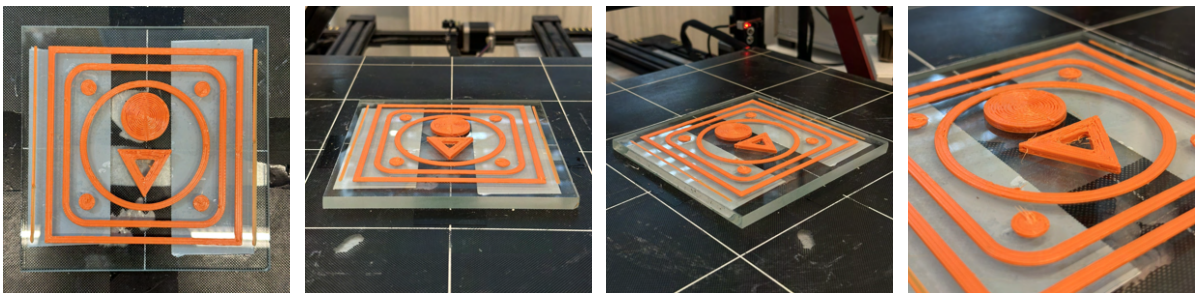

Figure B.18: PETG-HF - Sample 4

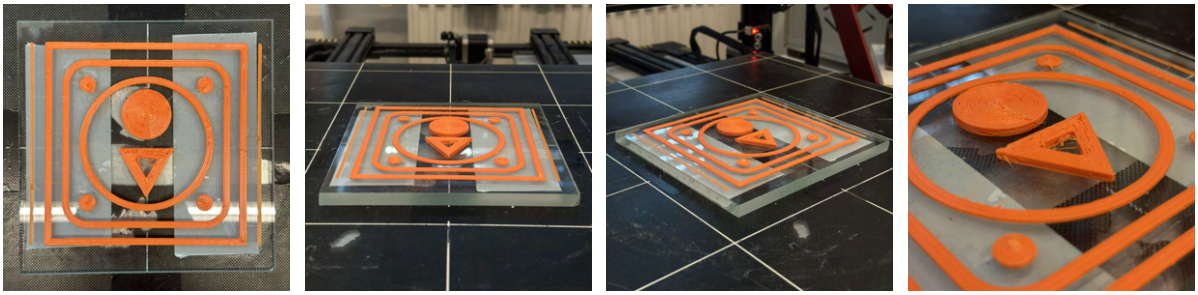

Figure B.19: PETG-HF - Sample 5

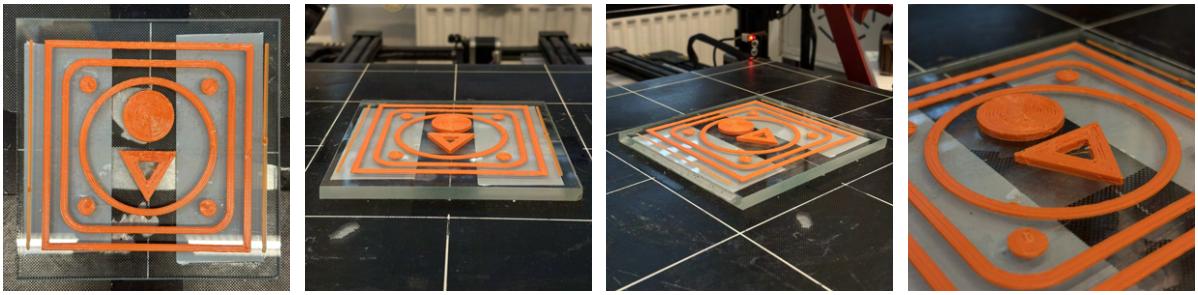

Figure B.20: PETG-HF - Sample 6

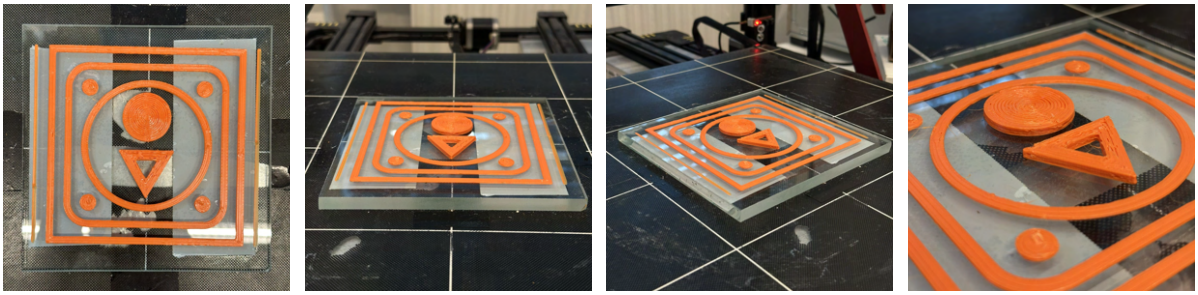

Figure B.21: PETG-HF - Sample 7

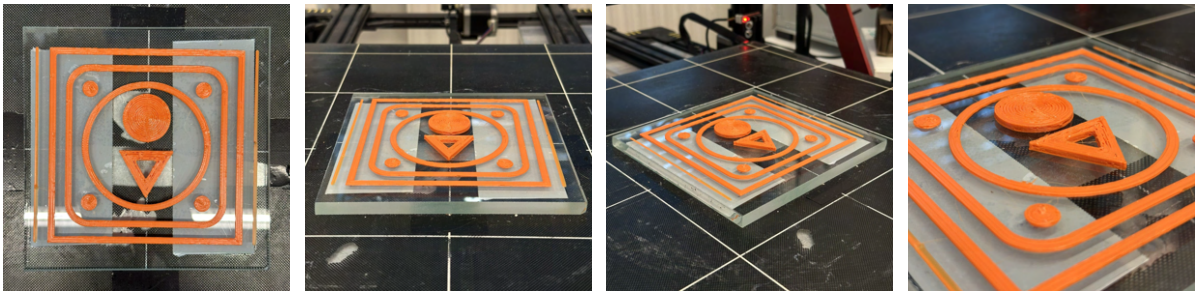

Figure B.22: PETG-HF - Sample 8

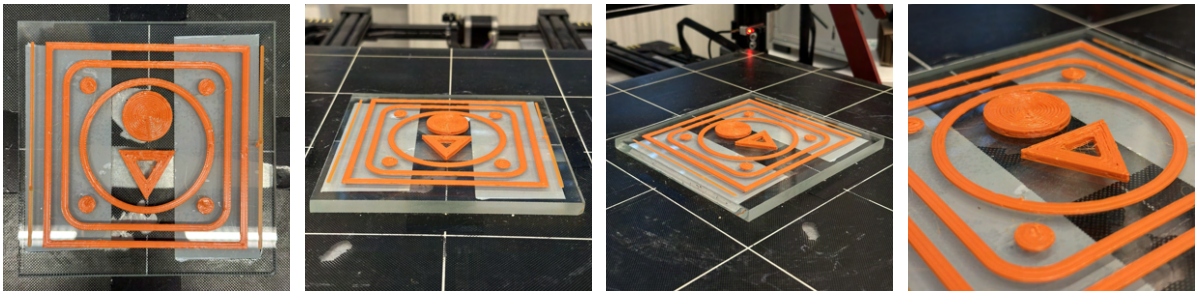

Figure B.23: PETG-HF - Sample 9

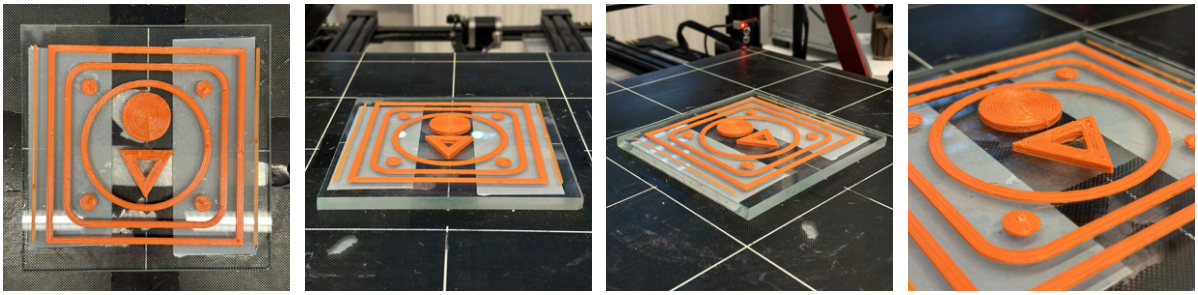

Figure B.24: PETG-HF - Sample 10

B.4. PETG-GF

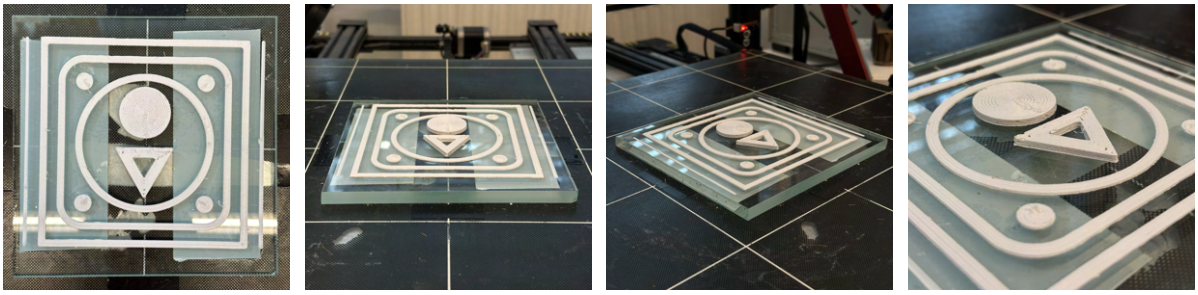

Figure B.25: PETG-GF - Sample 0

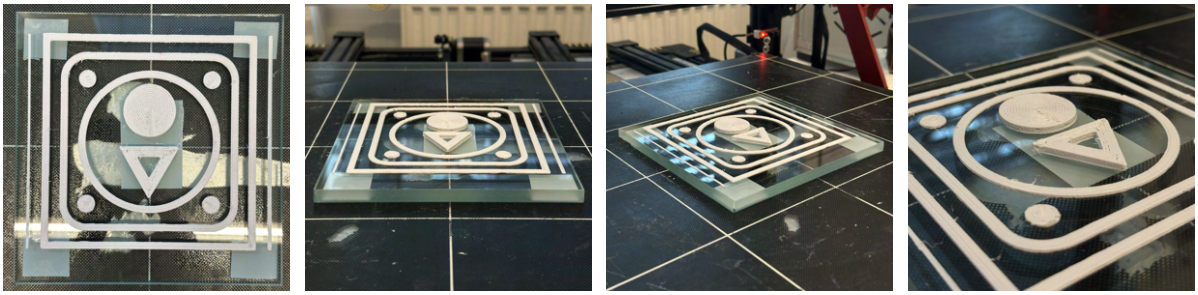

Figure B.26: PETG-GF - Sample 4

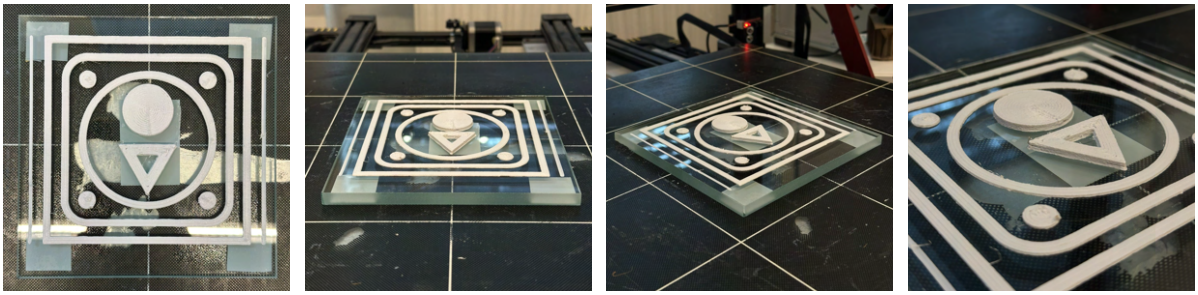

Figure B.27: PETG-GF - Sample 5

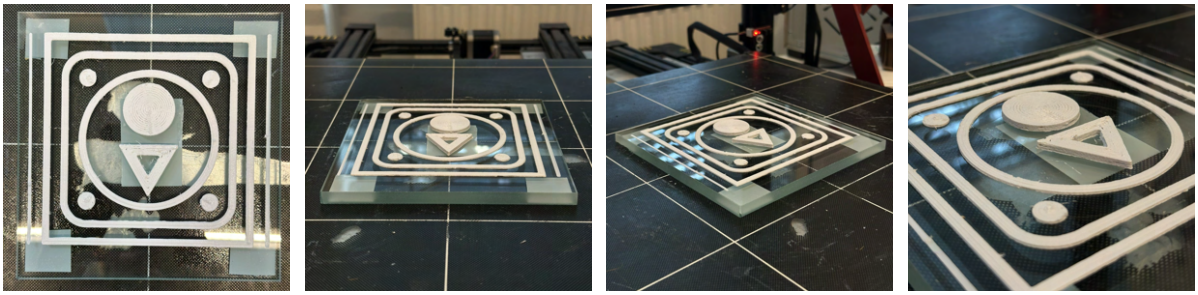

Figure B.28: PETG-GF - Sample 6

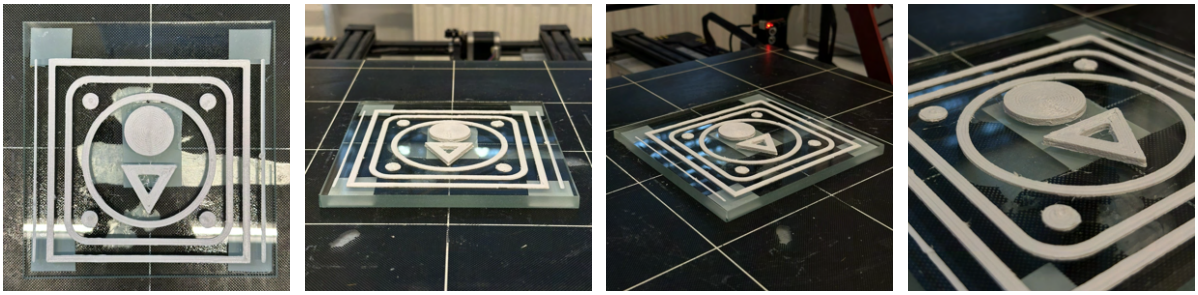

Figure B.29: PETG-GF - Sample 7

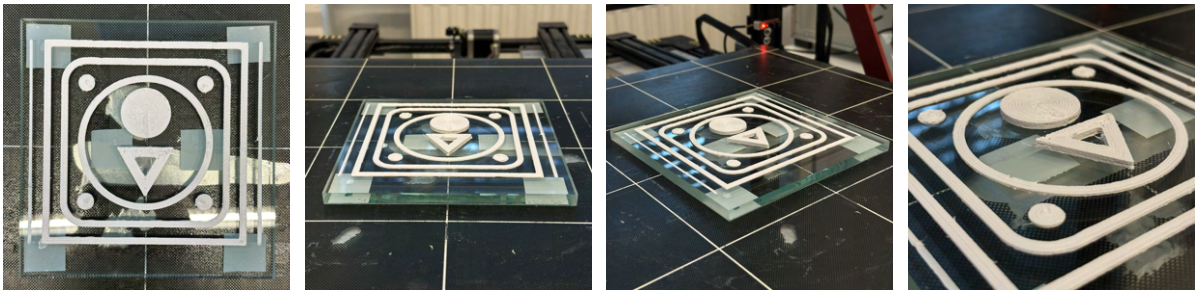

Figure B.30: PETG-GF - Sample 8

B.5. PETG-CF

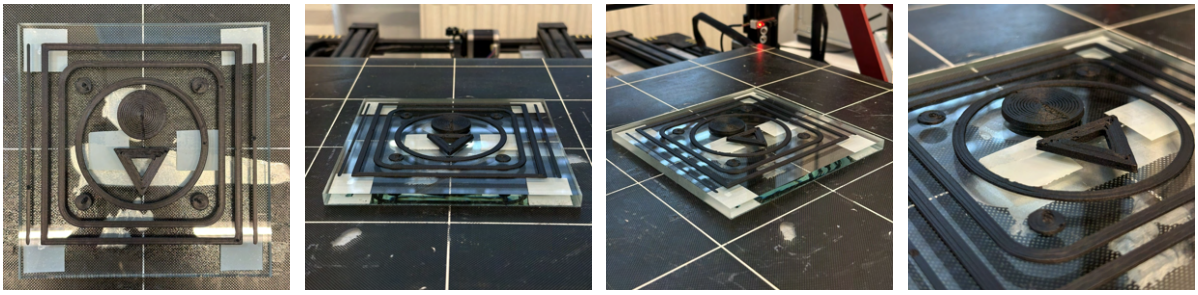

Figure B.31: PETG-CF - Sample 0

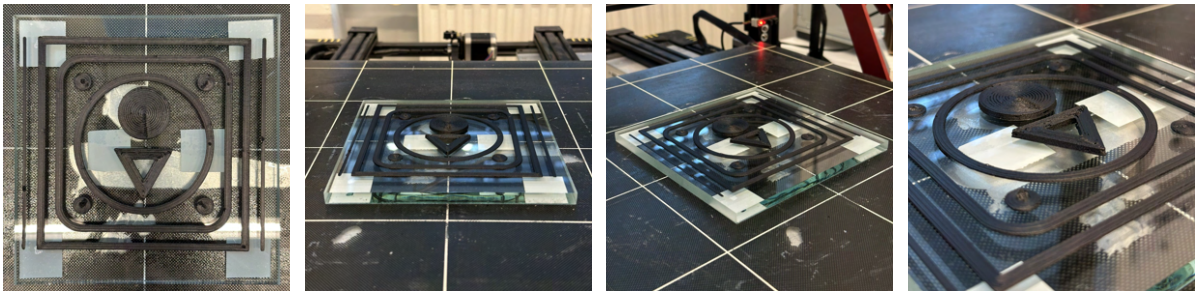

Figure B.32: PETG-CF - Sample 2

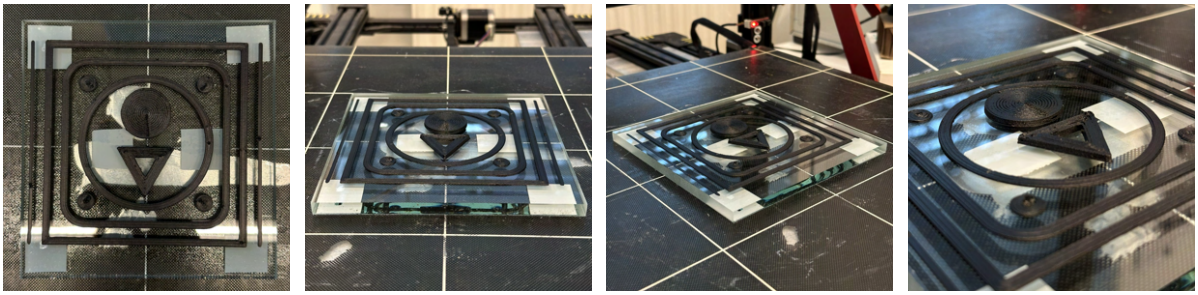

Figure B.33: PETG-CF - Sample 3

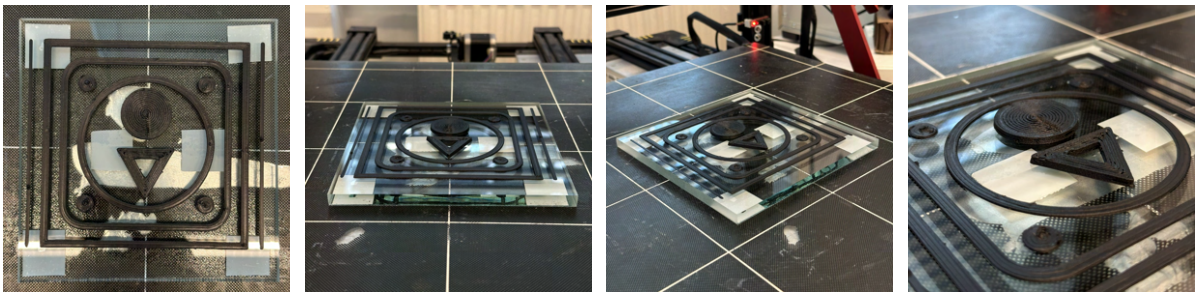

Figure B.34: PETG-CF - Sample 4

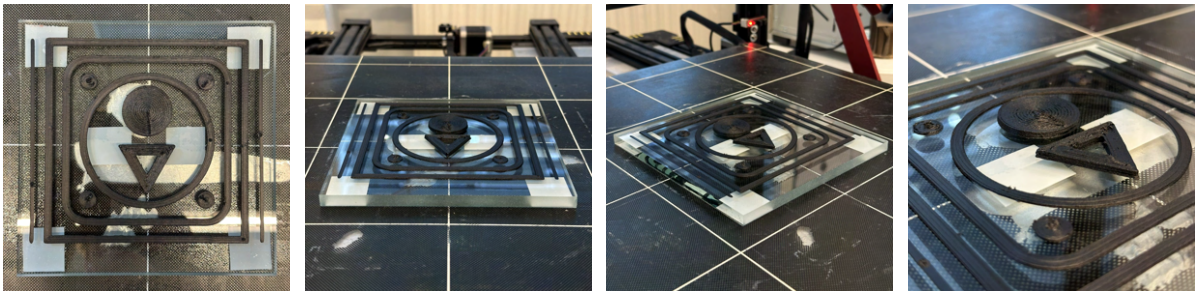

Figure B.35: PETG-CF - Sample 6

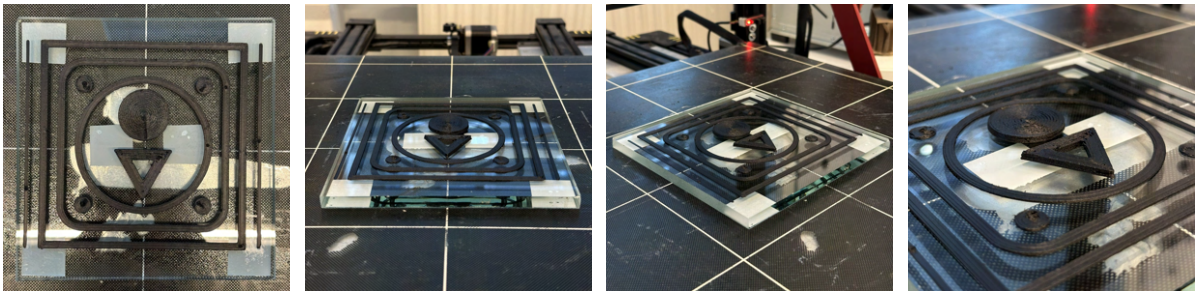

Figure B.36: PETG-CF - Sample 7

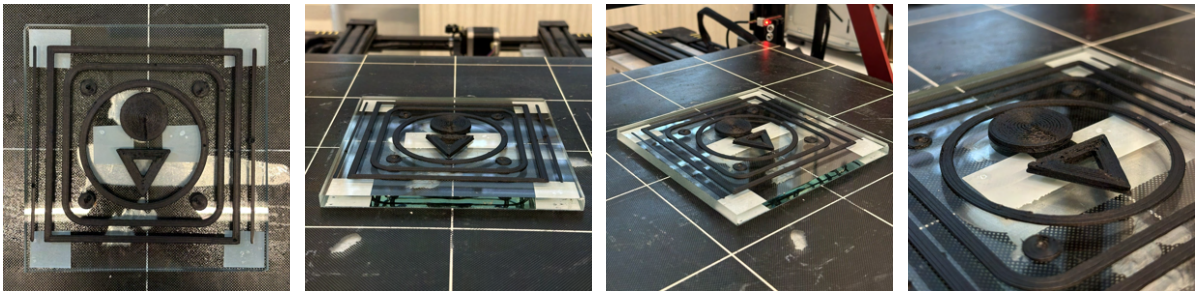

Figure B.37: PETG-CF - Sample 8

B.6. PET-CF

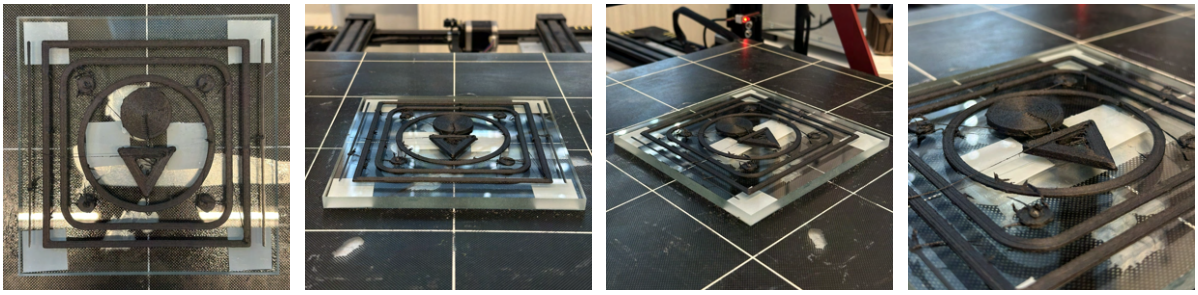

Figure B.38: PET-CF - Sample 0

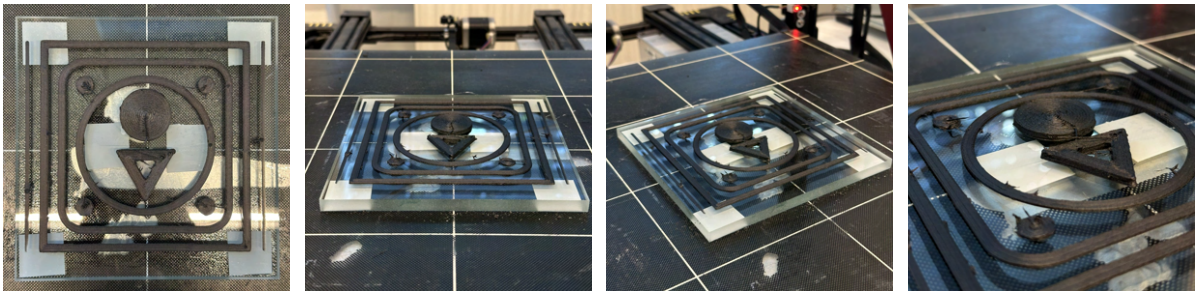

Figure B.39: PET-CF - Sample 1

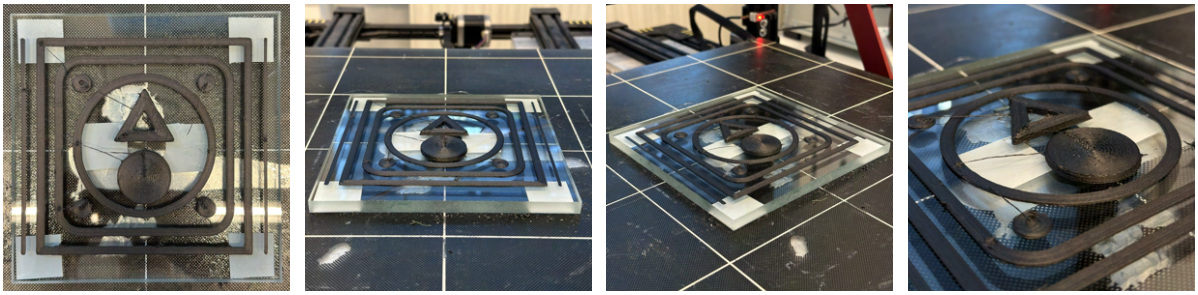

Figure B.40: PET-CF - Sample 2

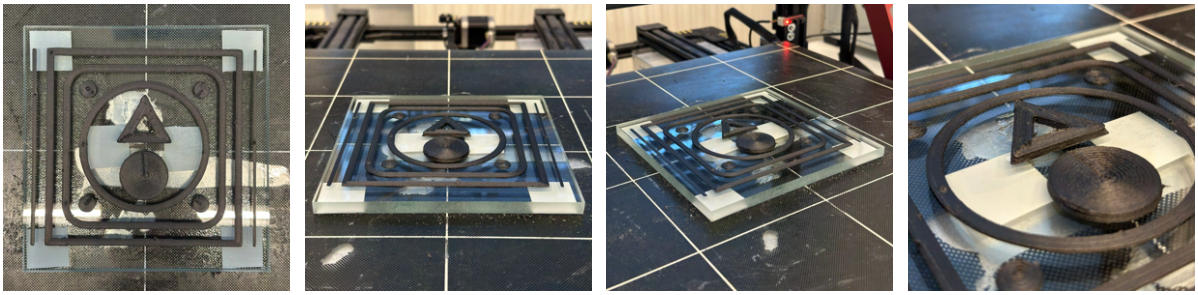

Figure B.41: PET-CF - Sample 4

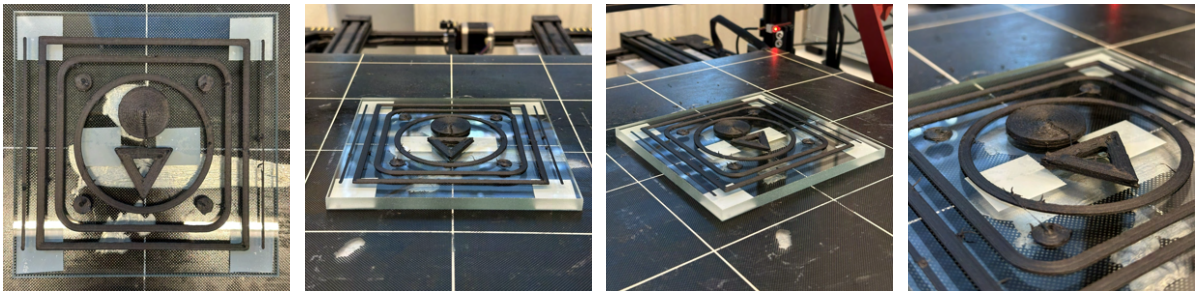

Figure B.42: PET-CF - Sample 5

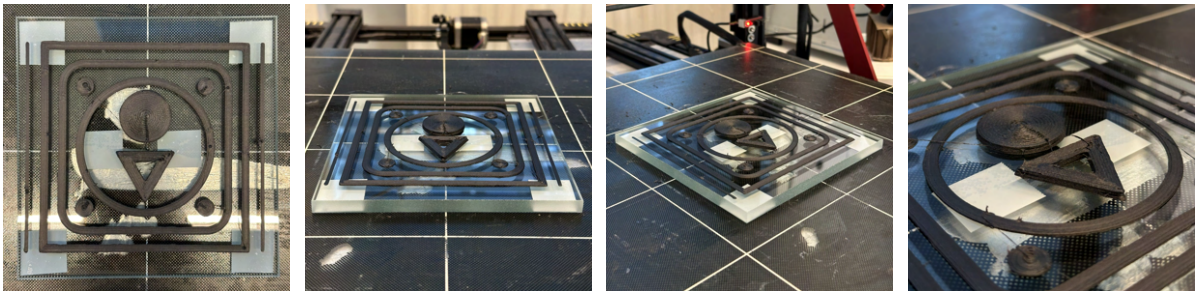

Figure B.43: PET-CF - Sample 6

C

Vault drawings

Top view

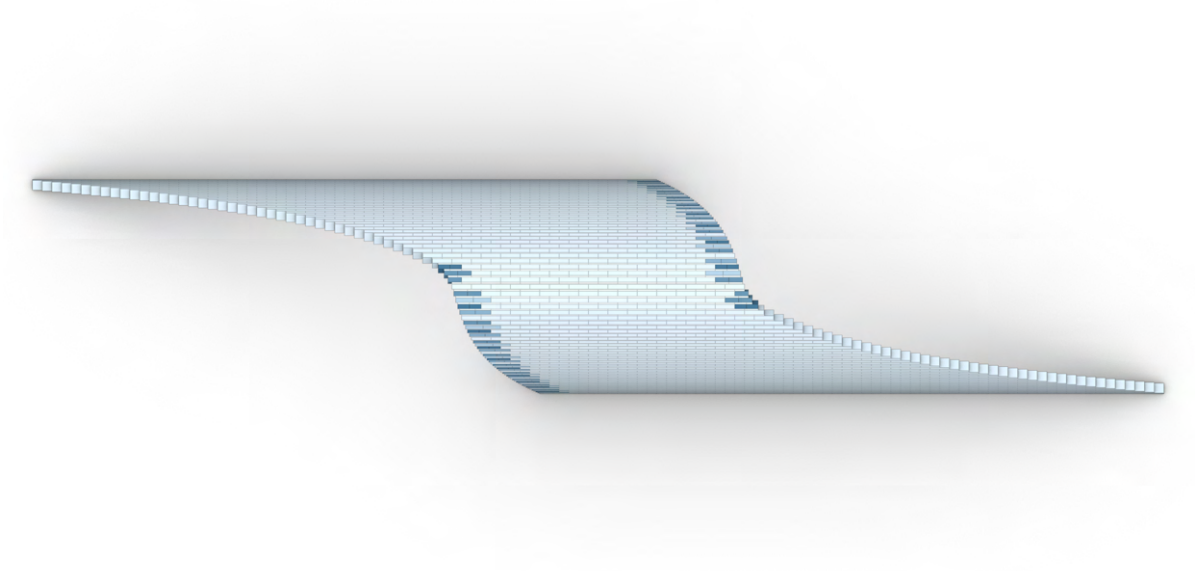

Elevation

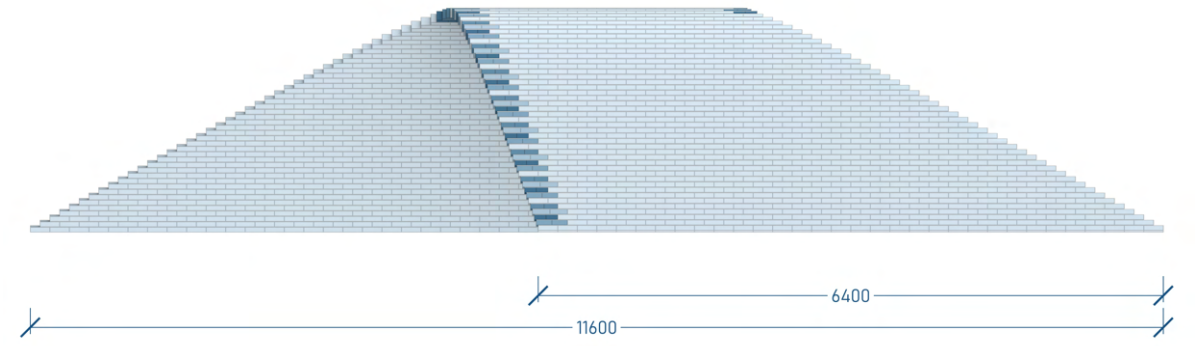

Sections

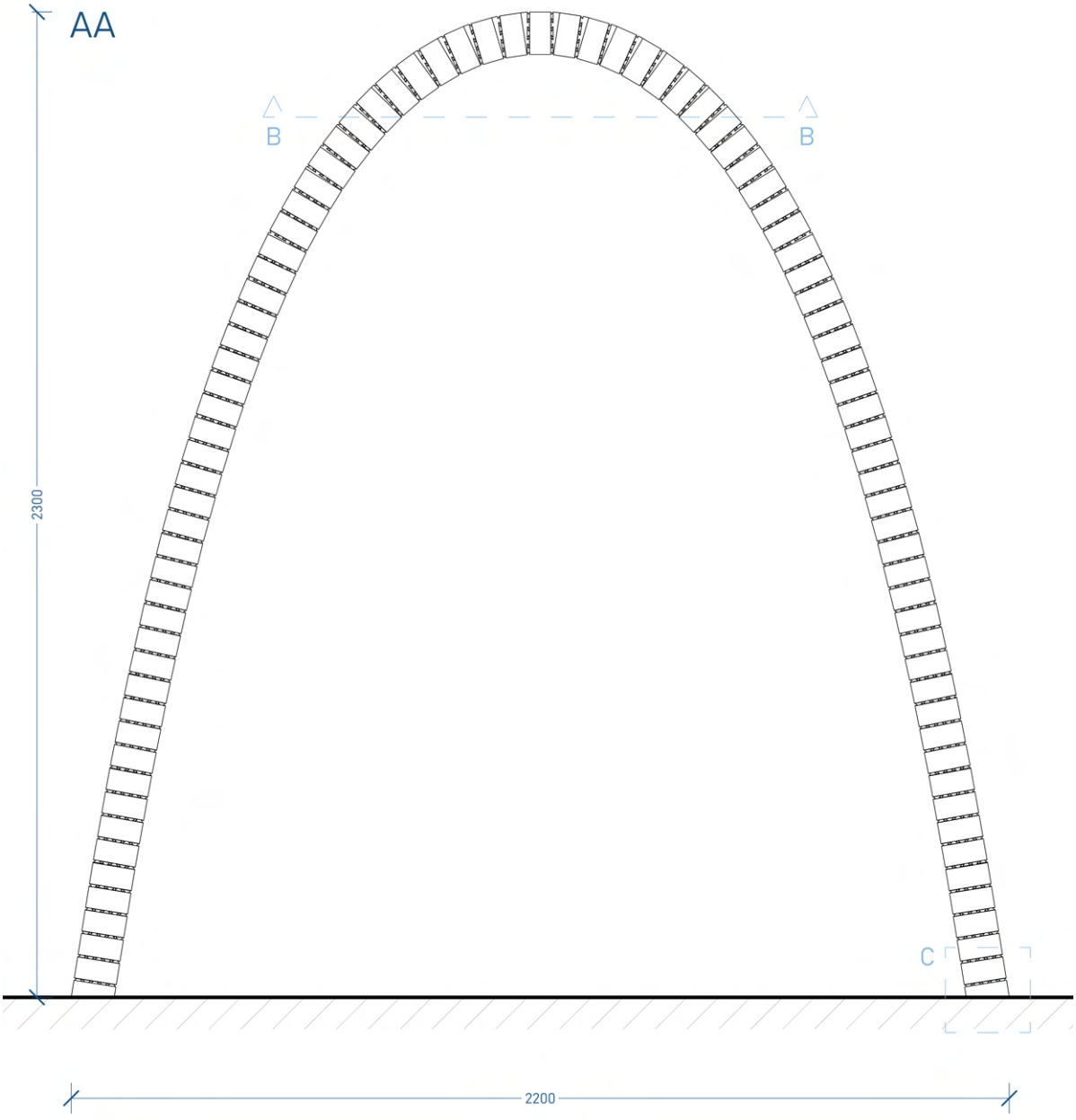

Details

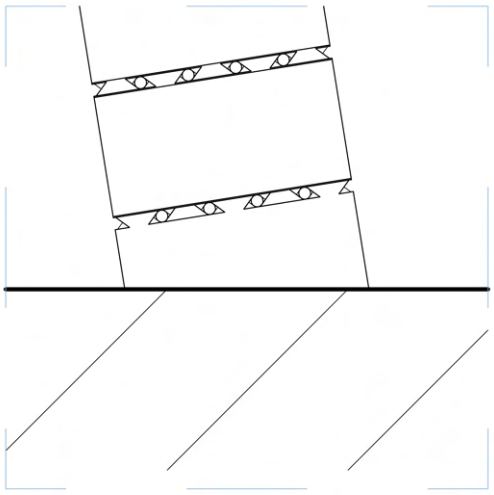

C

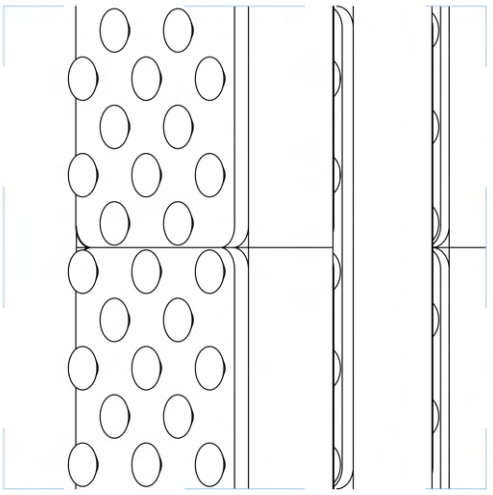

D

D

Wind load calculation & analysis

Assumptions

Basic wind velocity:	v_b	=	27.0 m/s
Terrain category:		=	II
Reference height:	z_e	=	2.3 m
Orography factor at reference height:	$c_0(z_e)$	=	1.0
Air density:	ρ	=	1.25 kg/m^3
Roughness length:	z_0	=	0.050 m
Minimum height:	z_{min}	=	2.0 m

D.1. Calculation of wind peak velocity pressure

Terrain factor:

$$k_r = 0.19 \cdot (z_0/z_{0,II})^{0.07}$$
$$= 0.19 \cdot (0.050\,m/0.050\,m)^{0.07} = 0.1900$$

Roughness factor:

$$c_r(z_e) = k_r \cdot \ln(\max\{z_e, z_{min}\}/z_0)$$
$$= 0.1900 \cdot \ln(\max\{2.300\,m, 2.0\,m\}/0.050\,m) = 0.7274$$

Mean wind velocity:

$$v_m(z_e) = c_r(z_e) \cdot c_0(z_e) \cdot v_b$$
$$= 0.7274 \cdot 1.000 \cdot 27.00\,m/s = 19.64\,m/s$$

Turbulence intensity:

$$I_v(z_e) = k_l/[\,c_0(z_e) \cdot \ln(\max\{z_e, z_{min}\}/z_0)\,]$$
$$= 1.000/[\,1.000 \cdot \ln(\max\{2.300\,m, 2.0\,m\}/0.050\,m)\,] = 0.2612$$

Basic velocity pressure:

$$q_b = (1/2) \cdot \rho \cdot v_b^2$$
$$= (1/2) \cdot 1.25\,kg/m^3 \cdot (27.00\,m/s)^2 = 0.456\,kN/m^2$$

Peak velocity pressure:

$$q_p(z_e) = (1 + 7 \cdot I_v(z_e)) \cdot (1/2) \cdot \rho \cdot v_m(z_e)^2$$
$$= (1 + 7 \cdot 0.2612) \cdot (1/2) \cdot 1.25\,kg/m^3 \cdot (19.64\,m/s)^2$$
$$\Rightarrow \mathbf{q_p(z_e) = 0.682\,kN/m^2}$$

D.2. Karamba FEA

Figure D.1 shows the Grasshopper script that was set up using the Karamba3D plug-in to perform a Finite Element Analysis (FEA) on the reversible vault geometry designed in Chapter 7 to determine the maximum shear forces the structure is experiencing.

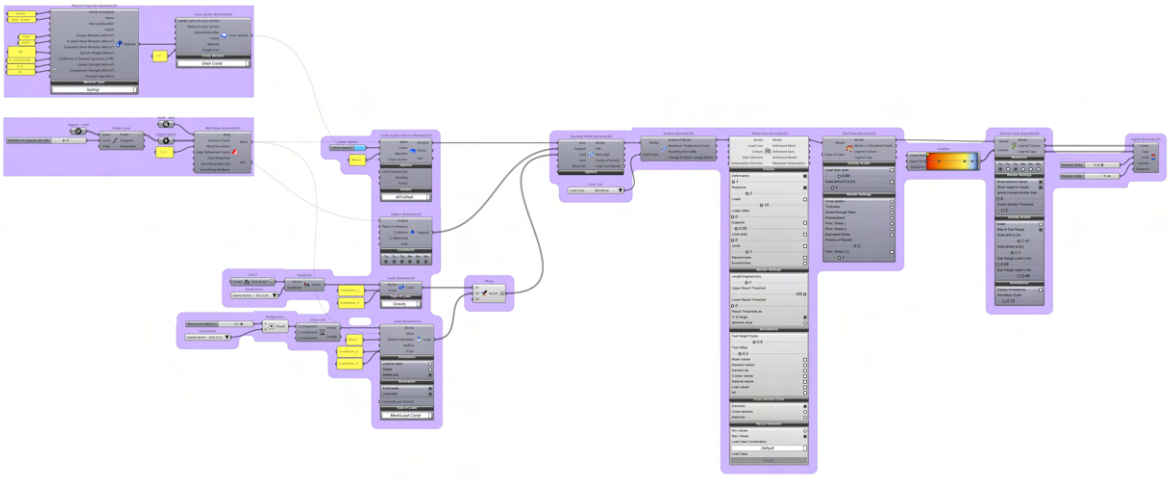

Figure D.1: Grasshopper script using Karamba3D for structural modelling and finite element analysis

The demountable vault geometry from Chapter 7 was simplified to a single surface that serves as the input mesh for the Karamba model. This mesh was assigned a thickness of 100 mm to define the shell element. Next, fully fixed support conditions (restraining all translations and rotations) are applied at the positions of all bricks directly connected to the foundation (see Figure D.2). This configuration ensures that during the analysis, each reaction force can be directly traced back to one specific brick element, thereby facilitating easy calculation of the corresponding shear stress since the area is known.

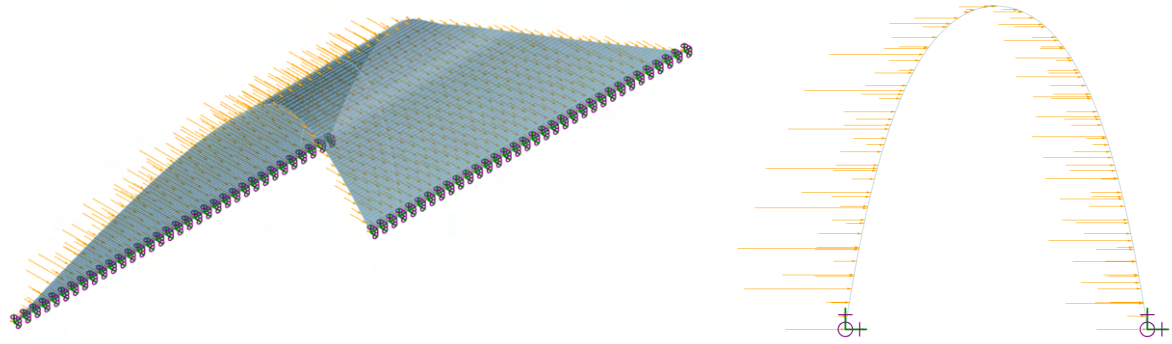

(a) Isometric view **(b)** Front elevation

Figure D.2: Karamba3D simulation model showing support constraints and applied wind pressure.

Finally, the design loads are applied. First, gravity (self-weight) is applied to the structure with a partial safety factor of 1.35. Subsequently, the wind peak velocity pressure calculated in Section D.1 of 0.7 kN/m^2 is projected onto the shell with a safety factor of 1.5 (see Figure D.2).

D.2.1. Results

The finite element analysis yields the support reaction forces across the foundation under the critical Ultimate Limit State (ULS) load combination ($1.35 \cdot Gravity + 1.5 \cdot Wind$). Because each vector links directly to an individual brick, these outputs provide the exact localized forces required to verify the shear capacity of individual interlayers in the reversible vault assembly.

Figure D.3 shows that the isolated normal reaction force exhibit a maximum compressive reaction of 2.58 kN along the base, driven by the cumulative downward action of the vault's self-weight and wind pressure. No vertical tensile forces are observed, confirming the vault remains entirely in compression.

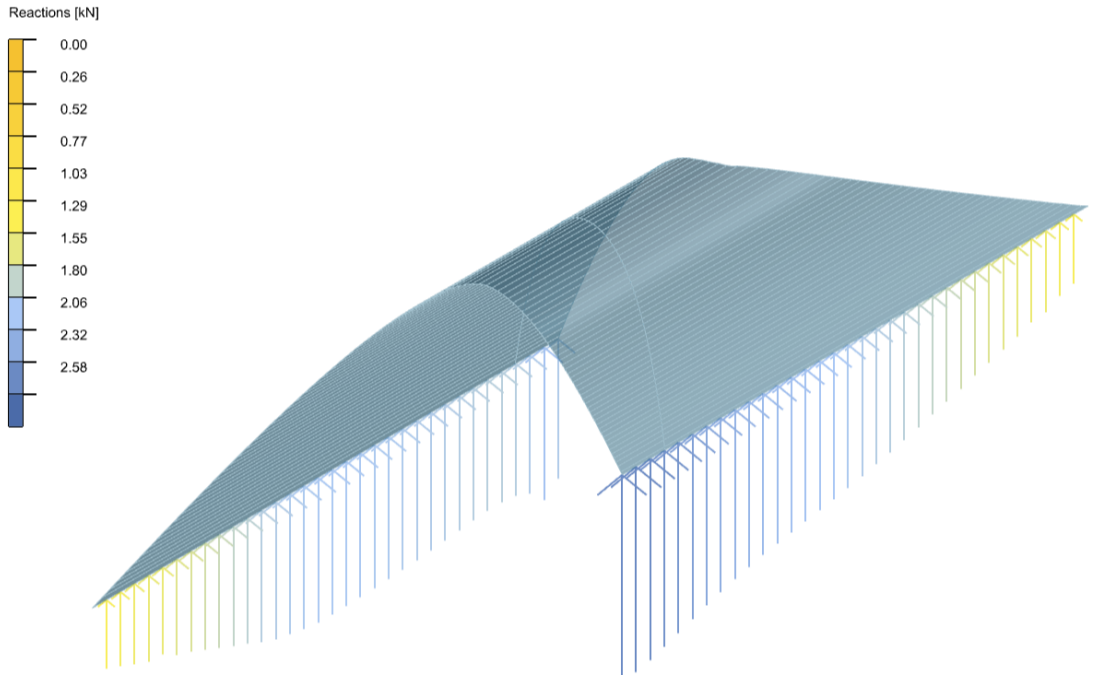

Figure D.3: Isolated normal (vertical) support reactions under ULS gravity and wind loading (Max: 2.58 kN).

The isolated lateral shear reactions reveal a peak horizontal force of 1.10 kN acting outward at the foundation (see Figure D.4). These outward shear forces are a direct result of the arching shell combined with the horizontal wind pressure, and it establishes the minimum combined interlocking and friction resistance required between the base bricks and the foundation to prevent shear failure.

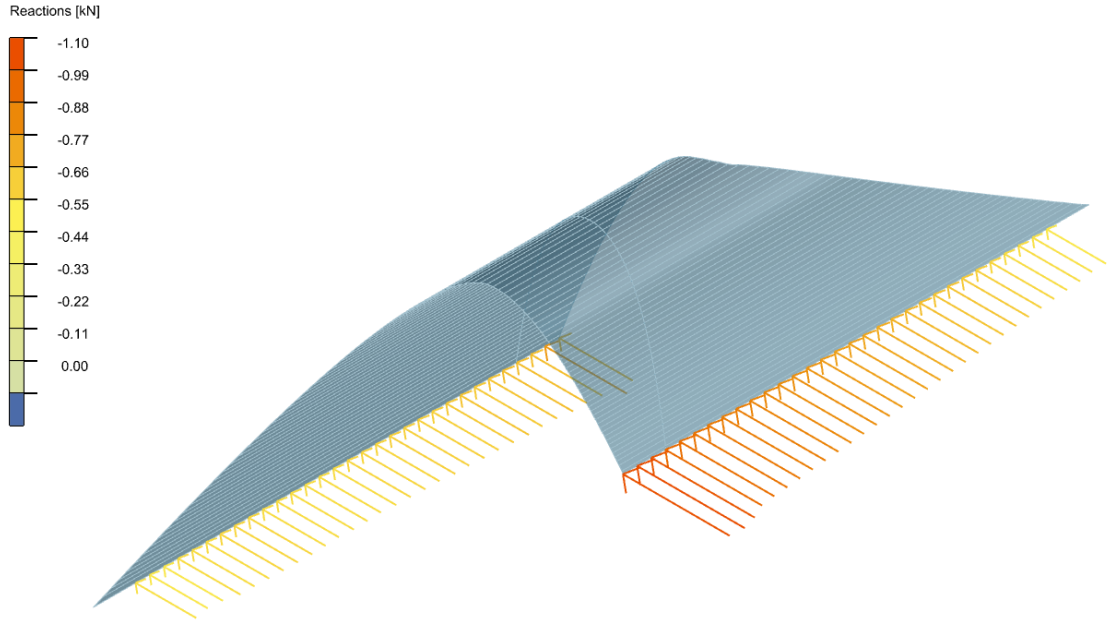

Figure D.4: Isolated lateral (horizontal) support reactions under ULS gravity and wind loading (Max: 1.10 kN).

Finally, the combined normal and shear support reactions in Figure D.5 demonstrate the total combined interaction across the full assembly, providing a holistic map of all the forces transferred to the ground via the foundation.

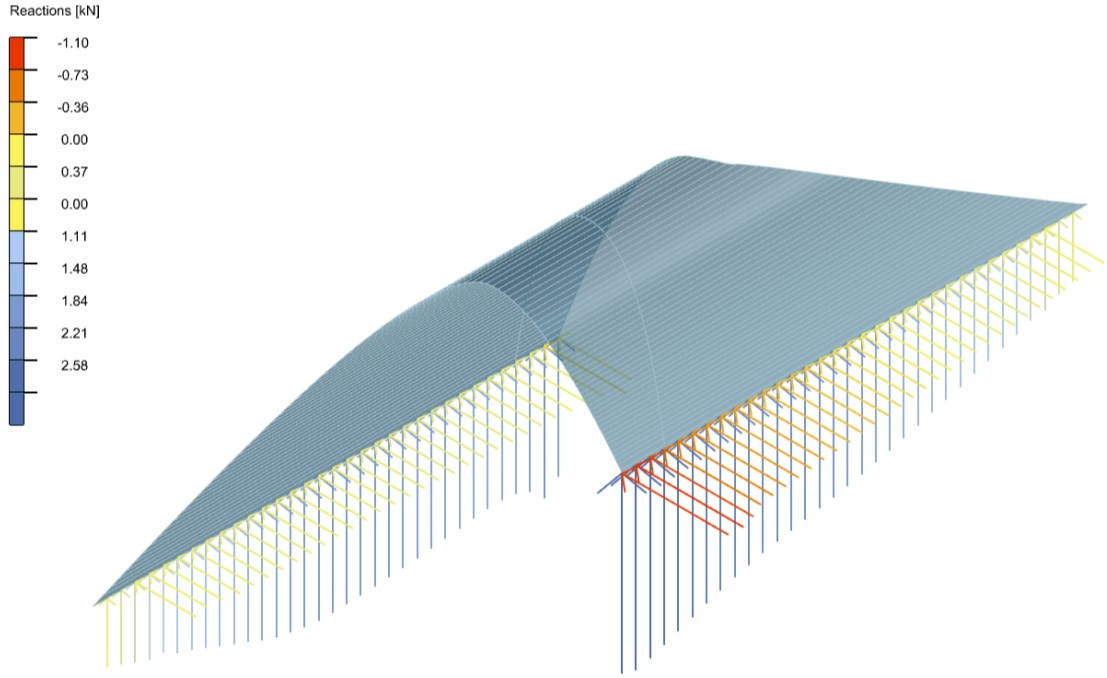

Figure D.5: Combined normal and shear support reactions under ULS gravity and wind loading.

E

Mechanical validation

E.1. Normal load calculation

This section determines the representative compressive load acting on the lowest and therefore most heavily loaded brick in the reversible glass vault design. The self-weight of the bricks and stainless-steel keys within one half of the vault section is considered to estimate the normal force acting on a single brick.

Assumptions

Glass brick dimensions:		$=$	$20 \times 10 \times 5$ cm
Density glass:	ρ_{glass}	$=$	2.5 g/cm^3
Self weight glass brick:		$=$	2.5 kg
Stainless-steel keys dimensions:		$=$	20 cm, $\varnothing\, 0.5$ cm
Density stainless-steel:	ρ_{steel}	$=$	8.0 g/cm^3
Self weight stainless-steel keys (4x):		$=$	0.125 kg
Total unit weight:		$=$	2.625 kg
Full arch:		$=$	91 bricks
Half arch:		$=$	45.5 bricks

Calculation

Normal force (half arch):

$$F_n = 45.5 \times 2.625 \times 9.81$$
$$= 1171.7 \text{ N}$$

Normal stress:

$$\sigma_n = 1171.7/(200 \times 100)$$
$$= 0.059 \text{ N/mm}^2$$

Normal force on samples:

$$= 0.059 \times (100 \times 100)$$
$$= 585.8 \text{ N}$$
$$\Rightarrow \mathbf{F}_{\text{sample}} \sim \mathbf{0.6} \text{ kN}$$

E.2. Specimen design

The four selected interlayer geometries from Chapter 6 were adapted to fit 100 × 100 × 15 mm float-glass samples. This size was chosen to make the production and shear testing of the specimens manageable within the available test setup and timeframe, while still allowing the glass–interlayer–glass interface to be evaluated. Figure E.1 shows that for each of the four geometries, the knob pattern was shifted and slightly scaled so that the specimen edges cut through the centre of the outer knobs. This was done to make the specimens symmetrical in both directions, while also keeping the interface between the keys, knobs and base layer clearly visible during testing.

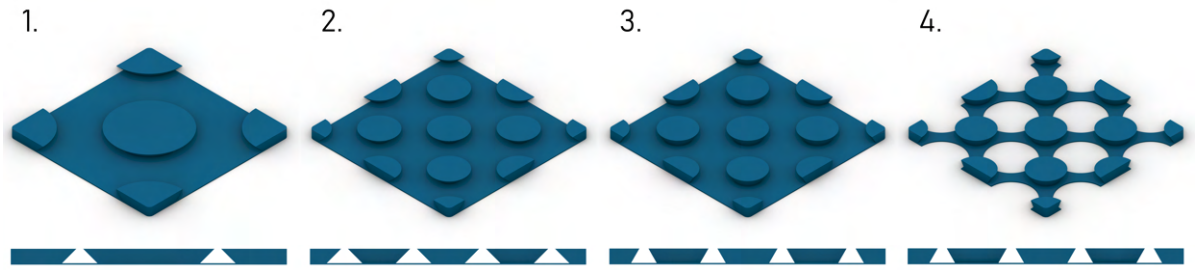

Figure E.1: Bottom halves of the geometries modified for shear testing

Printing the modified geometries from Figure E.1 close to the specimen edges increased the risk of initial edge delamination. To limit this anticipated risk, a 1.0 mm brim was added around the internal and external edges of the printed interlayer. A full test specimen consisted of a top and bottom glass sample, each printed with the corresponding interlayer half. These two halves were mechanically connected using the stainless-steel keys, thereby creating a small-scale representation of the intended connection in the reversible glass vault.

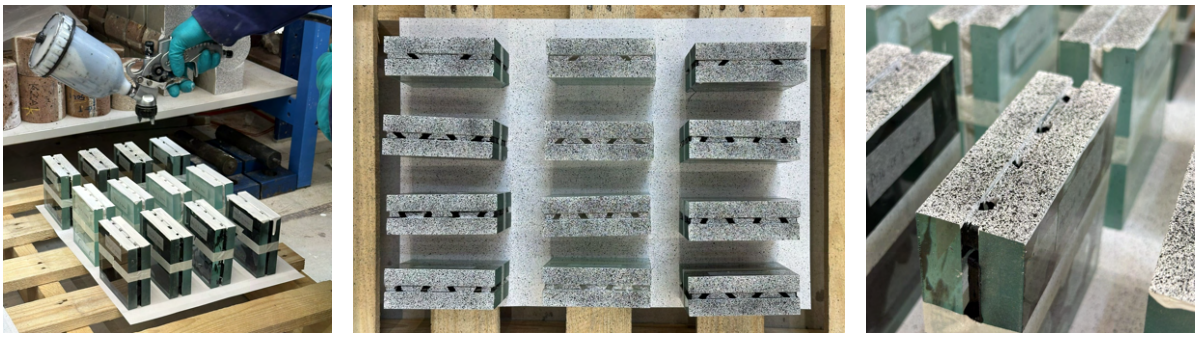

(a) Application of the speckles **(b)** Overview of all 12 specimens **(c)** Close up

Figure E.2: Application process of high-contrast speckles for DIC analysis

For the intended digital image correlation (DIC) analysis, one visible side of each assembled specimen was prepared with a high-contrast speckle pattern, as shown in Figure E.2. First, the side was painted white to create a uniform background. After drying, black paint was applied using a spray gun to create a random pattern of speckles with varying sizes. These identifiable surface features were intended to allow the DIC software to track local surface movement during testing and calculate relative displacement and strain development across the monitored side of the specimen. However, although the specimens were prepared and the image sequence was recorded, the DIC post-processing could not be completed due to software licensing issues within the available project timeframe. The recorded images were therefore used only for qualitative observation of deformation and failure behaviour.

This modified specimen design also introduced several limitations. Printing close to the edge significantly increased the likelihood of initial delamination, as this behaviour was not observed during the earlier experiments in Chapter 4 and Chapter 6. In addition, initial delamination allowed some of the paint to penetrate between the interlayer and the glass, further degrading the bond. Furthermore, the modified geometry could not include the same filleted corners as the full-scale prototype and the samples tested in Chapter 4 and Chapter 6, making the specimens more vulnerable to stress concentrations and thermal shrinkage.

E.3. Test setup

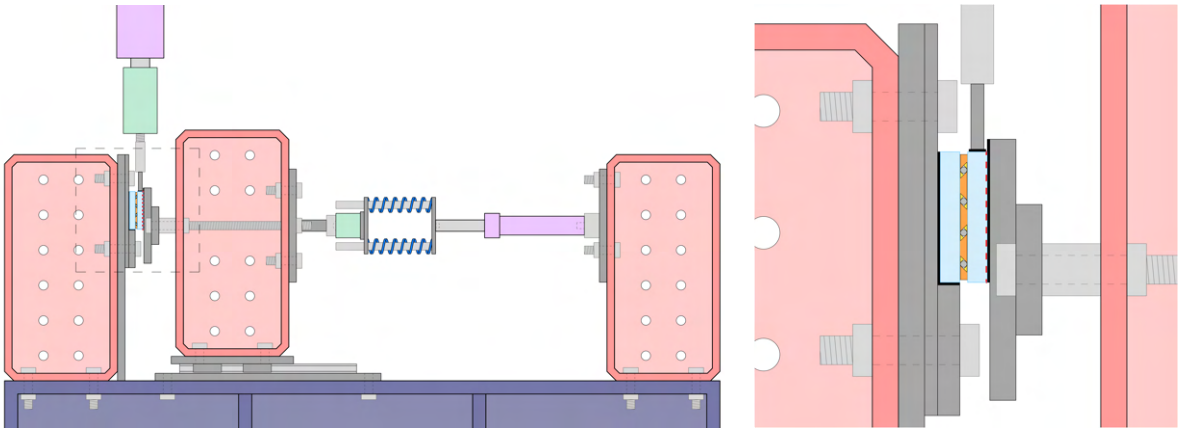

(a) Complete assembly showing the horizontal loading mechanism (actuator and springs), and vertical shear load application system.

(b) Zoomed in detail of the test specimen located in the assembly

Figure E.3: Schematic illustration of the custom-built shear test setup at the stevin II lab, CitG

The shear tests were conducted using a custom-built setup illustrated in Figure E.3. Two red steel support blocks were fixed to the large rigid beam at the base of the setup. Between these fixed supports, a central red steel block was mounted on a rail system, allowing it to move horizontally.

The normal load system was positioned to the right of the movable block. From right to left, this system consisted of a manually operated hydraulic cylinder, a spring system, and a load cell. The hydraulic cylinder, illustrated in pink in Figure E.3a, was used to apply the normal load. The spring system dampened possible vibrations transmitted between the cylinder and the specimen. The load cell, illustrated in green, was used to monitor the applied normal load, which was set to approximately 0.6 kN. Due to manual hydraulic loading and the accuracy of the load cell, the applied normal load may have varied by approximately ±10% between specimens.

The specimen was positioned on the left side of the movable block, where the vertical shear load was applied. The shear load was introduced by a vertical hydraulic piston, also illustrated in pink, with a second load cell positioned underneath it, illustrated in green. Figure E.3b shows a detailed view of the specimen region. The two glass substrate halves are shown in light blue, with the printed polymer interlayer shown in orange.

One glass half was supported vertically by a steel ridge, created using a metal plate with a thickness selected so that only this glass half rested on it. The interlayer and the opposite glass half remained unsupported in the vertical direction, allowing shear displacement to occur through the interlayer. All glass edges that came into contact with steel were separated using neoprene pads, shown in black.

To reduce friction between the moving glass half and the lateral support, a thin PTFE film was placed between the glass and neoprene. Silicone spray was applied only to the side of the PTFE film facing the glass. This created a low-friction interface, allowing the moving half of the specimen to displace vertically with limited restraint. This also helped prevent rotation of the specimen, which had been a recurring issue in the similar setup used by Van Kessel (2025). The free glass half was additionally equipped with an LVDT sensor to measure its relative vertical displacement with respect to the stationary half, as shown in Figure E.4c.

Between the right glass half of the specimen and the normal load cylinder, a loose 10 mm thick steel plate was inserted. A 2 mm neoprene layer was again placed between the steel and glass. The cylinder head had a rounded contact surface. Together with the loose steel plate, this allowed the normal force to be distributed over the full height of the specimen while still allowing slight rotation if needed. This avoided a fully rigid connection, which could otherwise damage the brittle glass substrate.

Finally, a camera with a flash system was positioned perpendicular to the speckled front face of the specimen. During testing, the camera captured one image every 5 seconds for the intended DIC analysis and subsequent qualitative observation of the failure process.

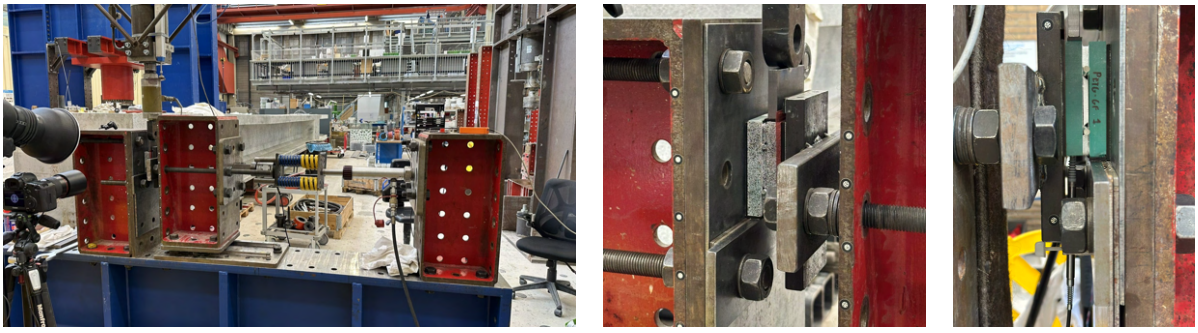

(a) Full shear test setup **(b)** Specimen positioned in the setup **(c)** LVDT sensor

Figure E.4: Mechanical shear test setup, showing the full setup, specimen position, and LVDT displacement measurement

E.4. Test procedure

The following procedure was followed for each tested specimen:

1. Assemble the top and bottom halves of the specimen using the stainless-steel keys.
2. Place the assembled specimen on the support ridge of the test setup.
3. Insert the PTFE film, freshly coated with silicone spray.
4. Clamp the specimen using the normal-load piston to keep it in position.
5. Attach the Linear Variable Differential Transformer (LVDT) to the free-hanging half of the specimen.
6. Start data acquisition and photo capture.
7. Manually apply a normal load of 0.6 kN.
8. Apply the vertical shear load at the prescribed loading speed.
9. Stop the test after failure.
10. Release the normal load from the specimen.
11. Remove and photograph the specimen.
12. Document the observed failure mode and any visible damage.

E.5. Results per specimen

Specimen S1 — PETG-CF, Geometry 1

The PETG-CF-S1 specimen was tested under normal load of 0.6 kN and a shear loading speed of 0.01 mm/s. Prior to testing, the specimen already showed moderate initial delamination, especially directly underneath the knobs (see Figure E.6). During loading, the specimen showed a gradual increase in shear force up to a peak load of **2689.6 N** at **4.17 mm** sliding displacement, with a maximum recorded displacement of **8.15 mm**. The initial stiffness was **765.1 N/mm** between 10–20% of the peak load, decreasing to **669.3 N/mm** between 10–40% and **645.1 N/mm** over the full 0–peak range, indicating progressive local deformation before failure. At peak load, the average shear stress was approximately **0.29 MPa** over the base area of **9211 mm^2** and **1.35 MPa** over the effective knob area of **1994 mm^2**, showing that the load was mainly concentrated in the interlocking knob features. Failure occurred primarily through **bearing failure** at the top key-knob interface, where the top side showed one dominant contact point and the bottom side showed two contact points. However, the glass directly underneath the failed knob also fractured, indicating that the observed failure was a combination of local bearing failure and substrate failure. The post-peak response showed a stepwise loss of resistance rather than immediate full delamination, suggesting progressive local damage.

Overall, PETG-CF-S1 confirms that it can transfer high shear forces, but the load concentration at a limited number of knob-key contact points make it sensitive to local bearing failure and local glass damage.

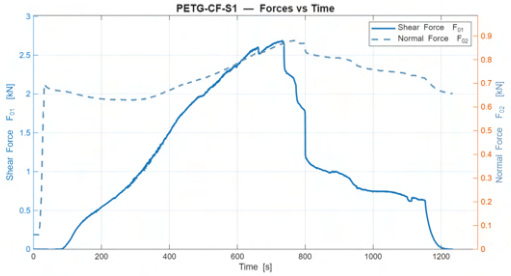

(a) Shear and normal force over time

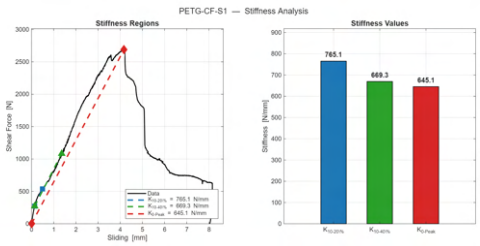

(b) Stiffness analysis

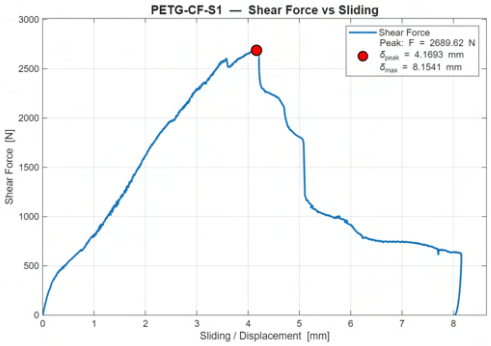

(c) Shear force-sliding displacement response

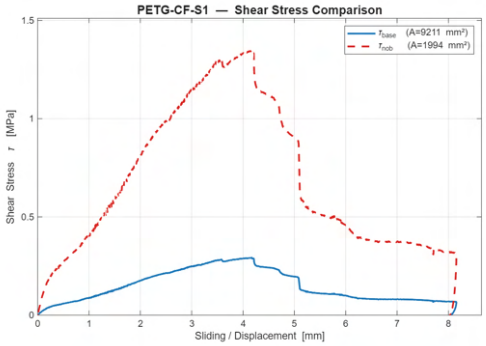

(d) Shear stress comparison based on base area and knob area

Figure E.5: Results for specimen S1 — PETG-CF, Geometry 1

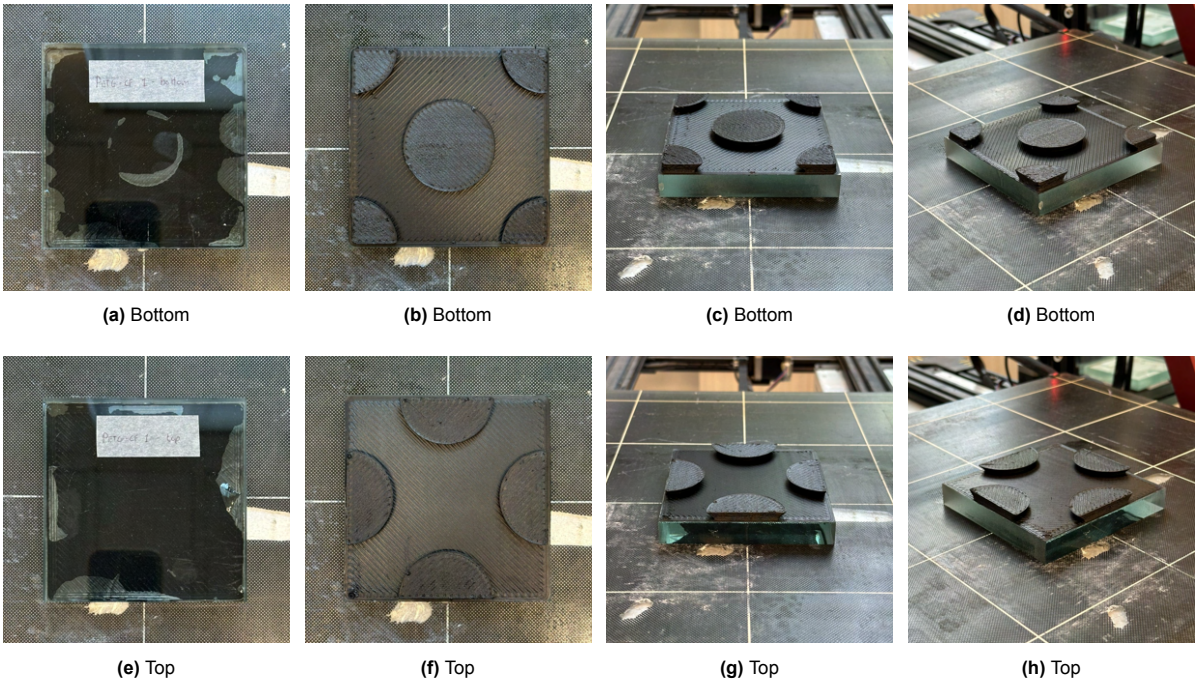

(a) Bottom **(b)** Bottom **(c)** Bottom **(d)** Bottom

(e) Top **(f)** Top **(g)** Top **(h)** Top

Figure E.6: Specimen S1 — PETG-CF, Geometry 1 prior to testing

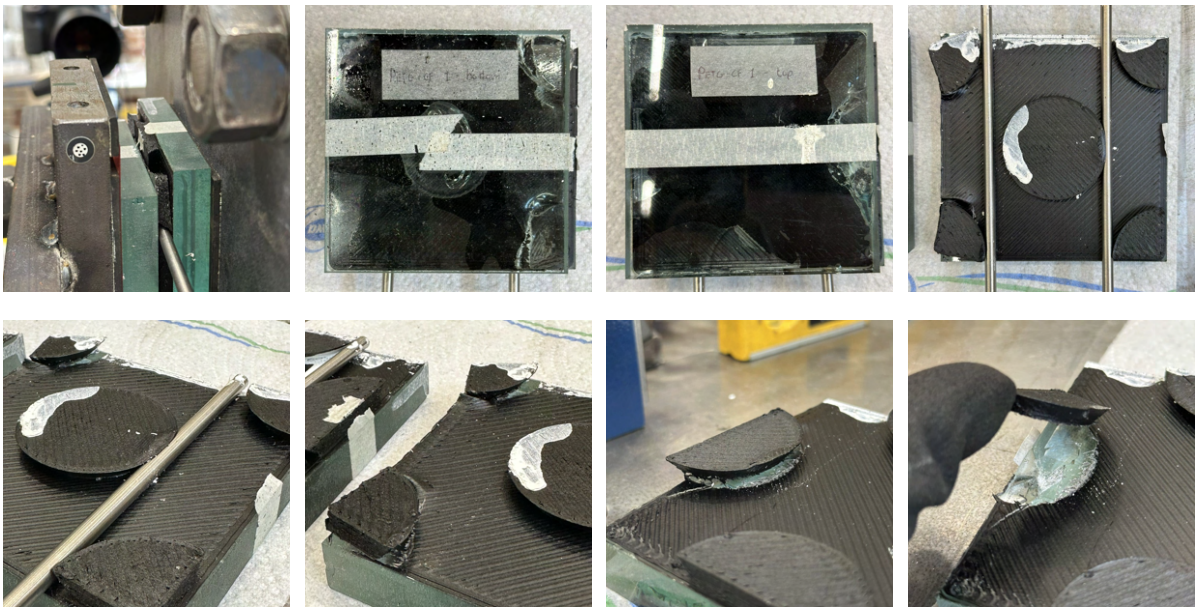

Figure E.7: Specimen S1 — PETG-CF, Geometry 1 after testing

Specimen S2 — PETG-CF, Geometry 2

The PETG-CF-S2 specimen was tested under a normal load of 0.6 kN and a shear loading speed of 0.01 mm/s. Prior to testing, only minor initial edge delamination was visible (see Figure E.9). During loading, the specimen showed a steep and relatively continuous increase in shear force up to a peak load of **3158.2 N** at **2.61 mm** sliding displacement, with a maximum recorded displacement of **8.64 mm**. The stiffness analysis showed a stiffness of **986.7 N/mm** between 10–20% of the peak load and **983.4 N/mm** between 10–40%, while the overall 0–peak stiffness was **1209.4 N/mm**. This indicates a relatively stiff response, with only limited early stiffness degradation before peak load. At peak load, the average shear stress reached approximately **0.34 MPa** over the base area of **9211 mm^2** and approximately **3.72 MPa** over the effective knob area of **850 mm^2**. Failure occurred through **bearing failure**, with multiple knobs breaking off at their base. The load appeared to be distributed well across the interlocking elements, making this a more favourable failure mode than failure at a single dominant contact point. During testing, the normal load increased significantly due to rotation of the angled knobs around the round stainless-steel keys, generating an additional normal force component. After reaching the peak load, the specimen did not lose all resistance immediately, but showed a gradual post-peak reduction with residual load capacity over a large displacement range.

Overall, PETG-CF-S2 demonstrates that it can provide strong and well-distributed mechanical engagement, although repeated failure at the knob base confirms a critical region for further refinement.

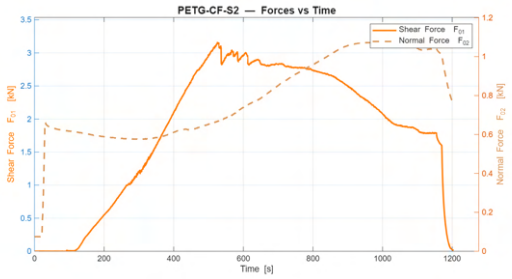

(a) Shear and normal force over time

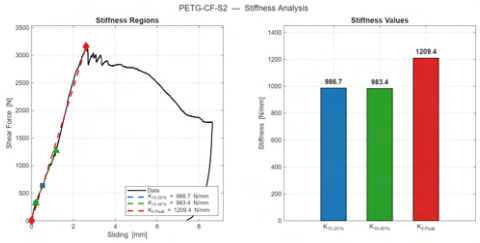

(b) Stiffness analysis

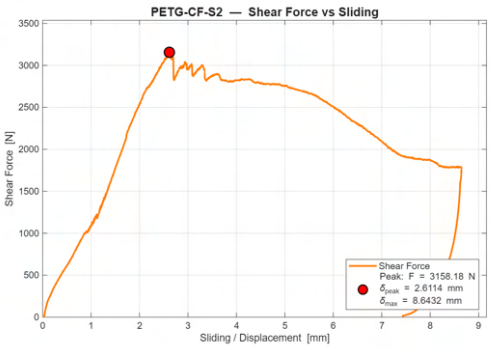

(c) Shear force-sliding displacement response

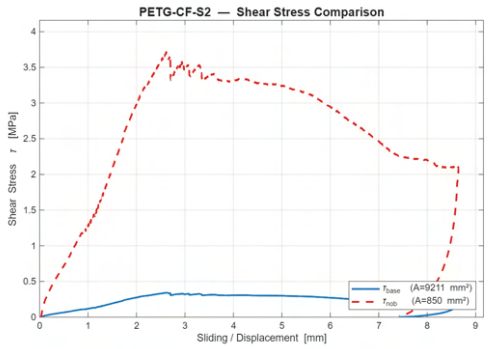

(d) Shear stress comparison based on base area and knob area

Figure E.8: Results for specimen S2 — PETG-CF, Geometry 2

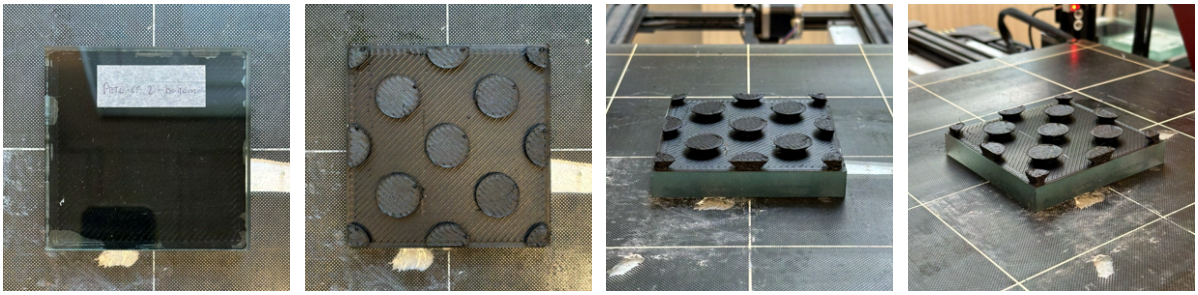

(a) Bottom **(b)** Bottom **(c)** Bottom **(d)** Bottom

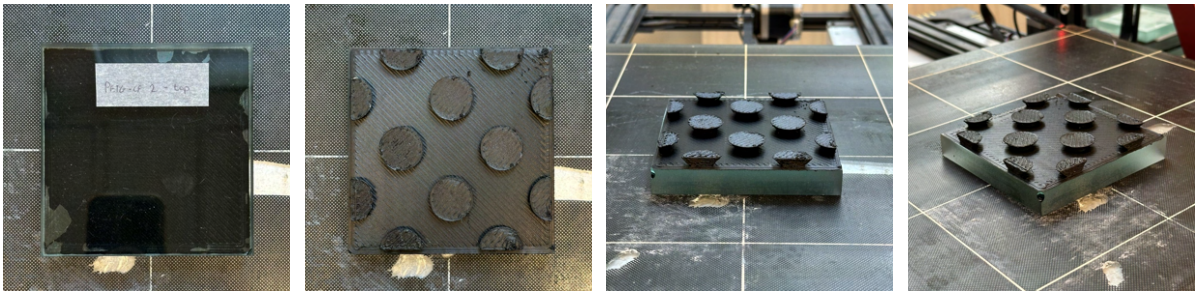

(e) Top **(f)** Top **(g)** Top **(h)** Top

Figure E.9: Specimen S2 — PETG-CF, Geometry 2 prior to testing

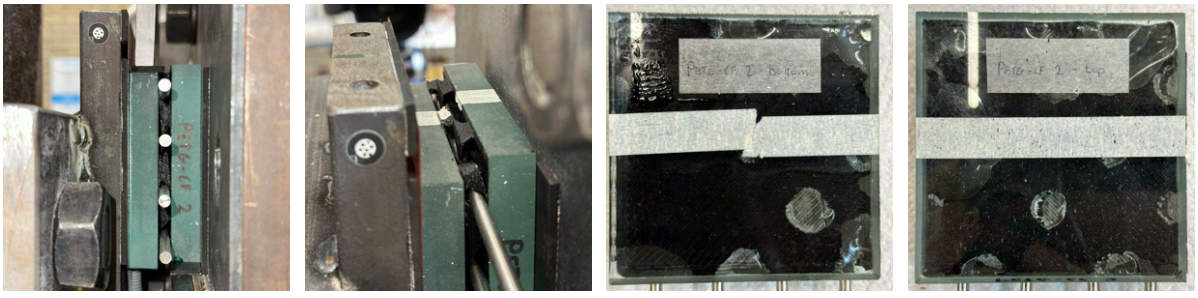

Figure E.10: Specimen S2 — PETG-CF, Geometry 2 after testing

Specimen S3 — PETG-CF, Geometry 3

The PETG-CF-S3 specimen was tested under a normal load of 0.6 kN and a shear loading speed of 0.01 mm/s. Prior to testing, the specimen's bottom half showed only minor initial edge delamination, while the top half showed slightly more moderate delamination extending further inward from the edge (see Figure E.12). During loading, the specimen showed a strong and relatively continuous increase in shear force up to a peak load of **5137.1 N** at **3.82 mm** sliding displacement, with a maximum recorded displacement of **8.47 mm**. The stiffness analysis showed a stiffness of **1404.8 N/mm** between 10–20% of the peak load, **1710.6 N/mm** between 10–40%, and **1345.4 N/mm** over the full 0–peak range. At peak load, the average shear stress reached approximately **0.57 MPa** over the base area of **9211 mm^2** and approximately **3.59 MPa** over the effective knob area of **1432 mm^2**. Failure occurred mainly through **bearing failure**, combined with **shear rupture failure** of the printed interlayer. Similar to PETG-CF-S2, the load appeared to be well distributed across the knobs rather than concentrated in a single contact point. Additionally, the normal force increased again during testing due to rotation of the angled knobs around the round stainless-steel keys, generating an additional normal force component. After the peak load, the specimen showed several stepwise drops in resistance while still maintaining residual load capacity over a large displacement range.

Overall, PETG-CF-S3 demonstrates the highest shear capacity of the PETG-CF series so far and confirms that geometry 3 provides effective load distribution. Bearing failure again indicates that the base of the knobs remains the governing weak point. However, the additional occurrence of shear rupture suggests that the 60° knob angle provides greater resistance against local bearing failure than geometry 2, allowing the connection to develop higher shear resistance before failure.

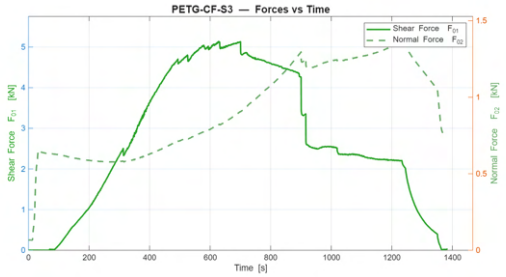

(a) Shear and normal force over time

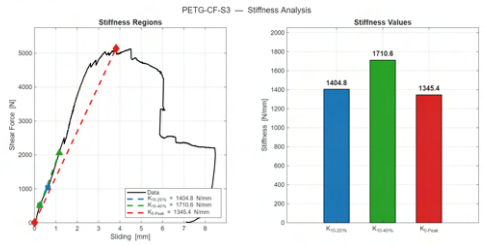

(b) Stiffness analysis

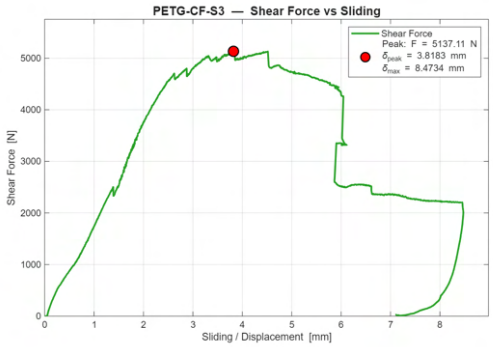

(c) Shear force-sliding displacement response

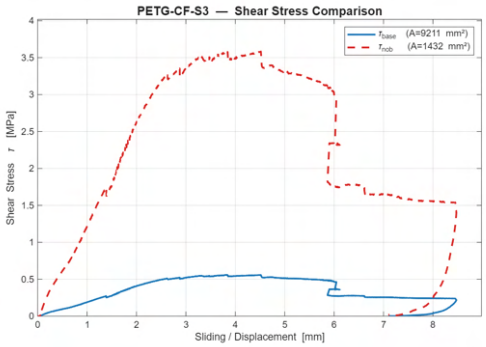

(d) Shear stress comparison based on base area and knob area

Figure E.11: Results for specimen S3 — PETG-CF, Geometry 3

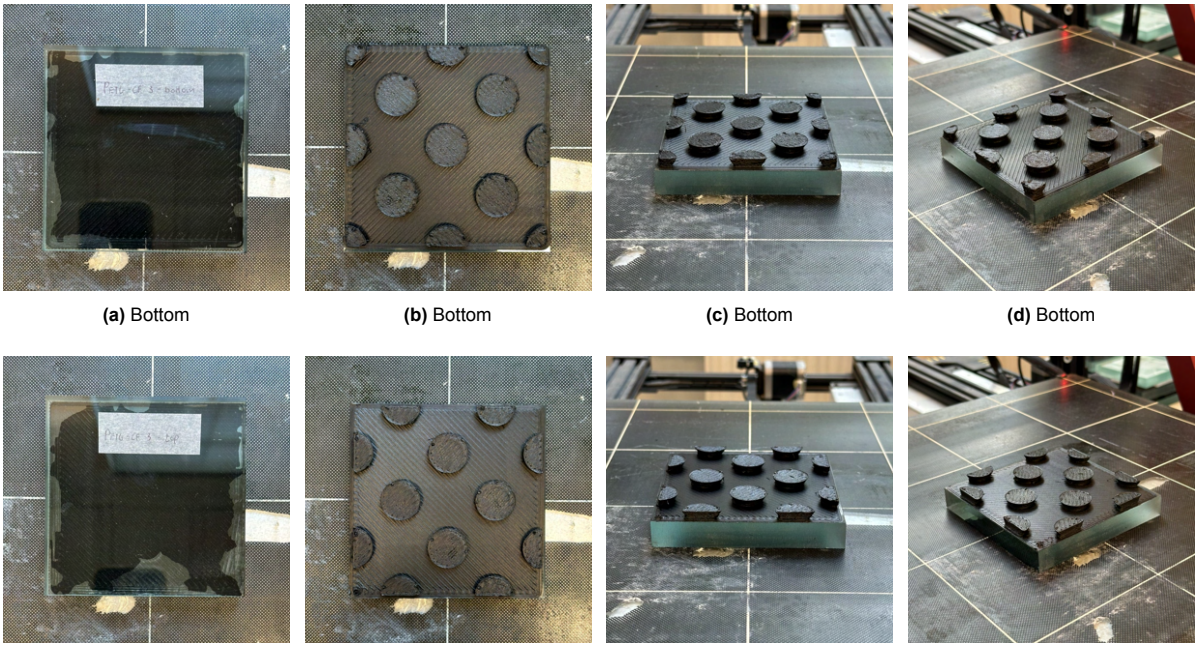

(a) Bottom **(b)** Bottom **(c)** Bottom **(d)** Bottom

(e) Top **(f)** Top **(g)** Top **(h)** Top

Figure E.12: Specimen S3 — PETG-CF, Geometry 3 prior to testing

Figure E.13: Specimen S3 — PETG-CF, Geometry 3 after testing

Specimen S4 — PETG-CF, Geometry 4

The PETG-CF-S4 specimen was tested under a normal load of 0.6 kN and a shear loading speed of 0.01 mm/s. Prior to testing, the specimen's bottom half showed only minor initial delamination, mostly limited to the edges, while barely any initial delamination was observed on the top half (see Figure E.15). During loading, the specimen showed a relatively steep increase in shear force up to a peak load of **3656.7 N** at **2.93 mm** sliding displacement, with a maximum recorded displacement of **9.06 mm**. The stiffness analysis showed a stiffness of **1730.2 N/mm** between 10–20% of the peak load, decreasing to **1461.5 N/mm** between 10–40% and **1249.4 N/mm** over the full 0–peak range. At peak load, the average shear stress reached approximately **0.80 MPa** over the reduced base area of **4589 mm²** and approximately **2.56 MPa** over the effective knob area of **1428 mm²**. Failure occurred mainly through **shear rupture** of the base layer, with additional **local bearing failure** of the knobs. This indicates that geometry 4 does not provide sufficient bonded surface area for the interlayer to remain fully engaged with the glass substrate under high shear loading. Instead of forcing the knobs to fail primarily in bearing, parts of the interlayer started to delaminate and rupture through the thinner base structure. After the peak load, the specimen showed several large drops and partial recoveries in resistance, indicating progressive damage rather than a single clean failure event.

Overall, PETG-CF-S4 shows that the reduced organic cross-hatch base of geometry 4 improves neither load distribution nor interface reliability. The specimen still reached a considerable shear force, but the severe base-layer rupture confirms that this geometry is mechanically less robust than the previous full-base geometry variations.

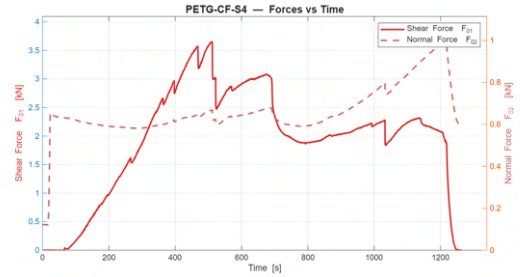

(a) Shear and normal force over time

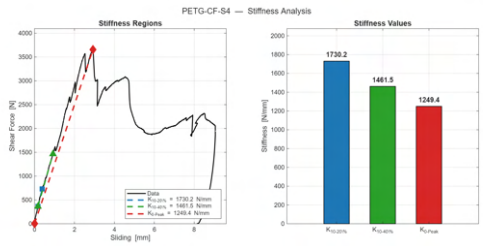

(b) Stiffness analysis

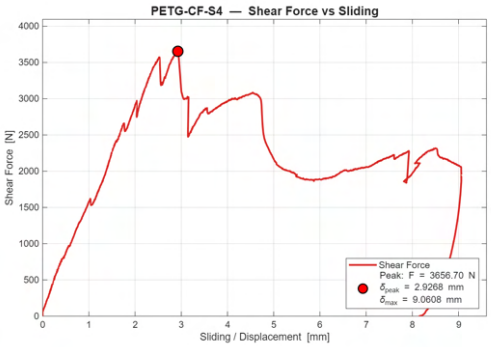

(c) Shear force-sliding displacement response

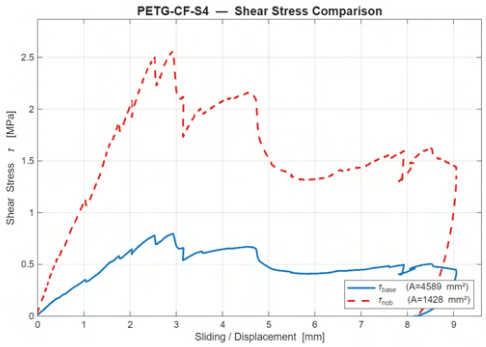

(d) Shear stress comparison based on base area and knob area

Figure E.14: Results for specimen S4 — PETG-CF, Geometry 4

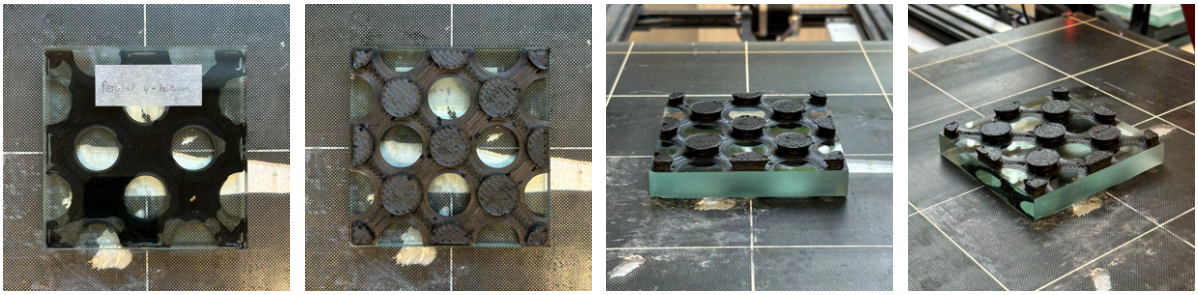

(a) Bottom **(b)** Bottom **(c)** Bottom **(d)** Bottom

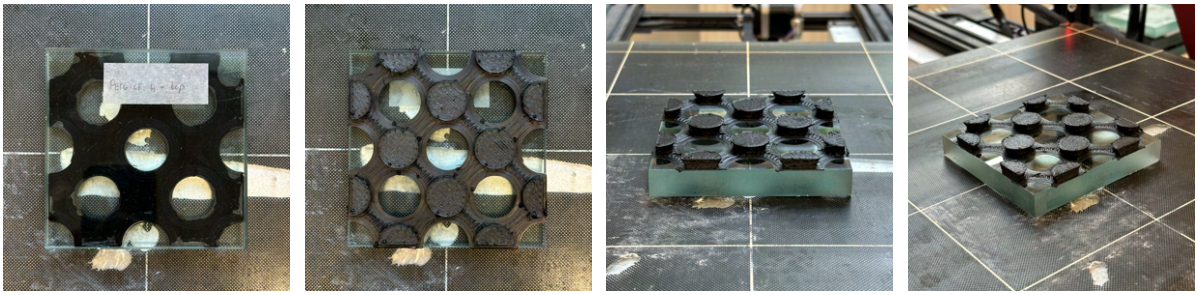

(e) Top **(f)** Top **(g)** Top **(h)** Top

Figure E.15: Specimen S4 — PETG-CF, Geometry 4 prior to testing

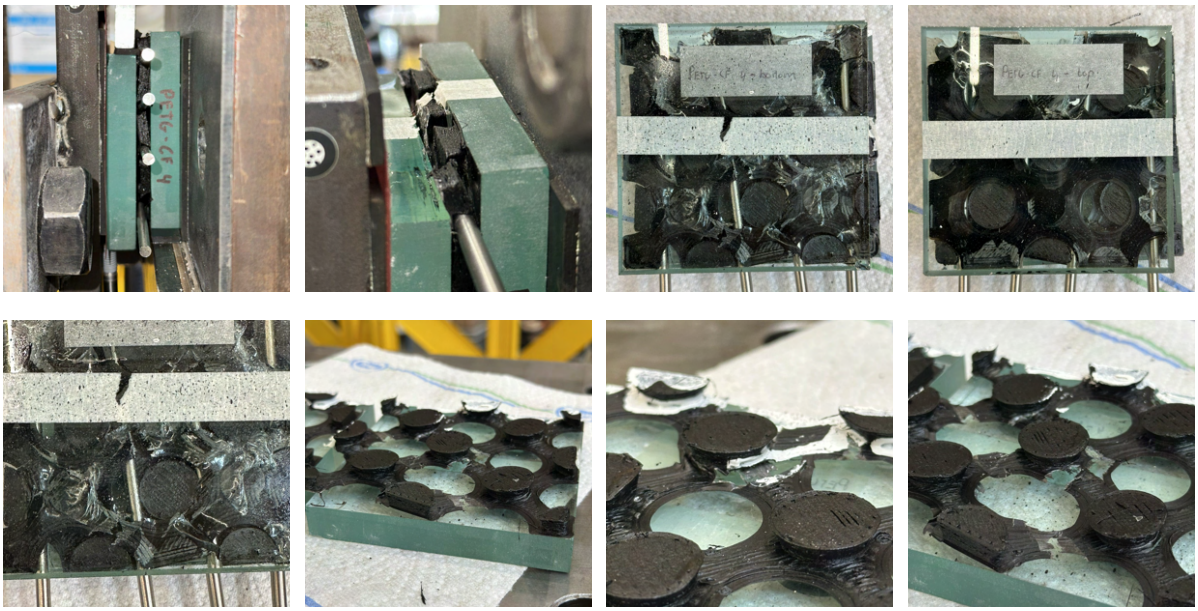

Figure E.16: Specimen S4 — PETG-CF, Geometry 4 after testing

Specimen S5 — PET-CF, Geometry 1

The PET-CF-S5 specimen was tested under a normal load of 0.6 kN and a shear loading speed of 0.02 mm/s. Prior to testing, the bottom half showed minor to moderate initial delamination, mainly limited to the areas directly underneath the knobs. The top half, however, showed severe initial delamination, with more than half of the specimen area already detached before testing (see Figure E.18). During loading, the specimen reached a peak shear force of **773.7 N** at **2.08 mm** sliding displacement, with a maximum recorded displacement of **8.56 mm**. The stiffness analysis showed a high initial stiffness of **1882.2 N/mm** between both 10–20% and 10–40% of the peak load, while the overall 0–peak stiffness was much lower at **372.2 N/mm**. This difference reflects the unstable response caused by the already compromised interface. At peak load, the average shear stress reached only approximately **0.083 MPa** over the base area of **9211 mm^2** and approximately **0.39 MPa** over the effective knob area of **1994 mm^2**. Failure occurred through **sudden full delamination** of the top-side interlayer base layer. After this abrupt loss of adhesion, the specimen still showed a relatively stable residual resistance over a large displacement range, but this was governed by sliding/frictional resistance. Very minor to no damage was observed on the glass substrate after testing (see Figure E.19).

Overall, PET-CF-S5 shows that geometry 1 was in this specimen not able to properly activate the intended mechanical interlocking, primarily due to the severe initial delamination of the top half. Although the clean detachment is favourable from a demountability perspective, the sudden full delamination and low shear capacity make this result structurally unfavourable.

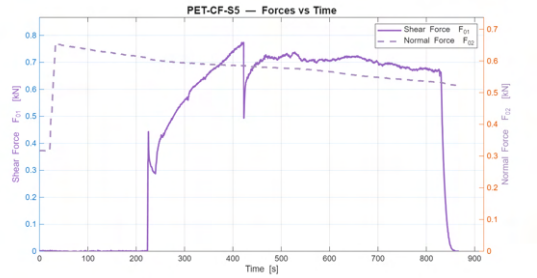

(a) Shear and normal force over time

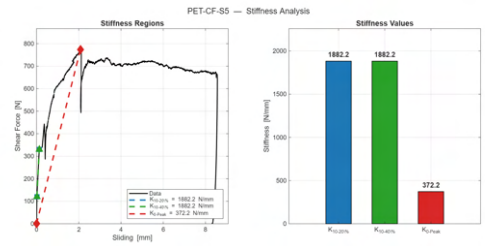

(b) Stiffness analysis

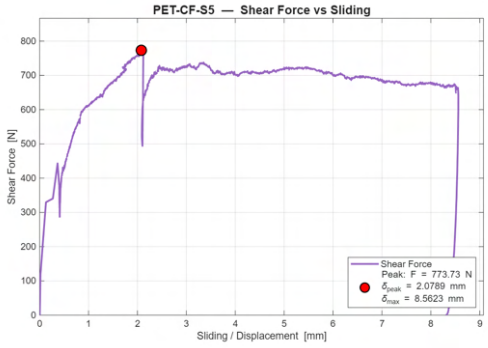

(c) Shear force-sliding displacement response

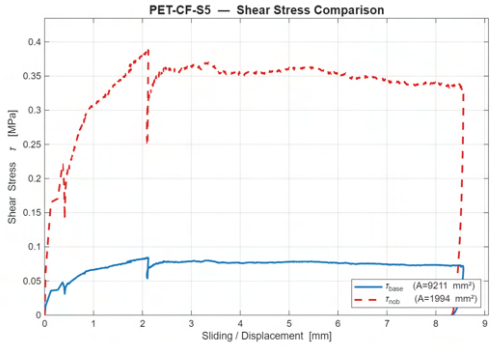

(d) Shear stress comparison based on base area and knob area

Figure E.17: Results for specimen S5 — PET-CF, Geometry 1

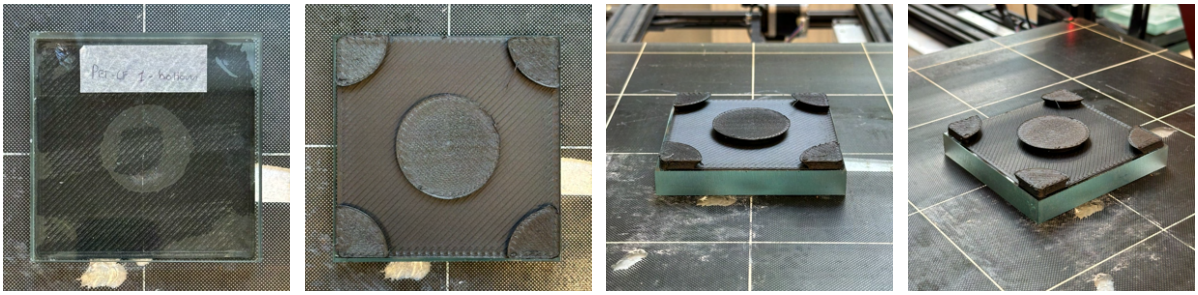

(a) Bottom **(b)** Bottom **(c)** Bottom **(d)** Bottom

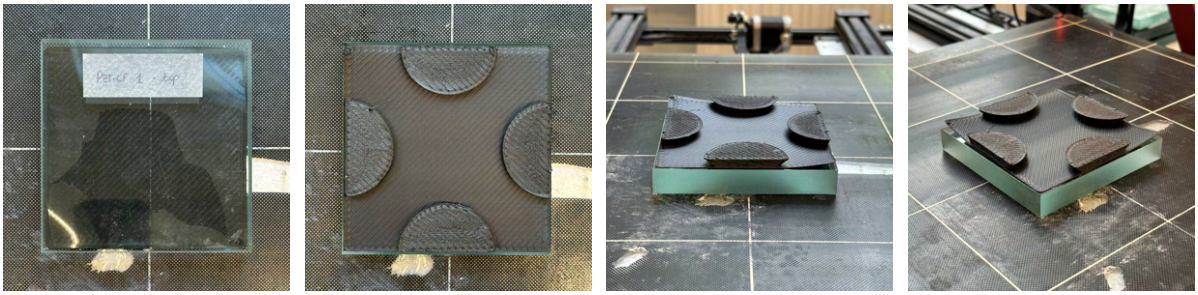

(e) Top **(f)** Top **(g)** Top **(h)** Top

Figure E.18: Specimen S5 — PET-CF, Geometry 1 prior to testing

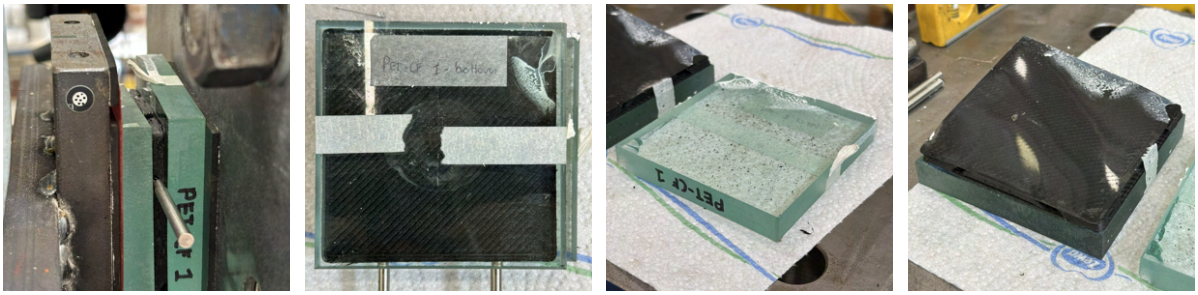

Figure E.19: Specimen S5 — PET-CF, Geometry 1 after testing

Specimen S6 — PET-CF, Geometry 2

The PET-CF-S6 specimen was tested under a normal load of 0.6 kN and a shear loading speed of 0.02 mm/s. Prior to testing, both specimen halves showed only very minor initial delamination, mostly limited to the edges and slightly more pronounced near the corners (see Figure E.21). During loading, the specimen reached a peak shear force of **2116.4 N** at **2.42 mm** sliding displacement, with a maximum recorded displacement of **10.08 mm**. The stiffness analysis showed a high initial stiffness of **1940.3 N/mm** between 10–20% of the peak load, followed by a lower stiffness of **883.8 N/mm** between 10–40% and **873.1 N/mm** over the full 0–peak range. This indicates that the specimen initially responded very stiffly, after which progressive local damage and deformation reduced the effective stiffness. At peak load, the average shear stress reached approximately **0.23 MPa** over the base area of **9211 mm^2** and approximately **2.50 MPa** over the effective knob area of **850 mm^2**. Failure occurred through a combination of **shear rupture failure**, **bearing failure**, and local **pure shear failure** of one knob. A clear bearing failure was observed in one of the central knobs, while shear rupture occurred in one of the corners. In addition, one knob failed in pure shear and fully snapped off slightly above the base layer (see Figure E.22). The normal force increased during testing, again indicating that rotation of the angled knobs around the round stainless-steel keys generated an additional normal force component (see Figure E.20a). After peak load, the specimen retained considerable residual resistance over a large displacement range, with several stepwise reductions corresponding to progressive local failures.

Overall, PET-CF-S6 shows that geometry 2 was able to effectively distribute the load, but the combination of bearing, shear rupture and pure shear failure indicates a more brittle and locally concentrated failure behaviour than observed in the PETG-CF specimens.

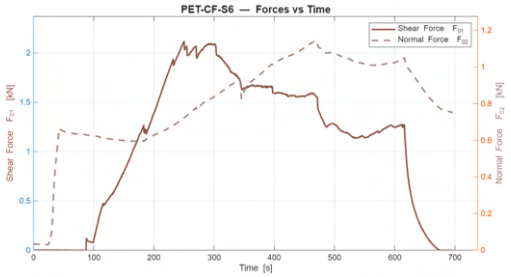

(a) Shear and normal force over time

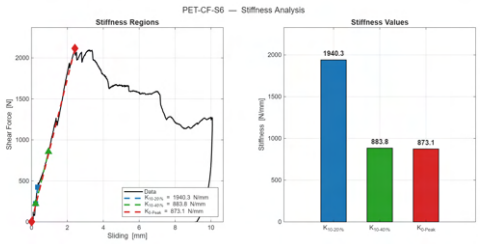

(b) Stiffness analysis

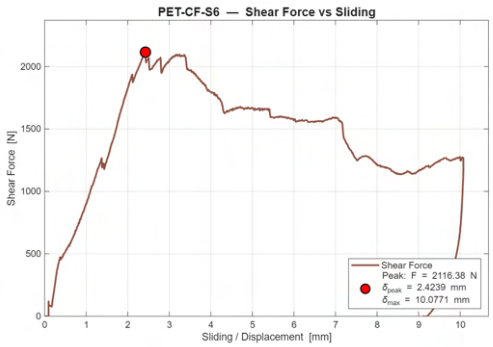

(c) Shear force-sliding displacement response

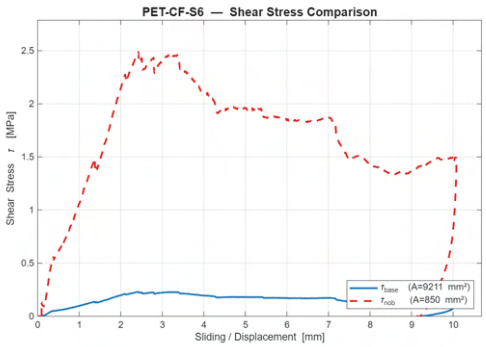

(d) Shear stress comparison based on base area and knob area

Figure E.20: Results for specimen S6 — PET-CF, Geometry 2

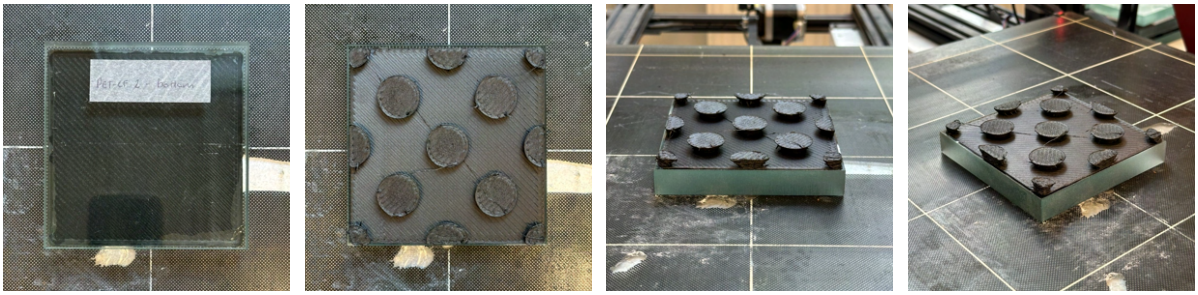

(a) Bottom **(b)** Bottom **(c)** Bottom **(d)** Bottom

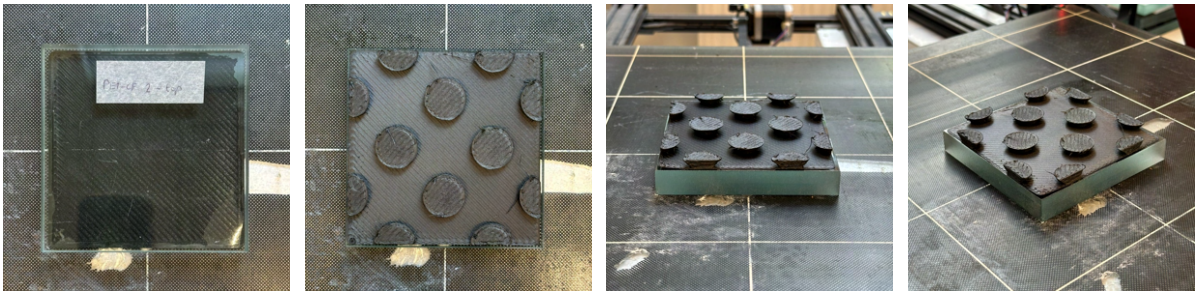

(e) Top **(f)** Top **(g)** Top **(h)** Top

Figure E.21: Specimen S6 — PET-CF, Geometry 2 prior to testing

Figure E.22: Specimen S6 — PET-CF, Geometry 2 after testing

Specimen S7 — PET-CF, Geometry 3

The PET-CF-S7 specimen was tested under a normal load of 0.6 kN and a shear loading speed of 0.02 mm/s. Prior to testing, the bottom half showed minor initial delamination, with one edge showing more moderate delamination, while the top half showed consistent minor edge delamination around the perimeter (see Figure E.23). During loading, the specimen reached a peak shear force of **3049.6 N** at **4.67 mm** sliding displacement, with a maximum recorded displacement of **8.93 mm**. The stiffness analysis showed a stiffness of **1268.9 N/mm** between 10–20% of the peak load and **1264.1 N/mm** between 10–40%, while the overall 0–peak stiffness was lower at **652.4 N/mm**. This difference reflects the extended plateau-like response before peak load, where the specimen maintained a high shear force while local damage progressively developed. At peak load, the average shear stress reached approximately **0.33 MPa** over the base area of **9211 mm^2** and approximately **2.13 MPa** over the effective knob area of **1432 mm^2**. Failure occurred through a combination of **shear rupture failure**, **bearing failure**, and local **pure shear failure**, similar to PET-CF-S6. Bearing failure was observed in several knobs, shear rupture occurred in two corners, and one knob failed in pure shear, snapping off slightly above the base layer (see Figure E.25). The normal force increased during testing, indicating that interaction between the angled knobs and the round stainless-steel keys again generated an additional normal force component. After peak load, the specimen showed a sudden drop in resistance, followed by a lower residual load plateau over a large displacement range.

Overall, PET-CF-S7 shows that geometry 3 achieved a higher shear capacity than PET-CF-S6, but still failed through a combination of local rupture and knob damage. This indicates that the 60° geometry improves resistance compared with geometry 2, but the PET-CF material still shows relatively brittle local failure once the printed features are critically loaded.

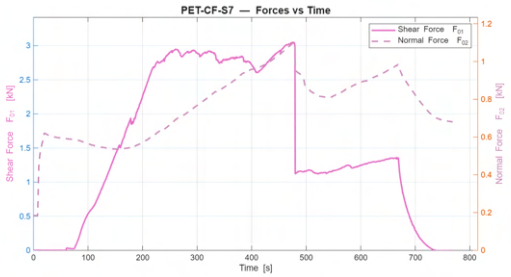

(a) Shear and normal force over time

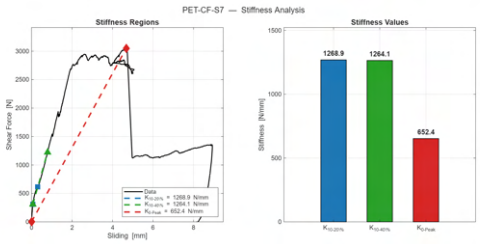

(b) Stiffness analysis

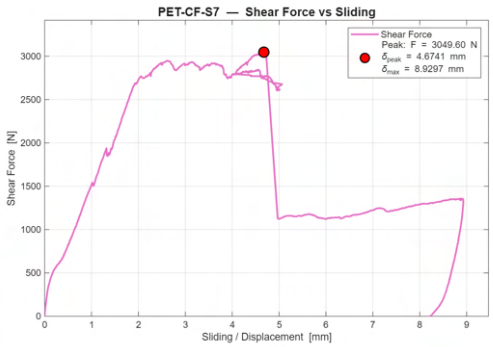

(c) Shear force-sliding displacement response

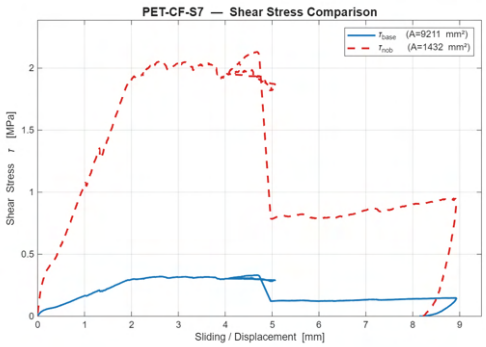

(d) Shear stress comparison based on base area and knob area

Figure E.23: Results for specimen S7 — PET-CF, Geometry 3

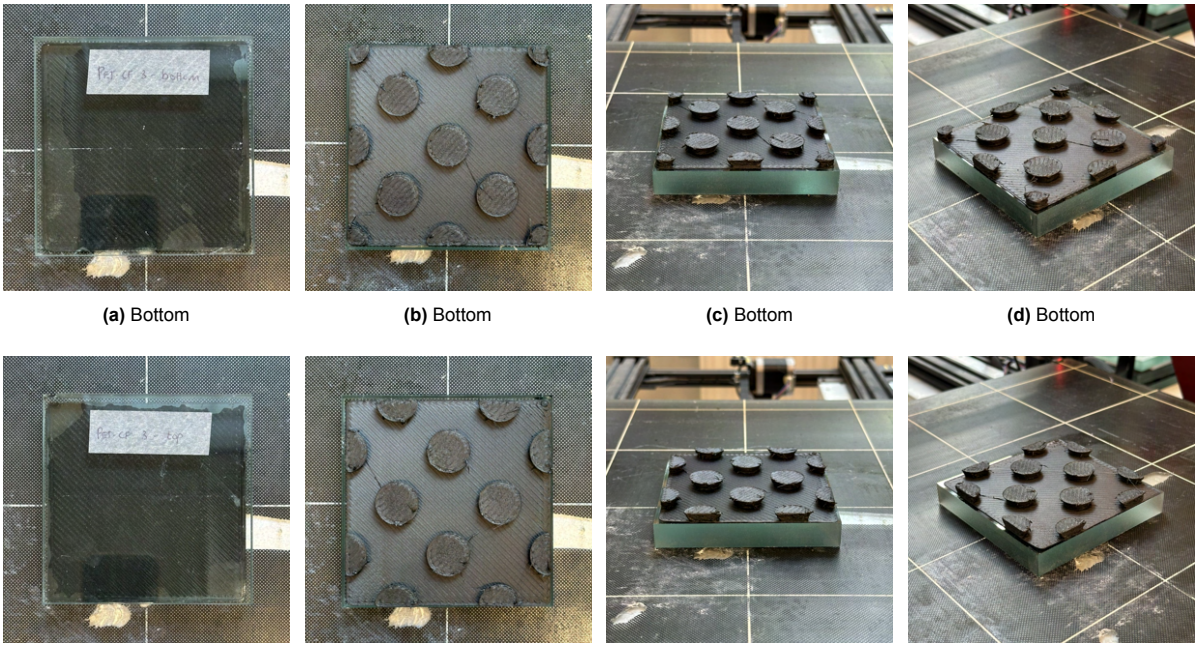

(a) Bottom **(b)** Bottom **(c)** Bottom **(d)** Bottom

(e) Top **(f)** Top **(g)** Top **(h)** Top

Figure E.24: Specimen S7 — PET-CF, Geometry 3 prior to testing

Figure E.25: Specimen S7 — PET-CF, Geometry 3 after testing

Specimen S8 — PET-CF, Geometry 4

The PET-CF-S8 specimen was tested under a normal load of 0.6 kN and a shear loading speed of 0.02 mm/s. Prior to testing, the bottom half showed moderate to severe initial delamination, especially near the corners, while the top half showed only very minor initial delamination (see Figure E.27). During loading, the specimen reached a peak shear force of **853.6 N** at **0.99 mm** sliding displacement, with a maximum recorded displacement of **6.49 mm**. The stiffness analysis showed an initial stiffness of **1124.4 N/mm** between 10–20% of the peak load, decreasing to **801.1 N/mm** between 10–40%, while the overall 0–peak stiffness was **864.0 N/mm**. At peak load, the average shear stress reached approximately **0.19 MPa** over the reduced base area of **4589 mm^2** and approximately **0.60 MPa** over the effective knob area of **1428 mm^2**. Failure occurred mainly through **delamination**, combined with **tensile rupture** of one of the smaller interlayer regions that remained attached after the largest part had detached. The moderate to severe initial delamination of the bottom half strongly influenced the failure behaviour, resulting in full delamination at a relatively low shear force. The tensile rupture occurred in one corner where the applied force was perpendicular to the printed layer lines in the base, highlighting the anisotropic weakness introduced by the parallel layer deposition direction. After the initial peak, the specimen showed several unstable force fluctuations followed by a gradual reduction in residual resistance.

Overall, PET-CF-S8 confirms that geometry 4 is highly sensitive to reduced bonded surface area and initial delamination. In this specimen, the organic cross-hatch base pattern did not provide sufficient interface reliability, and the observed tensile rupture further shows that print direction becomes critical when thin base regions are loaded perpendicular to their layer lines.

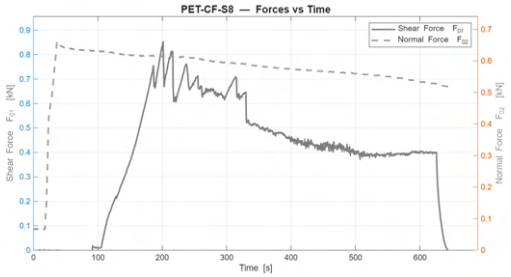

(a) Shear and normal force over time

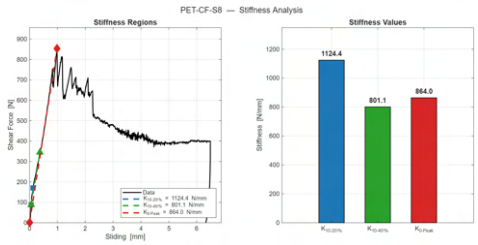

(b) Stiffness analysis

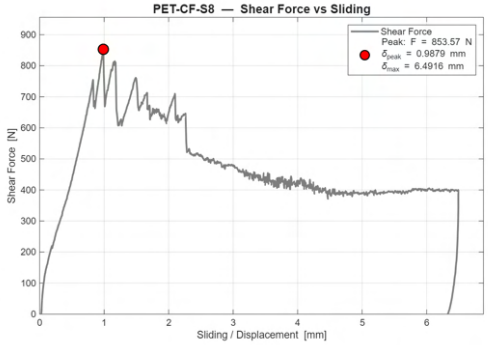

(c) Shear force-sliding displacement response

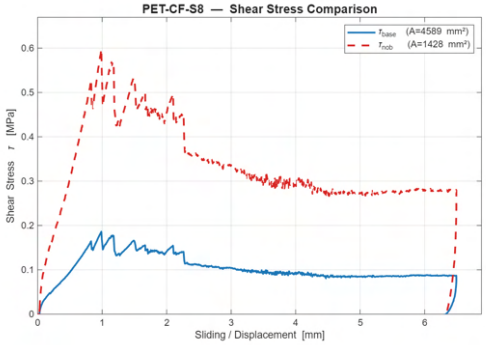

(d) Shear stress comparison based on base area and knob area

Figure E.26: Results for specimen S8 — PET-CF, Geometry 4

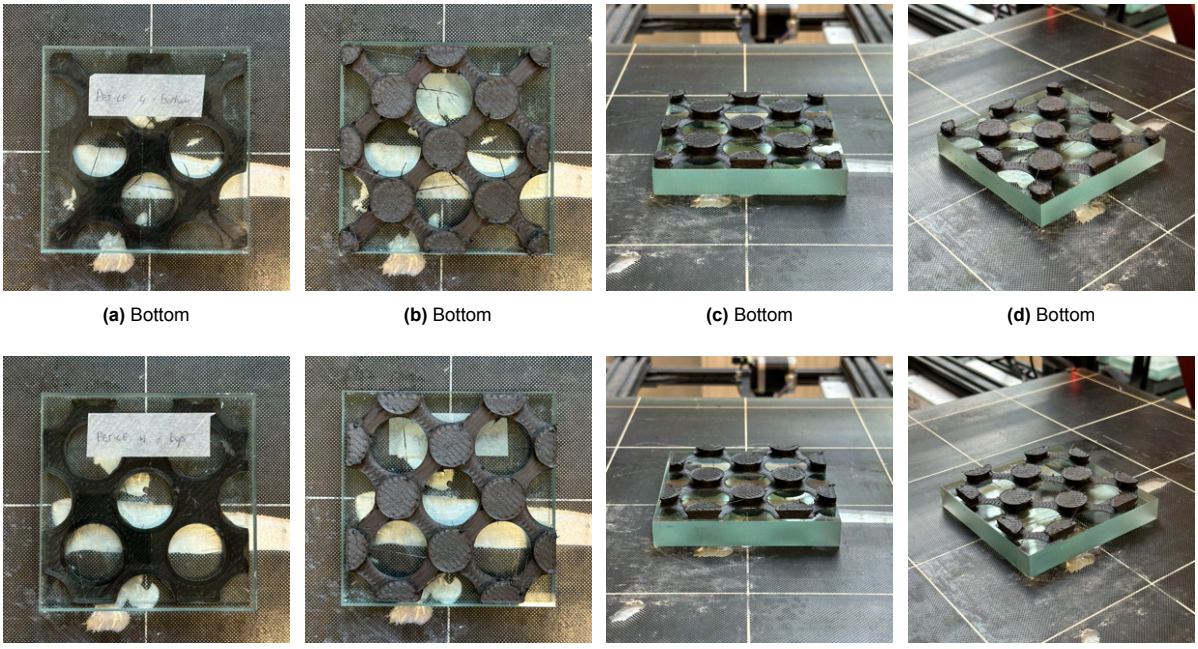

(a) Bottom **(b)** Bottom **(c)** Bottom **(d)** Bottom

(e) Top **(f)** Top **(g)** Top **(h)** Top

Figure E.27: Specimen S8 — PET-CF, Geometry 4 prior to testing

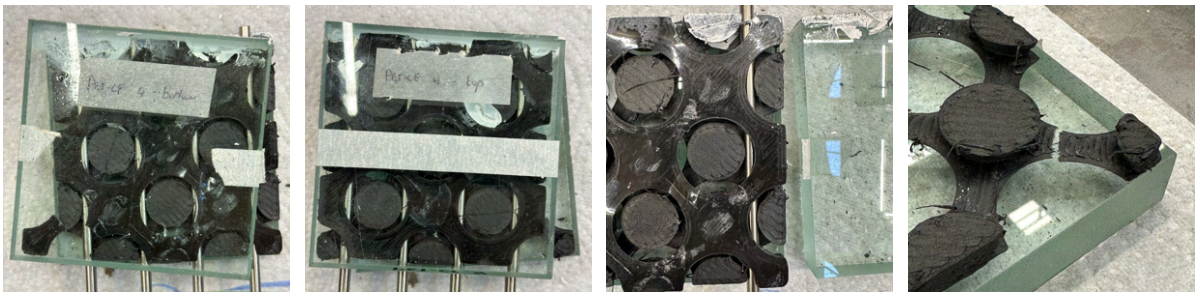

Figure E.28: Specimen S8 — PET-CF, Geometry 4 after testing

Specimen S9 — PETG-GF, Geometry 1

The PETG-GF-S9 specimen was tested under a normal load of 0.6 kN and a shear loading speed of 0.02 mm/s. Prior to testing, the bottom half showed moderate initial delamination, while the top half showed severe initial delamination. In addition, major glass chipping was already visible directly underneath the full and half knobs before the start of the shear test (see Figure E.30). During loading, the specimen reached a peak shear force of **1184.7 N** at **1.81 mm** sliding displacement, with a maximum recorded displacement of **4.27 mm**. The stiffness analysis showed a high initial stiffness of **2246.2 N/mm** between 10–20% of the peak load, decreasing to **864.1 N/mm** between 10–40% and **655.0 N/mm** over the full 0–peak range. This indicates a stiff initial response followed by sudden degradation of the effective connection stiffness as the already damaged interface became increasingly unstable. At peak load, the average shear stress reached approximately **0.13 MPa** over the base area of **9211 mm^2** and approximately **0.59 MPa** over the effective knob area of **1994 mm^2**. Failure occurred through sudden **full delamination** of the interlayer. After delamination, the specimen retained only a low residual resistance governed by frictional contact. Severe glass chipping was observed after testing directly underneath the full knob and half knobs, but not underneath the quarter knobs at the corners. However, this damage was mainly already present before loading, indicating that the material–geometry combination had already compromised the glass substrate prior to mechanical testing.

Overall, PETG-GF-S9 shows that geometry 1 combined with PETG-GF is problematic, as severe initial delamination and local glass damage prevented the interlayer from developing enough shear resistance and a controlled mechanical failure mode.

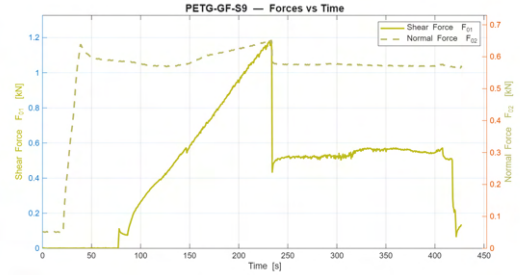

(a) Shear and normal force over time

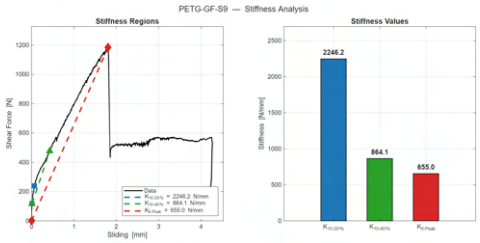

(b) Stiffness analysis

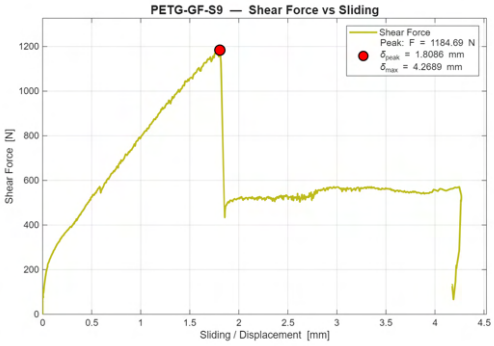

(c) Shear force-sliding displacement response

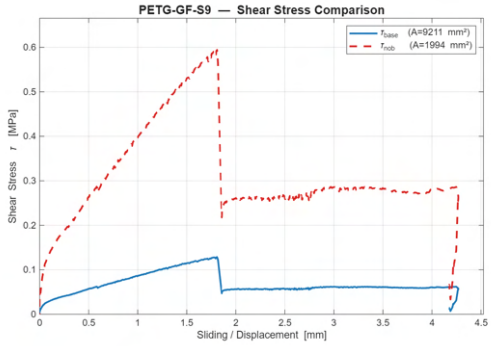

(d) Shear stress comparison based on base area and knob area

Figure E.29: Results for specimen S9 — PETG-GF, Geometry 1

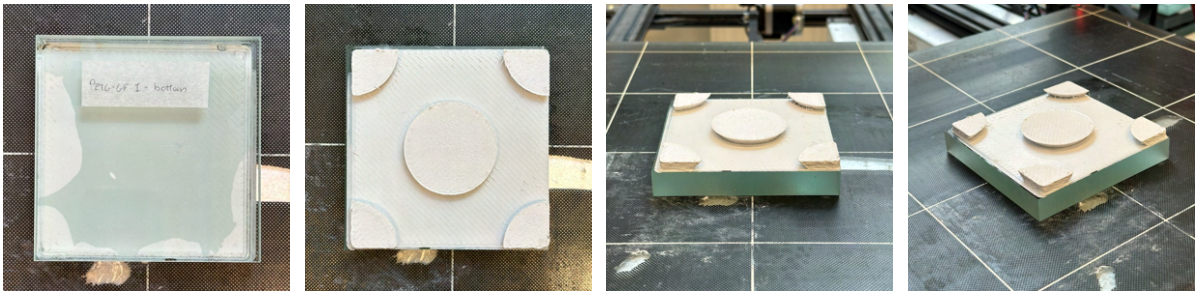

(a) Bottom **(b)** Bottom **(c)** Bottom **(d)** Bottom

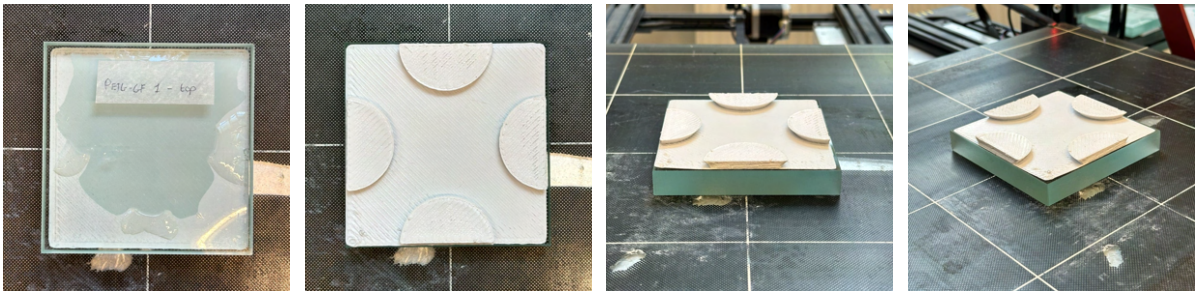

(e) Top **(f)** Top **(g)** Top **(h)** Top

Figure E.30: Specimen S9 — PETG-GF, Geometry 1 prior to testing

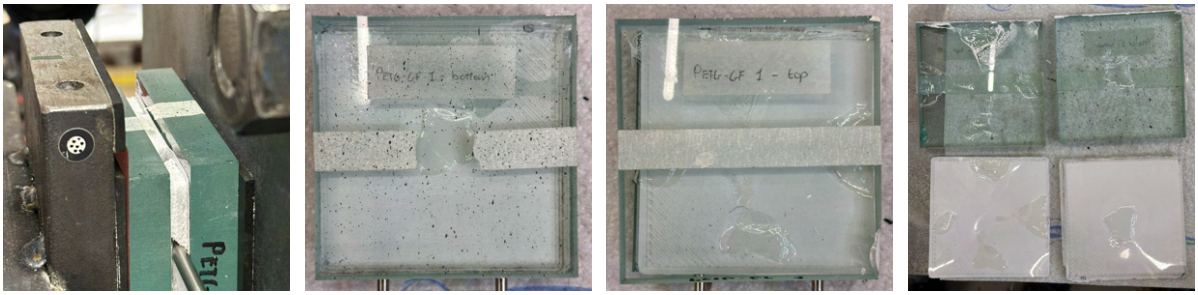

Figure E.31: Specimen S9 — PETG-GF, Geometry 1 after testing

Specimen S10 — PETG-GF, Geometry 2

The PETG-GF-S10 specimen was tested under a normal load of 0.6 kN and a shear loading speed of 0.02 mm/s. Prior to testing, the bottom half showed major initial delamination in one of the four corners, while the top half showed only minor edge delamination (see Figure E.33). During loading, the specimen reached a peak shear force of **2613.6 N** at **2.74 mm** sliding displacement, with a maximum recorded displacement of **6.38 mm**. The stiffness analysis showed a stiffness of **1148.0 N/mm** between 10–20% of the peak load, **944.7 N/mm** between 10–40%, and **954.9 N/mm** over the full 0–peak range. This indicates a relatively consistent initial loading response, although the later force drops show that the interface became unstable before final failure. At peak load, the average shear stress reached approximately **0.28 MPa** over the base area of **9211 mm^2** and approximately **3.07 MPa** over the effective knob area of **850 mm^2**. Failure occurred through sudden **full delamination** of the interlayer. After two minor drops, the specimen still showed temporary residual resistance, but this was followed by a further major sudden loss of capacity and a final low residual plateau. Moderate glass substrate damage was observed after testing.

Overall, PETG-GF-S10 reached a considerably higher shear force than PETG-GF-S9, but the governing failure mechanism remained sudden delamination. This indicates that geometry 2 can transfer higher loads than geometry 1 for PETG-GF, but the interface reliability remains insufficient for a controlled and reversible structural connection.

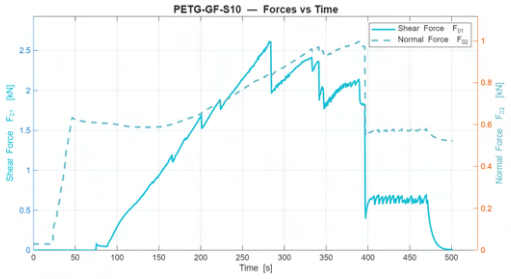

(a) Shear and normal force over time

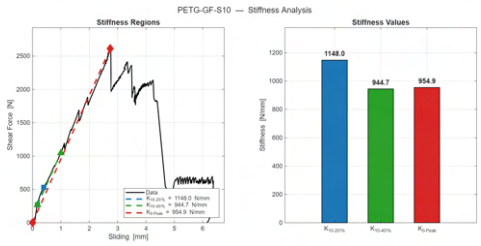

(b) Stiffness analysis

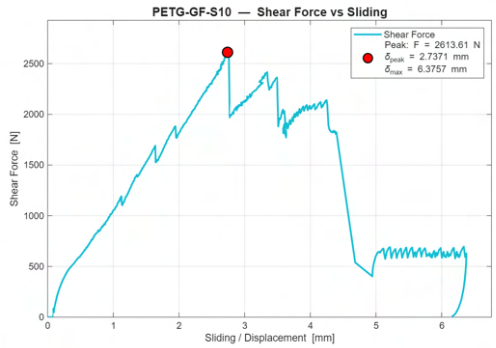

(c) Shear force-sliding displacement response

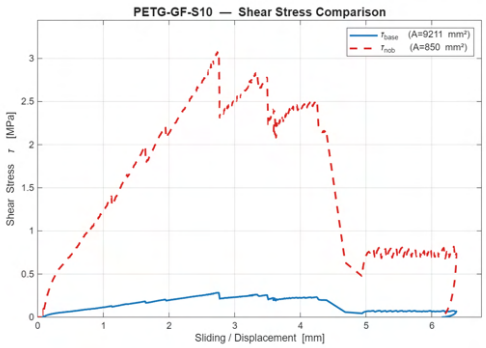

(d) Shear stress comparison based on base area and knob area

Figure E.32: Results for specimen S10 — PETG-GF, Geometry 2

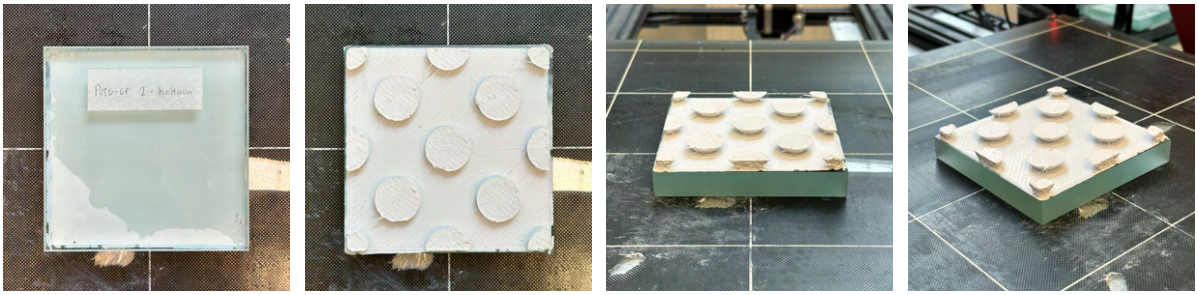

(a) Bottom **(b)** Bottom **(c)** Bottom **(d)** Bottom

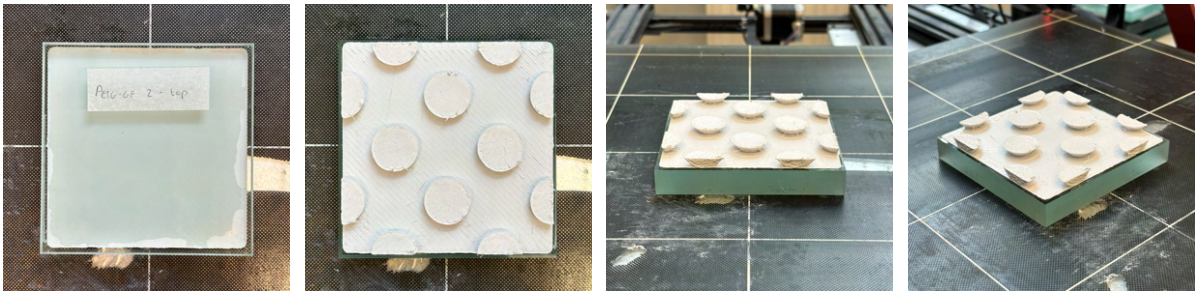

(e) Top **(f)** Top **(g)** Top **(h)** Top

Figure E.33: Specimen S10 — PETG-GF, Geometry 2 prior to testing

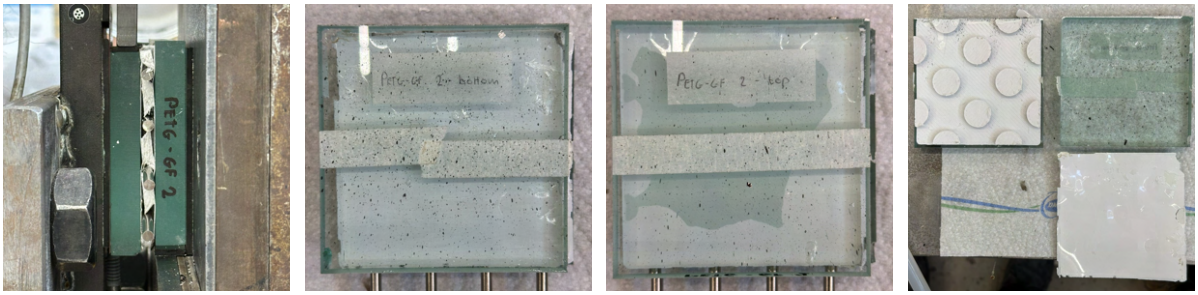

Figure E.34: Specimen S10 — PETG-GF, Geometry 2 after testing

Specimen S11 — PETG-GF, Geometry 3

The PETG-GF-S11 specimen was tested under a normal load of 0.6 kN and a shear loading speed of 0.02 mm/s. Prior to testing, both the top and bottom halves showed minor initial edge delamination consistently around the full perimeter (see Figure E.36). During loading, the specimen reached a peak shear force of **1773.7 N** at **2.05 mm** sliding displacement, with a maximum recorded displacement of **6.40 mm**. The stiffness analysis showed a high initial stiffness of **2098.0 N/mm** between 10–20% of the peak load, decreasing to **798.7 N/mm** between 10–40% and **866.7 N/mm** over the full 0–peak range. This indicates a stiff initial response, followed by progressive interface instability before the main failure event. At peak load, the average shear stress reached approximately **0.19 MPa** over the base area of **9211 mm^2** and approximately **1.24 MPa** over the effective knob area of **1432 mm^2**. Failure occurred through sudden **full delamination** of the interlayer. After the main drop in force, the specimen retained a lower residual resistance for a limited displacement range, but this response was governed by the damaged interface rather than by controlled mechanical engagement of the knobs. Moderate glass substrate damage was observed after testing (see Figure E.37).

Overall, PETG-GF-S11 confirms the recurring behaviour of the PETG-GF series: even with only minor initial delamination, the governing failure mode remained sudden full delamination. This suggests that the PETG-GF interface is, in general and independent from geometry, not reliable enough for the intended interlayer application.

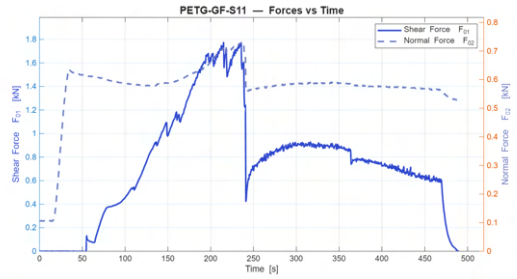

(a) Shear and normal force over time

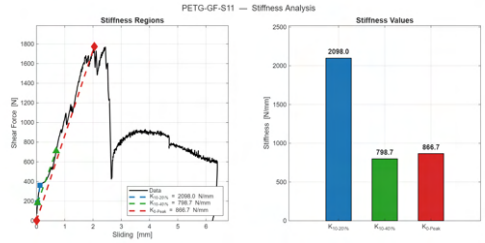

(b) Stiffness analysis

(c) Shear force-sliding displacement response

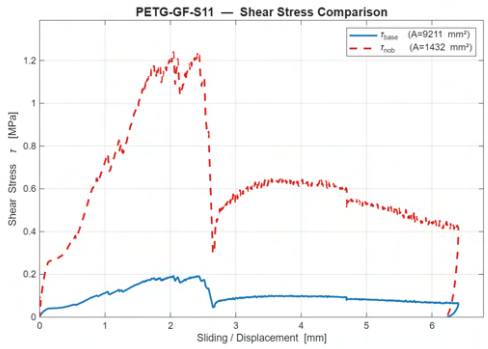

(d) Shear stress comparison based on base area and knob area

Figure E.35: Results for specimen S11 — PETG-GF, Geometry 3

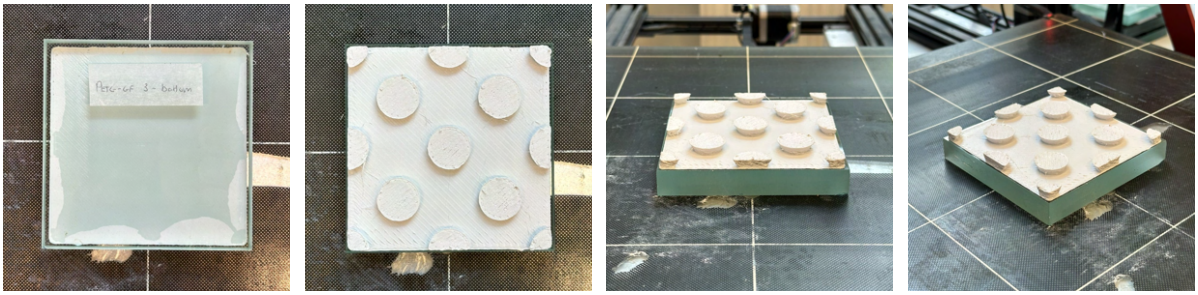

(a) Bottom **(b)** Bottom **(c)** Bottom **(d)** Bottom

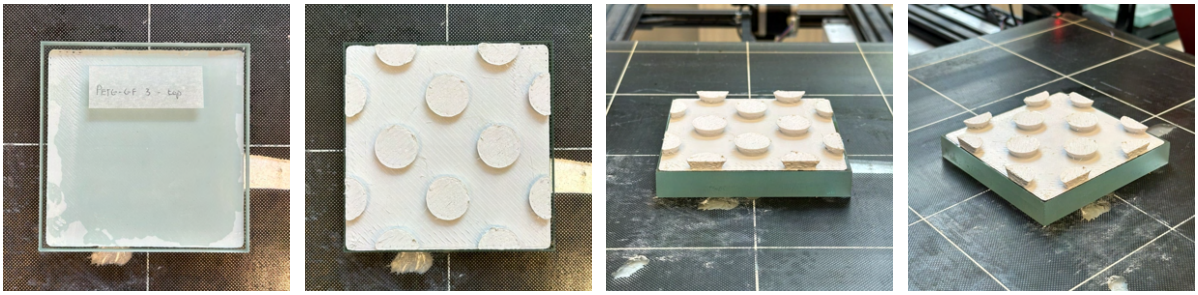

(e) Top **(f)** Top **(g)** Top **(h)** Top

Figure E.36: Specimen S11 — PETG-GF, Geometry 3 prior to testing

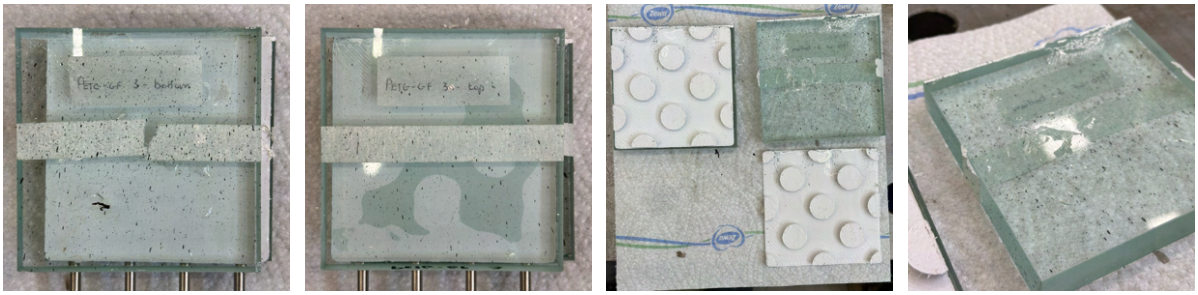

Figure E.37: Specimen S11 — PETG-GF, Geometry 3 after testing

Specimen S12 — PETG-GF, Geometry 4

The PETG-GF-S12 specimen was tested under a normal load of 0.6 kN and a shear loading speed of 0.02 mm/s. Prior to testing, the bottom half showed very severe initial delamination, with only the central region still visibly adhering to the glass. The top half showed slightly more remaining bonded areas, but also suffered from major to severe initial delamination (see Figure E.39). During loading, the specimen reached a peak shear force of **617.7 N** at **1.69 mm** sliding displacement, with a maximum recorded displacement of **8.36 mm**. The stiffness analysis showed an initial stiffness of **1443.0 N/mm** between 10–20% of the peak load, decreasing to **686.3 N/mm** between 10–40% and **365.0 N/mm** over the full 0–peak range. This strong reduction indicates that the already compromised interface progressively degraded during loading. At peak load, the average shear stress reached approximately **0.13 MPa** over the reduced base area of **4589 mm^2** and approximately **0.43 MPa** over the effective knob area of **1428 mm^2**. Failure occurred through **full delamination** of the interlayer, governed primarily by the severe initial delamination already present before testing. After the peak load, the specimen showed a gradual reduction in resistance over a large displacement range, suggesting sliding and frictional contact rather than effective mechanical engagement. No visible glass substrate damage was observed after testing.

Overall, PETG-GF-S12 confirms that geometry 4 is not mechanically reliable for PETG-GF in this configuration. The reduced base area, combined with severe initial delamination, prevented the interlayer from developing sufficient adhesion and properly activating the intended interlocking mechanism.

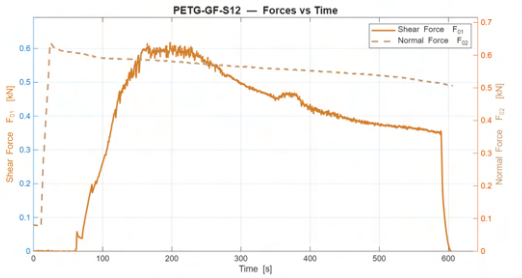

(a) Shear and normal force over time

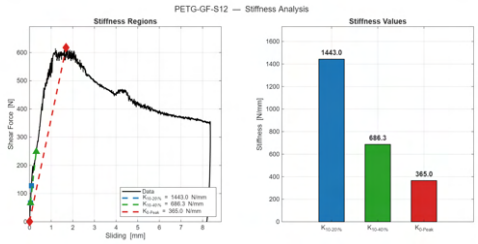

(b) Stiffness analysis

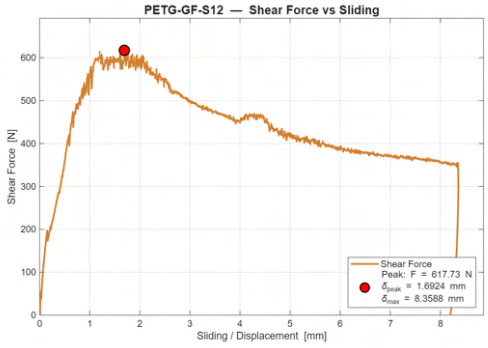

(c) Shear force-sliding displacement response

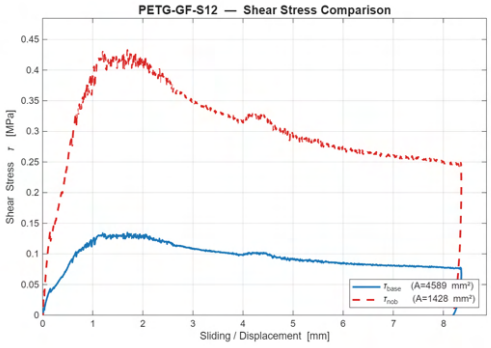

(d) Shear stress comparison based on base area and knob area

Figure E.38: Results for specimen S12 — PETG-GF, Geometry 4

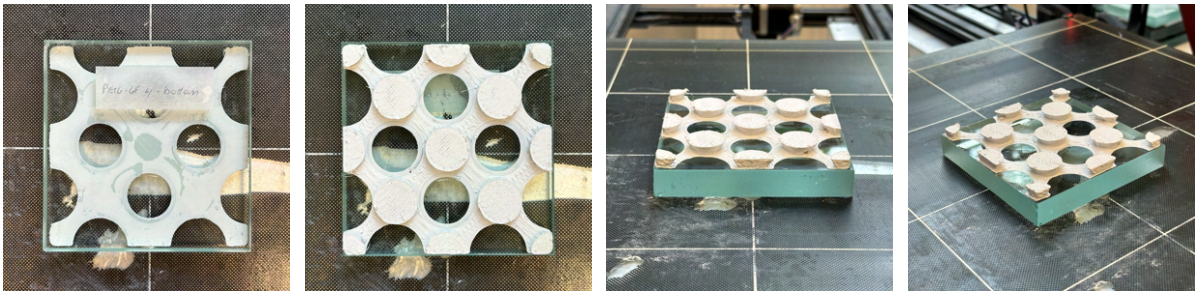

(a) Bottom **(b)** Bottom **(c)** Bottom **(d)** Bottom

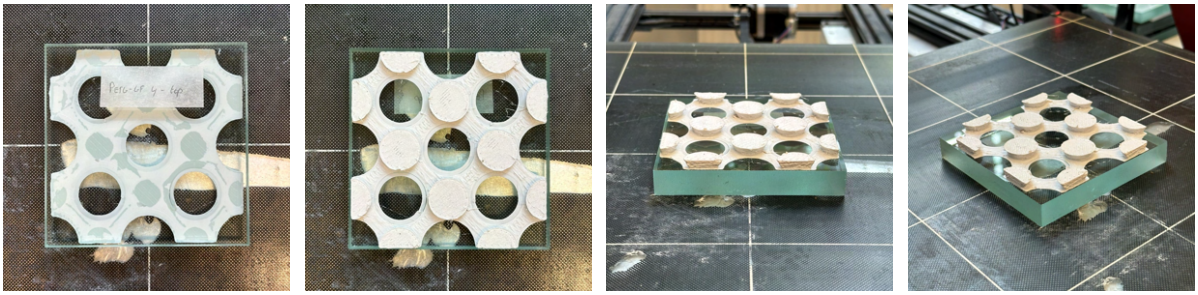

(e) Top **(f)** Top **(g)** Top **(h)** Top

Figure E.39: Specimen S12 — PETG-GF, Geometry 4 prior to testing

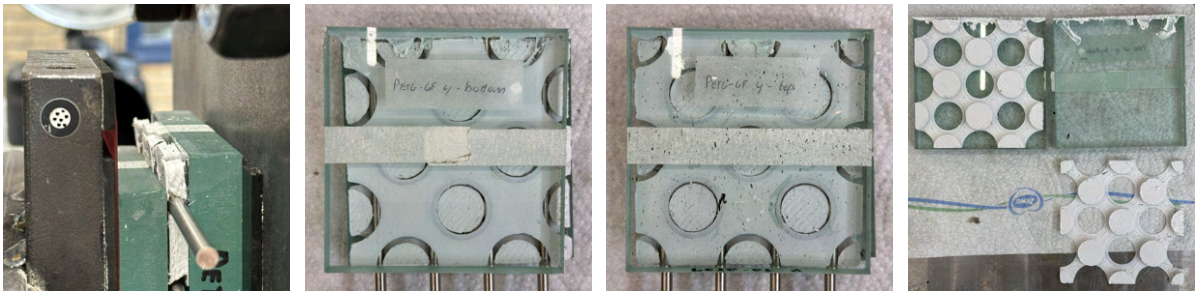

Figure E.40: Specimen S12 — PETG-GF, Geometry 4 after testing

E.6. Comparative analysis of all tested specimens

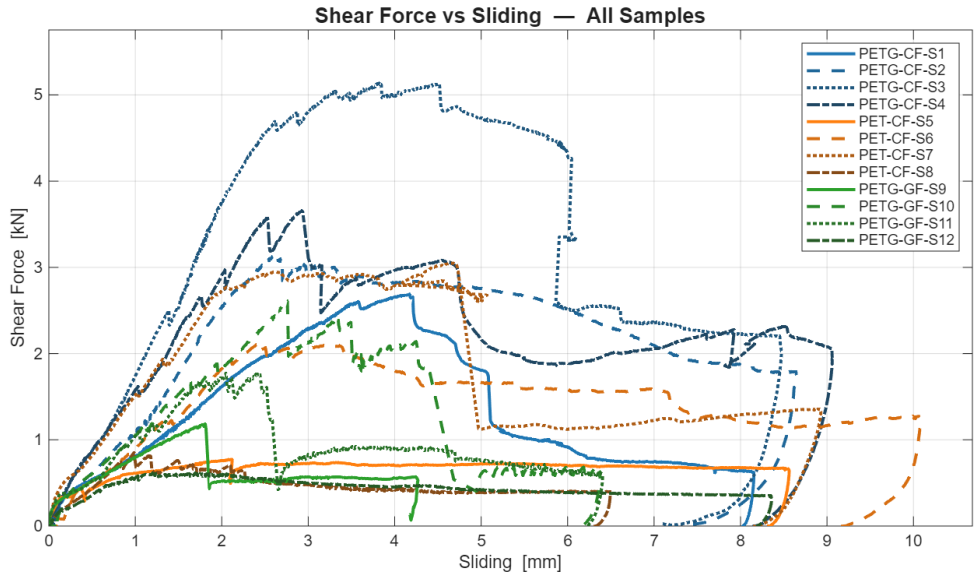

Figure E.41: Combined shear force–displacement response of all tested specimens, showing differences in load-bearing capacity, post-peak behaviour, and displacement at failure across the tested material–geometry combinations

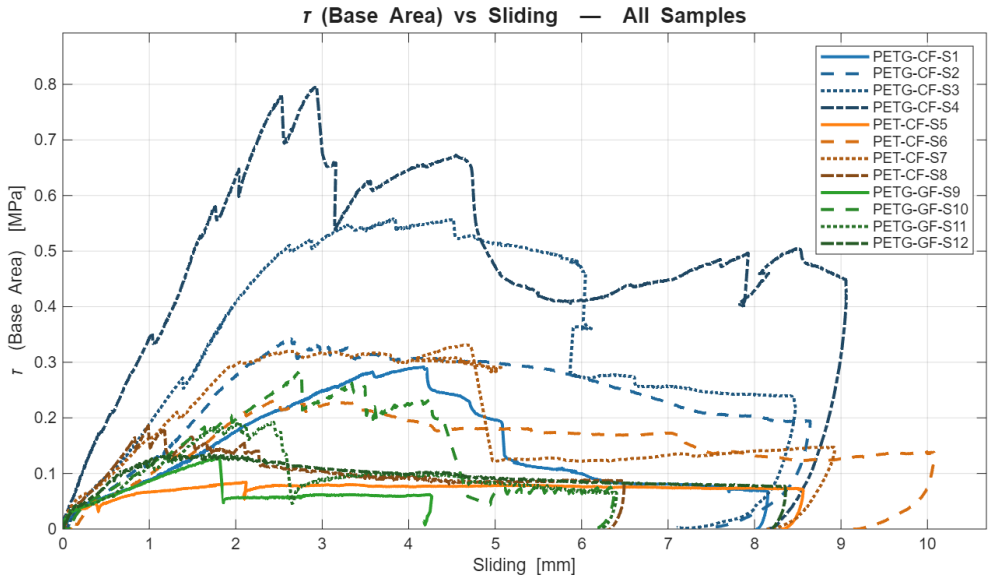

Figure E.42: Combined base-area shear stress–displacement response of all tested specimens, showing differences in stress capacity, post-peak behaviour, and displacement at failure across the tested material–geometry combinations.

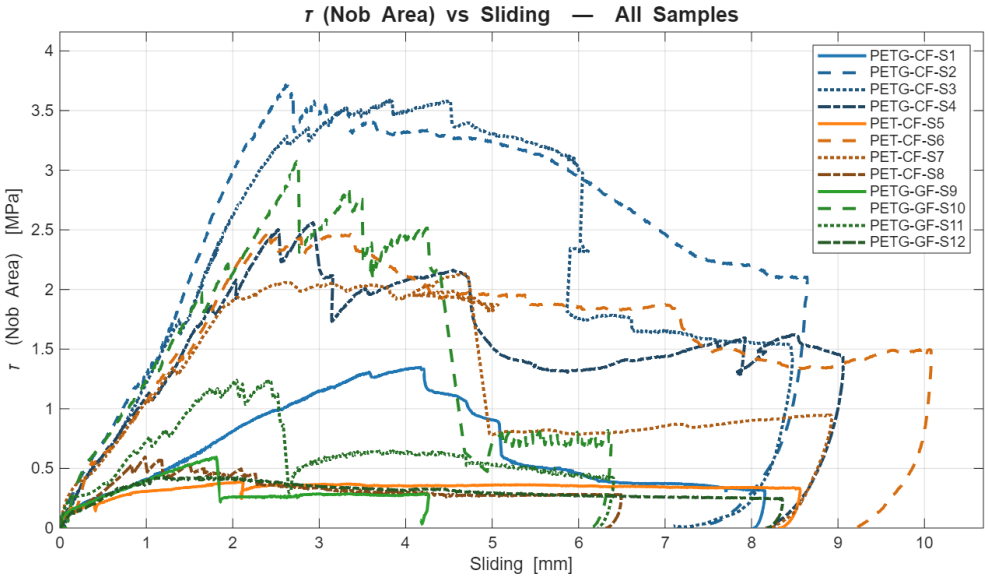

Figure E.43: Combined knob-area shear stress–displacement response of all tested specimens, showing differences stress capacity, post-peak behaviour, and displacement at failure across the tested material–geometry combinations.

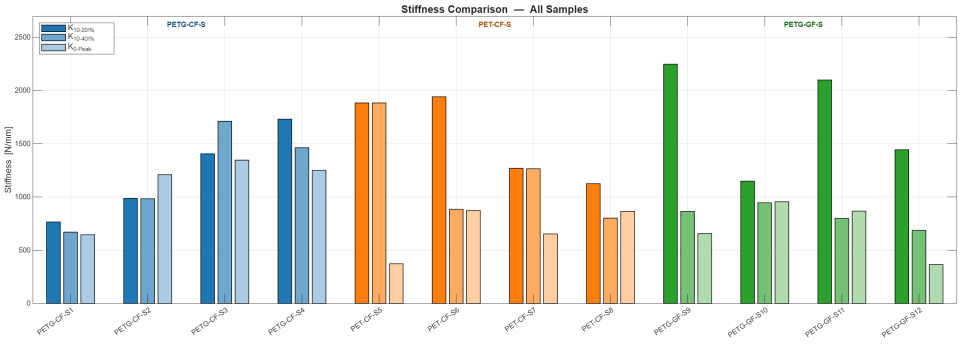

Figure E.44: Comparison of the calculated stiffness values for all tested specimens, showing the stiffness between 10–20%, 10–40%, and 10%–peak load intervals for each material–geometry combination

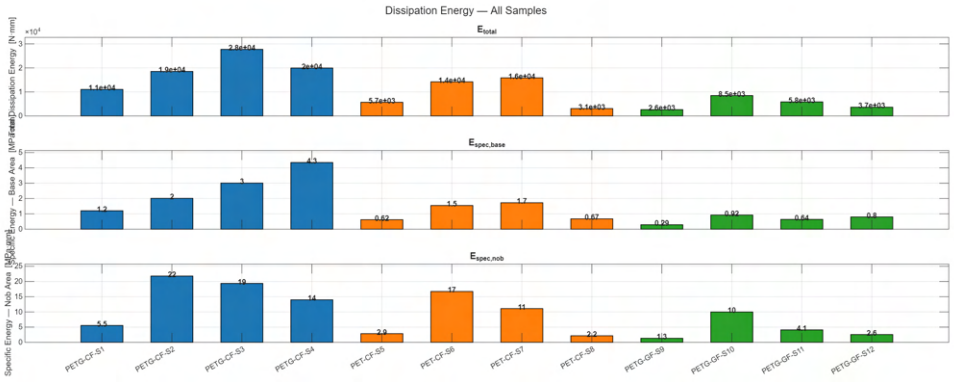

Figure E.45: Comparison of energy dissipation for all tested material–geometry combinations, including total dissipated energy, base-area specific energy dissipation, and knob-area specific energy dissipation